

Electronic Thesis and Dissertation Repository

---

5-17-2021 10:00 AM

# A Study of The Deep Learning-based Monitoring and Efficient Numerical Modeling Methodologies for Crystallization Processes

Yuanyi Wu, *The University of Western Ontario*

Supervisor: Rohani, Sohrab, *The University of Western Ontario*

A thesis submitted in partial fulfillment of the requirements for the Doctor of Philosophy degree in Chemical and Biochemical Engineering

© Yuanyi Wu 2021

Follow this and additional works at: <https://ir.lib.uwo.ca/etd>



Part of the [Process Control and Systems Commons](#)

---

## Recommended Citation

Wu, Yuanyi, "A Study of The Deep Learning-based Monitoring and Efficient Numerical Modeling Methodologies for Crystallization Processes" (2021). *Electronic Thesis and Dissertation Repository*. 7813. <https://ir.lib.uwo.ca/etd/7813>

This Dissertation/Thesis is brought to you for free and open access by Scholarship@Western. It has been accepted for inclusion in Electronic Thesis and Dissertation Repository by an authorized administrator of Scholarship@Western. For more information, please contact [wlsadmin@uwo.ca](mailto:wlsadmin@uwo.ca).

## Abstract

Driven by the increasing demands of producing consistent and high-quality crystals for high value-added products such as pharmaceutical ingredients, the operation and design of a crystallization process have phased from an empirical trial-and-error approach to the modern frameworks powered by the online process analytical technologies (PATs) and model-based process optimization techniques.

The one-dimensional crystal size distribution (CSD) measured by the well-established PATs is inadequate due to the missing particle morphology information. A major contribution of this thesis is to develop an image analysis-based PAT powered by the deep learning image processing techniques, whose accuracy and functionality outperformed the traditional PATs and other image analysis techniques. The PAT was deployed to monitor and study the slurry mixture of glass beads and catalyst particles as well as a taurine-water batch crystallization process. The results confirmed the superb accuracy of two-dimensional size and shape characterization in a challengingly high solids concentration. The classification capability enabled unparalleled functionalities including quantification of agglomeration level and characterization of different polymorphs based on their distinct appearances. A computerized crystallization platform was built with the developed PAT, which could automate the time-consuming experiments for determining the metastable zone width (MSZW) and induction time of a crystallization system. The application of the PAT revealed the potential to simplify and speed up the research and development stage of a crystallization process.

The rich two-dimensional crystal size and shape information provided by our PAT enabled more descriptive multi-dimensional modeling for the better prediction of the crystallization process. The novel population array (PA) solver developed in this thesis could solve the multi-dimensional crystallization population balance equation (PBE) more computationally efficient than the existing discretization-based numerical methods without compromising the accuracy. The PA solver could accurately model the complex phenomena including agglomeration, breakage, and size-dependent growth. The efficient computation enables solving the complex multi-dimensional PBE for crystal morphology modeling. The combination of the innovative PAT and modeling technique is a significant contribution to

the crystallization field that enables better understanding and more effective control of a crystallization process.

## **Keywords**

Crystallization process; Image analysis; Deep learning; Automated experiments; Process analytical technology; Shape and size characterization; Raman spectroscopy; Parameter estimation; Solution of population balance equation

## **Summary for Lay Audience**

Many food, drug, and industrial products are in crystalline form. The size, shape, and many other attributes of the crystals will affect the process efficiency and product quality, which is especially critical for the pharmaceutical industry. Therefore, process analytical technologies (PATs) were developed to monitor the process variables and ensure product quality.

An efficient PAT instrument for the size and shape characterization, which was powered by the latest artificial intelligence algorithms was developed. The accuracy of the proposed PAT was validated by comparing the measurement results with the established particle sizing methodologies. The PAT was proven not only accurate but could also differentiate the type of the crystals and perform multi-dimensional size measurement, which was very challenging for the existing instruments. The crystal size and shape data were used to build a dynamic model to predict and optimize the product quality of a crystallization process.

The crystallization modeling helps to design optimal crystallization processes. A numerical solver was proposed to efficiently solve the mathematical model of a crystallization process. The proposed solver was tested under various scenarios. The accuracy and computational efficiency have improved compared to the conventional approaches.

The PAT and the modeling techniques were combined in the development of an automated crystallization experiment platform, which aimed to automate the repetitive and time-consuming crystallization experiments. The homemade instruments enabled automated data acquisition and process manipulation. With the automated platform, the research and development of a crystallization process could be significantly simplified.



## Co-Authorship Statement

**Chapter 2:** The experimental work, software development, and data analysis were performed by Yuanyi Wu. The manuscript was prepared by Yuanyi Wu and reviewed by Dr. Sohrab Rohani. Mengxing Lin aided this work in the data processing.

A version of this chapter has been published in *Chemical Engineering Research and Design*: Wu, Y., Lin, M. & Rohani, S. (2020). Particle characterization with on-line imaging and neural network image analysis. *Chemical Engineering Research and Design*, 157, 114-125.

**Chapter 3:** The experimental work, software development, and data analysis were performed by Yuanyi Wu. The manuscript was prepared by Yuanyi Wu and reviewed by Dr. Sohrab Rohani. Zhenguo Gao aided this work in experimental design.

A version of this chapter has been submitted to *Chemical Engineering Research and Design*: Wu, Y., Gao, Z. & Rohani, S. (2021). Deep Learning-Based Oriented Object Detection for In-Situ Image Monitoring and Analysis: A Process Analytical Technology (PAT) Application for Taurine Crystallization.

**Chapter 4:** The hardware and software development and data analysis were performed by Yuanyi Wu. The manuscript was prepared by Yuanyi Wu and reviewed by Dr. Sohrab Rohani.

A version of this chapter will be submitted to *Organic Process Chemistry and Development* under the title: Automated measurement of the MSZW and induction time: Comparison of a new platform to the existing platforms.

**Chapter 5:** The numerical algorithm and the numerical case studies were developed by Yuanyi Wu. The manuscript was prepared by Yuanyi Wu and reviewed by Dr. Sohrab Rohani.

A version of this chapter will be submitted to *AIChE Journal* under the title: A New Highly Efficient and Stable Population Array (PA) Algorithm to Solve Multi-Dimension Population Balance Equation in the Presence of Agglomeration and Breakage.

## **Acknowledgments**

The works and this thesis would not have been possible without the inspiration and support of my family, my supervisor, and my friends – my thanks and appreciation to all wonderful individuals who gave me continuous support. I would like to express my sincere gratitude to my family for their continuous and unparalleled love. I wish to express my deep appreciation to my supervisor, Dr. Sohrab Rohani, for his support and guidance throughout this work. His insightful perspectives motivated my research work in developing the essential methodologies for the crystallization field. My colleague and friends, Zhenguo Gao, Mengxing Lin, Soroush Ahmadi Nasrabadi, Pradip Mondal, and Weizhong Gong are invaluable treasures in the journey of my life. Without their enthusiasm, support, and continuous optimism my work would hardly have been completed. This thesis marks the achievement of my Ph.D. study and the milestone of my life. I would like to share my joy and happiness with every wonderful individual in my life.

# Table of Contents

Abstract.....	ii
Summary for Lay Audience.....	iv
Co-Authorship Statement.....	v
Acknowledgments.....	vi
Table of Contents.....	vii
List of Tables.....	xii
List of Figures.....	xiii
List of Appendices.....	xx
List of Acronyms.....	xxi
Chapter 1 Introduction.....	2
1.1. Introduction to Crystallization Process.....	2
1.1.1. Background of Crystallization Process.....	2
1.1.2. Crystallization in The Pharmaceutical Industry.....	4
1.2. Process Analytical Technology (PAT) in Crystallization.....	8
1.2.1. Solute Concentration PATs.....	8
1.2.2. Polymorphic Forms PATs.....	10
1.2.3. Crystal Size and Shape PATs.....	13
1.3. Crystallization Process Modeling and Simulation.....	19
1.3.1. Population Balance Equation (PBE).....	19
1.3.2. Numerical Solution of the PBE.....	20
1.4. Research Objectives and Organization of Thesis.....	22
1.4.1. Research Objectives and Approach.....	22
1.4.2. Thesis Organization.....	24
1.5. References.....	25

Chapter 2 Particle Characterization with On-line Imaging and Neural Network Image Analysis.....	34
Abstract .....	34
2.1. Introduction.....	34
2.2. Background.....	38
2.2.1. Mask RCNN.....	38
2.2.2. Training and Dataset preparation.....	39
2.2.3. Progressive Labeling Strategy .....	39
2.2.4. Neural Network Performance Evaluation.....	40
2.2.5. Particle Size Descriptor.....	41
2.2.6. Solids Concentration and Pixel Fill Ratio.....	42
2.3. Experimental Setup and Procedures .....	44
2.3.1. Neural Network Training Parameters .....	44
2.3.2. Particle Imaging Process Setup.....	45
2.3.3. Camera Scale Calibration .....	46
2.3.4. Particle Sample Preparation .....	46
2.4. Results and Discussion .....	51
2.4.1. Neural Network Training and Progressive Labeling .....	51
2.4.2. Particle Size Extrapolation Performance .....	53
2.4.3. Detection Performance in The Increasing Solids Concentration .....	56
2.4.4. Multi-species Classification and Measurement Reproducibility .....	62
2.5. Conclusions.....	63
2.6. References.....	64
Chapter 3 Deep Learning-Based Oriented Object Detection for In-Situ Image Monitoring and Analysis: A Process Analytical Technology (PAT) Application for Taurine Crystallization .....	68
Abstract .....	68

3.1. Introduction.....	69
3.2. Methodologies.....	71
3.2.1. Oriented Object Detection Model.....	71
3.2.2. Materials and Experimental Setup.....	72
3.2.3. Imaging Dataset Preparation and <i>S<sup>2</sup>A-Net</i> Model training.....	76
3.2.4. Cooling Crystallization Experiments and Image Analysis Process.....	79
3.2.5. Concentration Calibration and Measurement with Raman Spectroscopy	81
3.2.6. Secondary Nucleation and Growth Rate Estimation.....	83
3.3. Results and Discussion.....	84
3.3.1. Evaluation of Concentration Measurement Performance.....	84
3.3.2. Evaluation of Image Analysis Performance.....	86
3.3.3. Particle Counts Analysis.....	87
3.3.4. Particle Size and Shape Analysis.....	90
3.3.5. Estimation and Validation of The Kinetic Parameters.....	94
3.4. Conclusion.....	97
3.5. References.....	98
Chapter 4 Computerized Crystallization Platform for Automated Experiment and Measurements of Crystallization Parameters.....	103
Abstract.....	103
4.1. Introduction.....	103
4.2. Automated Cooling Crystallization Platform.....	107
4.3. Hardware Components.....	110
4.3.1. The IoT Microcontroller – Espressif ESP8266.....	111
4.3.2. Stirring Motor.....	112
4.3.3. Water Baths and Switch Valves.....	113
4.3.4. Imaging System.....	116

4.4. Software Architecture .....	117
4.4.1. Device Communication and Data Exchange .....	117
4.4.2. Data Hooking for Raman spectroscopy and FBRM .....	118
4.4.3. Microcontroller Firmware.....	119
4.4.4. Automated Experiment Execution .....	119
4.5. Results and Discussion .....	121
4.6. Conclusion .....	129
4.7. References.....	130
Chapter 5 A New Highly Efficient and Stable Population Array (PA) Algorithm to Solve Multi-Dimension Population Balance Equation in the Presence of Agglomeration and Breakage.....	134
Abstract .....	134
5.1. Introduction.....	135
5.2. Proposed Method .....	139
5.2.1. Nucleation and Growth Modeling .....	142
5.2.2. Agglomeration Modelling.....	143
5.2.3. Breakage Modeling.....	145
5.2.4. Continuous Operation .....	149
5.2.5. Row Compression.....	149
5.2.6. Adaptive Time Step Size .....	152
5.2.7. CSD Reconstruction.....	152
5.3. Simulation Case Studies .....	154
5.3.1. Nucleation and Growth.....	154
5.3.2. Concentration-dependent Kinetics in Batch and Continuous Crystallization Processes.....	157
5.3.3. Polymorphic Transformation .....	164
5.3.4. Agglomeration and Breakage .....	168

5.3.5. Computation Efficiency .....	176
5.4. Conclusion .....	184
5.5. References .....	185
Chapter 6 Conclusions and Recommendations.....	191
6.1. Conclusions.....	191
6.1.1. Development of Image-based PAT for Particle Size and Shape Characterization .....	192
6.1.2. Development of An Automated Crystallization Platform .....	193
6.1.3. Development of An Efficient Population Array (PA) Numerical Solver for Modelling Crystallization Process .....	194
6.2. Recommendation of The Future Works.....	195
6.3. References .....	197
Appendices.....	198
Curriculum Vitae .....	201

## List of Tables

Table 2-1 Experiments description .....	50
Table 2-2. Extrapolation test evaluation metrics .....	56
Table 2-3. Summary of the previous image analysis studies at a high solids concentration ..	62
Table 3-1 Training data statistics .....	77
Table 3-2 Summary of the crystallization kinetics of taurine analyzed by image analysis ....	97
Table 4-1 The 95% confidence of the interval metastable zone width (MSZW) of the aqueous taurine solution measured using FBRM and image analysis. ....	128
Table 4-2 The 95% confidence interval of the induction time of aqueous taurine solution measured using FBRM and image analysis. ....	129
Table 5-1 Kinetic parameters and properties of KNO <sub>3</sub> for the batch process (Miller, 1993) .....	158
Table 5-2 Kinetic parameters and properties of the polymorphic system (L-glutamic acid) (Lin, Wu & Rohani, 2020a) .....	166



## List of Figures

Figure 1-1 Schematic of the various research scales of solution crystallization: from molecular to industrial manufacturing. ....	3
Figure 1-2 The main research branches in the solution crystallization process: crystal engineering and crystallization process design and control.....	5
Figure 1-3 Schematic of the ATR-FTIR in a crystallization process .....	10
Figure 1-4 Schematics of Raman spectroscopy. (a) The energy level diagram of Rayleigh scattering and Stokes Raman scattering and anti-Stokes Raman scattering. (b) Illustration of the mechanism of an in-situ back-scattering Raman spectrometer for the crystallization process.....	12
Figure 1-5 Common particle sizing PATs for the crystallization process. ....	15
Figure 1-6 Schematic of a simple convolution operation: (a) input pixels; (b) convolution weights; (c) output; (d) convolutional block. (Manee, Zhu & Romagnoli, 2019).....	17
Figure 1-7 Three main tasks achieved by deep learning-based image analysis and the predicted outputs .....	19
Figure 1-8 Demonstration of the numerical diffusion caused by the discretization methods.	22
Figure 2-1 Schematic of progressive labeling strategy workflow .....	40
Figure 2-2 Illustration of the concepts of two PFRs. Function A stands for the area of the objects. ....	44
Figure 2-3 Flow cell imaging experimental setup .....	45
Figure 2-4 Dark-field microscopic image of (a) glass bead (un-sieved) and (b) FCC catalyst sample. ....	47
Figure 2-5 (a) Neural network training loss and validation metrics (full glass beads training set); (b) validation image with overlays of GTs and the masks predicted by the neural network (240,000 epoch training). The orange masks are true positives (TPs) (overlapping	

GT and prediction); the yellow masks are false negatives (FNs) (GT only); the red masks are false positives (FPs) (prediction only); (c) Neural network performance after 60,000 epochs with different training set sizes. .... 52

Figure 2-6 Particles small extrapolation test results with sieved glass beads sample (row 1: 20-32- $\mu\text{m}$ ; row 2: 125-150- $\mu\text{m}$ ; row 3: 150-300- $\mu\text{m}$ ). (a-c) The particle size distributions obtained by different size extraction models compared with the result from Malvern Mastersizer 2000 (converted from volume-based to number-based size distribution). The grey lines stand for the sieve size ranges.; (d-f) sample validation images with GT and prediction overlays. Refer to Figure 2-5 for the color codes. .... 55

Figure 2-7 Sample images array for the small (32-45- $\mu\text{m}$ ), medium (63-75- $\mu\text{m}$ ), and large (106-125- $\mu\text{m}$ ) glass beads samples in rows and different solids concentrations in columns (average total PFR). The detected instances were overlaid with multiple colors. .... 57

Figure 2-8 Performance evaluation results for the small (32-45- $\mu\text{m}$ ), medium (63-75- $\mu\text{m}$ ), and large (106-125- $\mu\text{m}$ ) glass beads samples at different solids concentrations. (a)-(c) the size distribution statistics (D90, D50, D10, and mean) and the PFR at the increasing solids concentrations. The Mastersizer 2000 number-based size statistics (horizontal dash lines) were included for reference; (d) The validation metrics at increasing solids concentrations (PFR) and the baselines; (e) The average number of detected particles per frame at various *PFRT* levels; (f) The simulated and experimental overlapping ratio at various *PFRT* levels 59

Figure 2-9 Sample images with overlays colored based on the classification results (Red: glass beads, blue: FCC particle). (a) an image captured in pure glass beads sample; (b) an image captured in pure FCC particle sample; (c) an image captured in the mixture; (d) area equivalent circle distributions of glass beads and FCC before and after mixing..... 62

Figure 3-1 PXRD pattern of taurine crystal. The sample and simulated curves were obtained from the ground sample from BioShop Inc. and the Mercury simulation, respectively..... 73

Figure 3-2 (a) Dark field microscopy of the prepared seeds. (b) 2D size distribution of the seeds ..... 74

Figure 3-3 Schematic diagram of the experimental setup ..... 76

Figure 3-4 (a) The equivalent label formats. i, ii: the longer edge as height (h); iii, iv: the shorter edge as height. i, iii: angle  $\alpha$  between  $0, \pi$ ; ii, iv: angle  $\alpha$  between  $-\pi, 0$ . (b) Example of a labelled training image. The red and blue bounding boxes are labels of crystals and clusters, respectively. .... 78

Figure 3-5 Image analysis flow diagram. The red and blue labels are crystal and cluster, respectively. .... 81

Figure 3-6 The performance summary of the concentration measurement with Raman spectroscopy. (a) the visualization of a cycle of unseeded crystallization. (b) the distribution of relative training errors (c) The graph of actual concentration versus the concentration predicted by the Raman spectroscopy..... 85

Figure 3-7 The performance summary of the image analysis. ACC and REC stand for accuracy and recall metrics, respectively..... 87

Figure 3-8 The particle and cluster counts and the solute concentration (Conc.) during the linear cooling experiments ( $0.5 \text{ }^{\circ}\text{C}/\text{min}$ ) of (a) unseeded, (b) 1% seed loading, and (c) 3% seed loading. The solubility (Sol.) was computed with the model (Wu et al., 2017). The dashed lines of FBRM counts were the missing data due to probe contamination. The breakout frame in (a) showed the detected crystals at the onset of nucleation. .... 88

Figure 3-9 Visualization of the online images and the analysis result of the unseeded and seeded experiments at 1) nucleation onset or seed addition, 2) after the temperature dropped by  $0.5 \text{ }^{\circ}\text{C}$ , 3) when the temperature reached  $25 \text{ }^{\circ}\text{C}$ , and 4) final state. The bounding boxes were padded and enlarged by 5 pixels ( $8 \mu\text{m}$ ) in each direction for better viewing. Each frame was cropped to one-quarter of its original size. The red and blue labels stand for crystals and clusters, respectively. .... 90

Figure 3-10 The crystal size and shape (aspect ratio) trends during the linear cooling experiments ( $0.5 \text{ }^{\circ}\text{C}/\text{min}$ ) of (a) unseeded, (b) 1% seed loading, and (c) 3% seed loading. The data before nucleation onset in (a) were ignored. The shaded areas show the 10<sup>th</sup>-quantile ( $D_{10}$ ) to the 90<sup>th</sup>-quantile ( $D_{90}$ ) ranges of each statistic and the solid lines were the median ( $D_{50}$ ). The height is the longer edge in the image analysis result. .... 92

Figure 3-11 The 2D CSDs of the seeds and the products of 1% and 3% seed loading experiments. The marginal histograms are the count-based size distribution of each dimension; the marginal filled curves are the volume-weighted size distribution of each dimension.....	93
Figure 3-12 a, b: results of the nucleation and growth rate estimation; c (unseeded run), d (1% seed loading run), e (3% seed loading): experimental data and simulation results with the estimated kinetic parameters.....	96
Figure 4-1 A commercial automated crystallization platform (Mettler Toledo EasyMax) (Mettler Toledo, 2021).....	106
Figure 4-2 Temperature profiles of rapid cooling and linear cooling experiments .....	109
Figure 4-3 Schematic of the automated crystallization platform.....	111
Figure 4-4 WeMos D1 mini ESP8266 board.....	112
Figure 4-5 The stirring motor and the optical RPM measurement sensor.....	113
Figure 4-6 Two thermostat water baths and the switch valves.....	114
Figure 4-7 The switching valves and the operation configurations.....	115
Figure 4-8 The flow-through cell imaging system .....	117
Figure 4-9 Software architecture and data flow of the platform.....	118
Figure 4-10 Flow chart of the automated linear cooling and rapid cooling experiments. The blue blocks are the procedures requiring human intervention, and the black blocks are the automated tasks.....	121
Figure 4-11 Temperature profiles of the linear and rapid cooling experiments for the aqueous taurine solution saturated at 30 °C.....	122
Figure 4-12 Nucleation onset detection during the linear cooling experiment (0.1 °C/min) using different techniques. The saturated temperature is 30 °C.....	125

Figure 4-13 Nucleation onset detection during the rapid cooling experiment (supercooling temperature = 28.5 °C) using different techniques. The saturated temperature is 30 °C. .... 126

Figure 4-14 Undesired objects (a, b) that may cause false detection of nucleation and the true nucleation onset (c) with crystals detected in the consecutive images. .... 127

Figure 5-1 Flow diagram of simulating a crystallization process with the proposed method. .... 141

Figure 5-2 Illustration of two-dimensional agglomeration along the internal coordinates. (a) the grid representation of agglomeration. Each scattering point represents the location of a row in the population array.  $\Omega_1$  and  $\Omega_2$  are the agglomeration domain of the crystal represented by the row  $ra$ . (b) the visualization of the agglomeration along the two internal coordinates. Note that the agglomerate dimensions are not the summation of the agglomerating dimensions but calculated from the conserved volume. .... 145

Figure 5-3 (a) Illustration of one-dimensional breakage on a volume grid for uniform and parabolic probability distributions. The size of the points represents the relative count of the daughter crystals; (b) demonstration of two-dimensional and three-dimensional breakage by cuts along the breakage dimensions; (c) visualization of two-dimensional breakage. Note that the grid is not linear if the volume power of the breaking dimension is not one. .... 148

Figure 5-4 Illustration of row compression procedures of a one-dimensional and a two-dimensional population array. .... 150

Figure 5-5 Demonstration of the effect of the grid interval on the reconstructed CSD. .... 153

Figure 5-6 Batch crystallization simulation results obtained with the high-resolution (HR), upwind (UW), and population array (PA) methods compared with the analytical solutions. (a) One-dimensional growth-only simulation ( $G = 0.7\mu m/s$ ,  $\Delta t = 1 s$ ,  $\Delta L = 1 \mu m$ , and  $t_{end} = 200 s$ ). (b) CSD contours of the two-dimensional growth-only simulation of a step initial condition. (c) Constant nucleation and growth simulation ( $B = 105 \# \cdot m^{-3} \cdot s^{-1}$ ,  $G = 0.7\mu m/s$ ,  $\Delta t = 1 s$ ,  $\Delta L = 1 \mu m$ ). PAC: the rows in the population array are compressed to a grid of  $1 \mu m$  interval at the end of each simulation step. (d) Size-dependent growth simulation case solved analytically by Ramabhadran et al. (1976). .... 156

Figure 5-7 Concentration-dependent kinetics and size-dependent growth simulation for a batch process. (a) Initial and final CSD simulated with high resolution (HR), upwind (UW), population array (PA), and population array with row compression (PAC). (b) CSD of the crystals grown from the seeds. (c) Concentration profiles. (d) Crystal count profiles. The intervals of the coarse and fine grids are  $0.5 \mu\text{m}$  and  $0.1 \mu\text{m}$ , respectively..... 160

Figure 5-8 Concentration-dependent kinetics and size-dependent growth simulation for a continuous process. The suffixes +, -, 0 stand for positive, negative size-dependent and size-independent growth kinetics a) steady-state CSD simulated with various numerical methods. b) Relative concentration profile of the positive size-dependent growth. c) Count profile of the positive size-dependent growth..... 163

Figure 5-9 The simulated concentration, crystal counts, and crystal volumes profile of the polymorphic transformation from the unstable  $\alpha$ -form to the stable  $\beta$ -form crystals. (a-c): nucleation-limiting case; (d-f): dissolution-limiting case. .... 167

Figure 5-10 Relative error of the concentration profile compared to the results simulated with the smallest time step (scaled by 0.1). The curves depict the mean relative error and the shaded areas show the 90% confidence interval..... 168

Figure 5-11 Simulation results of one-dimensional agglomeration and breakage. (a) constant agglomeration kernel on a linear size grid; (b) constant agglomeration kernel on a logarithmic volume grid; (c) linear-volume breakage kernel  $\beta = v$  on a logarithmic volume grid; (d) squared-volume breakage kernel ( $\beta = v^2$ ) on a logarithmic volume grid. .... 172

Figure 5-12 (a) The count profile of the agglomeration and breakage simulation generated by the PA and grid methods. (b) Crystal volume profile to demonstrate the relative volume change during the agglomeration and breakage. The Aggl and Break in the legends refer to agglomeration and breakage, respectively. .... 175

Figure 5-13 Two-dimensional agglomeration and breakage simulation results using the PA method. (a) The initial condition of the agglomeration simulation. (b) Final CSD of the agglomeration simulation. (c) The initial condition of the breakage simulation. (d) Final CSD of the breakage simulation. .... 176

Figure 5-14 Nucleation and growth simulation speed comparison between the grid methods and the PA method.....	179
Figure 5-15 Simulation speed comparison of the concentration-dependent cases. ....	180
Figure 5-16 Agglomeration and breakage simulation speed profiling .....	183
Figure 5-17 Computation speed of various operations for population array method at different numbers of rows. ....	184

## List of Appendices

Appendix A: Copyright permission .....	198
Appendix B: Source code repositories.....	200



## List of Acronyms

<b>API</b>	Active pharmaceutical ingredient
<b>AR</b>	Aspect ratio
<b>ARF</b>	Active rotating filters
<b>Async</b>	Asynchronous
<b>ATR-FTIR</b>	Attenuated total reflection Fourier Transform infrared spectroscopy
<b>CFD</b>	Computational fluid dynamics
<b>CLD</b>	Chord length distribution
<b>CSD</b>	Crystal size distribution
<b>CSV</b>	Comma-separated values
<b>FBRM</b>	Focused Beam Reflectance Measurement
<b>FBRM</b>	Focused Beam Reflectance Measurement
<b>FDA</b>	Food and Drug Administration
<b>GB</b>	Glass beads
<b>IR</b>	Infrared
<b>JIT</b>	Just-in-time compile
<b>KDE</b>	Kernel density estimation
<b>LGA</b>	L-glutamic acid
<b>MBE</b>	Mass balance equation
<b>MoM</b>	Method of moment
<b>MPC</b>	Model predictive control
<b>MQTT</b>	Message Queuing Telemetry Transport
<b>MSZW</b>	Metastable zone width
<b>MSZW</b>	Metastable zone width
<b>OOD</b>	Oriented object detection
<b>PA</b>	Population Array
<b>PAT</b>	Process analytical technology
<b>PBE</b>	Population balance equation

<b>PFR</b>	Pixel fill ratio
<b>PVM</b>	Mettler Toledo Particle Vision and Measurements
<b>PWM</b>	Pulse width modulation
<b>PXRD</b>	Powder X-ray diffraction
<b>QbC</b>	Quality-by-control
<b>QbD</b>	Quality-by-design
<b>RCNN</b>	Regional convolutional neural network
<b>RPM</b>	Revolution per minute
<b>SDK</b>	Software Development Kit
<b>SSC</b>	Supersaturation control
<b>UAS</b>	Ultrasonic attenuation spectroscopy
<b>UW</b>	Upwind discretization method

# **Chapter 1**

## **Introduction**

## Chapter 1 Introduction

### 1.1. Introduction to Crystallization Process

#### 1.1.1. Background of Crystallization Process

Chemical separation is one of the main branches of chemical engineering in the chemical industry, in which crystallization plays an important role in separating and engineering solid-state products from a solution, molten or directly from a gas. Depending on the operation modes, crystallization can be categorized into evaporative crystallization, cooling crystallization (from solution or molten state), and precipitation (reactive and anti-solvent crystallization). The solution crystallization process refers to the solute molecules being organized into a crystalline form driven by supersaturation (Eq. 1-1). The driving force may come from the increasing solute concentration ( $c$ ) by evaporation of solvent or decreasing the solubility ( $c^*$ ) by cooling or reaction of the solution system.

$$\sigma = \frac{c}{c^*} - 1 \quad (1-1)$$

The supersaturation has a direct effect on the two primary processes of solution crystallization: nucleation and growth. The nucleation refers to the generation of nuclei in a supersaturated solution. The next step is for these nuclei to grow larger by the addition of solute molecules from the supersaturated solution, which is known as crystal growth (Myerson, 2002). The primary nucleation occurs when no crystal or other substance exists in the solution. Due to the large energy barrier, the primary nucleation occurs only when the supersaturation exceeds a threshold known as the metastable limit (Mullin & Nývlt, 1971). The presence of crystals in the supersaturated solution lowers the energy barrier and leads to more controllable secondary nucleation.

The solution crystallization is preferred for the separation of thermosensitive substances due to its mild operating conditions, especially in the areas of pharmaceutical, solid

intermediate chemical products, solid-state functional materials, etc. More importantly, compared with other separation methods, the solution crystallization process provides an additional ability to engineer or fine-tune the solid-state product properties such as the structure at the molecular level and the powder performance like particle morphology and crystal size distribution (CSD), which impose a significant impact on the performance of the downstream processes such as filtration and drying (Bourcier et al., 2016).

From the interactions at the molecular level to the product powder properties in industrial production, solution crystallization involves interdisciplinary research fields that cover the studies of scales span from nanostructure ( $10^{-10}$  m) to macroscale (about  $10^{-3}$  m), which has plenty of room for product quality improvement and process efficiency optimization (Merkus, 2009). As shown in Figure 1-1, the research and industrialization of the solution crystallization process contain the mechanism and regulation of molecular assembly, bench-scale process development and optimization, process design, and industrial realization. The research in solution crystallization area attracts much attention in the molecular level design of crystal structure as well as the process development and control, especially in high-value-added crystalline products (Gao et al., 2017).

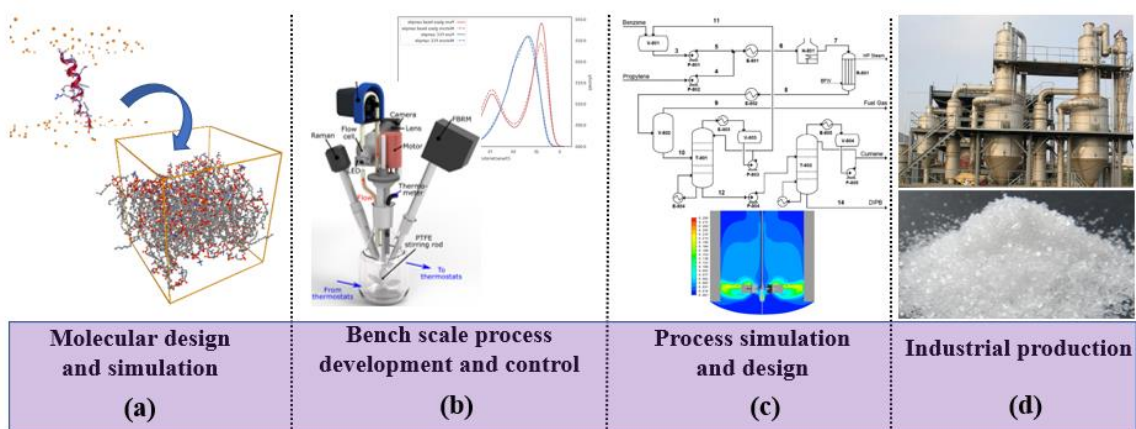


**Figure 1-1** Schematic of the various research scales of solution crystallization: from molecular to industrial manufacturing.

### 1.1.2. Crystallization in The Pharmaceutical Industry

Over 90% of the small molecule drugs in the market exist in crystalline form (Alvarez & Myerson, 2010). Solution crystallization is a widely used technology in the purification of active pharmaceutical ingredients (APIs) as well as define the properties of crystalline pharmaceuticals such as polymorphism, morphology, crystal size, etc. Pharmaceuticals, as high value-added products, have strict requirements and regulations for product quality which will directly affect the drug function. The crystalline product consistency, as well as the robustness of the crystallization process, are crucial factors for successful commercialization.

Regarding regulating the quality of crystalline API, there are two main research branches in the solution crystallization process: 1) crystal engineering at the molecular level; 2) crystallization process design and control (Gao et al., 2017). Figure 1-2 demonstrates the major topics of interest in the branches. In crystal engineering, the focus is concentrated on discovering and investigating the polymorphism and the multi-component crystals with the aid of the analytical technologies from the crystallography. Polymorphism refers to the same solute molecules to crystallize in more than one crystal structure with different molecular packing arrangements and conformation. The polymorphism exhibited in the crystalline API leads to different solubility and dissolution dynamics, which significantly impact the stability and bioavailability of the pharmaceutical products (Lee, Erdemir & Myerson, 2011). Over 40% of existing drug products have limited aqueous solubility and hence cannot be delivered to the body using conventional techniques (Kalepu & Nekkanti, 2015). Multi-component crystal engineering is a novel approach to modify the physicochemical properties of a crystalline API by forming the cocrystal with other pharmaceutically acceptable substances, which offers the potential of improved solubility via modification of the underlying crystal structure, thus potentially rendering the compound bioavailable (Karimi-Jafari et al., 2018). The marketed cocrystal and salts of pharmaceutical products have achieved great success by improving the bioavailability and oral absorption of the insoluble APIs (Emami et al., 2018).

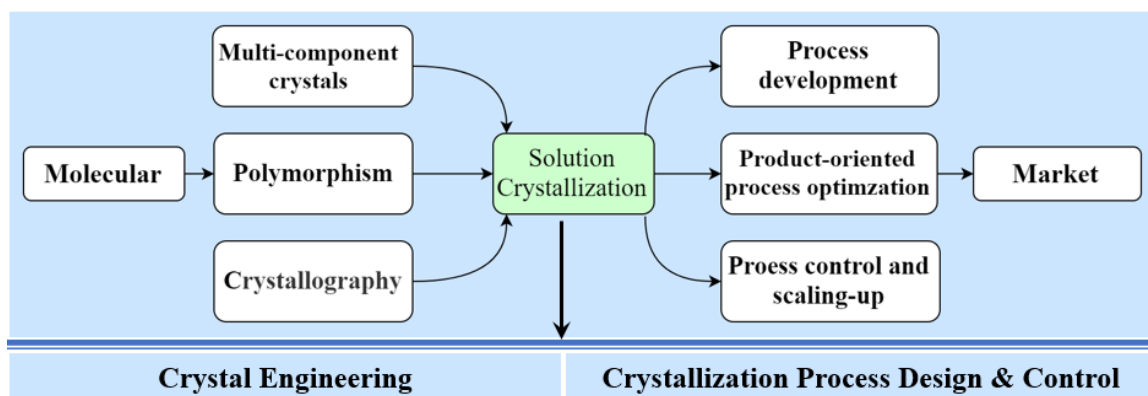


**Figure 1-2** The main research branches in the solution crystallization process: crystal engineering and crystallization process design and control

This work focused on the topic of crystallization process engineering that concerns the implementation of the production scale-up and optimization of the crystalline product quality after the pathway to synthesize the desired crystalline product has been designed by chemists and crystal engineers. The objectives of a pharmaceutical crystallization process include improving the yield, product purity, polymorphic form, and the crystal size and morphology; significantly affect the downstream processability and the bioavailability of the pharmaceutical product (Nagy et al., 2013a). Typically, large and uniform crystals with low-aspect-ratio morphology are desired, whereas fine or needle-like particles are unwanted since they can cause problems in filtration and drying, leading to residual solvent and unacceptable product quality (Bourcier et al., 2016; Yang, Song & Nagy, 2015). The optimal crystallization process is achieved by combining the proper design of the crystallizer and the effective control strategy during operation. The former involves optimizing the geometry of the internal structure and the agitation system of the crystallizer to ensure sufficient mass and energy transportation, which has been greatly enhanced with the aid of computational fluid dynamics (CFD) simulation (Rane et al., 2014). The latter involves effective scheduling of the crystallizer temperature, evaporation rate, or the anti-solvent addition rate to provide an optimal level of supersaturation that balances the productivity and quality of the product crystals. The pioneering work of supersaturation control (SSC) was done by Mullin (1971), who

demonstrated that controlling the supersaturation within the metastable zone width (MSZW) following an optimal cooling curve can suppress the undesired excessive nucleation while promoting the growth of large crystals. This control strategy is simple yet effective as the MSZW can be determined experimentally. However, its open-loop nature implies no effective compensation against the process shift due to unexpected disturbances such as incrustation.

With the tightening regulations requiring the consistent pharmaceutical product, the United States Food and Drug Administration (FDA) introduced the guidance concerning the concepts of quality-by-design (QbD) and quality-by-control (QbC). The use of process analytical technologies (PATs) and feedback control strategies enables dynamically adjusting the operating conditions according to the online measurements to compensate the disturbances and reduce the product variations, therefore improving the process robustness (Yang, Song & Nagy, 2015). The effectiveness of the closed-loop SSC with online supersaturation measurement was confirmed with attenuated total reflection Fourier Transform infrared spectroscopy (ATR-FTIR), conductivity meter, and density meter (Sheikhzadeh, Trifkovic & Rohani, 2008; Wijaya Hermanto et al., 2013). Direct nucleation control (DNC) is a novel control strategy that controls the count of crystals provided by FBRM (Focused Beam Reflectance Measurement) measurement using temperature cycle between dissolution and growth (Saleemi, Rielly & Nagy, 2012). This approach is based on the fact that if a smaller number of particles is maintained the resulting mean size of the product will be larger and vice versa (Nagy et al., 2013b). The DNC strategy was proven to produce large crystals with no agglomeration and eliminated problems with solvent inclusion (Saleemi et al., 2012).

In the pharmaceutical industry, the continuous crystallization process has received increasing attention due to its improved product robustness and consistency compared to traditional batch crystallization. Continuous crystallization operates at a steady state after the startup process, allowing constant product quality without batch-to-batch variation. The FDA has come out in strong support of the implementation of continuous



pharmaceutical manufacturing as a methodology to achieve improved process quality and control (Wood et al., 2019). Powell et al. (2016) used an integrated PAT array to monitor and control the early onset of fouling and encrustation in a mixed suspension mixed product removal (MSMPR) crystallizer to achieve the extended operating periods. Yang and Nagy (2015) demonstrated that using an appropriate startup policy facilitated with PATs can reduce approximately 50% of the startup time in the anti-solvent/cooling continuous crystallization. Furthermore, the periodic steady-state flow crystallization process was investigated that employed intermittent slurry transportation to solve the product classification and clogging problems (Powell et al., 2015). The PAT played an important role in determining the oscillatory steady state of the process and the variation of the product attribute within each operating cycles.

The recent development of the PAT enables the online monitoring of a more variety of system states, which leads to the expanded quality objectives towards better crystal process control. Raman spectroscopy is the most effective online analytical tool to quantitatively determine the composition of different polymorphic forms. Pataki et al. (2013) performed controlled crystallization based on the feedback of real-time Raman signals to ensure that the product of the drugs was free of undesired polymorph. The advancement of in-situ microscopic imaging and deep-learning-based image analysis enables the online monitoring of multi-dimensional crystal size and morphology. Gao et al. (2018) implemented the novel crystal image analysis algorithm that not only could accurately measure the size of needle-like  $\beta$ -form L-glutamic crystal, but also differentiate the polymorphic forms based on the distinct morphologies and achieved a similar detection accuracy as the Raman spectroscopy. More studies have shown the potential of coupling the PATs and the process intensification technologies such as wet milling, ultrasonic, and microwave irradiation to achieve the more challenging controls of crystal morphology, size distribution, and polymorph purity (Ahmed et al., 2019; Hatkar & Gogate, 2012; Kacker et al., 2016; Yang et al., 2016).

The significance of the PAT in crystallization process engineering has been acknowledged by industry, which motivates our study of improving the current PAT to facilitate better process monitoring and control.

## 1.2. Process Analytical Technology (PAT) in Crystallization

The PAT framework was proposed by the U.S. FDA in 2004, which intended to encourage the development and implementation of the timely measurement of critical quality attributes of the product and process to achieve better product quality assurance in designing, analyzing, and controlling the process (U.S. Food and Drug Administration, 2004). The framework consists of a set of guidance of data acquisition, multivariate process analysis, and process control strategies. In this section, the important characterization technologies that quantify the key attributes of a crystallization process are reviewed.

### 1.2.1. Solute Concentration PATs

The supersaturation of the crystallization process can be inferred from solution concentrations. Accurate measurement of the solute concentration can be obtained by sampling the solid-free solution and weighing the evaporated dry sample, but such an approach is prohibitively time-consuming for real-time control. The PATs infer the solute concentration by measuring other attributes that are correlated to solute concentration. The density (Garside & Mullin, 1966), reflective index (Helt & Larson, 1977), speed of sound (Stelzer, Pertig & Ulrich, 2013), and conductivity (Lin, Wu & Rohani, 2019) were employed to provide calibration and online estimation of the solute concentration. The application is limited depending on the system properties and working conditions, e.g., the conductivity of the majority of organic solute is too low for reliable measurement (Zhang et al., 2017). Also, monitoring the scalar attributes are less effective for simultaneous measurement of the solute concentrations of multiple compounds. With the rapid development of spectroscopy technology, the corresponding instruments for non-invasive solute concentration measurement have been developed for the crystallization process, including attenuated total reflectance Fourier transform infrared spectroscopy

(ATR-FTIR) and ATR-UV/vis. The stretching, bending, and twisting of the molecular bonds cause the absorption of photons at various frequency. The intensity of absorption from the spectrum can be used to estimate the solute concentration of a substance with specific molecular bonds or groups. The ATR accessory reflects the beam at the interface and evaluates the solution IR absorption with the evanescent wave of low penetrates depth (2-3  $\mu\text{m}$ ), which avoids the disturbance of crystals suspended in the crystallization system (Figure 1-3). The recent works demonstrated the effectiveness of the Raman spectroscopy in simultaneous solid phase and solute concentration measurement (Lin, Wu & Rohani, 2020). Lin et al. (2020) compared the data processing approaches and showed that the neural network model outperformed the least squares analysis for extracting the solid and solute concentrations from the Raman spectra. The calibration of Raman spectroscopy to obtain solute concentration requires a large number of calibration experiments because Raman spectral response is a function of temperature, solute concentration, slurry density, crystal polymorph, and the CSD (Kristova, Hopkinson & Rutt, 2015). In Chapter 3 of this thesis, a Raman spectroscopy calibration strategy is proposed that uses the data acquired in the automated temperature-cycle experiments to obtain the accurate calibration model of solute concentration, which simplifies the process of adopting Raman spectroscopy as a PAT for solute concentration monitoring.

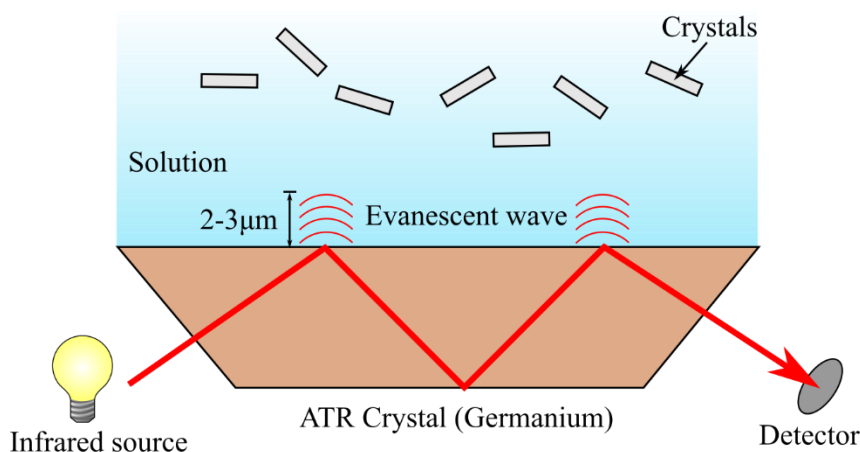


**Figure 1-3** Schematic of the ATR-FTIR in a crystallization process

### 1.2.2. Polymorphic Forms PATs

On-line monitoring and control of the polymorphic forms not only improves the product quality assurance but also helps in identifying the transient unstable polymorphs during the research and development stage (Roy, Chamberlin & Matzger, 2013). The definitive evidence for the existence of polymorphism is via single-crystal X-ray diffraction (Yu et al., 2004). Other methods including X-ray powder diffraction and thermal analysis require lengthy preparation and measurement process, rendering these approaches inapplicable as an online polymorphic PAT monitoring candidates.

In contrast, Raman spectroscopy is capable to provide qualitative and quantitative polymorphic information of the solid phase as well as the solution properties in real-time. Raman spectroscopy functions based on the principle of light scattering (Figure 1-4.a). After the incident light activates the molecules to an excited state, the majority of the molecules undergoes Rayleigh scattering and return to the original energy state with the emission of the photon with the same wavelength. A small portion of excited molecules undergoes Raman scattering and relaxes to a different vibrational state, emitting photons with a different wavelength than the incident light. The Raman scattering spectra can

distinguish the vibrational modes of the molecules in different crystalline structures, enabling the characterization of fingerprints associated with each polymorph (Weber & Merlin, 2013). Figure 1-4.b depicts the schematic of an in-situ Raman spectroscopy for monitoring a crystallization process. In order to detect the weak Raman scattering signal, a set of optical devices is used to focus the laser beam on the slurry, redirect the reflected light, and filter the non-Raman scattering light with the same wavelength as the incident light. Finally, the spectral data is acquired by a cooled optical sensor (approximately  $-40^{\circ}\text{C}$ ) using a long exposure time to accumulate the signal.

Raman spectroscopy has been actively employed in quantitatively monitoring the polymorphic transformation of L-glutamic acid (LGA), p - aminobenzoic acid (PABA), and paracetamol in a solution crystallization process (Ono, Ter Horst & Jansens, 2004; Wang et al., 2011; Yang, Wang & Ching, 2009). Other works have demonstrated the ability to track the reactive crystallization system and indicating the reaction endpoint (Hart et al., 2015; Qu et al., 2009). Esmonde-White et al. (2017) reviewed the applications of Raman spectroscopy in the pharmaceutical manufacturing process for product quality control. As discussed in the previous section, the Raman spectroscopy is able to provide simultaneous solid-phase characterization as well as the solute concentration measurement.

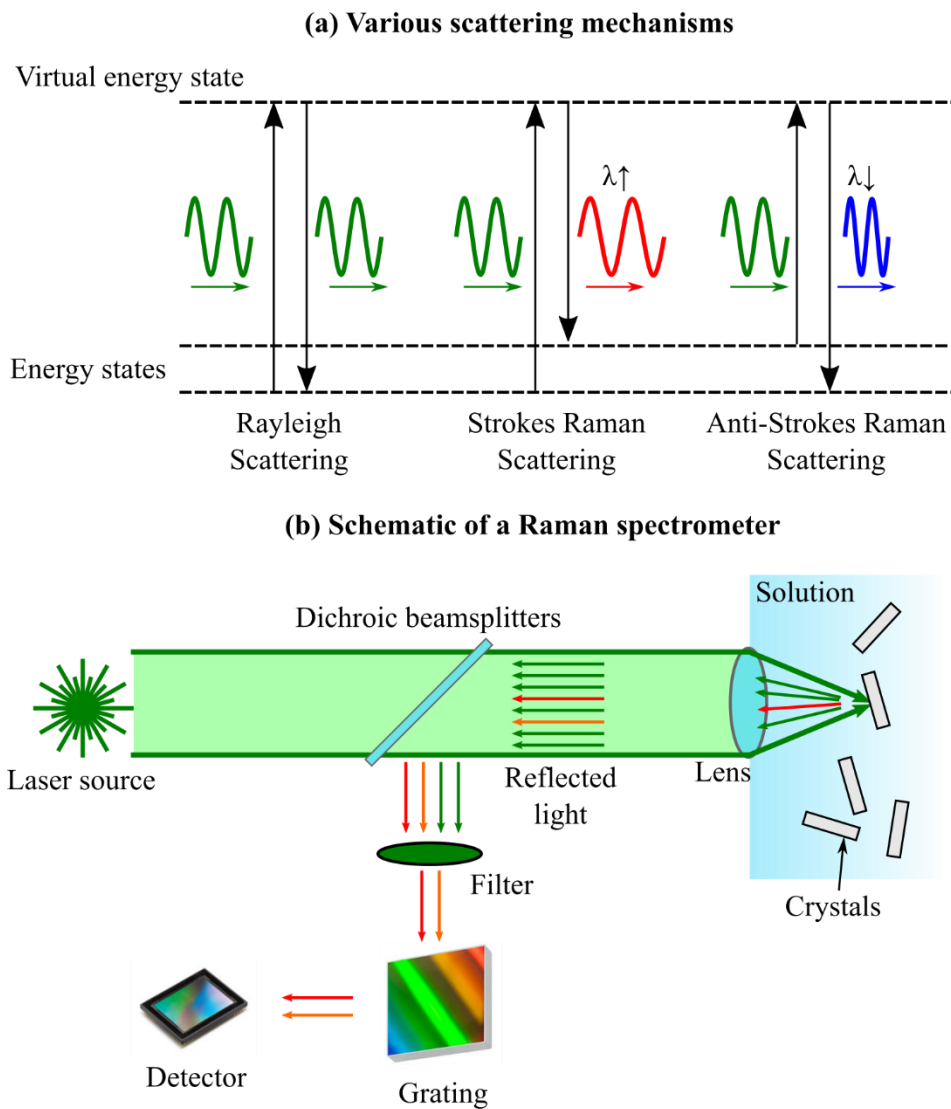


**Figure 1-4** Schematics of Raman spectroscopy. (a) The energy level diagram of Rayleigh scattering and Stokes Raman scattering and anti-Stokes Raman scattering. (b) Illustration of the mechanism of an in-situ back-scattering Raman spectrometer for the crystallization process.

### 1.2.3. Crystal Size and Shape PATs

#### 1.2.3.1. Traditional Particle Sizing PATs

Developing the PAT for crystal size and shape monitoring is one of the core topics in this thesis. The modern particle sizing instruments measure the electric, optical, or acoustic properties of the slurry to infer the CSD information. The Coulter Counter makes use of the difference in an electrical impedance caused by a crystal flowing through a sensing zone (Figure 1-5.a). The crystal size measured with the Coulter counter is the equivalent diameter of the sphere whose volume is equal to that of the particle (Presles, 2010). The main advantage is the capability of precise particle volume measurement. Although the Coulter Counter for in-situ monitoring was studied in 1965, it is mainly used as an offline analytical approach due to its limiting requirement of slurry density and suspension medium (Garslde & Shah, 1980; Maddux & Kanwisher, 1965). Figure 1-5.b depicts the ultrasonic attenuation spectroscopy (UAS) instrument. The UAS is based on the interaction between the sound wave and crystals of different size and shape that contribute to attenuation at different frequencies ranging from 0.1 – 200 MHz (Merkus, 2009). The significant advantage of UAS is the ability to operate in the concentrated systems up to 70% volume fraction, making it an ideal PAT instrument without the need for dilution (Li, Wilkinson & Patchigolla, 2005). In a concentrated system above 5% volume fraction, the inter-particle interactions and multiple scattering mechanisms may have to be taken into account (Merkus, 2009). Bar-yosef et al. (2004) demonstrated that the UAS could determine the CSD as well as the solute concentration with a neural network-based calibration model. The main limitation of the UAS approach is the requirement of the physical properties of both the liquid and particle phases at different states, which can be difficult to obtain. Laser diffraction (LD) is one of the most accurate and reproducible particle sizing technologies, which measures the scattering pattern of a monochromatic laser light by particles with an array of detectors positioned at different angles (Figure 1-5.c). The signals are then deconvoluted to a size distribution using Mie theory (Li et al., 2008). The LD technology typically works with the best accuracy in low solids concentration, implying its main application in offline measurement (Merkus,

2009). The FBRM (Focused Beam Reflectance Measurement) instrument is arguably the most popular online PAT for crystallization process monitoring and control device (Yu, Chow & Tan, 2008). The FBRM works with a rotating focused laser beam that scans the particles traveling through its focal volume (Figure 1-5.d). The back-scattering light from the crystal surface is measured as the chord length. As shown in Figure 1-5.d, the chord length is arbitrary, so the conversion from chord length to particle size is challenging (Heinrich & Ulrich, 2012a). The in-depth discussion of the existing PATs can be found in Chapter 2 of this thesis and the recommended book by (Merkus, 2009).



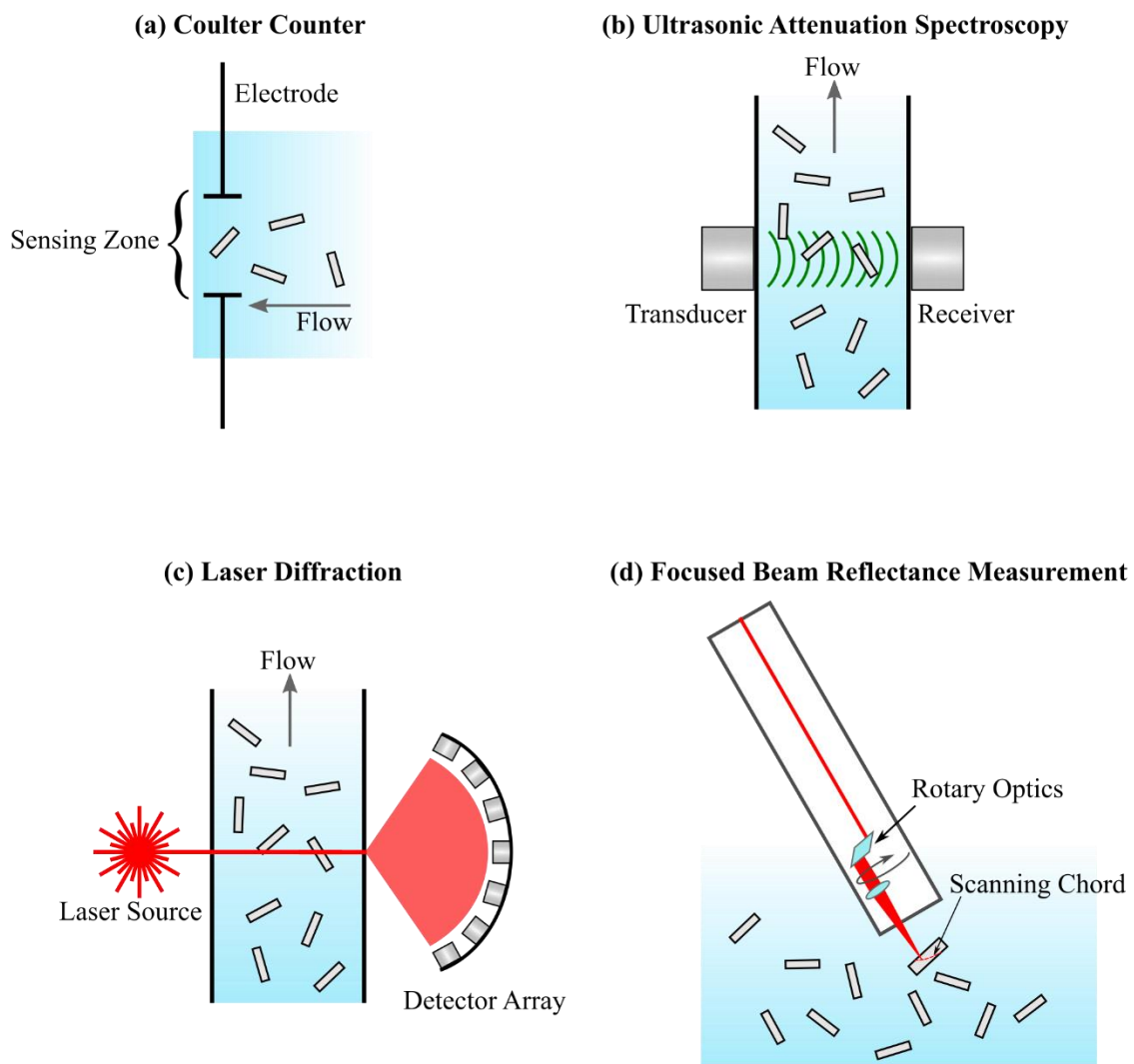


**Figure 1-5** Common particle sizing PATs for the crystallization process.

### 1.2.3.2. Image-based Particle Sizing PATs

The abovementioned particle sizing approaches require an assumption of the particle shape, leading to a one-dimensional distribution of equivalent size. For high-aspect-ratio (needle-like) crystals, the assumption does not hold. Recovering the morphology information from the one-dimensional CSD requires complex modeling work and is

difficult to generalize in broader applications (Szilagyí et al., 2017). In addition, the validity of the size measurement is questionable in the slurry with other discrete phases such as impurities and air bubbles, which require cross-validation with other methods, such as optical microscopic imaging. These limitations of existing PATs and the demand for more intuitive size and shape measurement motivated the development of the in-situ imaging PAT powered by image analysis technologies in this work.

Several commercial hardware for crystallization imaging is available, including PVM and EasyViewer (Mettler Toledo, Chicago, United States) and SOPAT (SOPAT GmbH, Berlin, Germany) (Ahmed et al., 2019; Kacker et al., 2018). We will demonstrate a homemade flow-through cell imaging set up in the Chapters 2 and 3 in this thesis. The external circulation of the flow-through cell adds up the complexity and requires extra thermal isolation to prevent undesired crystal growth outside the crystallizer. However, this setup enables a more straightforward arrangement of camera and illumination units that are otherwise difficult in the limited space in an insertable probe, making it a favorable setup to deploy the customized imaging system for a crystallization system.

Although crystallization imaging devices have existed for a long time, they are primarily employed as a qualitative visualization tool of a process. Despite the visual particle information, quantitatively extracting the crystal size and shape information using an automated algorithm is deemed challenging due to the complexity of the crystallization images. The motion blur and out-of-focus artifacts cause confusion in determining the type and the boundary of the objects. Another major problem emerges when distinguishing the intersecting or overlapping crystals. These robustness issues prevent the extensive use of the image-based particle sizing PAT (Ferreira et al., 2011).

Over the years, the researchers proposed innovations in the particle image analysis field to improve detection performance, including the multi-variate analysis (Sarkar et al., 2009), adaptive threshold algorithms (Lu et al., 2018) for solving the uneven background problem; the salient corner segmentation; model-based object detection (Larsen, Rawlings & Ferrier, 2007); and pattern matching (Huo et al., 2017; Kacker et al., 2018)

algorithms for differentiating the agglomerate cluster and single crystals (Liu et al., 2017; Lu et al., 2019). Due to the complexity and specialization of these methods, they tend to be computation-intensive and difficult to generalize. The parameter tuning heavily depends on human interference, thus unable to fully automate the analysis process.

The recent development of the deep learning-based image analysis enables successful applications including autonomous driving and medical diagnoses where the image complexity is very high (Hassaballah & Awad, 2020). This motivated our research to study the feasibility to incorporate the new technology into the crystallization image analysis. The model consists of a set of convolutional operators (Figure 1-6.b), which are small square matrices of weights (typically  $3 \times 3$  pixels) that scan the image from left to right and top to bottom, computing dot products with the pixel values in its path (Figure 1-6). The weights of the operators will be adjusted so that a specific local feature can be captured by one of the operators (Lecun et al., 1998). By stacking the convolutional block multiple times, the depth and capacity of the model are significantly improved to learn increasingly complex features at different scales (Figure 1-6.d).

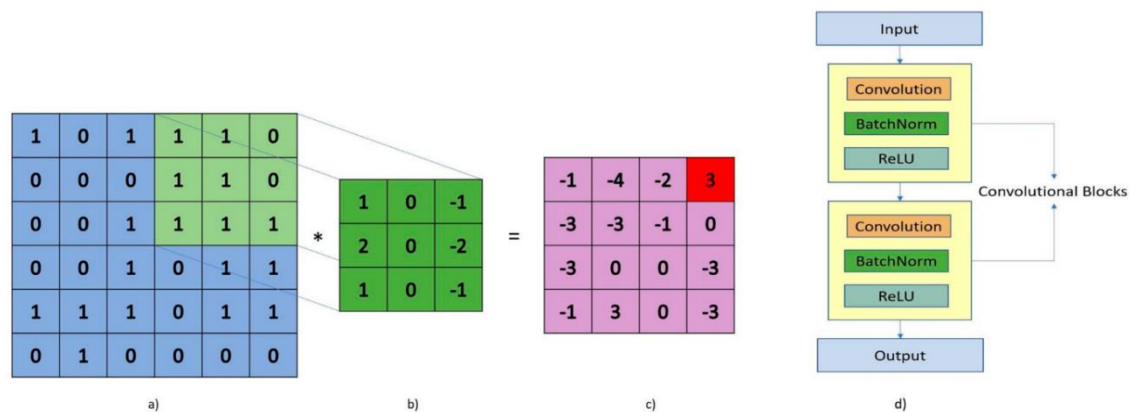


**Figure 1-6** Schematic of a simple convolution operation: (a) input pixels; (b) convolution weights; (c) output; (d) convolutional block. (Manee, Zhu & Romagnoli, 2019)

Compared to the conventional image analysis methods where human decision plays a significant part in identifying the features in the images and hard coding them into pattern

recognition algorithms, the deep learning-based image analysis approaches use the workflow of training the model by feeding the input images and the labeled targets. This allows the model to heuristically determine the optimal parameters that minimize the difference between the model prediction and the labels. By providing abundant labeled training data, the model is capable to learn the common features and parameters that can be generalized for all scenarios in the process. This workflow allows simple and robust modeling that requires only a basic understanding of the crystal morphology to create the polygon labels in software rather than the knowledge of the need for complex modeling techniques in computer vision. Our pioneering study (Gao et al., 2018) showed that the deep learning-based image analysis did not only maintain the accuracy, even when the crystals were overlapping, but also could differentiate the polymorphic forms of L-glutamic acid crystals based on their morphologies to generate the size distribution for the individual forms. Despite the tremendous computational scale, the parallel computation capability provided by the modern GPU, drastically reduces the computational time, enabling real-time image analysis and the application of the proposed deep learning image analysis technique as an online PAT solution.

Three main tasks can be achieved using deep learning-based image analysis (Figure 1-7). Image classification generates categorical predictions such as whether input images contain crystal or not, which can be extended to classify the types of the crystals based on the appearances. Object detection localizes with bounding boxes and applies classification to distinct objects. The geometries of the bounding boxes can be used to represent the two-dimensional size of the crystals with a rectangular shape. Image segmentation is similar to the object detection task except that the objects are localized using pixel-wise masks instead of predefined shapes. The mask provides more versatility to describe irregularly shaped particles such as an agglomerate. In this work, the capabilities of image segmentation and object detection in particle size and shape measurement are presented in Chapter 2 and Chapter 3 in this thesis.

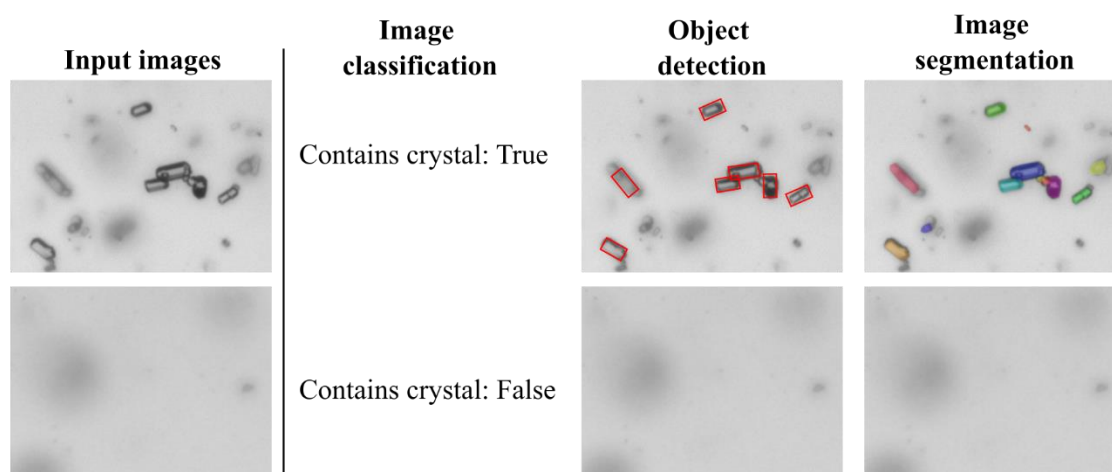


**Figure 1-7** Three main tasks achieved by deep learning-based image analysis and the predicted outputs

### 1.3. Crystallization Process Modeling and Simulation

#### 1.3.1. Population Balance Equation (PBE)

Crystallization modeling and simulation are effective tools for design and control to investigate the impact of the operating conditions on the system states and crystalline product properties. In the process development stage, the data acquired by the PATs can be used to estimate the parameters of the kinetic models. The model helps to optimize the operating conditions and scale up the process with a limited number of experiments. The population balance equation (PBE) is an established technique to describe the change of crystal size distribution (CSD) caused by various mechanisms such as growth, dissolution, nucleation, agglomeration, and breakage of particles. PBE was first proposed by Hulburt and Katz (1964) and further developed for the crystallization process by Randolph et al. (1971) and Ramkrishna (2014). Eq. 1-2 depicts a general form of the PBE for a well-stirred batch or continuous crystallization system, which is a partial differential equation (PDE) expressed in terms of the number density of the CSD,  $n$ , with respect to time,  $t$ , and internal coordinates of each dimension (often referred to as the characteristic size),  $L_i$  (Myerson, 2002).

$$\frac{\partial n}{\partial t} + \underbrace{\sum_i \frac{\partial(G_i \cdot n)}{\partial L_i}}_{\text{growth, dissolution}} + \underbrace{\frac{n - n_{in}}{\tau}}_{\text{continuous}} = \underbrace{B - D}_{\text{agglomeration, breakage, nucleation}} \quad (1-2)$$

Due to the hyperbolic nature of the growth/dissolution term and the non-linearity from the kinetics and the coupled solute mass balance equation (MBE), analytical solution of a PBE model is not possible except for a few simplified cases (Gunawan, Fusman & Braatz, 2004; Sanjeev, 1996). Thus, numerical approaches have been developed to solve the PBE for crystallization process simulation.

### 1.3.2. Numerical Solution of the PBE

The numerical solution techniques of PBE have been reviewed by Omar and Rohani (2017). Method of moments (MoM) and discretization (grid) method are two widely employed techniques. MoM involves converting the PBE into a set of ordinary differential equations (ODEs) in terms of the moments, which can be integrated numerically. The main advantage of MoM is the relatively low computational effort thanks to tracking only specific moments instead of the full CSD, leading to its popularity in the CFD simulation (Y. Ma et al., 2020). The drawback of MoM is the unclosed moment problem that a moment in the set of ODEs depends on higher-order moments. The specific moment approximation technique must be applied for complicated kinetics such as size-dependent growth and breakage (Szilágyi, Agachi & Lakatos, 2015; Yuan, Laurent & Fox, 2012). Also, MoM does not provide the full CSD, and the inversion of the moments to recover the CSD is not trivial and is still an open area of research (Omar & Rohani, 2017). When the full CSD information or complex kinetics is required, the more general discretization method is preferred.

The discretization method uses a grid with a finite number of bins that represent the crystal count in the given size range. The derivatives in the growth term of PBE could be replaced with the discretized arithmetic operations ( $F$ ) so that the time-derivative of each bin could be computed and integrated (Eq. 1-3). The  $F$  functions can be represented using

the upwind scheme (Eq. 1-4) or the high-resolution scheme (Eq. 1-5) (Gunawan, Fusman & Braatz, 2004).

$$n_k^{m+1} = n_k^m + F(\Delta t, \Delta L, n, G) \quad (1-3)$$

$$F = -\frac{G_i \Delta t}{\Delta L} (n_k^m - n_{k-1}^m) \quad (1-4)$$

$$F = -\frac{G_i \Delta t}{\Delta L} (n_k^m - n_{k-1}^m) - \frac{G_i \Delta t}{2\Delta L} \left(1 - \frac{G_i \Delta t}{\Delta L}\right) [(n_{k+1}^m - n_k^m)\phi_k - (n_k^m - n_{k-1}^m)\phi_{k-1}] \quad (1-5)$$

Despite the ability to handle the complex kinetic models, the main drawback is the numerical diffusion and the massive computational cost to scale up the dimensionality. As shown in Figure 1-8, the numerical diffusion refers to that the solution becomes smeared or damped when the local gradient of CSD is large. This has been partially resolved after the high-resolution scheme was introduced (Gunawan, Fusman & Braatz, 2004). The computational efficiency problem of the discretization method originates from the limitation of the discretization grid. In order to conserve the crystal mass and count, the upper limit of the grid must be sufficiently large such that no crystal would grow or agglomerate to the size beyond the assumed scope of the grid, leading to the wasted computation on the grid points without any data. Furthermore, the increase in grid dimensionality will lead to a polynomial scale-up of the computational cost (Szilagyí et al., 2017). For example, to achieve the same resolution, the number of grid points should scale up from one thousand for a 1D PBE to one million for a 2D PBE. The efficiency problem deteriorates on a high-dimensional grid because, most CSD data will densely distribute along the characteristic line, while the rest of the grid remains unused and waste the efforts spent to update them. We will propose an alternative numerical method, namely the population array (PA) method in Chapter 5, and demonstrate that the accuracy and computational cost problems can be addressed by the proposed method.

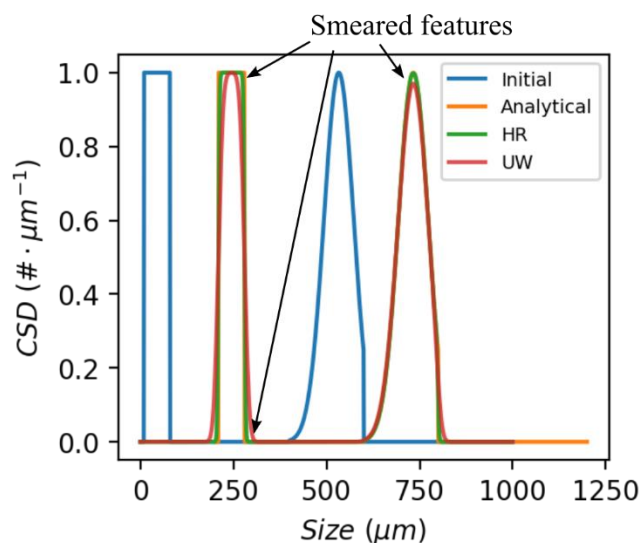


**Figure 1-8** Demonstration of the numerical diffusion caused by the discretization methods.

## 1.4. Research Objectives and Organization of Thesis

### 1.4.1. Research Objectives and Approach

The overall objective of this thesis is to enhance the methodologies and tools for the development, monitoring, and control of a crystallization process. The objectives of the thesis include:

- To develop and validate an efficient image-based PAT instrument, including the imaging hardware and the deep learning-based image analysis system, for crystal size and shape characterization.
- To develop an automated crystallization setup and the controlling software to utilize the developed PAT instruments to automatically carry out the lengthy experiments and data processing works, which not only reduces the amount of laboratory work but also generates reproducible kinetic data.



- To develop an improved numerical solver for crystallization process simulation to outperform the conventional numerical techniques in the computational efficiency and accuracy.

For the study of the image-based PAT, the performance of the proposed setup and algorithm was evaluated in two steps. First, the glass beads (GB) and the fluid catalytic cracking (FCC) catalyst particles were chosen as the model particles because of the well-defined shape and surface texture. The particles were monitored using a homemade flow-through cell imaging device to capture the microscopic images in the concentrated slurry. The image segmentation model, Mask RCNN, was trained to extract the size and classification of the particles in the images. The detection accuracy was confirmed by comparing with the measured CSD by laser diffraction, the sieve method, and the manually labeled validation images. Next, the proposed PAT was deployed as the monitoring system of the seeded batch cooling crystallization using the taurine-water system. The object detection model, S<sup>2</sup>A-Net, was employed to measure the multi-dimensional CSD and the aspect ratio as well as quantifying the agglomeration level. The Raman spectroscopy was used to measure the solute concentration. The FBRM was used as the reference particle sizing PAT to compare the sensitivity and the accuracy of the proposed image-based PAT technique. The combined methodology of spectroscopy and the image-based PAT was employed for the kinetic study of the nucleation, growth, and agglomeration of taurine-water system with accurate multi-dimensional information.

The simulation of the crystallization process using the proposed PA solver was implemented in Python, with some performance-sensitive functions implemented in C++ for maximum runtime speed. The accuracy and simulation speed of the solver were compared with the analytical solutions reported in the literature and the numerical solver implemented using the high-resolution discretization scheme as the reference.

An automated experimental setup was built based on the internet-of-things (IoT) microcontrollers, ESP8266, that provided the wireless connectivity for the hardware and instruments. The data was exchanged using Message Queuing Telemetry Transport

(MQTT) protocol. The execution of the experiments was scheduled on IPython Jupyter Notebook, which also serves as the dashboard to visualize the real-time process parameters.

#### 1.4.2. Thesis Organization

This thesis is written in the integrated-article format.

Chapter 1 briefly discusses the research background and the status of PAT and numerical simulation of the crystallization process. The motivation, objectives, and thesis structure are introduced in this chapter.

Chapter 2 and Chapter 3 emphasize the topic of the development of image-based PAT. In Chapter 2, the deep learning-based in situ microscopic image analysis system for detecting particles and performing size analysis in a high-density slurry is investigated. The ability to classify visually distinct particles (glass beads and FCC catalyst particles) and generate the accurate size distribution of individual classes is confirmed by comparing with other established particle sizing technologies. Pixel fill ratio (PFR) is proposed as a scale-invariant descriptor of solid concentration level and complexity of an image. Chapter 3 extends the work by investigating the proposed PAT in a batch crystallization process of taurine crystal for in-situ estimation of the two-dimensional CSD, count, and shape statistics. Combined with the Raman Spectroscopy calibrated with an automated online calibration strategy, the PATs provided effective online crystal size and shape measurement as well as the parameter estimation of the growth and nucleation mechanisms.

Chapter 4 introduces an automated crystallization platform equipped with the PAT introduced in Chapters 2 and 3. The hardware design and software architecture are discussed to achieve cost-effective customization of the existing laboratory instruments. The time-consuming experiments for determining the metastable zone width (MSZW)

and induction time of a crystallization process were successfully automated, indicating the promising application of the PAT and the crystallization platform in simplifying and speeding up the research and development stage of a crystallization process.

In Chapter 5, the numerical algorithm used in Chapter 3 for parameter estimation is further investigated. By learning from the advantages and drawbacks of the existing numerical techniques, a simple numerical technique, namely the population array (PA) method, is proposed to solve the one-dimensional as well as multi-dimensional PBE problems involving various challenging kinetic behavior including size-dependent growth, agglomeration, breakage, and polymorphic transformation. The row compression algorithm is proposed to facilitate the PA method to reduce the computation scale while maintaining accuracy.

Chapter 6 summarizes the research work and gives recommendations for future works.

## 1.5. References

- Ahmed, B., Brown, C. J., McGlone, T., Bowering, D. L., Sefcik, J. & Florence, A. J. (2019). Engineering of acetaminophen particle attributes using a wet milling crystallisation platform. *International Journal of Pharmaceutics*, 554(August 2018), 201–211. <https://doi.org/10.1016/j.ijpharm.2018.10.073>
- Alvarez, A. J. & Myerson, A. S. (2010). Continuous plug flow crystallization of pharmaceutical compounds. *Crystal Growth and Design*, 10(5), 2219–2228. <https://doi.org/10.1021/cg901496s>
- Bar-yosef, P., Fu, H., Li, M., Wilkinson, D., Patchigolla, K., Mougin, P., ... Tweedie, R. (2004). On-Line Crystallization Process Parameter Measurements Using Ultrasonic Attenuation Spectroscopy. *Crystal Growth & Design*, 4(5), 955–963. <https://doi.org/10.1021/cg030041h>
- Bourcier, D., Féraud, J. P., Colson, D., Mandrick, K., Ode, D., Brackx, E. & Puel, F. (2016). Influence of particle size and shape properties on cake resistance and compressibility during pressure filtration. *Chemical Engineering Science*, 144, 176–187. <https://doi.org/10.1016/j.ces.2016.01.023>

- Emami, S., Siahi-Shadbad, M., Adibkia, K. & Barzegar-Jalali, M. (2018). Recent advances in improving oral drug bioavailability by cocrystals. *BioImpacts*, 8(4), 305–320. <https://doi.org/10.15171/bi.2018.33>
- Esmonde-White, K. A., Cuellar, M., Uerpmann, C., Lenain, B. & Lewis, I. R. (2017). Raman spectroscopy as a process analytical technology for pharmaceutical manufacturing and bioprocessing. *Analytical and Bioanalytical Chemistry*, 409(3), 637–649. <https://doi.org/10.1007/s00216-016-9824-1>
- Ferreira, A., Faria, N., Rocha, F. & Teixeira, J. A. (2011). Using an Online Image Analysis Technique to Characterize Sucrose Crystal Morphology during a Crystallization Run. *Ind. Eng. Chem. Res.*, 50, 6990–7002. <https://doi.org/10.1021/ie2001499>
- Gao, Z., Rohani, S., Gong, J. & Wang, J. (2017). Recent Developments in the Crystallization Process: Toward the Pharmaceutical Industry. *Engineering*, 3(3), 343–353. <https://doi.org/10.1016/J.ENG.2017.03.022>
- Gao, Z., Wu, Y., Bao, Y., Gong, J., Wang, J. & Rohani, S. (2018). Image Analysis for In-line Measurement of Multidimensional Size, Shape, and Polymorphic Transformation of L-Glutamic Acid Using Deep Learning-Based Image Segmentation and Classification. *Crystal Growth and Design*, 18(8), 4275–4281. <https://doi.org/10.1021/acs.cgd.8b00883>
- Garside, J. & Mullin, J. W. (1966). Continuous measurement of solution concentration in a crystalliser. *Chemistry & Industry*, (48), 2007.
- Garside, J. & Shah, M. B. (1980). Crystallization Kinetics from MSMPR Crystallizers. *Industrial and Engineering Chemistry Process Design and Development*, 19(4), 509–514. <https://doi.org/10.1021/i260076a001>
- Gunawan, R., Fusman, I. & Braatz, R. D. (2004). High resolution algorithms for multidimensional population balance equations. *AIChE Journal*, 50(11), 2738–2749. <https://doi.org/10.1002/aic.10228>
- Hart, R. J., Pedge, N. I., Steven, A. R. & Sutcliffe, K. (2015). In situ monitoring of a heterogeneous etherification reaction using quantitative raman spectroscopy. *Organic Process Research and Development*, 19(1), 196–202. <https://doi.org/10.1021/op500027w>
- Hassaballah, M. & Awad, A. I. (2020). *Deep learning in computer vision: principles and applications*. CRC Press.
- Hatkar, U. N. & Gogate, P. R. (2012). Process intensification of anti-solvent crystallization of salicylic acid using ultrasonic irradiations. *Chemical Engineering and Processing: Process Intensification*, 57–58, 16–24. <https://doi.org/10.1016/j.cep.2012.04.005>

- Heinrich, J. & Ulrich, J. (2012). Application of Laser-Backscattering Instruments for In Situ Monitoring of Crystallization Processes - A Review. *Chemical Engineering and Technology*, 35(6), 967–979. <https://doi.org/10.1002/ceat.201100344>
- Helt, J. E. & Larson, M. A. (1977). Effects of temperature on the crystallization of potassium nitrate by direct measurement of supersaturation. *AIChE Journal*, 23(6), 822–830.
- Hulburt, H. M. & Katz, S. (1964). Some problems in particle technology: A statistical mechanical formulation. *Chemical Engineering Science*, 19(8), 555–574. [https://doi.org/https://doi.org/10.1016/0009-2509\(64\)85047-8](https://doi.org/https://doi.org/10.1016/0009-2509(64)85047-8)
- Huo, Y., Liu, T., Wang, X. Z., Ma, C. Y. & Ni, X. (2017). Online detection of particle agglomeration during solution crystallization by microscopic double-view image analysis. *Industrial and Engineering Chemistry Research*, 56(39), 11257–11269. <https://doi.org/10.1021/acs.iecr.7b02439>
- Kacker, R., Maaß, S., Emmerich, J. & Kramer, H. (2018). Application of inline imaging for monitoring crystallization process in a continuous oscillatory baffled crystallizer. *AIChE Journal*, 64(7). <https://doi.org/10.1002/aic.16145>
- Kacker, R., Salvador, P. M., Sturm, G. S. J., Stefanidis, G. D., Lakerveld, R., Nagy, Z. K. & Kramer, H. J. M. (2016). Microwave Assisted Direct Nucleation Control for Batch Crystallization: Crystal Size Control with Reduced Batch Time. *Crystal Growth and Design*, 16(1), 440–446. <https://doi.org/10.1021/acs.cgd.5b01444>
- Kalepu, S. & Nekkanti, V. (2015). Insoluble drug delivery strategies: Review of recent advances and business prospects. *Acta Pharmaceutica Sinica B*, 5(5), 442–453. <https://doi.org/10.1016/j.apsb.2015.07.003>
- Karimi-Jafari, M., Padrela, L., Walker, G. M. & Croker, D. M. (2018). Creating cocrystals: A review of pharmaceutical cocrystal preparation routes and applications. *Crystal Growth and Design*, 18(10), 6370–6387. <https://doi.org/10.1021/acs.cgd.8b00933>
- Kristova, P., Hopkinson, L. J. & Rutt, K. J. (2015). The effect of the particle size on the fundamental vibrations of the [CO<sub>3</sub><sup>2-</sup>] anion in calcite. *Journal of Physical Chemistry A*, 119(20), 4891–4897. <https://doi.org/10.1021/acs.jpca.5b02942>
- Larsen, P. A., Rawlings, J. B. & Ferrier, N. J. (2007). Model-based object recognition to measure crystal size and shape distributions from in situ video images. *Chemical Engineering Science*, 62(5), 1430–1441. <https://doi.org/10.1016/j.ces.2006.11.018>
- Lecun, Y., Bottou, L., Bengio, Y. & Haffner, P. (1998). Gradient-based learning applied to document recognition. *Proceedings of the IEEE*, 86(11), 2278–2324. <https://doi.org/10.1109/5.726791>
- Lee, A. Y., Erdemir, D. & Myerson, A. S. (2011). Crystal polymorphism in chemical process development. *Annual Review of Chemical and Biomolecular*

- Engineering, 2(July 2015), 259–280. <https://doi.org/10.1146/annurev-chembioeng-061010-114224>
- Li, M., Wilkinson, D. & Patchigolla, K. (2005). Comparison of particle size distributions measured using different techniques. *Particulate Science and Technology*, 23(3), 265–284. <https://doi.org/10.1080/02726350590955912>
- Li, R. F., Penchev, R., Ramachandran, V., Roberts, K. J., Wang, X. Z., Tweedie, R. J., ... Huguen, F. M. (2008). Particle shape characterisation via image analysis: From laboratory studies to in-process measurements using an in situ particle viewer system. *Organic Process Research and Development*, 12(5), 837–849. <https://doi.org/10.1021/op800011v>
- Lin, M., Wu, Y. & Rohani, S. (2019). A kinetic study of crystallization process of imatinib mesylate with polymorphic transformation phenomenon. *Journal of Crystal Growth*, 507(August 2018), 146–153. <https://doi.org/10.1016/j.jcrysgro.2018.10.061>
- Lin, M., Wu, Y. & Rohani, S. (2020). Simultaneous Measurement of Solution Concentration and Slurry Density by Raman Spectroscopy with Artificial Neural Network. *Crystal Growth and Design*, 20(3), 1752–1759. <https://doi.org/10.1021/acs.cgd.9b01482>
- Liu, T., Huo, Y., Ma, C. Y. & Wang, X. Z. (2017). Sparsity-based image monitoring of crystal size distribution during crystallization. *Journal of Crystal Growth*, 469, 160–167. <https://doi.org/10.1016/j.jcrysgro.2016.09.040>
- Lu, Z. M., Zhu, F. C., Gao, X. Y., Chen, B. C. & Gao, Z. G. (2018). In-situ particle segmentation approach based on average background modeling and graph-cut for the monitoring of L-glutamic acid crystallization. *Chemometrics and Intelligent Laboratory Systems*, 178(July 2017), 11–23. <https://doi.org/10.1016/j.chemolab.2018.04.009>
- Lu, Z., Zhang, L., Jiang, Y., Zhang, C., Zhang, G. & Liu, M. (2019). Crystal Morphology Monitoring based on In-situ Image Analysis of L-glutamic Acid Crystallization, 88(Cnci). <https://doi.org/10.2991/cnci-19.2019.53>
- Ma, Y., Wu, S., Macaringue, E. G. J., Zhang, T., Gong, J. & Wang, J. (2020). Recent Progress in Continuous Crystallization of Pharmaceutical Products: Precise Preparation and Control. *Organic Process Research & Development*. <https://doi.org/10.1021/acs.oprd.9b00362>
- Maddux, W. S. & Kanwisher, J. W. (1965). An in situ Particle Counter. *Limnology and Oceanography*, 10(suppl), R162–R168.
- Manee, V., Zhu, W. & Romagnoli, J. A. (2019). A Deep Learning Image-Based Sensor for Real-Time Crystal Size Distribution Characterization. *Industrial and Engineering Chemistry Research*, 58, 23175–23186. research-article. <https://doi.org/10.1021/acs.iecr.9b02450>

- Merkus, H. G. (2009). Particle Size, Size Distributions and Shape. Particle Size Measurements. [https://doi.org/10.1007/978-1-4020-9016-5\\_2](https://doi.org/10.1007/978-1-4020-9016-5_2)
- Mullin, J. W. & Nývlt, J. (1971). Programmed cooling of batch crystallizers. *Chemical Engineering Science*, 26(3), 369–377. [https://doi.org/https://doi.org/10.1016/0009-2509\(71\)83012-9](https://doi.org/https://doi.org/10.1016/0009-2509(71)83012-9)
- Myerson, A. S. (2002). *Handbook of industrial crystallization*. Boston: Butterworth-Heinemann. Retrieved from <http://site.ebrary.com/id/10206621>
- Nagy, Z. K., Fevotte, G., Kramer, H. & Simon, L. L. (2013a). Recent advances in the monitoring, modelling and control of crystallization systems. *Chemical Engineering Research and Design*, 91(10), 1903–1922. <https://doi.org/10.1016/j.cherd.2013.07.018>
- Nagy, Z. K., Fevotte, G., Kramer, H. & Simon, L. L. (2013b). Recent advances in the monitoring, modelling and control of crystallization systems. *Chemical Engineering Research and Design*, 91(10), 1903–1922. <https://doi.org/10.1016/j.cherd.2013.07.018>
- Omar, H. M. & Rohani, S. (2017). Crystal Population Balance Formulation and Solution Methods: A Review. *Crystal Growth and Design*, 17(7), 4028–4041. <https://doi.org/10.1021/acs.cgd.7b00645>
- Ono, T., Ter Horst, J. H. & Jansens, P. J. (2004). Quantitative measurement of the polymorphic transformation of L-glutamic acid using in-situ Raman spectroscopy. *Crystal Growth and Design*, 4(3), 465–469. <https://doi.org/10.1021/cg0342516>
- Pataki, H., Csontos, I., Nagy, Z. K., Vajna, B., Molnar, M., Katona, L. & Marosi, G. (2013). Implementation of Raman signal feedback to perform controlled crystallization of carvedilol. *Organic Process Research and Development*, 17(3), 493–499. <https://doi.org/10.1021/op300062t>
- Powell, K. A., Saleemi, A. N., Rielly, C. D. & Nagy, Z. K. (2015). Periodic steady-state flow crystallization of a pharmaceutical drug using MSMPR operation. *Chemical Engineering and Processing: Process Intensification*, 97, 195–212. <https://doi.org/10.1016/j.cep.2015.01.002>
- Powell, K., Keddon A., Saleemi, A. N., Rielly, C. D. & Nagy, Z. K. (2016). Monitoring Continuous Crystallization of Paracetamol in the Presence of an Additive Using an Integrated PAT Array and Multivariate Methods. *Organic Process Research and Development*, 20(3), 626–636. <https://doi.org/10.1021/acs.oprd.5b00373>
- Presles, B. (2010). Novel image analysis method for in situ monitoring the particle size distribution of batch crystallization processes. *Journal of Electronic Imaging*, 19(3), 031207. <https://doi.org/10.1117/1.3462800>
- Qu, H., Alatalo, H., Hatakka, H., Kohonen, J., Louhi-Kultanen, M., Reinikainen, S. P. & Kallas, J. (2009). Raman and ATR FTIR spectroscopy in reactive crystallization: Simultaneous monitoring of solute concentration and polymorphic state of the

- crystals. *Journal of Crystal Growth*, 311(13), 3466–3475.  
<https://doi.org/10.1016/j.jcrysgro.2009.04.018>
- Ramkrishna, D. & Singh, M. R. (2014). Population balance modeling: Current status and future prospects. *Annual Review of Chemical and Biomolecular Engineering*, 5, 123–146. <https://doi.org/10.1146/annurev-chembioeng-060713-040241>
- Randolph, A. D. & Larson, M. A. (1971). Chapter 3 - THE POPULATION BALANCE. In A. D. RANDOLPH & M. A. B. T.-T. of P. P. LARSON (Eds.) (pp. 41–63). Academic Press. <https://doi.org/https://doi.org/10.1016/B978-0-12-579650-7.50008-7>
- Rane, C. V., Ganguli, A. A., Kalekudithi, E., Patil, R. N., Joshi, J. B. & Ramkrishna, D. (2014). CFD simulation and comparison of industrial crystallizers. *Canadian Journal of Chemical Engineering*, 92(12), 2138–2156.  
<https://doi.org/10.1002/cjce.22078>
- Roy, S., Chamberlin, B. & Matzger, A. (2013). Polymorph Discrimination Using Low Wavenumber Raman Spectroscopy. *Organic Process Research & Development*, 17, 976–980. <https://doi.org/10.1021/op400102e>
- Saleemi, A. N., Steele, G., Pedge, N. I., Freeman, A. & Nagy, Z. K. (2012). Enhancing crystalline properties of a cardiovascular active pharmaceutical ingredient using a process analytical technology based crystallization feedback control strategy. *International Journal of Pharmaceutics*, 430(1–2), 56–64.  
<https://doi.org/10.1016/j.ijpharm.2012.03.029>
- Saleemi, A., Rielly, C. & Nagy, Z. K. (2012). Automated direct nucleation control for in situ dynamic fines removal in batch cooling crystallization. *CrystEngComm*, 14(6), 2196. <https://doi.org/10.1039/c2ce06288g>
- Sanjeev, K. (1996). On the solution of population balance equations by discretization—I. A fixed pivot technique, 51(8), 1311–1332.
- Sarkar, D., Doan, X. T., Ying, Z. & Srinivasan, R. (2009). In situ particle size estimation for crystallization processes by multivariate image analysis. *Chemical Engineering Science*, 64(1), 9–19. <https://doi.org/10.1016/j.ces.2008.09.007>
- Sheikhzadeh, M., Trifkovic, M. & Rohani, S. (2008). Real-time optimal control of an anti-solvent isothermal semi-batch crystallization process. *Chemical Engineering Science*. <https://doi.org/10.1016/j.ces.2007.09.049>
- Stelzer, T., Pertig, D. & Ulrich, J. (2013). Ultrasonic crystallization monitoring technique for simultaneous in-line measurement of liquid and solid phase. *Journal of Crystal Growth*, 362, 71–76. <https://doi.org/10.1016/J.JCRYSGRO.2011.11.027>
- Szilágyi, B., Agachi, P. Ş. & Lakatos, B. G. (2015). Numerical analysis of crystallization of high aspect ratio crystals with breakage. *Powder Technology*, 283, 152–162.  
<https://doi.org/10.1016/j.powtec.2015.05.029>



- Szilagyi, B., Borsos, A., Simone, E. & Nagy, Z. K. (2017). Model Based Estimation of 2D Crystallization Kinetics From Concentration and CLD Measurements. *Computer Aided Chemical Engineering* (Vol. 40). Elsevier Masson SAS. <https://doi.org/10.1016/B978-0-444-63965-3.50030-1>
- U.S. Food and Drug Administration. (2004). Guidance for Industry Guidance for Industry PAT — A Framework for Innovative Pharmaceutical, (September).
- Wang, I. C., Lee, M. J., Seo, D. Y., Lee, H. E., Choi, Y., Kim, W. S., ... Choi, G. J. (2011). Polymorph transformation in paracetamol monitored by in-line NIR spectroscopy during a cooling crystallization process. *AAPS PharmSciTech*, 12(2), 764–770. <https://doi.org/10.1208/s12249-011-9642-x>
- Weber, W. H. & Merlin, R. (2013). *Raman scattering in materials science* (Vol. 42). Springer Science & Business Media.
- Wijaya Hermanto, M., Phua, A., Shan Chow, P. & Tan, R. B. H. (2013). Improved C-control of crystallization with reduced calibration effort via conductometry. *Chemical Engineering Science*, 97, 126–138. <https://doi.org/10.1016/j.ces.2013.04.015>
- Wood, B., Girard, K. P., Polster, C. S. & Croker, D. M. (2019). Progress to Date in the Design and Operation of Continuous Crystallization Processes for Pharmaceutical Applications. *Organic Process Research and Development*, 23(2), 122–144. <https://doi.org/10.1021/acs.oprd.8b00319>
- Yang, X., Wang, X. & Ching, C. (2009). In situ monitoring of solid - state transition of p - aminobenzoic acid polymorphs using Raman spectroscopy. *Journal of Raman Spectroscopy*, 40, 870 - 875. <https://doi.org/10.1002/jrs.2185>
- Yang, Y. & Nagy, Z. K. (2015). Combined cooling and antisolvent crystallization in continuous mixed suspension, mixed product removal cascade crystallizers: Steady-state and startup optimization. *Industrial and Engineering Chemistry Research*, 54(21), 5673–5682. <https://doi.org/10.1021/ie5034254>
- Yang, Y., Song, L. & Nagy, Z. K. (2015). Automated Direct Nucleation Control in Continuous Mixed Suspension Mixed Product Removal Cooling Crystallization. *Crystal Growth and Design*, 15(12), 5839–5848. <https://doi.org/10.1021/acs.cgd.5b01219>
- Yang, Y., Song, L., Zhang, Y. & Nagy, Z. K. (2016). Application of wet milling-based automated direct nucleation control in continuous cooling crystallization processes. *Industrial and Engineering Chemistry Research*, 55(17), 4987–4996. <https://doi.org/10.1021/acs.iecr.5b04956>
- Yu, L. X., Lionberger, R. A., Raw, A. S., D'Costa, R., Wu, H. & Hussain, A. S. (2004). Applications of process analytical technology to crystallization processes. *Advanced Drug Delivery Reviews*, 56(3), 349–369. <https://doi.org/10.1016/j.addr.2003.10.012>

- Yu, Z. Q., Chow, P. S. & Tan, R. B. H. (2008). Interpretation of Focused Beam Reflectance Measurement (FBRM) Data via Simulated Crystallization, (4), 646–654. <https://doi.org/10.1021/op800063n>
- Yuan, C., Laurent, F. & Fox, R. O. (2012). An extended quadrature method of moments for population balance equations. *Journal of Aerosol Science*, 51, 1–23. <https://doi.org/10.1016/j.jaerosci.2012.04.003>
- Zhang, F., Liu, T., Wang, X. Z., Liu, J. & Jiang, X. (2017). Comparative study on ATR-FTIR calibration models for monitoring solution concentration in cooling crystallization. *Journal of Crystal Growth*, 459, 50–55. <https://doi.org/10.1016/j.jcrysgr.2016.11.064>

## Chapter 2

# Particle Characterization with On-line Imaging and Neural Network Image Analysis

A version of this chapter has been published in *Chemical Engineering Research and Design*: Wu, Y., Lin, M. & Rohani, S. (2020). Particle characterization with on-line imaging and neural network image analysis. *Chemical Engineering Research and Design*, 157, 114-125.

## Chapter 2 Particle Characterization with On-line Imaging and Neural Network Image Analysis

### Abstract

We proposed a deep learning-based in-situ microscopic image analysis system for detecting particles and performing size analysis in a high-density slurry, which shows great potential usage in the area of the solution crystallization process. A cost-effective imaging system consisting of a flow-through cell and a 3D-printed microscopic probe was built for high-quality image acquisition. The state-of-the-art deep learning model, Mask RCNN, was used to segment the overlapping particles and classify their categories with high accuracy. A comprehensive performance evaluation of the proposed system was conducted including extrapolation to unseen particle scale, detection in different solids concentration levels, and separation of two different types of particles. Compared with the previous studies, the solids concentration detection limit was improved by five times higher in terms of particle number per frame and three times higher regarding the particle pixel fill ratio (PFR). The categorized detections successfully classified the two different particles in a mixed suspension, and the individual particle size information was extracted, which showed high consistency with the particle information. What's more, a progressive labeling strategy was employed to improve the processing efficiency and accuracy, which would enable the transfer application in the solution crystallization process for various crystal species.

**Keywords:** Process analytical technology; Image analysis; Instance segmentation; Particle classification; High solids concentration; Mask RCNN

### 2.1. Introduction

The size and the shape of the solid products from a particulate process such as solution crystallization have a considerable impact on the final product quality and downstream

processability. For example, the size of the active pharmaceutical ingredient (API) crystals can affect the dissolution rate and bioavailability. The efficacy of the downstream filtering, drying, and blending processes are highly dependent on the powder properties determined by the crystal size and the shape. In order to design an efficient process and maintain the quality and consistency of the final product, various process analysis technologies (PATs) have been developed in the past decade for monitoring the size and shape of the solid products.

Some PATs perform the particle size analysis indirectly based on the size-dependent optical or acoustic properties. The laser backscattering method works with a rotating focused laser beam that scans the particles traveling through its focal volume. The time duration of backscattered light from particles is used to construct particle chord length distribution (CLD). Mettler Toledo FBRM (focused beam reflectance measurement) is a widespread commercial probe based on laser backscattering. Despite the capability of working at high solids concentration (about 30 vol%) (Merkus, 2009), transforming CLD into normal CSD is challenging and non-trivial because the optical properties and movement of the particles can affect the FBRM measurement (Heinrich & Ulrich, 2012). Ultrasonic attenuation spectroscopy (UAS) measures CSD based on the interaction between different sizes of particles and the sound wave that contributes to attenuation at different ultrasonic sound frequencies. The maximum solids concentration of UAS is about 70 vol%, making it an ideal online particle sizing instrument without the need to dilute the sample (Merkus, 2009). The laser diffraction (LD) method is an established particle size analysis method with extraordinary precision compared with many other techniques (Fisher et al., 2017). LD typically works with the best accuracy in solids concentration under 5 vol%, implying its main application in offline measurement (Merkus, 2009).

The indirect particle size analysis methods typically report the CSD in one-dimensional, shape-equivalent size distribution. Extracting shape information, such as aspect ratio, requires complex modeling work. In addition, the indirect size may require cross-

validation with other methods, such as optical microscopic imaging, to confirm the validity of the results. For example, the bubbles in the slurry can result in biased size distribution with the indirect methods. On the other hand, the combination of in-situ imaging and imaging analysis methods not only provides clear discrimination for different types of objects but can also extract more natural multi-dimensional size and shape information (El Arnaout, Cullen & Sullivan, 2016). Despite the visually natural particle information for manual examination, automated image analysis and feature extraction are deemed as challenging tasks because 1) illumination condition may lead to uneven background intensity; 2) visually overlapping particles and clusters introduce significant error in size and shape estimation; 3) out-of-focus and motion-induced blurriness cause undesired artifacts (Ferreira et al., 2011). Therefore, image analysis becomes extremely difficult when the suspension solids content exceeds 8-10% (Nagy et al., 2013).

Over the years, researchers have brought innovations into the particle image analysis field to improve detection performance. The contrast-based algorithms, such as edge-detection and thresholding, have been extensively used for their simplicity. These algorithms function by first scanning the image and extracting the features (edge or area) that contrasts significantly from the background. Then, the features will undergo a series of filtering and morphological operations to provide detailed information about the locations, sizes, and shapes of the particles. However, these primitive methods do not discriminate overlapping particles, and the optimal threshold can be inconsistent due to the heavy dependency on the human decision. The multi-variate analysis (Sarkar et al., 2009) and the adaptive threshold (Lu et al., 2018) algorithms have been employed to improve the robustness by providing more stable optimal parameters or introducing the mechanism to determine the local optimal parameters in different regions automatically. In order to address the problem of separating the overlapping or contacting particles, some special image features have been used to identify the contact points of multiple objects and split the detections into the individual particles. For example, Ahmad et al. (2012) developed a salient corner-based overlapping crystal segmentation method that

extracts the individual contour of the overlapping objects by classifying and grouping the detected salient points into multiple polygons based on their angular and spatial information. However, in the case of high solids concentration, a large number of semi-transparent overlapping objects present in the image might decrease the detection accuracy. Also, the polygon descriptor required a priori of the object shape, which may vary significantly for the crystals in the in-situ imaging due to breakage or polymorphic transformation. Larsen et al. (2007) developed a model-based crystal detector, SHARC, that functioned by extracting and matching the linear feature as the edges of the crystals. The SHARC algorithm was applied to analyze noisy in-situ images and monitored the size distribution of the high-aspect-ratio crystals. The highly overlapping objects will be discarded in favor of the reliability of the results. However, the probability of particles overlapping increases with higher solids concentration. The rejection of the overlapping objects makes the number of useful particles impractically low (less than ten percent of the total particles) (Larsen & Rawlings, 2009) and leads to a biased size evaluation over the small particles that have a lower chance of overlapping.

In this work, the state-of-the-art convolutional neural network model, Mask RCNN (He et al., 2017), was adopted to implement the overlapping object segmentation in high solids concentration and multi-species particle classification functionalities. Unlike the abovementioned conventional algorithms where the detection rules were exploited and concluded by a human, this approach achieved superior accuracy and robustness by enabling the neural network to discover the optimal underlying patterns in the images in the training process. The training is an iterative process that minimizes the difference between the calculated segmentation and the manually created labels (training loss) by automatically adjusting the parameters in the neural network model. Also, the fully parallelizable convolution operators can benefit from the parallel computation on a modern graphics processing unit (GPU), allowing the real-time (about 5 frames per second) image processing and process monitoring applications despite the tremendous computation scale. Our previous work (Gao et al., 2018) employed this approach to track the L-glutamic acid crystal nucleation, growth, dissolution, and polymorphic

transformation. A more recent work (Manee, Zhu & Romagnoli, 2019) presented monitoring a chloride sodium crystallization process with the customized neural network based on the single-stage RetinaNet (Lin et al., 2017) model, which featured faster speed and uncompromised detection accuracy.

This paper aimed to investigate the capabilities and limitations of the current Mask RCNN-based image analysis approach in the following aspects: 1) the detection accuracy in increasing solids concentration; 2) the capability to detect the particles of untrained size (scale extrapolation); 3) the ability to recover the individual size distribution after mixing two different particles (multi-species classification). Also, an efficient neural network training and labeling strategy were discussed in the background section. These conclusions will help researchers understand the feasibility of using this technology and speed up the model construction process.

## 2.2. Background

### 2.2.1. Mask RCNN

Mask RCNN (He et al., 2017) is a state-of-the-art two-stage instance segmentation framework proposed by Facebook Artificial Intelligence Research (FAIR). First, the input images are scanned by a backbone convolutional network (e.g., feature pyramid network (Lin et al., 2017)) to construct feature maps. The feature maps contain spatial semantic information at different scales. For example, the feature maps may reveal the locations of the long linear feature of needle-like crystals or the curly-shaped edge of glass beads. With the spatial information in the feature maps, the model proposes a set of regions of interest (RoI) that may contain objects with the regional proposal network (RPN). This operation narrows down the search scope and computational load of the following tasks. Also, the RPN allows overlapping proposals present with different aspect ratios, which enables the important overlapping objects segmentation feature for the in-situ crystallization monitoring. Next, the RoI Align module maps the multi-level



feature maps into the proposed regions and presents the cropped data for the following networks to further classify the detection category and find the precise bounding box and pixel-wise mask.

### 2.2.2. Training and Dataset preparation

The neural network was trained in an end-to-end manner that involved providing the raw image as input and the categories, bounding boxes, and masks of the objects present in the image as target or ground-truths (GTs). During training, the optimizer adjusts the parameters so that the model predictions match the desired GTs; in other words, minimize the training loss functions (He et al., 2017). Therefore, creating a sufficient and precise dataset is critical to train an efficient model. The dataset labeling process involves manually specifying the object boundaries with polygons or masks and assigning the categories for all objects in each image. In this study, the labeling process was done with an open-source web-based annotation software, Computer Vision Annotation Tool (CVAT) (Sekachev, Manovich & Zhavoronkov, 2019).

The training samples of each category were prepared separately to reduce confusion for manual labeling. Several labeling criteria were set to ensure consistency. Only typical objects that were seen frequently should be labeled, for example, a rod-like particle or a blob of particle cluster should not be labeled in a glass beads dataset. When encountering an object blurry due to out-of-focus, it should not be labeled because the casted shadow leads to incorrect size estimation, and the blurry looking will confuse the classification. The occluded objects should not be labeled if more than 20% area is invisible. For contacting objects with less than 20% overlapping, the hidden object boundaries should be predicted by inferring from its shape.

### 2.2.3. Progressive Labeling Strategy

Manually labeling thousands of objects is time-consuming and the optimal dataset size is difficult to estimate. The progressive labeling strategy is one of the automated labeling techniques that helps to offload the labor work and determine the dataset sufficiency.

Figure 2-1 depicts the procedure to implement the progressive labeling strategy. The training epochs in each iteration are selected by trial-and-error that balances the training time and label prediction accuracy. The accuracy target and relative improvement threshold were selected to be 80% and 10%, respectively. For simple-shaped objects like glass beads, the labeling can be completed with about 50 images.

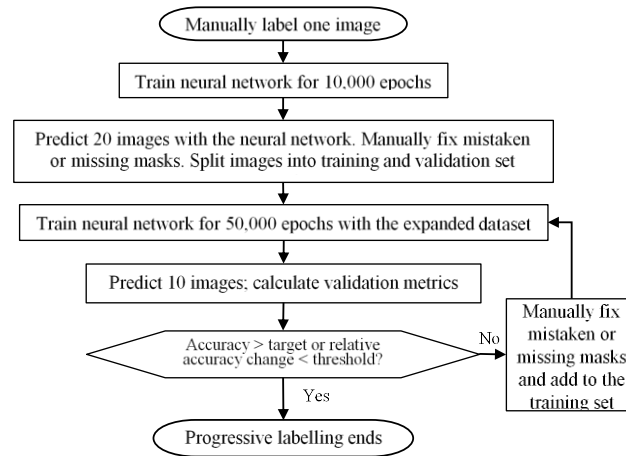


**Figure 2-1** Schematic of progressive labeling strategy workflow

#### 2.2.4. Neural Network Performance Evaluation

The image analysis performance can be evaluated externally or internally. The external evaluation compares the processed size distributions with the data from the manufacturer or the other instruments (Borchert et al., 2014; Cardona et al., 2018; Schorsch et al., 2014), while the internal evaluation compares the masks predicted by the image analysis with the GTs labeled by a trained expert and calculate the evaluation metrics. The evaluation metrics were used to assess the model prediction performance on validation and test datasets. The average precision (AP) measures how accurate the predicted masks match the GTs. The average recall (AR) measures the completeness of the prediction, i.e., find all GTs rather than miss them. The AP and AR are the trade-offs between finding fewer but more accurate samples and finding as many objects as possible regardless of the risk of mistake.

The match between masks is measured by intersection-over-union (IoU) that is the area of intersection of the masks being divided by the area of the union of the masks. When IoU between a GT and a prediction is greater than 0.5, they are considered matching. If a GT does not have any matching prediction, it is counted as a false negative; if a prediction does not have any matching GT, it is considered a false positive. For each GT, the prediction with the highest IoU is considered as true positive, while the rest are counted as false positives. The AP was calculated by averaging the IoUs of the true positives and false positives (IoU=0), while the AR was calculated by averaging the IoUs of the true positives and false negatives (IoU=0).

### 2.2.5. Particle Size Descriptor

In order to analyze the size distributions and various properties of particles, the geometric information should be extracted from the predicted masks. Based on the shape of interested particles, the optimal mask evaluation model should give the size that matches the actual dimension of the particle.

The objects cropped by the frame boundaries may affect the accuracy of size and shape measurement. Since the masks of some cropped objects may be underestimated so that they did not intersect with the image borders, we found that removing the predicted masks with their bounding-box-to-frame-boundary distance less than 2 pixels produced the optimal result without cropped objects while keeping the most valid samples.

$$D_{eq} = \sqrt{\frac{4 \cdot A_{mask}}{\pi}} \quad (2-1)$$

The area equivalent circular diameter is a one-dimensional size measurement that is defined by the diameter of a circle with the same area of the mask (Eq. 2-1), which is ideal to describe the size of spherical particles. The minimum area bounding rectangle size is a two-dimensional size obtained from the width and height of the smallest rotated

rectangle encompassing the mask. The size and aspect ratio of rod- or needle-like particles can be accurately determined from this method.

### 2.2.6. Solids Concentration and Pixel Fill Ratio

The solids concentration can be characterized by volume fraction (solids volume per slurry volume) or number density (number of particles per volume slurry). The scales of these statistics depend on the particle size. For example, smaller particle slurry has a high number density while a relatively low volume fraction. This scale inconsistency makes it difficult to compare the solids concentration for particles with different sizes. In the previous study (Larsen & Rawlings, 2009), the image complexity has been defined based on the depth of field, particle shape, and number density. However, the definition involves complex mathematics and requires a priori of the particle shape, thereby inapplicable for the images acquired in the real system. Inspired by the concept of the IoU metrics, we proposed the pixel fill ratio (PFR) as a simple descriptor of the solids concentration and image complexity in the imaging-based system. The PFR is defined as Eq. 2-2 given below. Note that due to object occluding, the total projected area can be larger than the observing field area. Therefore, the PFR can be greater than one. Higher PFR means more chance that particles are agglomerated or overlapped, implying more difficult analysis and lower accuracy.

During the experimental design stage, estimation of volume fraction, number of objects in each frame, and PFR can be performed by Eqs. 2-3 to 2-7, where  $m_{add}$  [kg] is the mass of added material;  $\rho_p$  [kg/m<sup>3</sup>] is the particle density;  $V_{slurry}$  [m<sup>3</sup>] is the slurry volume;  $A_{obs}$  is the observed area;  $N_t$  is the total number of objects in the system;  $N_{slurry}$  [m<sup>-3</sup>] is the particle volumetric number density;  $Vol\%$  is the volume fraction;  $N_{obs}$  is the number of objects in the observed volume, and  $PFR$  is the pixel fill ratio.  $V_p$ ,  $V_{obs}$ ,  $A_{proj}$  are functions to calculate per-particle the volume [m<sup>3</sup>], observed field volume [m<sup>3</sup>], and per-particle projected area [m<sup>2</sup>], respectively. The depth of field is required to calculate the observed volume, which can be treated as a tunable parameter

and is estimated by fitting the computed PFR or number of objects per frame with the experimental ones.

$$PFR \stackrel{\text{def}}{=} \frac{\text{Projected area of particles in the observing volume}}{\text{Observing field area}} \quad (2-2)$$

$$N_t = \frac{m_{add}}{V_p \cdot \rho_p} \quad (2-3)$$

$$N_{slurry} = \frac{N_t}{V_{slurry}} \quad (2-4)$$

$$Vol\% = N_{slurry} \cdot V_p \quad (2-5)$$

$$N_{obs} = N_{slurry} \cdot V_{obs} \quad (2-6)$$

$$PFR = \frac{A_{proj} \cdot N_{obs}}{A_{obs}} \quad (2-7)$$

With the image segmentation results, the masks of each object are used to calculate the total projected area in each frame. Since the masks can overlap, the *total mask area* can be greater than the frame area. On the other hand, the *non-overlapping area* is calculated with the area of the union of the masks, which does not count the overlapping area repeatedly and will not exceed the frame area. Therefore, two experimental *PFRs* can be defined based on the *total mask area* ( $PFR_T$ ) or *non-overlapping area* ( $PFR_N$ ) (Figure 2-2). The overlapping ratio  $r = PFR_T/PFR_N - 1$  is a quantity between zero to one that quantifies the level of object overlapping and obstruction, which can be used to determine whether the solids concentration is too high for accurate measurement. Alternatively, it may be used as a quantitative measurement of particle agglomeration.

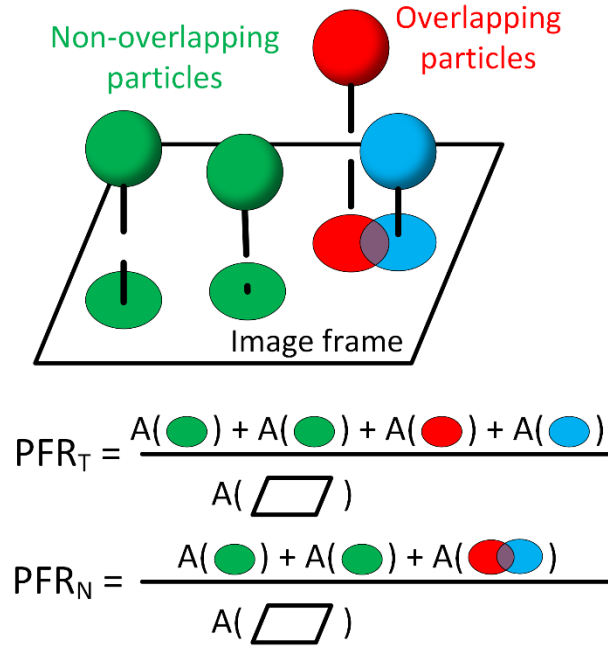


**Figure 2-2** Illustration of the concepts of two PFRs. Function A stands for the area of the objects.

## 2.3. Experimental Setup and Procedures

### 2.3.1. Neural Network Training Parameters

In this study, we built a deep learning model with the latest FAIR Detectron2 platform (Wu et al., 2019). A desktop computer with Intel i7-6700K CPU, 32 GB DDR3 RAM, and an NVIDIA GTX 1070 GPU (performance: 6.5 TFLOPs) was used for neural network training and inference. During training and evaluation, the processing speeds of the images (800 by 600 pixels resolution) were 3 frames per second (fps) and 5 fps, respectively. The computation power can be upgraded by using multiple GPUs or use the latest GPU that supports the mixed-precision training (Micikevicius et al., 2017), which trades marginal computation precision for significant speed improvement.

ResNet-101 was selected as the backbone of the neural network. The neural networks were trained for 240,000 epochs with the learning rates of 0.002 for the first 60,000 epoch and 0.0002 for the rest.

### 2.3.2. Particle Imaging Process Setup

Figure 2-3 demonstrates the experimental setup used in this study. During the experiment, the solid samples dispersed in 200-mL deionized water were added into a multi-port crystallizer. An overhead stirring motor working at 500 RPM drove a 50-mm Teflon anchor stirrer to provide sufficient mixing. The slurry was circulated by a peristaltic pump (Kamoer KCM-ODM, four rotors) at 120-mL/min in a 4-mm-diameter tubing, which ensured minimal clogging and classification effect. The flow cell was customized by welding circular glass tubing (3-mm I.D.) on both ends of a rectangular glass tubing (Friedrich & Dimmock, 2-m height, 4-mm width). The circular glass tubing served as a connection port, while the flat surface of a rectangular tubing provided a perfect observing window with minimal distortion. The similar internal dimensions and smooth welding transition ensured no dead zone inside the apparatus.

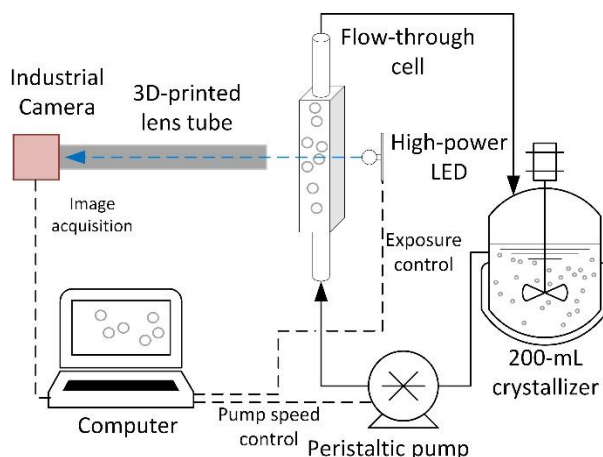


**Figure 2-3** Flow cell imaging experimental setup

A 3D-printed part bound together the flow cell, a high-power LED (CREE XHP70.2, 29-watt) for bright field lighting, and a lens. The lens consisted of an achromatic convex lens (10-mm-diameter, 30-mm-focal length) for optical imaging and a 3D-printed extension

tube that connected the convex lens to the camera. An industrial camera (Allied Vision Mako U-051) was used as the image acquisition device. In order to minimize the motion blurry of the objects, a strobe lighting strategy similar to the previous work (Simon et al., 2012) was implemented with an STM32F103 microcontroller, and the high-power LED that was capable to illuminate within several microseconds. Because of the short illumination period, the global-shutter-equipped industrial camera was required for full-frame exposure.

The software was developed to coordinate each component, store captured images, and perform various analyses. The industrial camera was interfaced with an open-source library, harvesters, which enabled fast development and provided excellent performance (Kudo, 2019). The exposure time controller and pump were controlled via serial ports, enabling automated experiments and data acquisition.

### 2.3.3. Camera Scale Calibration

The pixel size calibration was performed to convert the captured images into the actual scale. A standard hemocytometer was used as the size reference for calibration. ImageJ (Rueden et al., 2017) provides convenient tools for extracting the profile data (pixel gray value along a given line). The extrema of the profile were used to identify the intersections and lengths of the grids. The calibration statistics were obtained from repeated profile measurements in different locations of the image ( $1.286 \pm 0.001 \mu\text{m}/\text{pixel}, n = 8$ ).

### 2.3.4. Particle Sample Preparation

Glass beads and fluid catalytic cracking (FCC) catalyst particles were chosen as the model particles to study the performance of the image analysis model. Glass beads were transparent spherical particles (Figure 2-4.a), which were used as the model particle for neural network training and evaluation. The fluid catalytic cracking (FCC) catalyst particles (Figure 2-4.b) have an oval to grainy shape and an opaque body, which were used to evaluate the capability to differentiate different species of particles with a distinct



appearance. Compared with the common crystallization materials, the model particles are stable in the aqueous slurry with negligible breakage, agglomeration, or dissolution, allowing more accurate and stable solids concentration quantification. The regular and uniform shape makes it easy to define the characteristic size, calculate different types of size distribution, and compare with the measurements by other instruments.

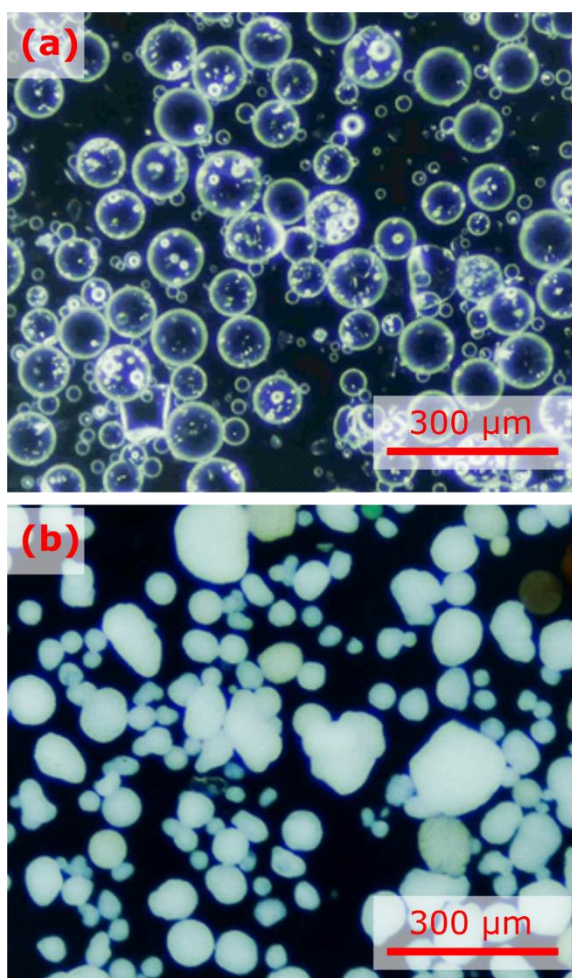


**Figure 2-4** Dark-field microscopic image of (a) glass bead (un-sieved) and (b) FCC catalyst sample.

#### 2.3.4.1. Experiments for preparing model training dataset

A GilSonic AutoSiever (Gilson Inc., OH, USA). was used to separate glass beads sizes into 10-cuts: 20, 32, 45, 53, 63, 75, 90, 106, 125, and 150  $\mu\text{m}$ . 20-32- $\mu\text{m}$ . These particles were used to collect training data. Glass beads with the size 125-150- $\mu\text{m}$  were reserved to evaluate particle size extrapolation capability. The added amounts of particles were calculated based on a flat number distribution (Table 2-1 No. 1). 51-images were labeled with a progressive labeling strategy. The dataset was split into the training set (41 images) and the validation set (10 images).

The FCC particles were used to test the model capability to differentiate different types of particles. The FCC training data was collected according to Table 2-1, No. 8. 28-images were labeled progressively and split into the training set (24 images) and validation set (4 images).

#### 2.3.4.2. Experiments for evaluating model performance

The model capability of predicting objects with unseen scales was assessed by analyzing smaller or larger particles than the trained scale range and comparing the validation metrics with manual labels and the size distribution measured by the laser diffraction size analysis with Malvern Mastersizer 2000 (Malvern Instrument, UK). The experimental procedure is described in Table 2-1, No. 2 to 4. The samples were tested by Malvern Mastersizer 2000 for size verification. Ten images in each run were manually labeled to calculate the validation metrics.

The model prediction accuracy at different solids concentration levels was evaluated. Three glass beads samples (small: 32-45- $\mu\text{m}$ , medium: 63-75- $\mu\text{m}$ , large: 106-125- $\mu\text{m}$ ) were used in each experiment (Table 2-1, No. 5 to 7) to evaluate how the solids concentration of different sized particles can affect the model performance. At each solids concentration level, ten images were labeled as validation GTs to evaluate the accuracy, and the size distributions were compared to evaluate the consistency. The final samples of each experiment were tested by Malvern Mastersizer 2000.

The size distributions of the glass beads and FCC particle samples were analyzed separately in two crystallizers (Table 2-1 No. 9). Then, the solid samples were filtered, mixed, and dispersed in 200 mL DI water. The size distributions of the mixed samples were analyzed and compared with the ones before mixing to evaluate the classification capability of the model.

**Table 2-1** Experiments description

No.	Objective	Material*	Solid concentration
1	Glass beads training data	Sieved glass beads mixture of which the number-based distribution was flat**	–
2	Size extrapolation (small)	20-32-micrometer glass beads: 1 g	number density: $2.5 \times 10^5 \text{ mL}^{-1}$ ; volume fraction: 0.2%; PFR: 9.2%.
3	Size extrapolation (large)	125-150-micrometer: 6 g	number density: $9.2 \times 10^3 \text{ mL}^{-1}$ ; volume fraction: 1.3%; PFR: 10.8%.
4	Size extrapolation (extreme large)	150-300-micrometer: 8 g	number density: $2.1 \times 10^3 \text{ mL}^{-1}$ ; volume fraction: 1.7%; PFR: 8.1%.
5	Solids concentration test (small)	32-45-micrometer glass beads 8 to 3.9 g, added separately	number density: 500 to $2.5 \times 10^5 \text{ mL}^{-1}$ ; volume fraction: 0.002% to 0.8%; PFR: 0.04% to 24.7%
6	Solid concentration test (medium)	63-75-micrometer glass beads 42 mg to 17 g, added separately	number density: 500 to $2.0 \times 10^5 \text{ mL}^{-1}$ ; volume fraction: 0.9% to 3.5%; PFR: 0.15% to 60.7%
7	Solids concentration test (large)	125-150-micrometer glass beads 200 mg to 15 g, added separately	number density: 500 to $3.8 \times 10^4 \text{ mL}^{-1}$ ; volume fraction: 0.04% to 3.1%; PFR: 0.4% to 32.1%
8	FCC training data	FCC particles, 3.0 g	–
9	Classification test	FCC particle 1.0 g; un-sieved glass beads 1.0 g	–

---

\* 200-mL DI water was added as the dispersion in each experiment.

## 2.4. Results and Discussion

### 2.4.1. Neural Network Training and Progressive Labeling

The neural network training loss and validation metrics at different training epochs are demonstrated in Figure 2-5.a. The training loss continued to decrease throughout the training process, and two sudden drops in the training loss were observed at epoch 40,000 and 60,000, where the learning rate was decreased by a factor of 0.5. The optimal training steps were found to be 60,000 epochs, where the validation performance stopped improving. After that, the validation metrics plateaued, indicating no significant overfitting occurred. The final validation AP and AR stabilized at 0.84 and 0.86, respectively.

Figure 2-5.b helps to interpret the validation metrics. The true positives (TPs) were the successful prediction that matched the GT whose overlapping metrics (IoU) contribute to the AP; the false positives (FPs) were unexpected predictions that lowered the validation AP; the false negatives (FNs) were missed predictions that lowered the validation AR. Note that the validation set was not involved in the training process. Some FNs and FPs were due to the inconsistent labels in the validation set. For example, the FPs could be some objects that were otherwise labeled and included in the training sets. If we only look at the successful predictions, the TPs, the average IoU could reach 88.9%, implying a very accurate mask segmentation.

---

\*\* Sieved glass beads addition: 32-45- $\mu\text{m}$ : 162-mg; 45-53- $\mu\text{m}$ : 314-mg; 53-63- $\mu\text{m}$ : 521-mg; 63-75- $\mu\text{m}$ : 878-mg; 75-90- $\mu\text{m}$ : 1504-mg; 90-106- $\mu\text{m}$ : 2509-mg; 106-125- $\mu\text{m}$ : 4110-mg.

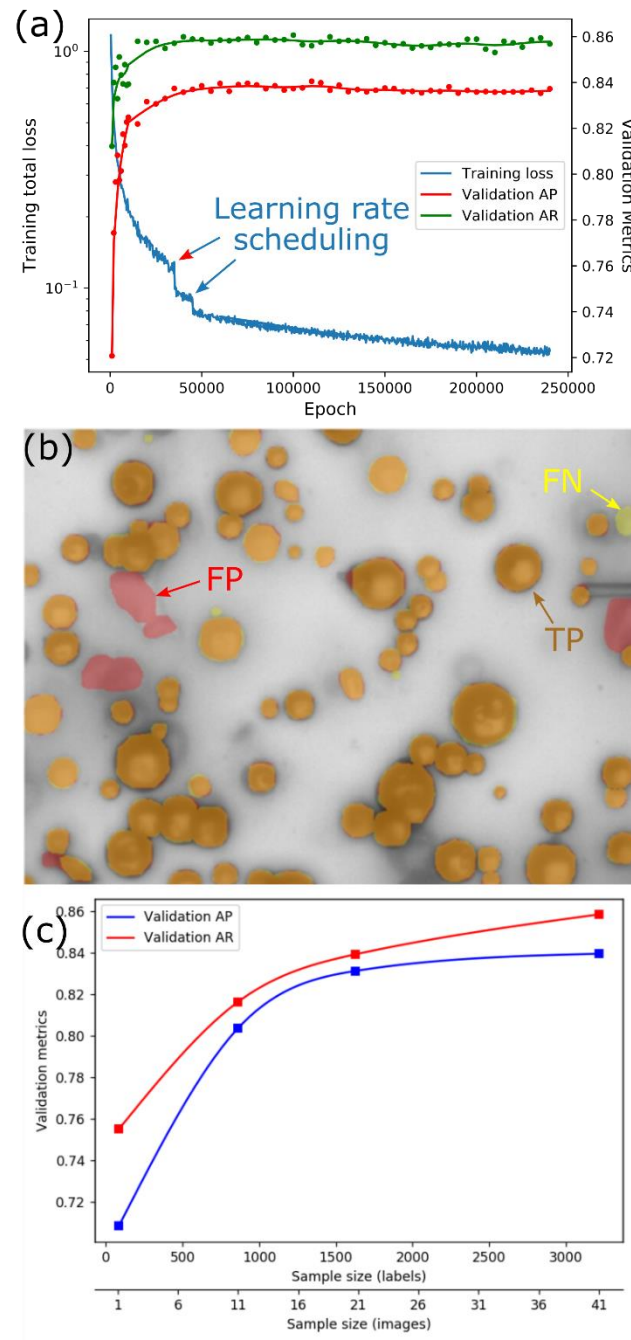


**Figure 2-5** (a) Neural network training loss and validation metrics (full glass beads training set); (b) validation image with overlays of GTs and the masks predicted by the neural network (240,000 epoch training). The orange masks are true positives (TPs) (overlapping GT and prediction); the yellow masks are false negatives (FNs) (GT only);

the red masks are false positives (FPs) (prediction only); (c) Neural network performance after 60,000 epochs with different training set sizes.

The progressive training exploited the relation between training set size and validation accuracy. The result is shown in Figure 2-5.c. Each neural network was trained from the same starting point for 60,000 epochs with different training set sizes. When only one image (82 label samples) was used for training, the AP and AR were higher than 0.7. With the increasing training data size, the AP was stable after 21 images (1628 samples), but the AR was still improving. This behavior could be attributed to the simple and uniform shape of the glass beads, which allowed learning the precise masks in a smaller number of samples. On the other hand, with expanding training samples, more rare cases or random human inconsistencies were learned, which reflected in fewer missed detections or false negatives, hence improving the AR metrics. This analysis of Figure 2-5.c is a powerful tool to help efficiently decide the sufficiency of dataset size. With the optimized training strategy, the training time was approximately five hours, and the total time for model preparation could be done within two days.

#### 2.4.2. Particle Size Extrapolation Performance

The particle size extrapolation tests reveal the generalization capability of the neural network model to detect the particle of unseen size, which were summarized in Figure 2-6 and Table 2-2. The small size extrapolation (20-32- $\mu\text{m}$ ) demonstrated the superior capability of the neural network to detect the objects smaller than the training objects. The area equivalent circle diameter and size calculation methods showed a good agreement in the predicted size distribution (Figure 2-6.a). The size distribution produced by the proposed method matches the sieved sample specifications and the Mastersizer 2000 laser diffraction analysis, whose default volume-based distribution was converted into number-based size distribution to ensure comparability. With training validation metrics as the baseline, the evaluation metrics (Table 2-2) of small size extrapolation showed an equal performance in AP and a decreased AR, which implied that the masks generated for small particles were still accurate, but they failed to find some objects

intended by the GTs. This behavior was an expected extrapolation issue because the neural network was confused by the scale variation (Kanazawa, Sharma & Jacobs, 2014).

The experiment with 125-150- $\mu\text{m}$  glass beads samples slightly extrapolated the range to the larger size. Due to sample contamination or errors during sieving, some small particles were mixed in, which was confirmed by microscopic images (Figure 2-6.e). Despite the good agreement between the image analysis and laser diffraction (Mastersizer 2000) results, the size distributions obtained by image analysis successfully reported the smaller particles, while the laser diffraction (Mastersizer 2000) failed to resolve the differences, possibly because the laser diffraction is volume-based size analysis, so that the volume fraction of large particles effectively masked the size distribution peak of the smaller particles, resulting in a lower resolution for small particles. The images and predicted masks were reviewed to ensure the size distribution was not due to the partition of large objects. From Table 2-2, the AR was consistent with the baseline, while the AP dropped, which was because the large particles were easier to find, but the shape of the mask may be variable and difficult to predict.

The neural network performance degraded significantly when processing the 150-300- $\mu\text{m}$  glass beads samples. Not only the predicted masks became incomplete and partitioned (Figure 2-6.f), the size distribution also failed to report the correct size range. From Table 2-2, the AP and the AR continued the trends in 125-150- $\mu\text{m}$  case.

In conclusion, it is necessary to prepare the training set with all possible scaled objects. Besides, the solids concentration specifications for each experiment matched the predictions.



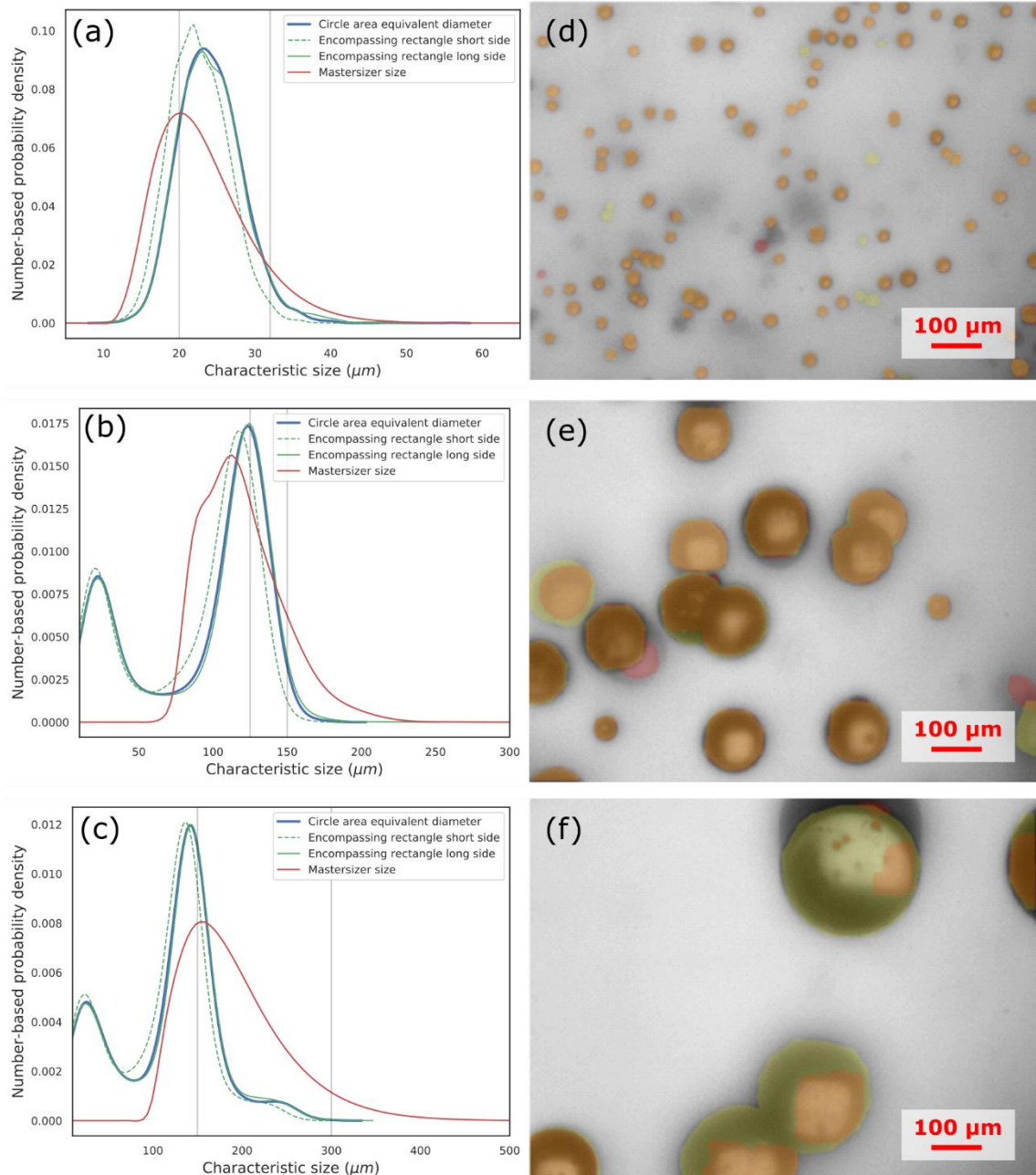


**Figure 2-6** Particles small extrapolation test results with sieved glass beads sample (row 1: 20-32- $\mu\text{m}$ ; row 2: 125-150- $\mu\text{m}$ ; row 3: 150-300- $\mu\text{m}$ ). (a-c) The particle size distributions obtained by different size extraction models compared with the result from Malvern Mastersizer 2000 (converted from volume-based to number-based size

distribution). The grey lines stand for the sieve size ranges.; (d-f) sample validation images with GT and prediction overlays. Refer to Figure 2-5 for the color codes.

**Table 2-2.** Extrapolation test evaluation metrics

Sieve size ( $\mu\text{m}$ )	AP	AR	PFR			Average objects per frame		Overlapping ratio
			calculated	PFR <sub>N</sub>	PFR <sub>T</sub>	calculated	measured	
20-32	0.8432	0.7938	9.2%	8.9%	9.1%	124.2	132.2	0.012
125-150	0.7987	0.8702	15.0%	10.8%	11.4%	15.3	11.8	0.039
150-300	0.6257	0.8469	8.1%	6.38%	7.25%	1.3	5.9	0.136

### 2.4.3. Detection Performance in The Increasing Solids Concentration

Figure 2-7 demonstrates the sample images and predicted masks for three different-sized particles at three levels of solids concentration. At the higher solids concentration, despite the drastically increasing complexity of the images and overlapping of the objects, the image segmentation performance was not compromised. By visual examination less than 2% of objects were missed (false negative); the contacting and overlapping objects (Figure 2-7.h) were segmented into multiple; the undistinguishable cluster (Figure 2-7.f) segmentation was attempted by picking up a few visible objects on the cluster, and some of the overlapping masks successfully predicted the invisible parts (Figure 2-7.e). The PFR was used as a scale-invariant solids concentration indicator that successfully classified the images with distinct visual complexity. Also, we observed the decreasing image brightness with the increasing PFR or solids concentration due to the obstruction of the particles out of the depth of field. This inconsistent exposure led to the wash-out looking of low solids concentration pictures in which the particles were difficult to detect. For the high solids concentration images, the excessive shadows might hide some particles and cause incorrect segmentation. Therefore, it is recommended to introduce closed-loop control to maintain the image brightness at an optimal level.

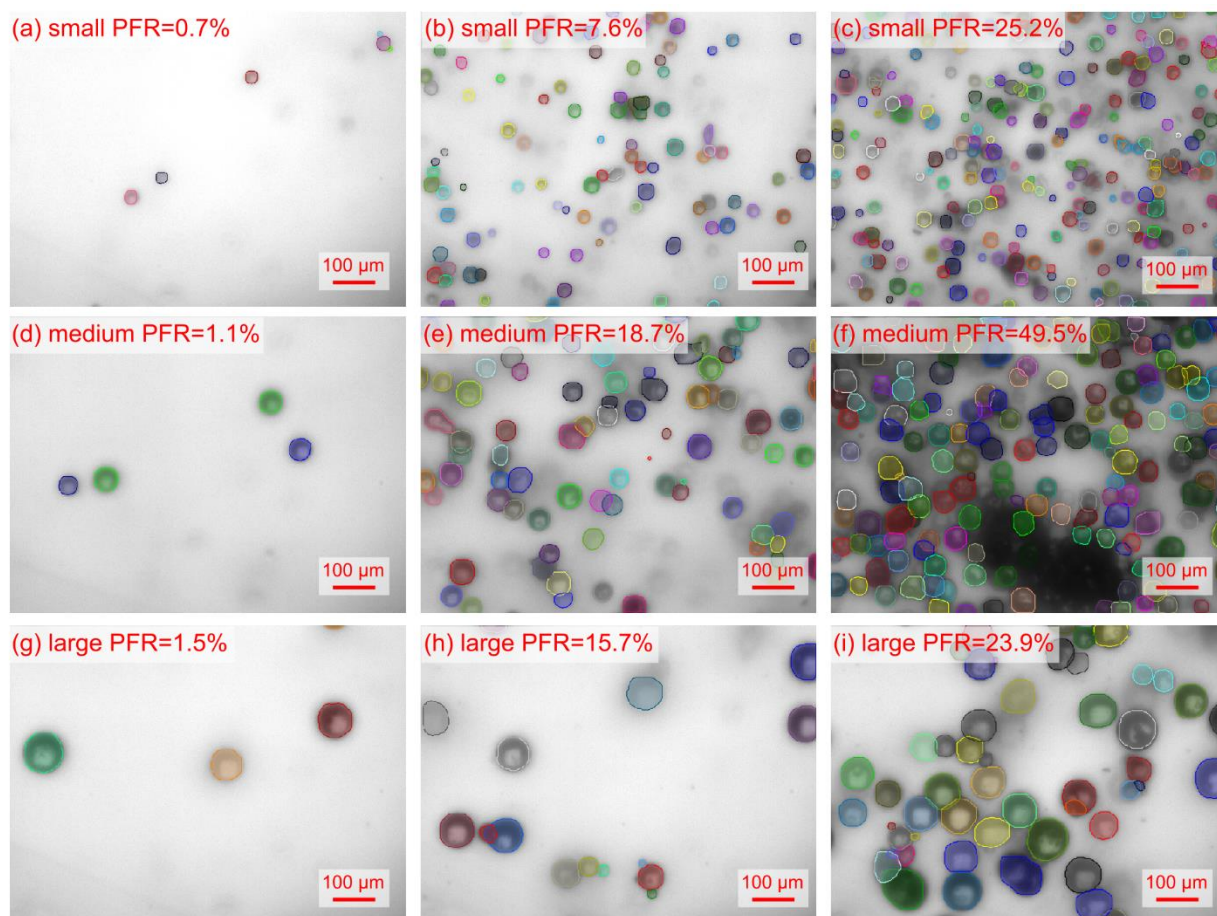


**Figure 2-7** Sample images array for the small (32-45- $\mu\text{m}$ ), medium (63-75- $\mu\text{m}$ ), and large (106-125- $\mu\text{m}$ ) glass beads samples in rows and different solids concentrations in columns (average total PFR). The detected instances were overlaid with multiple colors.

The size distributions and the performance metrics were summarized in Figure 2-8. The size distribution statistics were stable at different solids concentration levels (Figure 2-8.a-c). The size distribution for medium-sized samples (Figure 2-8.b) demonstrated a tendency to increase when the solids concentration was extremely high, possibly due to the unsuccessful segmentation of overlapping objects, which can be confirmed by the AP performance drop at high solids concentration (Figure 2-8.d). The Mastersizer 2000 number-based quantiles match the results from image analysis. For large particle samples

(Figure 2-8.c), the image analysis could differentiate the small particles that the laser diffraction failed to detect, leading to the difference in the D10 quantile. The PFR was found linearly correlated with the mass of particles when PFR was below 0.3. This relation was observed in all runs with different-sized particles, rendering it an effective scale-invariant solids concentration quantity.

The AR matched the performance of the baseline even at a very high solids concentration, which was confirmed by visual examination that only a few objects were missed. However, the AP started to drop when the particles became more crowded and complex, which implied approaching the solids concentration limit when the PFR was greater than 0.5. In this case, an in-situ dilution device is recommended to archive the best accuracy.

In summary, the size analysis by the neural network image analysis was consistent at various solids concentrations. The capability of high-resolution analysis and visual examination make it an ideal particle size analysis PAT.

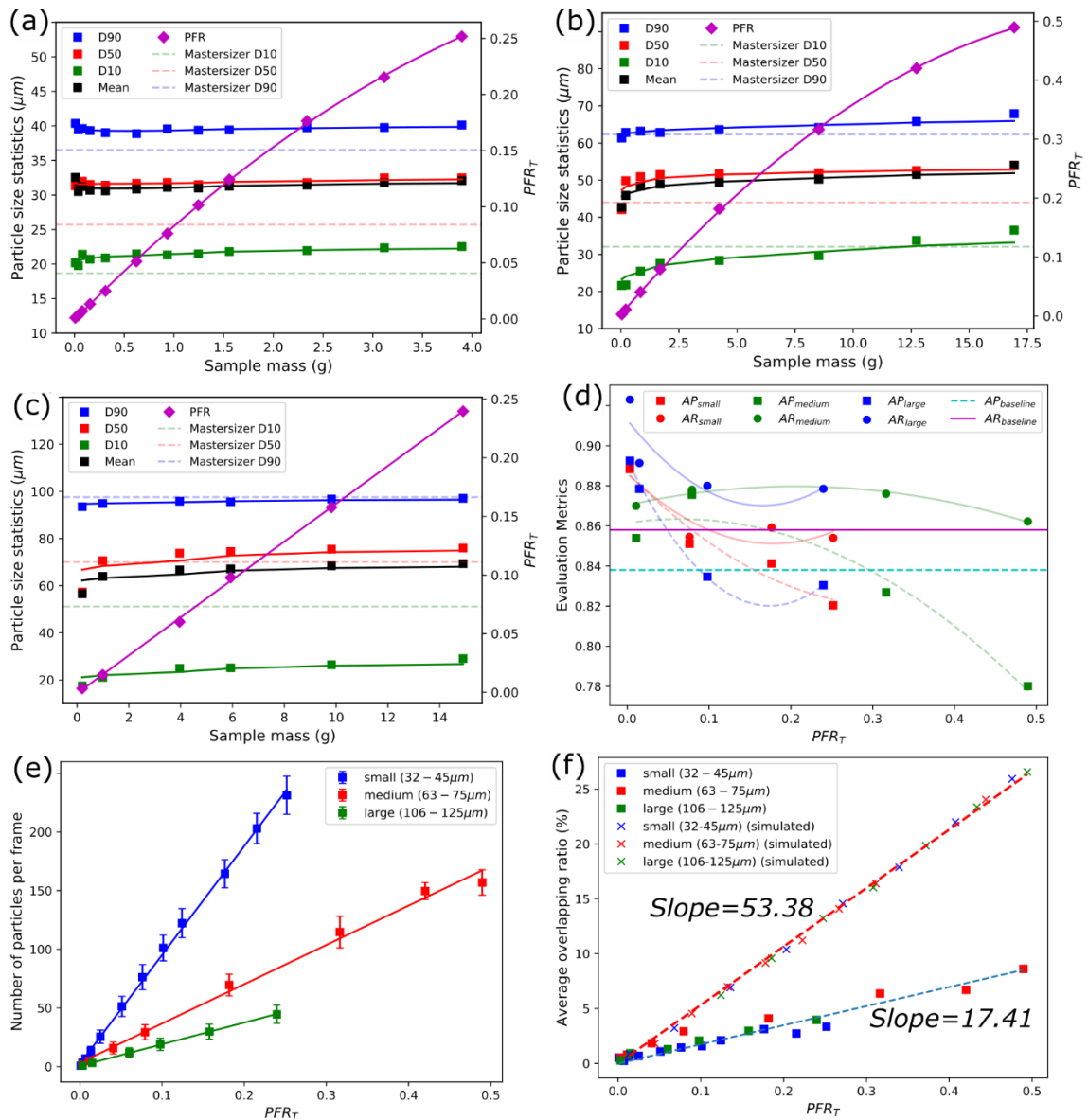


**Figure 2-8** Performance evaluation results for the small (32-45- $\mu\text{m}$ ), medium (63-75- $\mu\text{m}$ ), and large (106-125- $\mu\text{m}$ ) glass beads samples at different solids concentrations. (a)-(c) the size distribution statistics (D90, D50, D10, and mean) and the PFR at the increasing solids concentrations. The Mastersizer 2000 number-based size statistics (horizontal dash lines) were included for reference; (d) The validation metrics at increasing solids concentrations (PFR) and the baselines; (e) The average number of

detected particles per frame at various  $PFR_T$  levels; (f) The simulated and experimental overlapping ratio at various  $PFR_T$  levels

The further study of the effects of PFR shows its effectiveness to characterize the particle solids concentration and image complexity. Figure 2-8.e shows that the  $PFR_T$  has a linear relation with the number of the detected particle in each frame, thereby enabling it an effective predictor of the particle number density. In previous studies (Borchert et al., 2014; Cardona et al., 2018), the effective range of solids concentration for an image analysis system usually limited the number of particles to tens of particles per frame due to the limited ability to differentiate the overlapping particles. Larsen and Rawlings (2009) found that linear relationship between the number of identified objects per frame and the actual number density held only when the equivalent  $PFR_T$  is below 0.15, and above that the number of missed particles became dominant. On the other hand, our work successfully shows that the neural network image analysis is capable to measure the particle number density without major error up to the  $PFR_T$  of 0.49, implying its superior capability to measure the particle number density at the high solids concentration.

The  $PFR_T$  was also found to have a linear effect on the average overlapping ratio regardless of the particle size (Figure 2-8.f). The Monte Carlo method was used to simulate the average overlapping ratio by generating the circles of the specified diameter at random locations in an image. The  $PFR_T$  and  $PFR_N$  were obtained by measuring the total area of all generated objects and the object-occupied area, respectively. Although both simulated and experimental overlapping ratio showed a linear relation with the  $PFR_T$ , the slope of the simulated overlapping ratio was approximately three times greater than the slope of the experimental one, which is possibly attributed to the limitation of overlapping segmentation. When the overlapping area was more than approximately 1/3 of the area of the smaller object, the algorithm might recognize the cluster as a single particle, resulting in a reduced number of detections. Therefore, the overlapping ratio predicted in experiments was lower than the simulated cases, and the slope difference

between the experiments and simulations could be used to evaluate the overlapping segmentation performance.

The performance of the high solids concentration analysis has been studied in the previous works. Table 2-3 compares the image analysis result of this work at  $PFR_T = 0.252$  and  $PFR_T = 0.495$  and the images obtained from the other studies (Javier Cardona et al., 2018). Larsen and Rawlings (2009) studied their SHARC image analysis algorithm on artificial images. The  $PFR_T$  and the average recall were estimated from the data in the publication. The accuracy of the SHARC algorithm was obtained from the data from the similar in another study (Larsen, Rawlings & Ferrier, 2007) and the average recall was calculated based on the data in the paper (Larsen & Rawlings, 2009). Cardona et al. (2018) used edge detection algorithms and focus evaluation to filter out undesired objects. The  $PFR_T$ , AP, and AR were estimated with the image sets and the programs provided by the authors (Javier Cardona et al., 2018). Borchert et al. (2014) studied the cooling crystallization of potassium dihydrogen phosphate with conventional thresholding image analysis and used the shape descriptor to classify the single crystals and clusters. The  $PFR_T$ , AP, and AR were estimated with the data and figures in the paper (2014). Compared with the previous works, our method pushes the up limit of the solid concentration for image analysis to approximately three times higher than before, while maintaining the high AP and AR that outperforms any of the image analysis cases, which is considerably better than the previous state-of-the-arts.



**Table 2-3.** Summary of the previous image analysis studies at a high solids concentration

Reference	Maximum $PFR_T$	AP @ Maximum $PFR_T$	AR @ Maximum $PFR_T$	Comments
This work	0.495	0.78	0.865	
Larsen and Rawlings (2009)	~0.371	~0.5	~0.2	Artificial images
Cardona et al. (2018)	~0.179	~0.2	~0.5	
Borchert et al. (2014)	~0.133	~0.4	~0.7	

#### 2.4.4. Multi-species Classification and Measurement Reproducibility

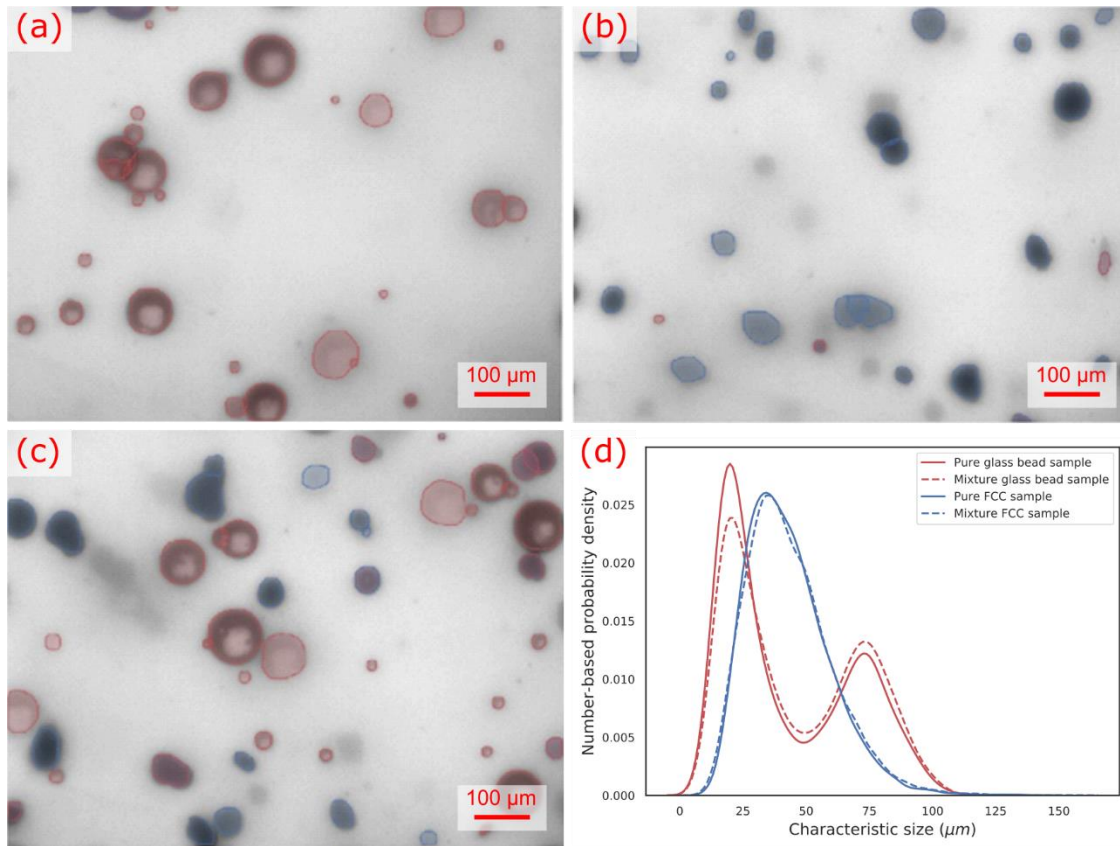


**Figure 2-9** Sample images with overlays colored based on the classification results (Red: glass beads, blue: FCC particle). (a) an image captured in pure glass beads sample; (b) an



image captured in pure FCC particle sample; (c) an image captured in the mixture; (d) area equivalent circle distributions of glass beads and FCC before and after mixing.

The results of distinguishing the visually distinct glass beads and FCC particles are demonstrated in Figure 2-9. Owing to the distinctive visual features of the glass beads, the neural network was able to correctly predict the mask and its kind. However, the opaque appearance of the FCC particle had little surface texture, and the blurry objects looked similar to the glass beads, leading to the unexpected glass beads detection in the pure FCC sample (Figure 2-9.b). After mixing (Figure 2-9.c) the neural network had no trouble identifying the objects, confirmed by the highly matching size distributions of each type of particle before and after mixing (Figure 2-9.d). The mixture was prepared by transferring the glass beads sample into the crystallizer with FCC particles, which explained the minor difference in the glass beads size distribution only. The classification ability can be used to analyze the size and concentration of different crystal forms that present distinct visual features (Gao et al., 2018) or detect air bubbles and solid particles in a three-phase reactor.

## 2.5. Conclusions

In this study, we presented the neural network image analysis method that was able to classify the particles and perform high-accuracy object segmentation for the contacting or overlapping objects. The detection capabilities of unseen-scaled objects and classification in high solids concentration were investigated. A scale-invariant solid concentration measurement, pixel fill ratio (PFR), was proposed to quantify the image complexity for an image analysis model. The image analysis model successfully extracted the image information in the concentrated slurry with approximately three times higher  $PFR_T$  than the previous studies without compromising the accuracy. The glass beads and FCC particles were successfully differentiated based on their appearance, and the individual size distributions were accurately measured. Assisted by the progressive labeling strategy

that simplifies and speeds up the model construction stage, the deep learning-based image analysis algorithm can serve as an innovative process monitoring technology for the crystallization process.

## 2.6. References

- Ahmad, O. S., Debayle, J., Gherras, N., Presles, B., Févotte, G. & Pinoli, J.-C. (2012). Quantification of overlapping polygonal-shaped particles based on a new segmentation method of in situ images during crystallization. *Journal of Electronic Imaging*, 21(2), 021115. <https://doi.org/10.1117/1.JEI.21.2.021115>
- Borchert, C., Temmel, E., Eisenschmidt, H., Lorenz, H., Seidel-Morgenstern, A. & Sundmacher, K. (2014). Image-based in situ identification of face specific crystal growth rates from crystal populations. *Crystal Growth and Design*, 14(3), 952–971. <https://doi.org/10.1021/cg401098x>
- Cardona, J., Ferreira, C., McGinty, J., Hamilton, A., Agimelen, O. S., Cleary, A., ... Tachtatzis, C. (2018). Image analysis framework with focus evaluation for in situ characterisation of particle size and shape attributes. *Chemical Engineering Science*, 191, 208–231. <https://doi.org/10.1016/j.ces.2018.06.067>
- El Arnaout, T., Cullen, P. J. & Sullivan, C. (2016). A novel backlight fiber optical probe and image algorithms for real time size-shape analysis during crystallization. *Chemical Engineering Science*, 149, 42–50. <https://doi.org/10.1016/J.CES.2016.04.025>
- Ferreira, A., Faria, N., Rocha, F. & Teixeira, J. A. (2011). Using an Online Image Analysis Technique to Characterize Sucrose Crystal Morphology during a Crystallization Run. *Ind. Eng. Chem. Res.*, 50, 6990–7002. <https://doi.org/10.1021/ie2001499>
- Fisher, P., Aumann, C., Chia, K., O'Halloran, N. & Chandra, S. (2017). Adequacy of laser diffraction for soil particle size analysis. *PLoS ONE*, 12(5), 1–20. <https://doi.org/10.1371/journal.pone.0176510>
- Gao, Z., Wu, Y., Bao, Y., Gong, J., Wang, J. & Rohani, S. (2018). Image Analysis for In-line Measurement of Multidimensional Size, Shape, and Polymorphic Transformation of L-Glutamic Acid Using Deep Learning-Based Image Segmentation and Classification. *Crystal Growth and Design*, 18(8), 4275–4281. <https://doi.org/10.1021/acs.cgd.8b00883>
- He, K., Gkioxari, G., Dollár, P. & Girshick, R. (2017). Mask R-CNN. *Proceedings of the IEEE International Conference on Computer Vision, 2017-Octob*, 2980–2988. <https://doi.org/10.1109/ICCV.2017.322>

- Heinrich, J. & Ulrich, J. (2012). Application of Laser-Backscattering Instruments for In Situ Monitoring of Crystallization Processes - A Review. *Chemical Engineering and Technology*, 35(6), 967–979. <https://doi.org/10.1002/ceat.201100344>
- Javier Cardona, A., Carla Sofia, F., John, M., Andrew, H., Okpeafoh, A., Alison, C., ... Christos, T. (2018). Data for: "Image analysis framework with focus evaluation for in situ characterisation of particle size and shape attributes" (sample) — University of Strathclyde. <https://doi.org/10.15129/b38fa44b-8d12-46ff-ae59-d6b31e6602a0>
- Kanazawa, A., Sharma, A. & Jacobs, D. (2014). Locally Scale-Invariant Convolutional Neural Networks. Retrieved from <http://arxiv.org/abs/1412.5104>
- Kudo, K. (2019). genicam/harvesters: The latest stable beta release of the prototype. <https://doi.org/10.5281/ZENODO.3548111>
- Larsen, P. A., Rawlings, J. B. & Ferrier, N. J. (2007). Model-based object recognition to measure crystal size and shape distributions from in situ video images. *Chemical Engineering Science*, 62(5), 1430–1441. <https://doi.org/10.1016/j.ces.2006.11.018>
- Larsen, P. A. & Rawlings, J. B. (2009). Assessing the reliability of particle number density measurements obtained by image analysis. *Particle and Particle Systems Characterization*, 25(5–6), 420–433. <https://doi.org/10.1002/ppsc.200701130>
- Lin, T., Doll, P., Girshick, R., He, K., Hariharan, B., Belongie, S. & Ai, F. (2017). Feature Pyramid Networks for Object Detection. *ArXiv*.
- Lin, T. Y., Goyal, P., Girshick, R., He, K. & Dollar, P. (2017). Focal Loss for Dense Object Detection. *Proceedings of the IEEE International Conference on Computer Vision, 2017-October*, 2999–3007. <https://doi.org/10.1109/ICCV.2017.324>
- Lu, Z. M., Zhu, F. C., Gao, X. Y., Chen, B. C. & Gao, Z. G. (2018). In-situ particle segmentation approach based on average background modeling and graph-cut for the monitoring of L-glutamic acid crystallization. *Chemometrics and Intelligent Laboratory Systems*, 178(July 2017), 11–23. <https://doi.org/10.1016/j.chemolab.2018.04.009>
- Manee, V., Zhu, W. & Romagnoli, J. A. (2019). A Deep Learning Image-Based Sensor for Real-Time Crystal Size Distribution Characterization. *Industrial and Engineering Chemistry Research*, 58, 23175–23186. research-article. <https://doi.org/10.1021/acs.iecr.9b02450>
- Merkus, H. G. (2009). Particle Size, Size Distributions and Shape. *Particle Size Measurements*. [https://doi.org/10.1007/978-1-4020-9016-5\\_2](https://doi.org/10.1007/978-1-4020-9016-5_2)
- Micikevicius, P., Narang, S., Alben, J., Diamos, G., Elsen, E., Garcia, D., ... Wu, H. (2017). Mixed Precision Training. Retrieved from <http://arxiv.org/abs/1710.03740>
- Nagy, Z. K., Fevotte, G., Kramer, H. & Simon, L. L. (2013). Recent advances in the monitoring, modelling and control of crystallization systems. *Chemical Engineering Research and Design*. <https://doi.org/10.1016/j.cherd.2013.07.018>

- Rueden, C. T., Schindelin, J., Hiner, M. C., DeZonia, B. E., Walter, A. E., Arena, E. T. & Eliceiri, K. W. (2017). ImageJ2: ImageJ for the next generation of scientific image data. *BMC Bioinformatics*, 18(1), 529. <https://doi.org/10.1186/s12859-017-1934-z>
- Sarkar, D., Doan, X. T., Ying, Z. & Srinivasan, R. (2009). In situ particle size estimation for crystallization processes by multivariate image analysis. *Chemical Engineering Science*, 64(1), 9–19. <https://doi.org/10.1016/j.ces.2008.09.007>
- Schorsch, S., Ochsenein, D. R., Vetter, T., Morari, M. & Mazzotti, M. (2014). High accuracy online measurement of multidimensional particle size distributions during crystallization. *Chemical Engineering Science*, 105, 155–168. <https://doi.org/10.1016/J.CES.2013.11.003>
- Sekachev, B., Manovich, N. & Zhavoronkov, A. (2019). Computer Vision Annotation Tool. <https://doi.org/10.5281/ZENODO.3497106>
- Simon, L. L., Merz, T., Dubuis, S., Lieb, A. & Hungerbuhler, K. (2012). In-situ monitoring of pharmaceutical and specialty chemicals crystallization processes using endoscopy-stroboscopy and multivariate image analysis. *Chemical Engineering Research and Design*, 90(11), 1847–1855. <https://doi.org/10.1016/j.cherd.2012.03.023>
- Wu, Y., Kirillov, A., Massa, F., Lo, W.-Y. & Girshick, R. (2019). Detectron2.

## Chapter 3

# **Deep Learning-Based Oriented Object Detection for In-Situ Image Monitoring and Analysis: A Process Analytical Technology (PAT) Application for Taurine Crystallization**

A version of this chapter has been submitted to *Chemical Engineering Research and Design*: Wu, Y., Gao, Z. & Rohani, S. (2021). Deep Learning-Based Oriented Object Detection for In-Situ Image Monitoring and Analysis: A Process Analytical Technology (PAT) Application for Taurine Crystallization

## Chapter 3 Deep Learning-Based Oriented Object Detection for In-Situ Image Monitoring and Analysis: A Process Analytical Technology (PAT) Application for Taurine Crystallization

### Abstract

Image analysis enables the estimation of critical process properties such as crystal size, morphology, and crystallization kinetics. Despite the rich image information, the lack of a robust image analysis technique has been an obstacle to promote its applications. In this work, an automated image analysis technique that combines the state-of-the-art oriented object detection model,  $S^2A-Net$ , was developed for in-situ estimation of the two-dimensional crystal size distribution (CSD) and the crystal counts. The model was trained to detect and classify both crystals and clusters to enable quantification of the extent of agglomeration and exclude unreliable detections. The effectiveness and robustness of extracting size and aspect ratio at various image complexities were verified by comparing with the focused beam reflective measurement (FBRM) and manually analyzed images in the experimental studies for taurine batch cooling crystallization with different seed loadings. An online calibration strategy for solute concentration measurement with Raman spectroscopy was introduced to eliminate the dedicated calibration experiments. The secondary nucleation and growth rate kinetics were evaluated from the online measurements and validated by Monte Carlo simulation. The proposed method provides a novel PAT strategy that enables accurate two-dimensional size measurement and shape characterization for online monitoring and control of a solution crystallization process.

**Keywords:** Deep learning-based image analysis; Oriented object detection; Crystal size and shape measurement; Cluster detection; Crystallization kinetics estimation; Raman spectroscopy

### 3.1. Introduction

Crystallization operation is the essential step to recover and purify the solids product from the upstream processes such as chemical synthesis and fermentation. The product crystal size and shape distribution will affect the powder properties (e.g., density and flowability) and the downstream processability. For example, the fine and high-aspect-ratio particles result in high resistance and low efficiency in the filtration step, which leads to difficulties and increasing costs in separation and drying (Bahar Basim & Khalili, 2015; Bourcier et al., 2016). Therefore, growing interests and efforts have been devoted to the development of the process analysis technology (PAT) that monitors and optimizes the sizes and shapes of particles.

Despite the complex nature of crystal morphologies, the majority of particle sizing PAT initiatives use a simplified particle size descriptor of the characteristic or equivalent length, resulting in one-dimensional crystal size distribution (CSD). However, the shape and orientation of high-aspect-ratio particles are known to affect optical and acoustic scattering, rendering the unreliable size estimations from ultrasonic attenuation spectroscopy (UAS) and laser diffraction (LD) techniques in these scenarios (Merkus, 2009). The chord length distribution (CLD) of FBRM is a function of crystal shape (Leyssens, Baudry & Hernandez, 2011). The confounding one-dimensional sizes not only cause inconsistency in CSD measurements but also leads to loss of critical shape information. Extracting multi-dimensional or shape distribution from the conventional PAT initiatives has been studied for FBRM (Irizarry et al., 2017; Leyssens, Baudry & Hernandez, 2011) and laser diffraction (Ma et al., 2000).

However, the recent development of online and offline image analysis techniques has shown superb advantages in precise multi-dimensional size and shape measurement. Ma et al. (2012) used both intrusive online imaging systems and off-line microscopy to measure and optimize the aspect ratio (AR) of the needle-like  $\beta$ -form L-glutamic acid. This work showed that the cooling profile could affect the crystal aspect ratio. By

controlling the supersaturation, the product shape can be fine-tuned. Three-dimensional reconstruction from double-view or orthogonal-view imaging systems were studied in (Huo et al., 2017; Ochsenein et al., 2014). The pictures taken by paired cameras from different angles were first aligned and the feature points were used to obtain the 3D geometry of the crystal, which can be used for shape/size measurement and growth kinetic estimation. Gao et al. (2018) reported a low-cost insertable probe imaging that tracked the polymorphic transformation of L-glutamic acid based on the differences in crystal habits. The consistency to the polymorphic transformation data from Raman spectroscopy prompted the good sensitivity and accuracy of crystal form classification from the image. In our previous work, we implemented a home-made flow-through cell imaging system and studied the accuracy of size measurement and particle classification at high slurry density (Wu, Lin & Rohani, 2020).

Extracting the geometrical and spatial information of the particles from the images is a challenging task especially at high solids concentration where the objects are occluded. The requirement of low solids concentration and sample dilution have limited the application of quantitative image analysis in crystallization systems (Nagy et al., 2013). The major drawback of the conventional image segmentation techniques lies in differentiating the contacting or overlapping particles. The recent research works in crystallization imaging analysis have extensively adopted the deep-learning-based image analysis methods to improve the image segmentation performance (Chen et al., 2019; Manee, Zhu & Romagnoli, 2019; Unnikrishnan et al., 2020). Our previous work presented that the application of the recent deep learning-based techniques could address the issues, enabling the analysis in a considerably wider range of solids concentration without sacrificing the accuracy (Gao et al., 2018; Wu, Lin & Rohani, 2020). In the present work, in addition to upgrading the camera and optics of the imaging system to acquire images with higher resolution and larger field of views, we have improved the image analysis algorithm. We have adopted the state-of-the-art oriented object detection technique, namely *S<sup>2</sup>A-Net* (Han et al., 2020), to further investigate the feasibility of characterizing the crystals as rotated rectangle boxes instead of the pixel-wise masks as in



the image segmentation methods. This can significantly decrease the computational load in model inference and post-processing. The two-dimensional size descriptor can be extracted from the width and height of the rotated boxes, resulting in two-dimensional CSDs (2D-CSDs). The detections were classified as single crystals and clusters, enabling the quantitative analysis of crystal agglomeration and more accurate size estimations by removing the detected crystal intersecting with the clusters. Combining with Raman spectroscopy and FBRM, the 2D-CSDs were used to estimate nucleation and two-dimensional growth kinetics, which have been proven challenging due to the lack of reliable measurement technology (Ochsenbein et al., 2014).

## 3.2. Methodologies

### 3.2.1. Oriented Object Detection Model

Most of the recent crystallization image analysis studies employed image segmentation algorithms, which predict the pixel-wise object masks. Due to the difficulty to measure the irregular-shaped mask, it is common practice to approximate the masks with some simple geometries. For example, the smallest rotated rectangle (minimum area) that surrounds the mask can be used to measure the two-dimensional sizes. The oriented object detection (OOD) task implements the shortcut to achieve this objective: it directly predicts each object with a rotated box (five parameters:  $x$ ,  $y$ , width, height, rotation) without the intermediate mask prediction (hundreds to thousands of parameters depending on the size). Given the similar accuracy, the OOD models are much faster because of the lack of mask prediction branches and less complex postprocessing thanks to the smaller number of parameters to process.

The *S<sup>2</sup>A-Net* (Single-Shot Alignment Network) is a state-of-the-art OOD algorithm (Han et al., 2020). In a regional convolutional neural network (RCNN), the feature extraction filters are rotation-variant, meaning that the different rotations of the same object are not equivalent. In the OOD task, learning all redundant rotations needs a large number of

model parameters, leading to a significant increase in the training time and risk of model overfitting (Zhou et al., 2017). In *S<sup>2</sup>A-Net*, this problem is addressed by predicting the local rotations to align the filters in the convolutional network to the objects with different orientations. Then, the active rotating filters (ARFs) are used to obtain the rotation-invariant feature maps by pooling the most significant responses from multiple rotations (Zhou et al., 2017). Finally, the oriented bounding boxes, scores, and classification are computed from the feature maps. The *S<sup>2</sup>A-Net* outperformed many latest OOD models in both speed and accuracy (Han et al., 2020). It is worth noting that is possible to include the ARF in an image segmentation model to benefit from the rotation-invariant feature and achieve better irregular-shaped particle (e.g., clusters) analysis.

### 3.2.2. Materials and Experimental Setup

Taurine (2-Aminoethane sulfonic acid) is an important nutrient in the development of the muscle and nerve system. It is widely used as an ingredient in pet food, energy drink, and pharmaceutical products. The aqueous taurine solution was selected as the model crystallization system because of 1) moderate crystal growth rate that keeps the experimental time manageable 2) the rod-like crystal morphology that is suitable to be approximated by the oriented bounding boxes for two-dimensional size estimation; 3) compared to the needle-like crystals (e.g.,  $\beta$ -form L-glutamic acid), the shorter edges of taurine crystals are substantial and measurable, making the two-dimensional CSD and growth kinetics analysis more practical (Ochsenbein et al., 2014).

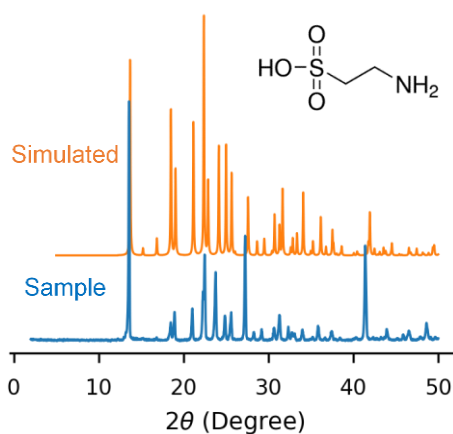


**Figure 3-1** PXRD pattern of taurine crystal. The sample and simulated curves were obtained from the ground sample from BioShop Inc. and the Mercury simulation, respectively.

The crystalline taurine (99% purity) was purchased from Bioshop Inc (Canada). The molecular structure and PXRD patterns are shown in Figure 3-1. The aqueous solution was prepared with the raw material and de-ionized water based on the solubility from the literature (Wu et al., 2017). The seeds were prepared by grinding the raw taurine crystals in a mortar pestle for 10 minutes and then sieving 35 to 53 microns crystals with GilSonic AutoSiever (Gilson Inc., USA). The mean size and the mean aspect ratio (longer axis / shorter axis) of the seeds were  $46.1 \mu\text{m}$  and 1.79, respectively. The two-dimensional CSD of the seeds is shown in Figure 3-2.

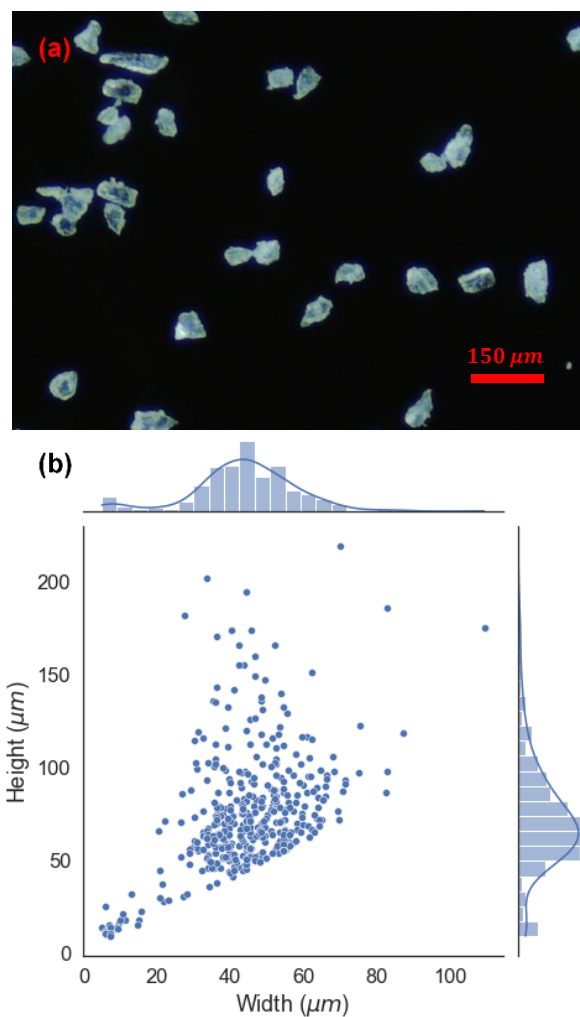


**Figure 3-2** (a) Dark field microscopy of the prepared seeds. (b) 2D size distribution of the seeds

The experimental setup is shown in Figure 3-3. A 120 mL double-jacket crystallizer was used with a customized mechanical stirrer integrated on the plug, which addressed the issue of shaft wobbling and PTFE debris from the stirrer due to the shaft misalignment when using an overhead agitation motor. The peristaltic pump circulated the slurry

through the flow cell (Rectangular quartz tube,  $2 \times 4 \text{ mm}$ , F&D Glass, USA). The residence time of the external circulation was 1.5 seconds that minimize the sample classification and clogging. A high-power LED light (XHP70.2, CREE Inc., USA) was used as the strobing light source. An industrial camera (MV-CA016-10UM, Hikvision Digital Technology, China) was installed on a re-purposed PCB microscopic lens for imaging. The resolution was 1440-by-1080 pixels and the calibration ratio was  $1.67 \mu\text{m}/\text{px}$ , which resulted in the field of view (FOV) of 2.4-by-1.8 mm. The exposure signal triggered the LED strobing for around 8 microseconds to prevent motion blur. The internal temperature was measured by a DS18B20 digital thermometer (Maxim Integrated, USA) and controlled by a thermostat (JULABO FP50, USA). A Raman spectroscopy (RXN1-785nm, Kaiser Optical System, USA) was employed to track the solute concentration. FBRM S400 (Mettler Toledo, USA) was used to detect fine particles and compare the performance of measuring the CSD and crystal counts. The control signals and the measurements in the set-up were centralized with the wireless microcontroller, ESP8266 (Espressif, China), and MQTT technology, which enabled automated experiment execution.

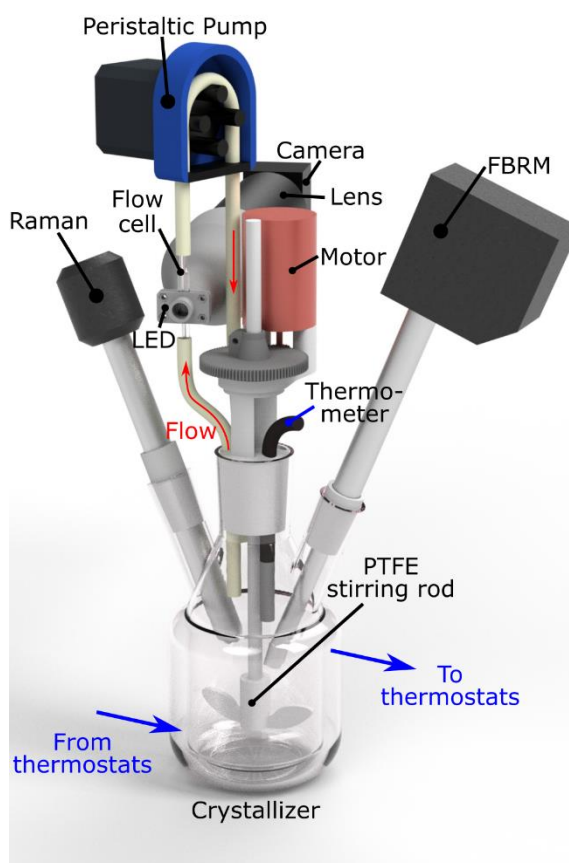


**Figure 3-3** Schematic diagram of the experimental setup

### 3.2.3. Imaging Dataset Preparation and $S^2A$ -Net Model training

The training dataset contained 29 images collected from various conditions (Table 3-1). The solution saturated at 30°C was prepared by adding 19.30 g taurine to 160 g deionized water. The images were selected from the process of linear cooling (0.2°C/min) from 30°C to 20°C. The clear solution dissolved at 40°C for 15 minutes. The low-, medium-, and high solids concentration frames were selected from the nucleation onset, when the temperature was around 25°C, and when the cooling profile was finished, respectively. The seeded images were taken in the linear cooling experiments with the seeds added at

the beginning of each experiment. The dissolution images were collected from linearly re-heating the slurry at a rate of 0.2°C/min from 20°C to 30°C.

**Table 3-1** Training data statistics

<b>Condition</b>	<b># Images</b>	<b># Crystals</b>	<b># Clusters</b>	<b>Median crystal size [<math>\mu\text{m}</math>]</b>	<b>Median cluster size [<math>\mu\text{m}</math>]</b>	<b>Median crystal AR</b>	<b>Median cluster AR</b>
<i>Low density (no seed)</i>	6	1482	144	22.9	107.1	2.02	1.71
<i>Medium density (no seed)</i>	5	993	204	78.3	159.5	2.83	1.71
<i>High density (no seed)</i>	6	1641	244	82.5	187.8	3.11	1.70
<i>Seeding</i>	7	858	7	30.8	111.2	1.78	1.67
<i>Dissolution</i>	5	1399	92	78.9	138.6	2.86	1.77
<i>Total</i>	29	6373	691	-	-	-	-

The open-source software, *labelimg2*, was used to label the oriented bounding boxes. The progressive labeling technique (Wu, Lin & Rohani, 2020) was employed to reduce the workload required to create a large number of labels. There are four equivalent representations depending on the angle and the relative length of the height and width (Figure 3-4.a). The duplication may cause confusion and inconsistency during training. Therefore, all labels were converted into the format of Figure 3-4.a before training. The labels were categorized into crystals and clusters (Figure 3-4.b). The crystals within the cluster boxes were labeled if their boundaries were identifiable. Due to the irregular shape of the clusters, they may be split into multiple labels that minimize the inclusion of background.

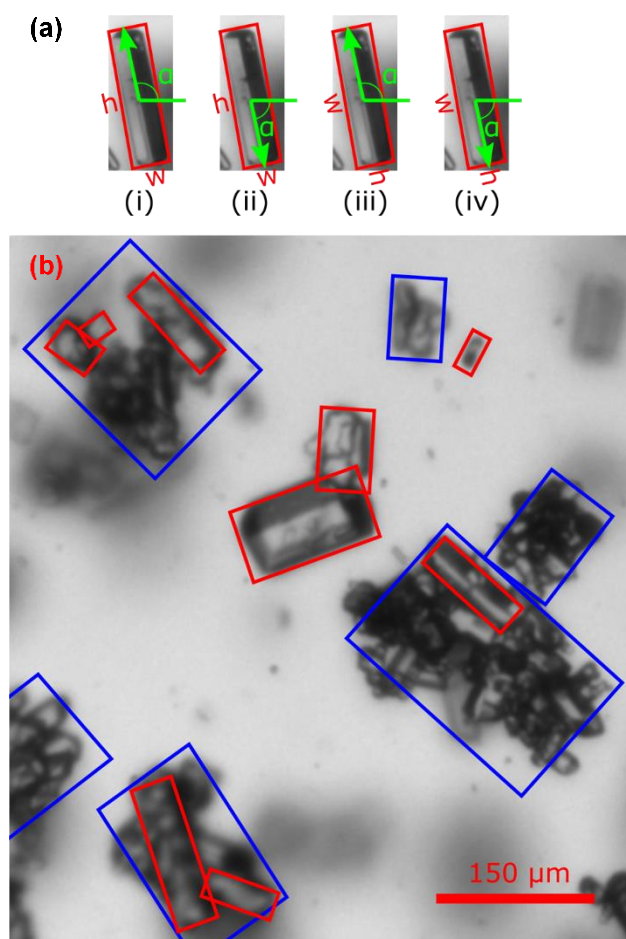


**Figure 3-4** (a) The equivalent label formats. i, ii: the longer edge as height ( $h$ ); iii, iv: the shorter edge as height. i, iii: angle  $\alpha$  between  $[0, \pi)$ ; ii, iv: angle  $\alpha$  between  $(-\pi, 0]$ . (b) Example of a labelled training image. The red and blue bounding boxes are labels of crystals and clusters, respectively.

ResNet-101 was used as the backbone of the  $S^2A$ -Net model. The model was trained for 20000 epochs with a learning rate of 0.01 for the first 15000 epochs and 0.001 for the rest. Data augmentation techniques were used to expand the training dataset. The training dataset was augmented by rotating the images every 5 degrees and adjusting the



brightness. With the full-sized input image (1440-by-1080 pixels), the model can process up to 4.5 frames per second (FPS) on an NVIDIA GTX 1070 GPU.

#### 3.2.4. Cooling Crystallization Experiments and Image Analysis Process

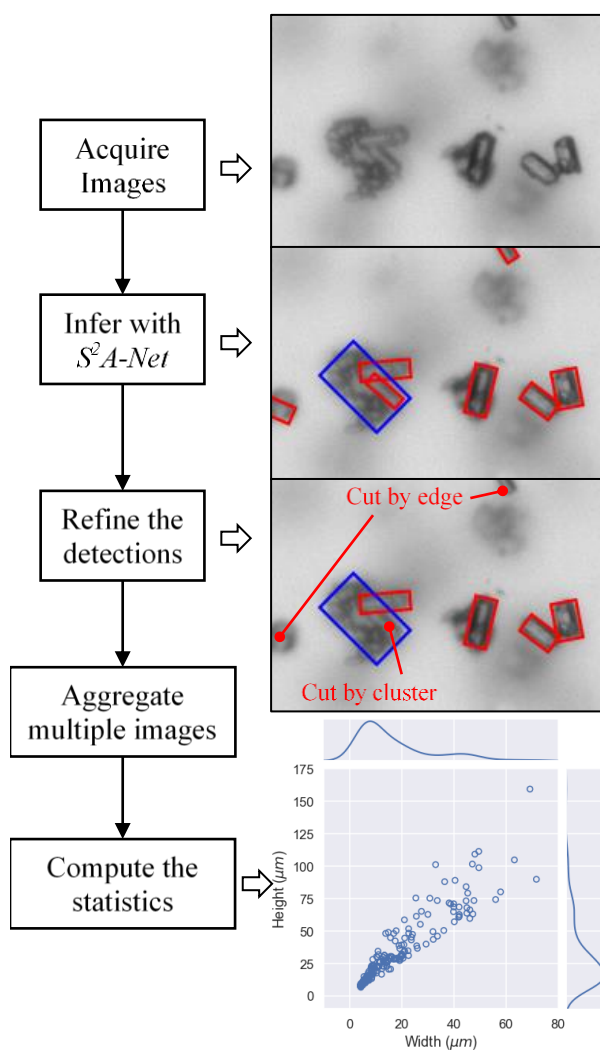
The trained model was used to extract the crystal sizes and counts in a set of cooling crystallization experiments with different cooling rates. The solution saturated at 30°C was prepared as described in the training data preparation section. The solution was first dissolved to clear at 40°C. It was cooled to the saturated temperature (30°C) and held for 10 minutes to reach equilibrium. In unseeded experiments, the solution was cooled to 20°C linearly at 0.5 °C/min then heated back to 40°C at 0.2 °C/min for next cycle. In seeded experiments, 0.1g or 0.3g seeds (1% or 3% solids of the final product) were added during the hold period at saturated temperature, then cooled to 20°C at 0.5 °C/min. The Raman spectra, temperature, FBRM data, and images were acquired during the entire duration of the experiments.

Figure 3-5 depicts the pipeline of the image analysis process and the sample images. The images were acquired at 0.5 FPS during heating dissolving and 1.0 FPS during cooling crystallization. The acquired images were fed to the  $S^2A-Net$  model to predict the oriented bounding boxes along with their scores and classifications. The labels were refined as follows. First, the low-confidence detections (score < 0.5) were removed. Next, the crystals cut by the frame edges were also removed since their sizes might be underestimated. Then, the intersection ratios of the remaining crystals were calculated with Eq. 3-1, where  $i$  and  $j$  represent the index of crystals and clusters, respectively; and  $B$  stands for the oriented bounding boxes. In the cluster-cut removal mode, the crystals with an intersection ratio greater than 0.4 were removed as the obstruction may lead to unreliable results. In the normal mode, this step was skipped. The detections were aggregated every 10 seconds to compute the counts and 2D CSDs of the crystals and clusters individually. Because of the hydrodynamic pattern inside the flow cell, it is assumed that the rod-like taurine crystals are aligned with the flow direction, so that the images of the crystals are the orthogonal projections of the height and width. By

approximating the size of the invisible axis (normal to the image plane) to the width of the crystal, the approximate volumes of individual crystals are estimated with Eq. 3-2, where  $W$  and  $H$  are width and height of a crystal, respectively.

$$R_i = \max_i \left\{ \frac{\text{area}(B_i \cap B_j)}{\min[\text{area}(B_i), \text{area}(B_j)]} \right\}, \quad j \in B_{clusters} \quad (3-1)$$

$$V = W^2 H \quad (3-2)$$



**Figure 3-5** Image analysis flow diagram. The red and blue labels are crystal and cluster, respectively.

### 3.2.5. Concentration Calibration and Measurement with Raman Spectroscopy

Raman spectroscopy was used as the solute concentration measurement instrument. Compared to the other online concentration monitoring PATs (e.g., FTIR, UV-Vis), the Raman spectroscopy has the potential to achieve simultaneous measurement of the solute

concentration and crystal polymorphic information (Lin, Wu & Rohani, 2020). Mapping Raman spectra to solute concentration requires a large number of calibration experiments since Raman spectroscopy depends on temperature, solute concentration, slurry density, crystal polymorph (taurine does not exhibit polymorphism in the scope of this study), and the CSD (Kristova, Hopkinson & Rutt, 2015). The number of factors makes the experimental calibration quite cumbersome. The previous studies demonstrated the calibration strategies with the Raman spectra and temperatures collected under numerous known solute and solids concentrations (Acevedo et al., 2018; Hu et al., 2005; Lin, Wu & Rohani, 2020b). In this study, we observed the slight differences in the Raman intensities when the operating conditions change (e.g., different seed loading). Therefore, a calibration methodology that could compensate for this mismatch was required. Based on the assumption that the system states were similar between the cooling and heating stages and the most states were near the solubility curve, we proposed a Raman spectroscopy calibration strategy that uses the data collected during the slow (0.2 °C/min) heating and dissolving process for solute concentration calibration. The exposure time was set to 3 seconds that achieved less than 5% relative error. During the heating process, the spectra and the temperature were concatenated as the input matrix ( $\mathbf{X}$ ) and the solubilities at the according temperature were used as target vector ( $\mathbf{Y}$ ). The target value was capped to saturated concentration when the temperature was above the saturation temperature. First, the input matrix  $\mathbf{X}$  was transformed with the orthogonal signal correction (OSC), which suppresses the non-relevant spectra components (e.g., ambient lighting) (Trygg & Wold, 2002). Then, the partial least square (PLS) regression was used to fit the transformed  $\mathbf{X}$  to the target  $\mathbf{Y}$  (Lin, Wu & Rohani, 2020). The number of components of the PLS model was set to 4 that achieved 99% explained variation. The model could be used to compute the solute concentration for the previous cooling stage. The accuracy of the concentration measurement was validated with an unseeded cooling experiment. Syringe filters were used to sample approximately 1.5 mL solid-free solution from the crystallizer. Two samples during the linear cooling and two samples during the slow heating were collected in the validation experiment. The samples were transferred to glass vials and weighted.

After vacuum drying at 60°C for 4 hours with lids open, the dried samples were weighted and the actual concentrations at the sample times could be calculated.

### 3.2.6. Secondary Nucleation and Growth Rate Estimation

The kinetic parameters of the secondary nucleation and growth rate could be estimated from the data extracted by image analysis. To obtain the nucleation parameters, the calibration that maps the crystal counts per frame to the volumetric density is required. This step was performed by first adding a known mass of seeds. Immediately, the 2D CSD of the seeds was measured by the image analysis model to compute the average volume of the seeds. Then, the number of seeds could be estimated, and the bulk volumetric seeds density can be computed. By dividing the observed crystal counts by the calculated seeds density, the volume observed by the camera could be computed, which was further converted to the penetration depth or the depth of field (DOF) with the known field of view of the frame (Wu, Lin & Rohani, 2020). The DOF of this imaging system was found to be 0.6 mm and it was assumed to be constant due to the relatively low solids concentration and agglomeration during the early nucleation stage.

The secondary nucleation model is shown in Eq. 3-3, where  $B_s$  is the nucleation rate [ $\# \cdot m^{-3} \cdot s^{-1}$ ];  $c$  is the concentration [ $g/g$ ];  $c^*$  is the solubility [ $g/g$ ];  $v_f$  is the solids volume fraction;  $b_0$ ,  $m$ , and  $j$  are model parameters. The concentration and the solubility were computed with the Raman spectroscopy and temperature measurements. The volume fraction was obtained from the image analysis CSD transformed by Eq. 3-3 and normalized with the crystal count calibration. The experimental nucleation rates were calculated with the filtered derivative of the crystal counts. Finally, the nucleation parameters were computed by fitting the model with the experimental data using a nonlinear optimizer (Virtanen et al., 2020).

$$B_s = b_0 \cdot \left( \frac{c - c^*}{c^*} \right)^m \cdot v_f^j \quad (3-3)$$

The two-dimensional growth rate model is shown in Eq. 3-4, where  $G$  is the growth rate [ $m/s$ ];  $i \in \{h, w\}$  is the dimension of the growth direction; the  $g$  and  $n$  are model parameters. The common practice to estimate the growth kinetics is to numerically solve the coupled mass balance and population balance model (PBM) and optimize the model parameters so that the error between the model prediction and experimental observation is minimized (Ochsenbein et al., 2014). With the rich information extracted from the image analysis, a direct growth kinetics estimation strategy was proposed to find the parameters without the need for solving the PBM. Conventionally, the experimental growth rate required for fitting the model was approximated with the time-derivative of the size statistics (e.g., mean, median, or quantiles). However, these values are prone to bias due to the non-growth mechanisms that cause CSD change such as nucleation and agglomeration. The data between seeds addition and onset of the agglomeration could be used to fit the model where the growth is the dominant mechanism. The CSD containing clusters can be avoided with the capability of cluster detection of the image analysis model. In the seeded experiment, the new-born nuclei are smaller than the seeds. After seeds addition, the seeds count in each frame was recorded as  $N_{seed}$ . In the following frames, only the  $N_{seed}$  largest crystals were used for computing the size statistics of height and width individually. The growth parameters could be estimated by fitting the model with the size statistics of each dimension.

$$G_i = g_i \cdot \left( \frac{c - c^*}{c^*} \right)^{n_i} \quad (3-4)$$

### 3.3. Results and Discussion

#### 3.3.1. Evaluation of Concentration Measurement Performance

Figure 3-6.a demonstrates a cooling-heating cycle of the unseeded validation experiment. The Raman spectra and temperatures collected in the heating segment were used as the training input ( $\mathbf{X}$ ). The solubility model reported in (Wu et al., 2017) was used to compute the solubility curve, which served as the training target ( $\mathbf{Y}$ ). The solubility was

capped to the concentration of the clear solution when the temperature was above 30°C. After training the OSC and PLS model with the data, the predicted concentration and the solubility target were in good agreement, with a relative error of less than  $\pm 0.4\%$  (Figure 3-6.b). The samples taken for confirming the solute concentration were marked in Figure 3-6.a. The differences between the predicted and actual concentration were shown in Figure 3-6.c. The maximum relative error in the validation data was  $\pm 3\%$ , which confirmed the accuracy and reliability of the proposed concentration measurement strategy with Raman spectroscopy.

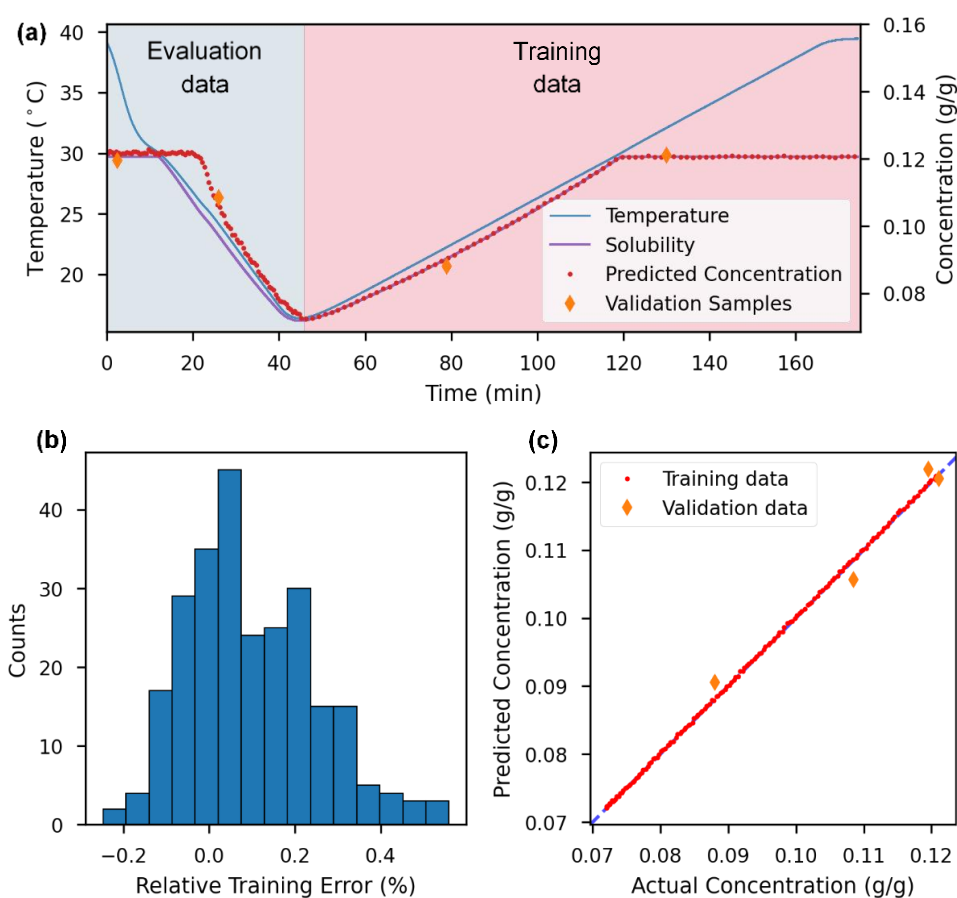


**Figure 3-6** The performance summary of the concentration measurement with Raman spectroscopy. (a) the visualization of a cycle of unseeded crystallization. (b) the distribution of relative training errors (c) The graph of actual concentration versus the concentration predicted by the Raman spectroscopy.

### 3.3.2. Evaluation of Image Analysis Performance

The performance of the image analysis was evaluated by comparing the model predictions and the manual-labeled ground truths (GTs). The match between the predictions and GTs is measured by intersection-over-union (IoU) that is the area of intersection between two rectangles being divided by the area of the union of the two rectangles. When the IoU is greater than 0.5, the prediction is considered as true positive (TP). A false positive (FP) is counted when a prediction failed to match a GT while a false negative (FN) is when a GT does not have any matching prediction. The performance metrics, average precision (AP), and average recall (AR) metrics are defined in Eqs. 3-5 and 3-6. The AP and AR are the trade-offs between finding less but more confident crystals and finding as many objects as possible regardless of the risks of the wrong prediction.

$$AP = \frac{TP}{TP + FP} \quad (3-5)$$

$$AR = \frac{TP}{TP + FN} \quad (3-6)$$

The AP and AR in four different conditions as described in the training data preparation section are summarized in Figure 3-7. The AR and AP were high in all conditions, with a slight dropping when the solids concentration increased. The cluster-cut removal mode removes the cluster contacting crystals, which sacrifice the AR to achieve a higher precision. The precision gain increases with increasing solids concentration and image complexity. In the application of CSD measurement, the cluster-cut removal helps to ensure the accuracy in size evaluation, while the normal mode is more beneficial for the measurements of crystal counts and total volume.



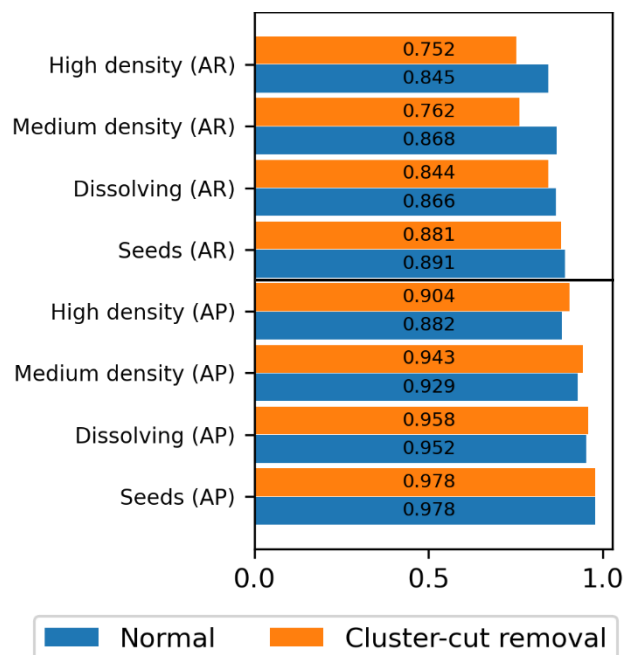


**Figure 3-7** The performance summary of the image analysis. AP and AR stand for accuracy and recall metrics, respectively.

### 3.3.3. Particle Counts Analysis

The particle counts and solute concentration tracking during the linear cooling experiments ( $0.5^{\circ}\text{C}/\text{min}$ ) at different seed loading are shown in Figure 3-8. In the unseeded experiment (Figure 3-8.a), the nucleation onsets reported by the image analysis and the FBRM were 7.8 minutes ( $26.9^{\circ}\text{C}$ ) and 8.8 minutes ( $26.4^{\circ}\text{C}$ ), respectively. Visual examination of the images confirmed the nucleation onset and the better sensitivity of the image analysis method. FBRM has strength in detecting fine particles (less than  $10\ \mu\text{m}$ ), but this range is often noisy due to the probe contamination and air bubbles from agitation, leading to an offset baseline and delayed nucleation detection. The classification capability of the image analysis and manual examination ensure immediate nucleation detection without undesired disturbances. Also, the FBRM counts can be biased due to the geometry, arrangement, and surface properties of the particles (Irizarry

et al., 2017), using the image analysis counts allows setting up a consistent nucleation threshold for different conditions.

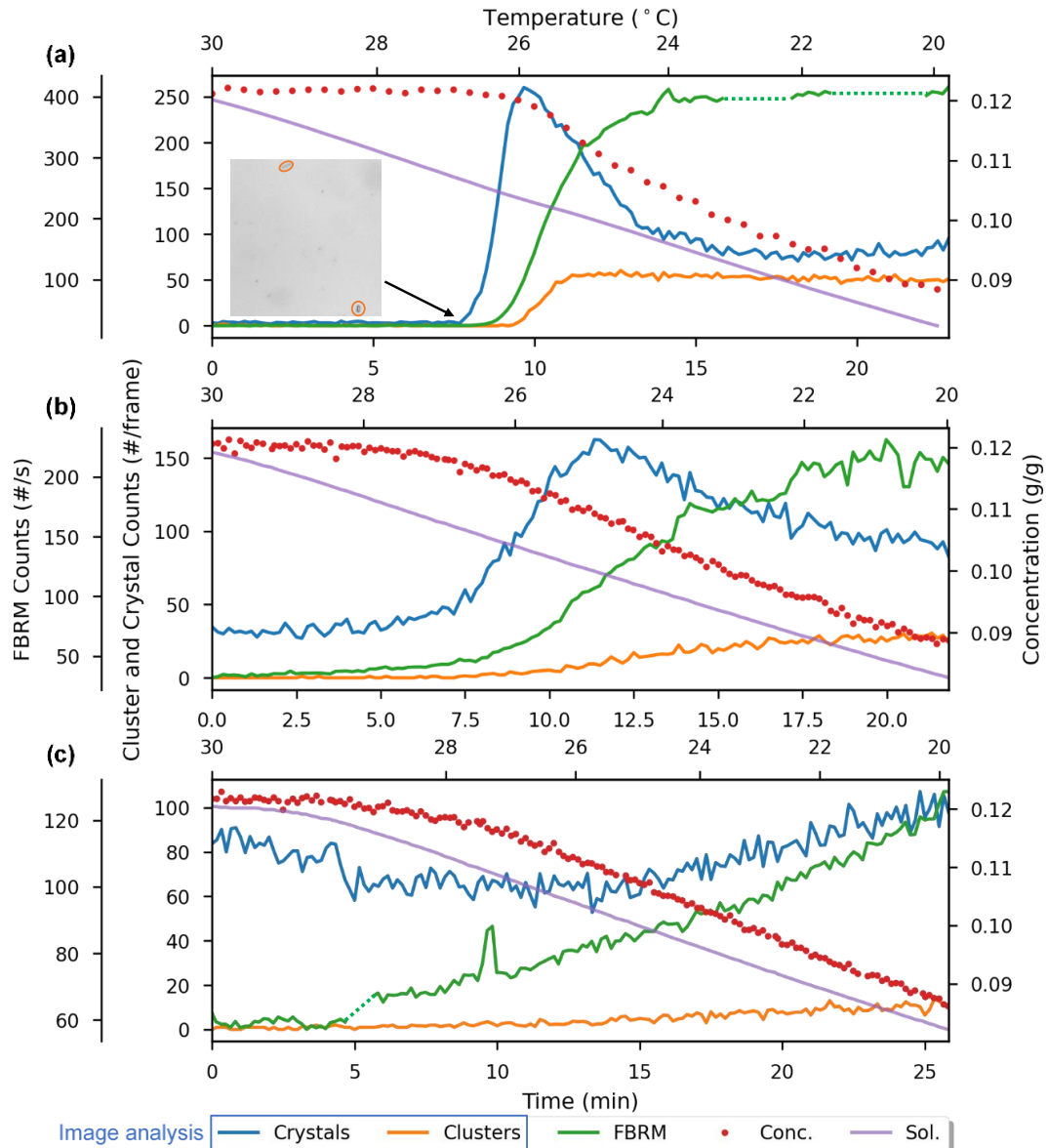


**Figure 3-8** The particle and cluster counts and the solute concentration (Conc.) during the linear cooling experiments (0.5 °C/min) of (a) unseeded, (b) 1% seed loading, and (c) 3% seed loading. The solubility (Sol.) was computed with the model (Wu et al., 2017). The dashed lines of FBRM counts were the missing data due to probe contamination. The breakout frame in (a) showed the detected crystals at the onset of nucleation.

The increasing seed loadings suppressed the nucleation, leading to the smoother increment of the FBRM counts. The image analysis counts not only matched the FBRM count trend but also revealed a peak of the counts that became less prominent with the increasing seed loading. In the unseeded and 1% seed loading runs, the cluster counts started to increase when the crystal counts reached the maximum, which suggested that the peak may be attributed to the agglomeration of the nucleated fine crystals. Figure 3-9 shows the visualization of the images and the detected objects that supported the different agglomeration levels. In the unseeded run, the number of fine crystals increased rapidly within the first minute after the nucleation onset. The image analysis successfully captured the process of crystal agglomeration that explained the drop in crystal counts. In the final state, the images were filled with clustered crystals, while only a few small crystals were detected, which suggested low nucleation and breakage level in the final state. In the 1% seed loading run, the nucleation was not fully suppressed due to the insufficient amount of seeds surface area. Despite the relatively fewer clusters compared to the unseeded ones, the coexistence of the crystals grown from seeds and nucleated crystals resulted in the undesired bimodal size distribution of the products (Kubota et al., 2001). The nucleation in the 3% seed loading experiment was weak as the number of crystals remained steady throughout the process, suggesting that the most supersaturation was consumed in crystal growth. The concentration measured by the Raman spectroscopy showed a smaller gap between the solubility and concentration curves with the increasing amount of seeds. The peak relative supersaturation for the unseeded, 1% seeded, and 3% seeded runs were 0.16, 0.11, and 0.07, respectively. The supersaturations remained within the reported metastable zone width (MSZW) of homogeneous primary nucleation (Wu et al., 2020). The secondary nucleation MSZW is in the range from 1.06 to 1.11, which is an important reference in the optimal supersaturation control (SSC) strategy (Ferreira et al., 2011; Ulrich & Strege, 2002).

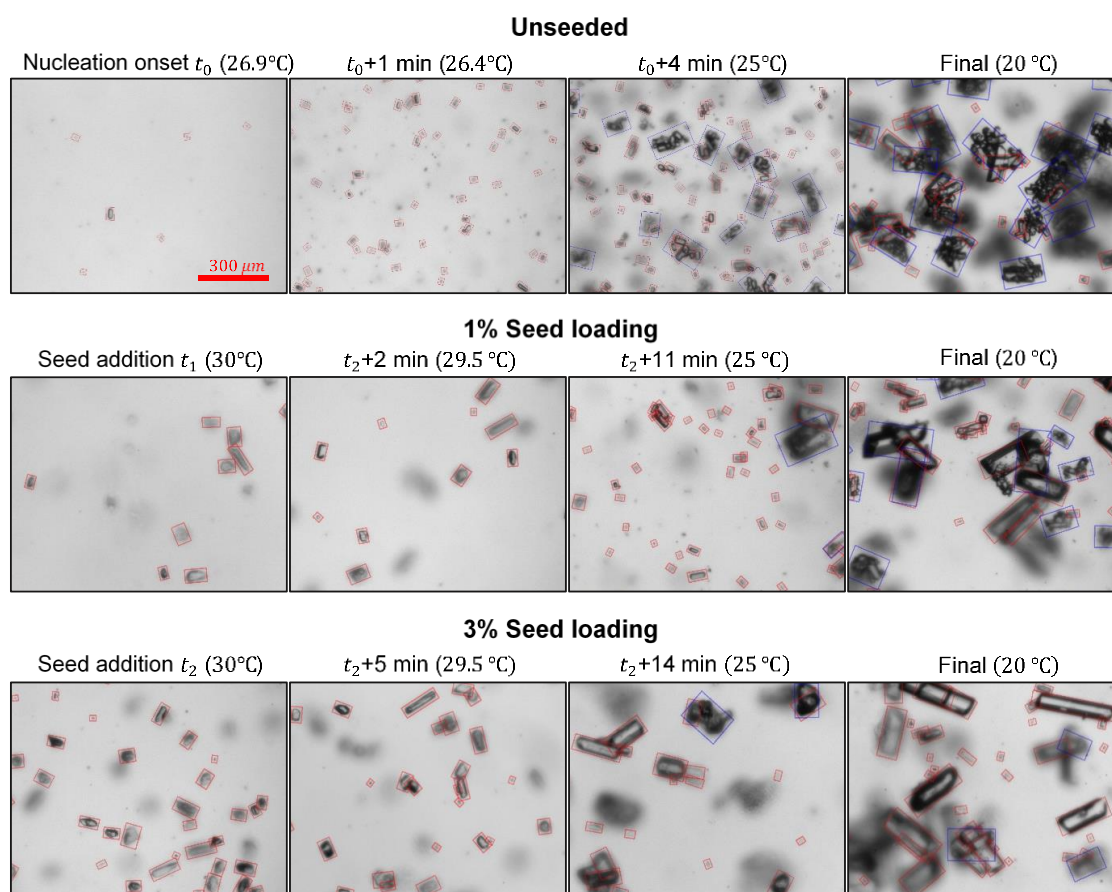


**Figure 3-9** Visualization of the online images and the analysis result of the unseeded and seeded experiments at 1) nucleation onset or seed addition, 2) after the temperature dropped by **0.5°C**, 3) when the temperature reached **25°C**, and 4) final state. The bounding boxes were padded and enlarged by 5 pixels (**8 μm**) in each direction for better viewing. Each frame was cropped to one-quarter of its original size. The red and blue labels stand for crystals and clusters, respectively.

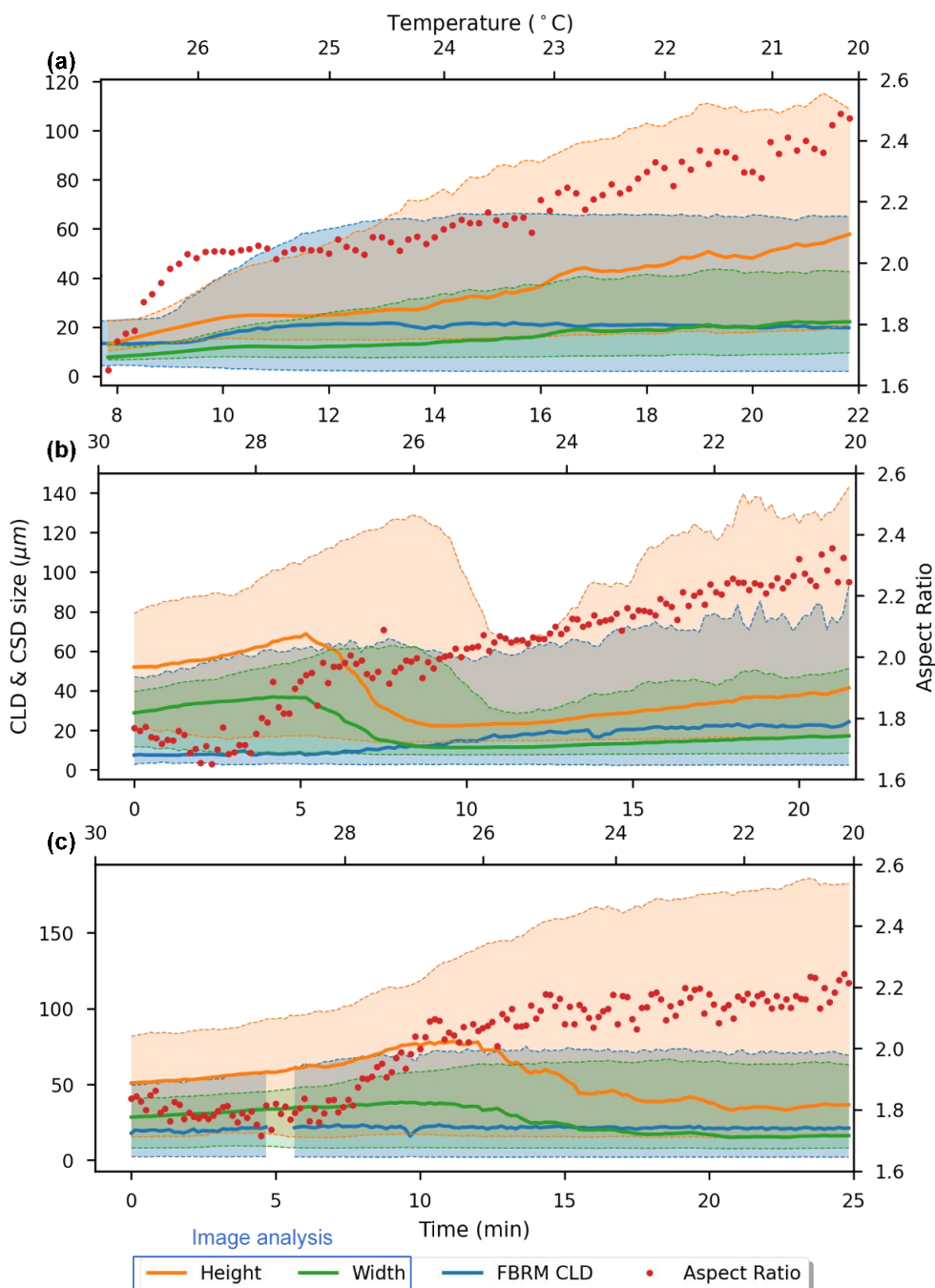
### 3.3.4. Particle Size and Shape Analysis

Figure 3-10 shows the time series of the size and shape statistics during the experiments. In the unseeded experiment, the crystal growth was captured by the image analysis. The

90<sup>th</sup>-quantile ( $D_{90}$ ) of the height (the longer edge) increased while the gap between the  $D_{10}$  and  $D_{90}$  of the heights enlarged due to strong nucleation. In the 1% seed loading run, a significant drop in the sizes was detected by the image analysis, which matched the nucleation time at 6 minutes in Figure 3-8. The decrease of  $D_{10}$ ,  $D_{50}$ , and  $D_{90}$  took place sequentially because of the progress of nucleation. Finally, the sizes rebounded as the result of growth. In the 3% seed loading run, the decrease in sizes was only observed in  $D_{10}$  and  $D_{50}$  of the heights, while the  $D_{90}$  kept growing constantly because the low nucleation level did not affect the high quantile statistics.

The FBRM chord length statistics only showed the monotonic increasing sizes. In the seeded experiments, before the agglomeration events, the FBRM  $D_{90}$  was close to the  $D_{90}$  of the widths (the shorter edge) because of the FBRM scanning mechanism that has a higher probability to scan the shorter edges of the high-aspect-ratio crystals (Szilagyi & Nagy, 2018). In the unseeded run, the FBRM chord length was higher than the width, possibly due to a large number of clusters in the system. The FBRM was capable to detect finer particles, with the smallest detectable particle size of  $0.125 \mu\text{m}$ , while the detection limit of the image analysis was  $3.3 \mu\text{m}$ .

The aspect ratio (AR) was extracted from the ratios between the heights and the widths of the detected crystals. In the unseeded experiment, the median ARs of the nuclei increased from 1.6 to 2.0 in 1 minute, then slowly progressed to 2.3. In the seeded runs, the initial AR was consistent with the AR of the seeds obtained from offline microscopy. The transition of the AR occurred approximately the same time when the nucleation started and the drop in the size statistics was observed. Combined with the supersaturation data in Figure 3-8, the increasing seed loading led to 1) the decreased average and peak supersaturation, 2) the lower AR of the products, and 3) the slower trend of AR increment after nucleation, suggesting that the higher supersaturation environment may favor the higher aspect-ratio of taurine crystals.



**Figure 3-10** The crystal size and shape (aspect ratio) trends during the linear cooling experiments (0.5 °C/min) of (a) unseeded, (b) 1% seed loading, and (c) 3% seed loading. The data before nucleation onset in (a) were ignored. The shaded areas show the 10<sup>th</sup>-

quantile ( $D_{10}$ ) to the 90<sup>th</sup>-quantile ( $D_{90}$ ) ranges of each statistic and the solid lines were the median ( $D_{50}$ ). The height is the longer edge in the image analysis result.

The 2D CSDs from image analysis are summarized in Figure 3-11. The count-based CSDs (the histograms) may cause confusion due to the massive amount of small crystals. To address this problem, the weighted CSDs are extensively used in many PATs to suppress the bias caused by small particles (nuclei) and emphasize the large ones. For example, the Mastersizer 2000 reports the volume-weighted size distribution. The crystal volume (Eq 3-2) was used to compute the volume-weighted CSD (the shaded curves in Figure 3-11). Compared to the 3% seed loading experiment, the 1% seed loading run showed a broader CSD due to nucleation and a higher maximum size because the supersaturation consumption was shared by the fewer seeds.

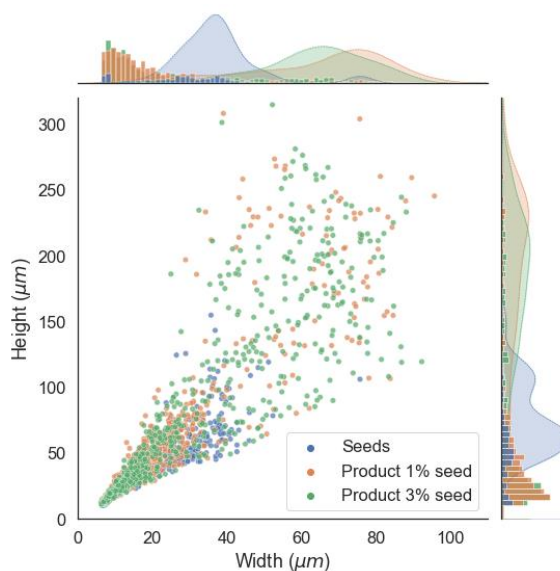


**Figure 3-11** The 2D CSDs of the seeds and the products of 1% and 3% seed loading experiments. The marginal histograms are the count-based size distribution of each dimension; the marginal filled curves are the volume-weighted size distribution of each dimension.

### 3.3.5. Estimation and Validation of The Kinetic Parameters

The nucleation model was fitted with the crystal counts and supersaturation data from the 7.6 to 9.3 minutes of the unseeded run and from the 6.1 to 9.1 minutes of the 1% seed loading run. The 3% seed loading run was excluded since the nucleation is insignificant in the growth-dominant condition. The fitted parameters were summarized in Table 3-2 and the comparison between the experimental and calculated nucleation rates was demonstrated in Figure 3-12.a. The nucleation rate in the unseeded run was higher due to the higher supersaturation. The nucleation rate of the 1% seed loading run was a magnitude slower, and the existence of seeds caused disturbances to the measurement, resulting in the less consistent prediction in Figure 3-12.a.

The crystal growth model was fitted with the first 7 minutes of data from the 1% seed loading run and the 7 to 14 minutes of the data from the 3% seed loading run. The unseeded experiment was excluded due to the high nucleation and agglomeration levels. The fitted parameters were listed in Table 3-2 and the relation between supersaturation and the two-dimensional growth rate was shown in Figure 3-12.b. The ratio of the growth rate between the major and minor dimensions was approximately two, which was consistent with the aspect ratio analysis in Figure 3-10.

The estimated kinetic model was validated by simulating the crystallization experiments with the Monte Carlo method (Van Peborgh Gooch & Hounslow, 1996). The comparison between the simulation results and the experimental data were demonstrated in Figure 3-12.c, d, and e. The simulated concentration trends were consistent with the concentration measured by Raman spectroscopy. The simulated crystal count density matched with the count density obtained from image analysis before the onset of massive agglomeration, which caused a significant decrease of the experimental counts. Also, the increasing solids concentration will decrease the DOF of the imaging system, leading to underestimated crystal count. In the 3% seed loading run, the nucleation and



agglomeration level were the lowest, so that the simulation could trace the crystal count of the entire run correctly. The agglomeration onset was also the separator of the consistent size measurements of crystal heights ( $H_{50}$ ) and widths ( $W_{50}$ ) and the diverging trends between the experimental and simulated data. The possible explanation is that when the solids concentration or the agglomeration level are high, compared to fine crystals, the larger crystals have a higher chance of being cropped or masked by the clusters, the image frames, and other crystals, leading to missed detection or underestimated sizes. Also, the count-based CSDs shown in Figure 3-11 demonstrate a positive skewness, so that the missed detections of the large crystals can cause significant bias and fluctuation in the size statistics. This can explain the mismatches in the size statistics of the 3% seed loading experiment despite the low agglomeration level.

In conclusion, the simulation study verified the estimated growth rate and secondary nucleation parameters of taurine. The simulation model successfully predicted the experimental concentration trends, which could be used to design the optimal cooling profiles that control the supersaturation within the desired range. The correct count density measurement confirmed the estimation of the nucleation rate. However, the mismatch after agglomeration onset suggested the need for modeling the agglomeration and breakage mechanisms in future works. The simulation model also achieved effective prediction of the heights and widths in relatively low solids concentration. The image analysis algorithms and the imaging hardware can be optimized by expanding the training data at high slurry density and employing the in-situ dispersion or dilution devices to enhance the performance of size measurement in high solids concentration environment.

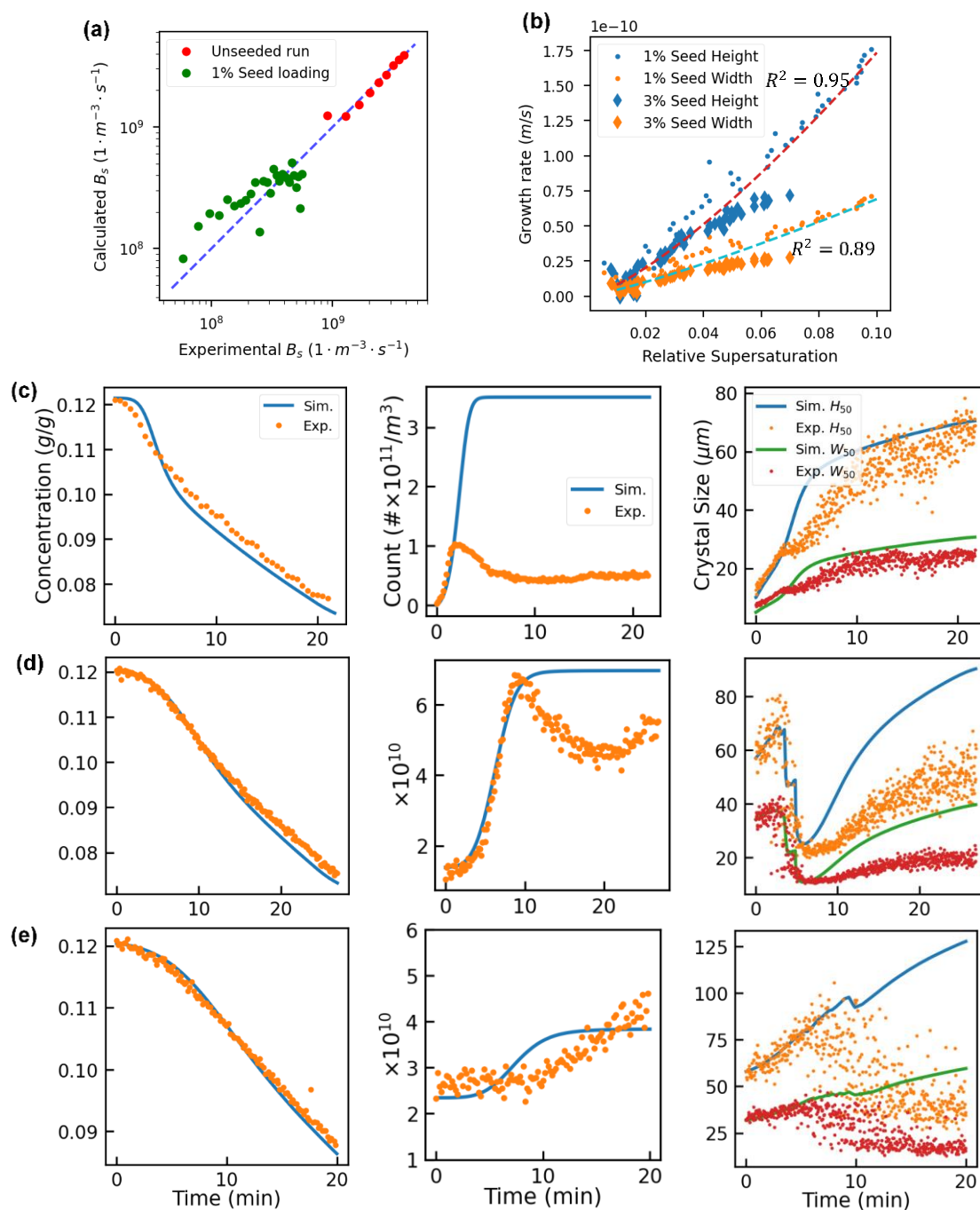


**Figure 3-12** a, b: results of the nucleation and growth rate estimation; c (unseeded run), d (1% seed loading run), e (3% seed loading): experimental data and simulation results with the estimated kinetic parameters.

**Table 3-2** Summary of the crystallization kinetics of taurine analyzed by image analysis

Kinetics	Parameters	Values	Units
<i>Nucleation</i> (eq. 3-3)	$b_0$	$5.05 \times 10^{14}$	$\# \cdot m^{-3} \cdot s^{-1}$
	$m$	6.07	–
	$j$	0.17	–
<i>Growth</i> (eq. 3-4)	$\{g_h, g_w\}$	$\{3.74 \times 10^{-6}, 1.09 \times 10^{-6}\}$	$m \cdot s^{-1}$
	$\{n_h, n_w\}$	{1.33, 1.19}	–

### 3.4. Conclusion

A novel PAT instrument for crystal monitoring was developed based on the in-situ flow-cell imaging system and the image analysis model, *S<sup>2</sup>A-Net*. The proposed system featured the state-of-the-art oriented object detection algorithm for accurate and fast crystal characterization. The system was tested with the taurine cooling crystallization of various seed loadings. The crystal and cluster detection and classification capabilities of the model were able to track the crystal counts, the two-dimensional CSDs, the aspect ratios, and the agglomeration levels. The precision of size measurement and sensitivity of nucleation detection outperformed the FBRM.

In the experimental study, the increasing seed loading prevented the accumulation of supersaturation and suppressed the level of nucleation and agglomeration. With approximately 3% seed loading, the process is growth dominant with negligible nucleation and clustering. When the seed loading was insufficient (1%), the nucleation led to undesired bimodal CSD of the product, which was confirmed by the previous study (Kubota et al., 2001).

An online calibration strategy for solute concentration measurement with Raman spectroscopy was introduced, which eliminated the dedicated calibration experiments and prevented degraded accuracy due to uncontrollable factors such as the CSD.

Combining the solid-phase information from the image analysis results and the liquid-phase concentration data from the Raman spectroscopy, the nucleation and growth kinetic parameters could be estimated without the need for solving the coupled mass balance and population balance model. The estimated parameters were validated by Monte Carlo simulation. The simulation study confirmed the consistent concentration prediction and the estimation of the count density and 2D sizes prior to the agglomeration onset. It was recommended to enhance the model with agglomeration and breakage mechanisms and improve the size measurement accuracy in high solids concentration conditions.

### 3.5. References

- Acevedo, D., Yang, X., Mohammad, A., Pavurala, N., Wu, W. L., O'Connor, T. F., Cruz, C. N. (2018). Raman Spectroscopy for Monitoring the Continuous Crystallization of Carbamazepine. *Organic Process Research and Development*, 22(2), 156–165. <https://doi.org/10.1021/acs.oprd.7b00322>
- Bahar Basim, G. & Khalili, M. (2015). Particle size analysis on wide size distribution powders; Effect of sampling and characterization technique. *Advanced Powder Technology*, 26(1), 200–207. <https://doi.org/10.1016/j.appt.2014.09.009>
- Bourcier, D., Féraud, J. P., Colson, D., Mandrick, K., Ode, D., Brackx, E. & Puel, F. (2016). Influence of particle size and shape properties on cake resistance and compressibility during pressure filtration. *Chemical Engineering Science*, 144, 176–187. <https://doi.org/10.1016/j.ces.2016.01.023>
- Chen, S., Liu, T., Xu, D., Huo, Y. & Yang, Y. (2019). Image based measurement of population growth rate for l-glutamic acid crystallization. *Chinese Control Conference, CCC, 2019-July*, 7933–7938. <https://doi.org/10.23919/ChiCC.2019.8866441>
- Ferreira, A., Faria, N., Rocha, F. & Teixeira, J. A. (2011). Using an Online Image Analysis Technique to Characterize Sucrose Crystal Morphology during a Crystallization Run. *Ind. Eng. Chem. Res*, 50, 6990–7002. <https://doi.org/10.1021/ie2001499>
- Gao, Z., Wu, Y., Bao, Y., Gong, J., Wang, J. & Rohani, S. (2018). Image Analysis for In-line Measurement of Multidimensional Size, Shape, and Polymorphic Transformation of l -Glutamic Acid Using Deep Learning-Based Image Segmentation and Classification. *Crystal Growth and Design*, 18(8), 4275–4281. <https://doi.org/10.1021/acs.cgd.8b00883>

- Han, J., Ding, J., Li, J. & Xia, G. S. (2020). Align deep features for oriented object detection. *ArXiv*, 1–10.
- Hu, Y., Liang, J. K., Myerson, A. S. & Taylor, L. S. (2005). Crystallization monitoring by raman spectroscopy: Simultaneous measurement of desupersaturation profile and polymorphic form in flufenamic acid systems. *Industrial and Engineering Chemistry Research*, 44(5), 1233–1240. <https://doi.org/10.1021/ie049745u>
- Huo, Y., Liu, T., Wang, X. Z., Ma, C. Y. & Ni, X. (2017). Online detection of particle agglomeration during solution crystallization by microscopic double-view image analysis. *Industrial and Engineering Chemistry Research*, 56(39), 11257–11269. <https://doi.org/10.1021/acs.iecr.7b02439>
- Irizarry, R., Chen, A., Crawford, R., Codan, L. & Schoell, J. (2017). Data-driven model and model paradigm to predict 1D and 2D particle size distribution from measured chord-length distribution. *Chemical Engineering Science*, 164, 202–218. <https://doi.org/10.1016/j.ces.2017.01.042>
- Kristova, P., Hopkinson, L. J. & Rutt, K. J. (2015). The effect of the particle size on the fundamental vibrations of the [CO<sub>3</sub><sup>2-</sup>] anion in calcite. *Journal of Physical Chemistry A*, 119(20), 4891–4897. <https://doi.org/10.1021/acs.jpca.5b02942>
- Kubota, N., Doki, N., Yokota, M. & Sato, A. (2001). Seeding policy in batch cooling crystallization. *Powder Technology*, 121(1), 31–38. [https://doi.org/10.1016/S0032-5910\(01\)00371-0](https://doi.org/10.1016/S0032-5910(01)00371-0)
- Leyssens, T., Baudry, C. & Hernandez, M. L. E. (2011). Optimization of a crystallization by online FBRM analysis of needle-shaped crystals. *Organic Process Research and Development*, 15(2), 413–426. <https://doi.org/10.1021/op100314g>
- Lin, M., Wu, Y. & Rohani, S. (2020). Simultaneous Measurement of Solution Concentration and Slurry Density by Raman Spectroscopy with Artificial Neural Network. *Crystal Growth and Design*, 20(3), 1752–1759. <https://doi.org/10.1021/acs.cgd.9b01482>
- Ma, C. Y. & Wang, X. Z. (2012). Closed-loop control of crystal shape in cooling crystallization of l-glutamic acid. *Journal of Process Control*, 22(1), 72–81. <https://doi.org/10.1016/j.jprocont.2011.10.007>
- Ma, Z., Merkus, H. G., De Smet, J. G. A. E., Heffels, C. & Scarlett, B. (2000). New developments in particle characterization by laser diffraction: Size and shape. *Powder Technology*, 111(1–2), 66–78. [https://doi.org/10.1016/S0032-5910\(00\)00242-4](https://doi.org/10.1016/S0032-5910(00)00242-4)
- Manee, V., Zhu, W. & Romagnoli, J. A. (2019). A Deep Learning Image-Based Sensor for Real-Time Crystal Size Distribution Characterization. *Industrial and Engineering Chemistry Research*, 58, 23175–23186. *research-article*. <https://doi.org/10.1021/acs.iecr.9b02450>

- Merkus, H. G. (2009). Particle Size, Size Distributions and Shape. Particle Size Measurements. [https://doi.org/10.1007/978-1-4020-9016-5\\_2](https://doi.org/10.1007/978-1-4020-9016-5_2)
- Nagy, Z. K., Fevotte, G., Kramer, H. & Simon, L. L. (2013). Recent advances in the monitoring, modelling and control of crystallization systems. *Chemical Engineering Research and Design*. <https://doi.org/10.1016/j.cherd.2013.07.018>
- Ochsenbein, D. R., Schorsch, S., Vetter, T., Mazzotti, M. & Morari, M. (2014). Growth rate estimation of  $\beta$ l-glutamic acid from online measurements of multidimensional particle size distributions and concentration. *Industrial and Engineering Chemistry Research*, 53(22), 9136–9148. <https://doi.org/10.1021/ie4031852>
- Szilagyi, B. & Nagy, Z. K. (2018). Aspect ratio distribution and chord length distribution driven modeling of crystallization of two dimensional crystals for real-time model based applications. *Crystal Growth & Design*, [acs.cgd.8b00758](https://doi.org/10.1021/acs.cgd.8b00758). <https://doi.org/10.1021/acs.cgd.8b00758>
- Trygg, J. & Wold, S. (2002). Orthogonal projections to latent structures (O-PLS). *Journal of Chemometrics*, 16(3), 119–128. <https://doi.org/10.1002/cem.695>
- Ulrich, J. & Stregge, C. (2002). Some aspects of the importance of metastable zone width and nucleation in industrial crystallizers. *Journal of Crystal Growth*, 237–239(1-4 III), 2130–2135. [https://doi.org/10.1016/S0022-0248\(01\)02284-9](https://doi.org/10.1016/S0022-0248(01)02284-9)
- Unnikrishnan, S., Donovan, J., Macpherson, R. & Tormey, D. (2020). In-process analysis of pharmaceutical emulsions using computer vision and artificial intelligence. *Chemical Engineering Research and Design*, 166, 281–294. <https://doi.org/10.1016/j.cherd.2020.12.010>
- Van Peborgh Gooch, J. R. & Hounslow, M. J. (1996). Monte Carlo Simulation of Size-Enlargement Mechanisms in Crystallization. *AICHE Journal*, 42(7), 1864–1874. <https://doi.org/10.1002/aic.690420708>
- Virtanen, P., Gommers, R., Oliphant, T. E., Haberland, M., Reddy, T., Cournapeau, D., ... SciPy 1.0 Contributors. (2020). {SciPy} 1.0: Fundamental Algorithms for Scientific Computing in Python. *Nature Methods*, 17, 261–272. <https://doi.org/10.1038/s41592-019-0686-2>
- Wu, D., Song, L., Zhu, C., Zhang, X., Guo, H. & Yang, C. (2017). Solubility of taurine and its application for the crystallization process improvement. *Journal of Molecular Liquids*, 241, 326–333. <https://doi.org/10.1016/j.molliq.2017.06.043>
- Wu, D., Zhang, B., Luo, W., Zhu, H., Xu, J., Zhou, L., ... Chen, W. (2020). Effect of Sodium Sulfate on Nucleation Behavior and the Crystal Morphology of Taurine. *Crystal Research and Technology*, 2000161, 1–10. <https://doi.org/10.1002/crat.202000161>

- Wu, Y., Lin, M. & Rohani, S. (2020). Particle characterization with on-line imaging and neural network image analysis. *Chemical Engineering Research and Design*, 157(Ld), 114–125. <https://doi.org/10.1016/j.cherd.2020.03.004>
- Zhou, Y., Ye, Q., Qiu, Q. & Jiao, J. (2017). Oriented response networks. *Proceedings - 30th IEEE Conference on Computer Vision and Pattern Recognition, CVPR 2017, 2017-Janua*, 4961–4970. <https://doi.org/10.1109/CVPR.2017.527>

## Chapter 4

# Computerized Crystallization Platform for Automated Experiment and Measurements of Crystallization Parameters

A version of this chapter will be submitted to *Organic Process Chemistry and Development* under the title: Automated measurement of the MSZW and induction time: Comparison of a new platform to the existing platforms



## Chapter 4 Computerized Crystallization Platform for Automated Experiment and Measurements of Crystallization Parameters

### Abstract

We present a computerized crystallization platform powered by an image-based PAT and various customized laboratory instruments for conducting the automated crystallization experiments. The hardware design and build enabled by the Internet-of-Things (IoT) microcontroller demonstrated the potential to equip the existing laboratory devices such as the stirring motor and thermostat water bath with wireless-network connectivity and remote-control capability. The communication of the acquired data and control commands was centralized at an MQTT (Message Queuing Telemetry Transport) broker. The software was developed to execute the experimental procedures by sending the instructions to the actuators based on the real-time data acquired by the PATs. The automated cooling crystallization experiments for determining the metastable zone width (MSZW) and induction time of the taurine-water system were demonstrated. The image-based PAT outperformed FBRM in providing a sensitive and reproducible nucleation detection when the supersaturation and nucleation rate were low. The edge detection-based image analysis was confirmed to be an effective alternative to the deep learning-based approach for nucleation detection. The automation of the time-consuming crystallization experiments reveals the potential of the proposed automated platform to simplify and speed up the research and development stage of a crystallization process.

**Keywords:** Crystallization process; Automated experiment; Metastable zone width; Induction time; Laboratory instrument development; Process analytical technology

### 4.1. Introduction

The operating variables such as agitation rate, cooling profile, and seed addition rate and policy can significantly affect the purity, size, and shape distributions of the crystalline product (Hu et al., 2005). Discovering the connection between the variables during the

research and development stage of a crystallization process requires a lot of experimental works, including the determination of the solubility, metastable zone width (MSZW), kinetic parameters, etc. Manually conducting these experiments is time-consuming and prone to human error.

Laboratory automation via a computerized smart platform has gained a lot of interest from the industry. The crystallization engineering field has adopted the robotic platform since 1994 to automate the screening process to obtain high-quality single crystals for the determination of the structures by X-ray diffraction (Bard et al., 2004; Chayen, Shaw Stewart & Baldock, 1994; Florence et al., 2006). Discovering the optimal co-crystal formulation and condition has been boosted by the automated sample preparation and analytical tools (Bysouth, Bis & Igo, 2011; Saxena & Kuchekar, 2013). Duros et al. (2017) suggested a machine learning-enabled automation system for exploring the crystallization variable space. The algorithm-based search could discover 6 times more crystallization space than humans and thus increased the prediction accuracy. Selekmán et al. (2016) developed an automated workflow for investigating polymorphic forms and assessing the risk of undesired polymorph. The samples prepared under different conditions are automatically scanned by Powder X-ray diffraction (PXRD) to generate a risk map where the allowed and unapplicable operating conditions can be intuitively visualized. Teychené et al. (2010) investigated the possibility of spherical crystallization without additive in the various solvent with the aid of an automated crystallization platform. Zhou et al. (2013) reviewed the automated platform for the development of crystallization processes. The PAT-enabled crystallization system allowed performing routine process evaluation such as solubility determination and executing feedback control of crystallization based on a predefined supersaturation profile via cooling and/or antisolvent addition.

The commercial automated crystallization platforms reported in the literature include the Mettler Toledo LabMax series (Teychené, Sicre & Biscans, 2010; Verma et al., 2018), HEL AutoLAB (Grön, Borissova & Roberts, 2003; Wang, Calderon De Anda & Roberts,

2007), and Atlas HD Automated Jacketed Reactor (Coliaie et al., 2019). As demonstrated in Figure 4-1, the main components of the crystallization automation platform consist of the jacketed crystallizer, the thermostat for temperature control, the mechanical stirrer for mixing the slurry, and various PATs and actuators for real-time data acquisition and execution of control commands. A computer interface provides the capability to programmatically execute the experiments or compose the feedback control logic. The widely adopted PATs include the temperature probe, turbidimeter for slurry density measurement, FBRM for online particle size measurement, Raman spectroscopy for monitoring the polymorphic forms, and ATR-FTIR for solute concentration estimation. Also, Mettler Toledo EasyViewer and Particle Vision and Measurements (PVM) have been employed to provide in-situ visualization of the crystal size and morphology (Haer et al., 2021; Zhou et al., 2015). The actuators adjust the operating conditions. Common actuators include a thermostat water bath for temperature control, a stirring motor for agitation strength control, and valves and pumps for anti-solvent addition and vacuum pressure control. The rapid development of innovative actuators and PATs over the last few years has brought more possibilities for automated platforms. The ultrasonic sonification was employed to promote and control nucleation (Fang et al., 2020). The in-situ wet milling was used to control the size and morphology of the crystals (Yang et al., 2016). The online image analysis techniques including the image-based PAT proposed in this thesis provided the capability of multi-dimensional size measurement.

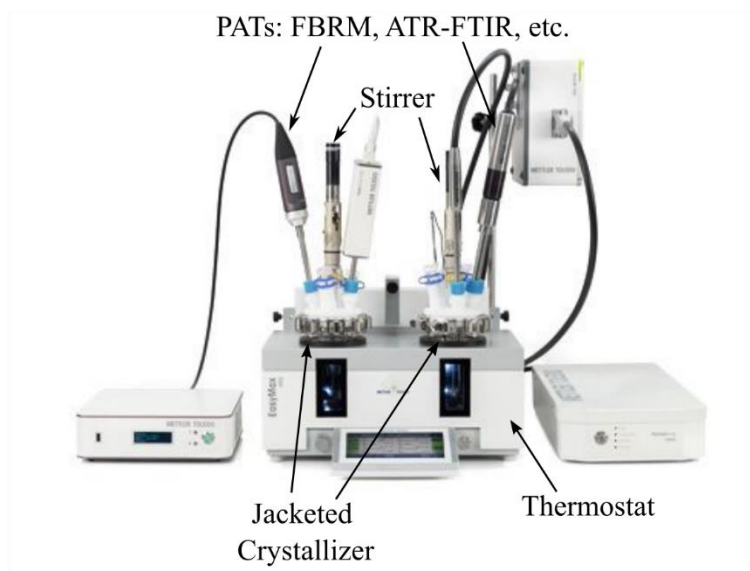


**Figure 4-1** A commercial automated crystallization platform (Mettler Toledo EasyMax) (Mettler Toledo, 2021).

Due to the lack of unified communication protocol and programming interface, integrating the non-compatible devices is usually challenging and requires strong programming skills. The cost of customizing the commercial platforms can be high due to their proprietary software interface. This chapter will discuss the development of a cost-effective and customizable automated crystallization solution by employing the latest Internet-of-Things (IoT) technologies to transform the existing laboratory equipment into a compatible wireless PAT platform. The image-based PAT solution proposed in Chapter 2 and Chapter 3 is integrated in this system to provide multi-dimensional size measurement and nucleation onset detection. The automated experiments are discussed to demonstrate the procedures of estimating the induction time, metastable zone width (MSZW), and kinetic parameters.

## 4.2. Automated Cooling Crystallization Platform

The automated crystallization platform was designed to conduct a series of common experiments to study the basic kinetic characteristics of an aqueous taurine system, including determining the metastable zone width (MSZW) at various cooling rates, the induction time at different supercooling temperatures, and the parameters of crystal growth and nucleation kinetics. These experiments need repetition to ensure reproducible and consistent results. Also, since the agitation level is associated with the mixing efficiency that ensures the proper energy and mass transfer in the crystallizer, as well as the shear force that causes agglomeration and breakage, the experiments need to be carried out under different stirring speeds to find the optimal agitation configuration for production scale-up (Myerson, 2002). The number of experimental works can be prohibitive for manual operation. Therefore, the automated platform that carries out the experiments uninterruptedly is perfectly highly desirable for offloading the tedious laboratory work from the operators.

For cooling crystallization, the induction time is the time duration between the creation of the supersaturation and the appearance of detectable nuclei at constant supersaturation. The formation of critical nuclei is related to the interfacial energy of the crystals, which is usually calculated from the induction time data in the literature (Omar, Mohnicke & Ulrich, 2006). The induction time is usually measured using the rapid cooling crystallization experiment (Figure 4-2.a). The solution was first held above the saturated temperature for 5–10 min to ensure a complete dissolution at the beginning of the experiment. As the cooling rate affects the nucleation and induction time (García-Ruiz, 2003), the solution should be rapidly cooled to the supercooling temperature. The nucleation event was detected by the PATs such as FBRM (Mitchell, Frawley & Ó'Ciardhá, 2011), turbidimeter (Saleemi, Rielly & Nagy, 2012), and other image-based detectors (Gao et al., 2017). The solution is then heated back to dissolution temperature to restart the cycle with a different supercooling.

When the crystallization system is cooled at a linear rate, nucleation will only occur if the supersaturation is sufficient to overcome the energy barrier associated with the creation of new interfaces of the solid phase. The gap between the nucleation supersaturation and the solubility is referred to as metastable zone width (MSZW). The cooling rate, agitation level, and temperature will affect the MSZW (Parsons, Black & Colling, 2003). The MSZW is deemed as the critical boundary between the ideal zone for crystal growth and the region of undesired explosive nucleation (Wood, 1997). Experimental determination of MSZW was achieved using the linear cooling profile shown in Figure 4-2.b. The solution was first held at the dissolution temperature for dissolving the crystals. Next, the system was cooled to the saturated temperature and held for equilibrium. Then, the solution would be cooled linearly at the predefined cooling rate until the final temperature. The temperature of nucleation onset was detected by the PATs. Finally, the temperature was slowly heated up to the saturated temperature to record the dissolution data. By recording the concentration, temperature, and size distribution of the whole process, the nucleation, growth, and dissolution behaviors can be studied.

The capability of the automated crystallization platform is not limited to the abovementioned experiments. For example, the effect of seed loading in Chapter 3 can be studied in a semi-automated fashion by manually handling the material addition. The application can be easily extended based on the current PAT and data processing frameworks. In the scope of this work, the design objectives of the automated crystallization platform are:

- Fully automated tasks (perform reproducible repetitions without human intervention)
  - Metastable zone width (MSZW) at various cooling rates
  - Induction time at different supercooling temperatures
  - Kinetic regression

- Semi-automated tasks (need human intervention and is not able to repeat automatically)
  - Seed addition
  - Adding materials to achieve different saturation temperatures/concentrations.

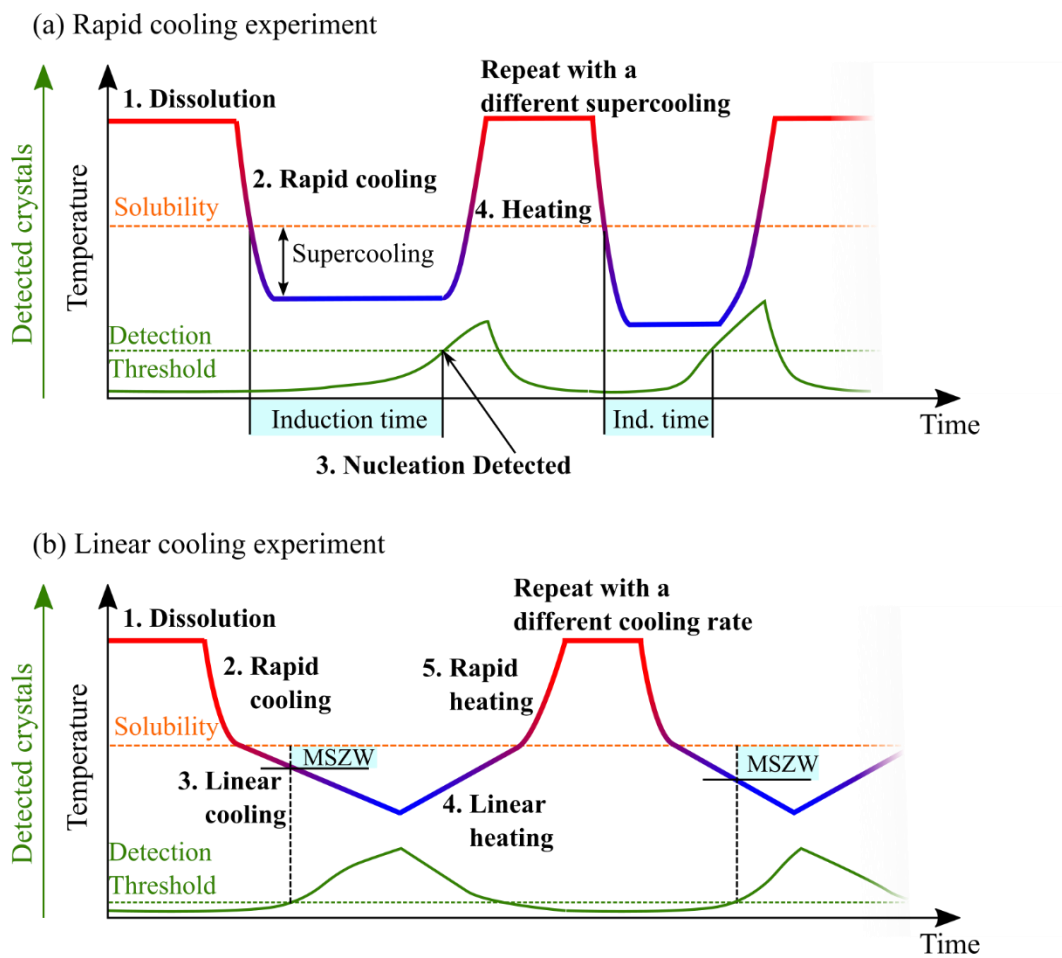


**Figure 4-2** Temperature profiles of rapid cooling and linear cooling experiments

### 4.3. Hardware Components

The overall structure of the crystallization platform is shown in Figure 4-3. All components except the image acquisition by the industrial camera were connected to the wireless network gateway to transfer measurement data and control commands. This system included several PATs including a Maxim DS18B20 temperature measurement, a Kaiser Optical Raman Spectroscopy, a Mettler Toledo FBRM S400, and a flow-through cell in-situ imaging system. The agitation level was controlled by a home-made stirring motor. The switch valves were used to select the water bath connected to the crystallizer jacket. Two water baths were used to provide a quick switch between the dissolving temperature and crystallization temperature to achieve rapid cooling for induction time measurement. Only one water bath is connected to the instrument network for an adjustable setpoint, while the other water bath is fixed at the desired dissolution temperature. It is worth noting that the rapid switching between dissolution and growth is also an ideal approach to achieve fines (crystals smaller than a given size, e.g.  $50\ \mu\text{m}$ ) dissolution by temperature cycling, which has been widely adopted as a direct nucleation control (DNC) strategy (Hansen et al., 2017).



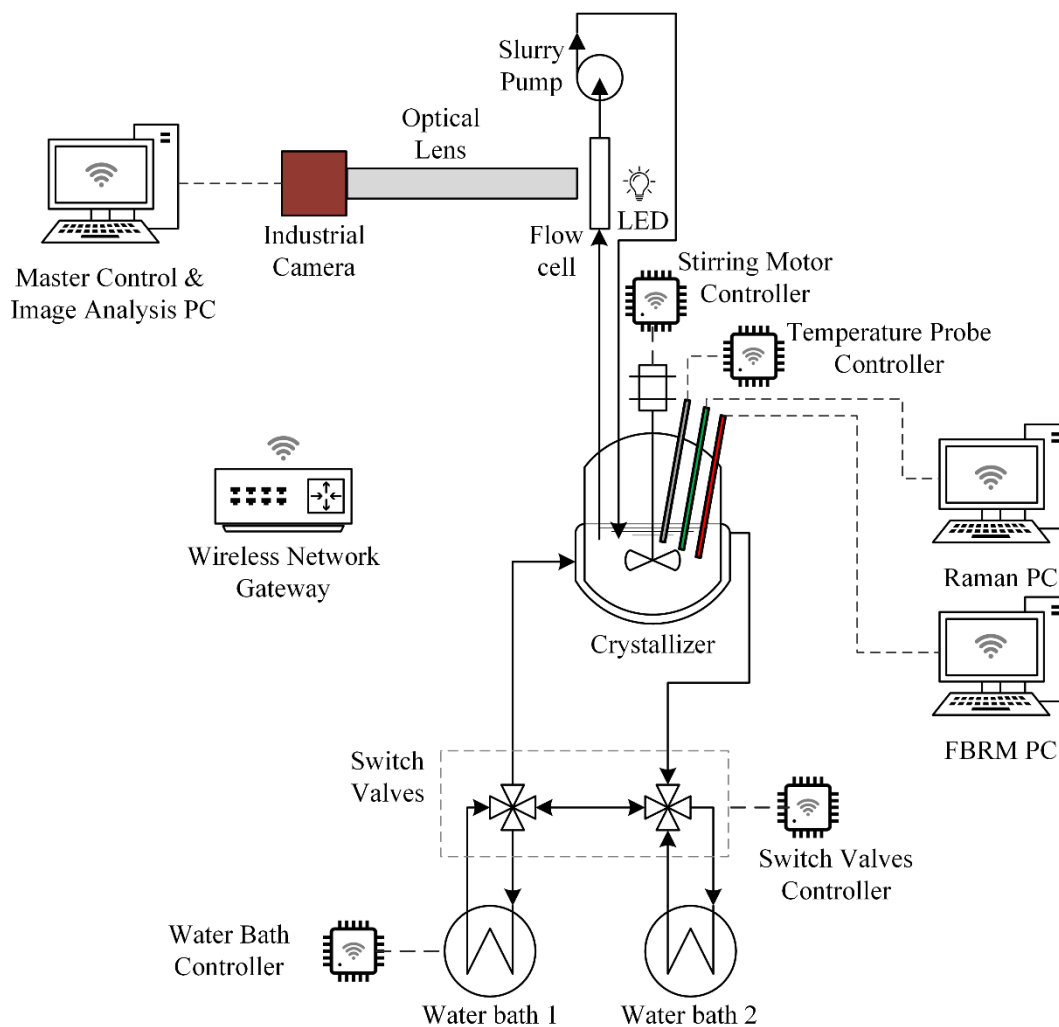


**Figure 4-3** Schematic of the automated crystallization platform.

#### 4.3.1. The IoT Microcontroller – Espressif ESP8266

The ESP8266 microcontroller board (Figure 4-4) is a modern microcontroller with built-in Wi-Fi connectivity and various peripheral interfaces (e.g., I2C, SPI, UART, etc.). The price of each unit is as low as 3 – 4 Canadian dollars. Due to its popularity, the user-community has developed various simplified programming interface for ESP8266 that enables fast and robust prototyping of an IoT project with very low requirement of the

programming skills. This makes it a perfect tool to transform the existing equipment into a wireless-enabled device. All devices associated with a symbol of “wireless integrated circuit” in Figure 4-3 are interfaced and controlled by this microcontroller.

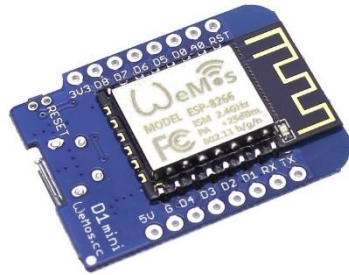


**Figure 4-4 WeMos D1 mini ESP8266 board**

#### 4.3.2. Stirring Motor

Mechanical stirring is generally preferred over magnetic stirring for the crystallization process because of the better mixing efficiency and less crystal breakage due to grinding (Coliaie et al., 2019). The common mechanical stirrer is driven using an overhead motor that is usually bulky, which causes stability issues due to elevated center of gravity and insufficient room for deploying the image PAT that shares the same overhead space. We borrowed the idea from the commercial products and used 3D printing to create a similar miniature overhead stirring motor (Figure 4-5.a). The stirring shaft was driven by a 540 DC motor. The agitation speed was adjusted using a PWM (pulse width modulation) signal generated by the ESP8266 microcontroller. The measurement for feedback control of the revolution per minute (RPM) was achieved using a Vishay TCRT 5000 reflective sensor (Figure 4-5.c), which served as a tachometer using infrared (IR) light to detect the passage of a black marker under the driven gear. A ball bearing was used to connect the driven gear and the main structure to reduce friction. The ratio of the driven gear and the driving pinion on the motor could be modified to adjust the speed ratio. In this design, the gear ratio was 5.6:1, which was ideal for the stirring rate between 100 to 1000 RPM.

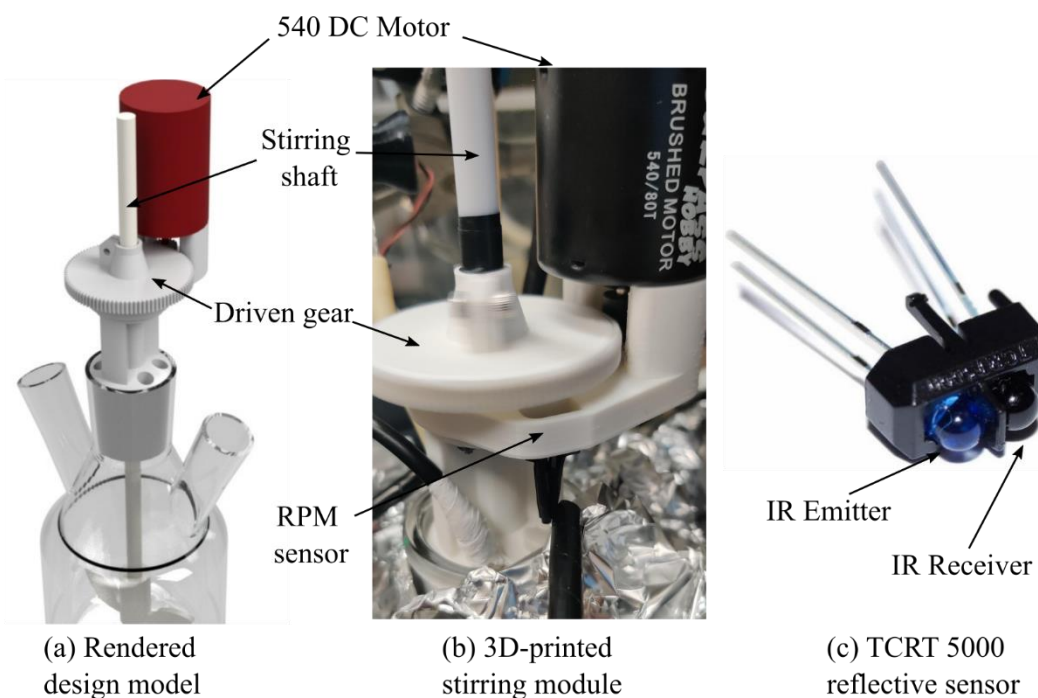


**Figure 4-5** The stirring motor and the optical RPM measurement sensor

#### 4.3.3. Water Baths and Switch Valves

Two thermostat water baths were connected to the crystallizer jacket through the switch valves for temperature control (Figure 4-6). The primary water bath (Julabo FP50) with cooling capability was connected to the instrument network to execute a variable temperature setpoint or temperature profile. The dissolution water (Thermo Neslab EX10) bath was manually set to 10°C above the saturated temperature. The tubing was wrapped with glass fiber insulation due to the large temperature difference to the room temperature.

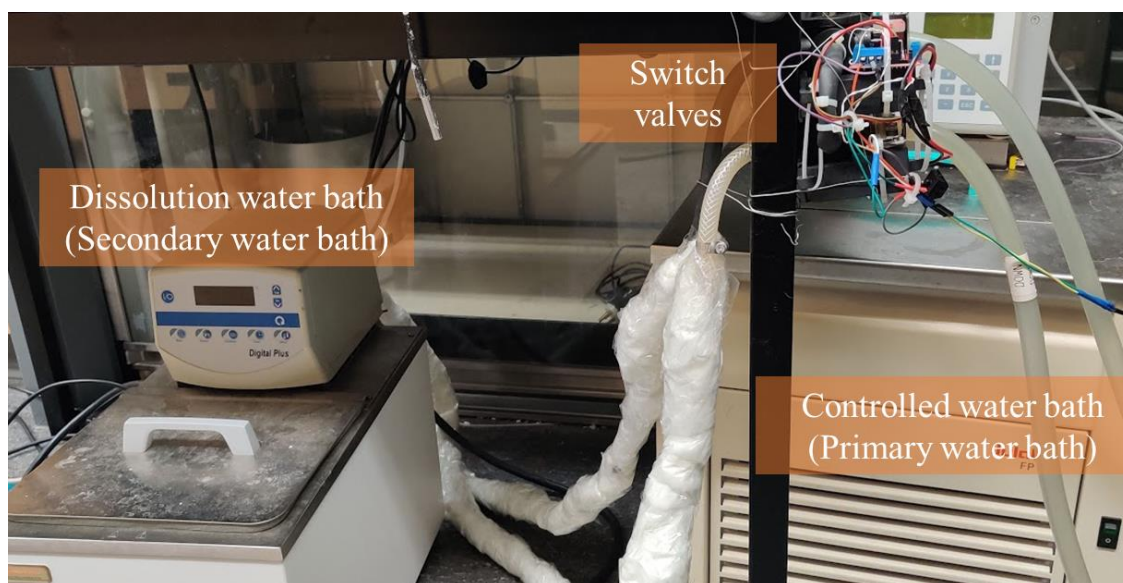
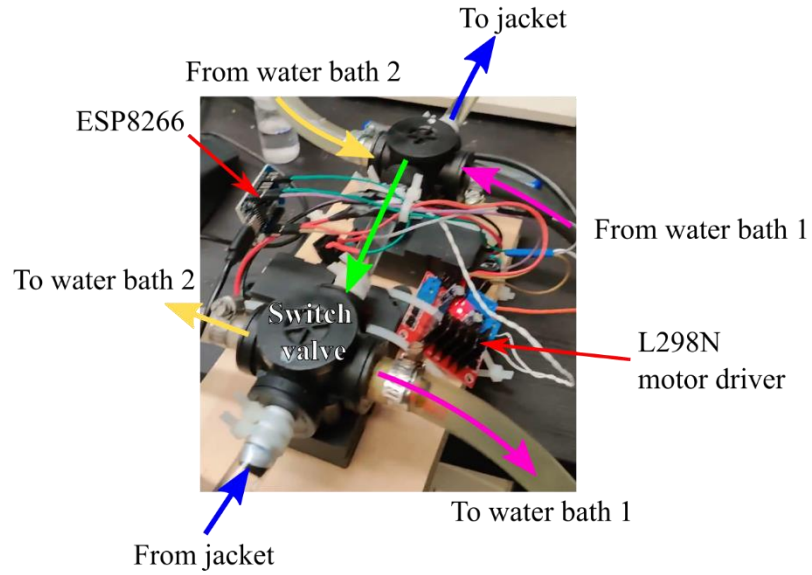


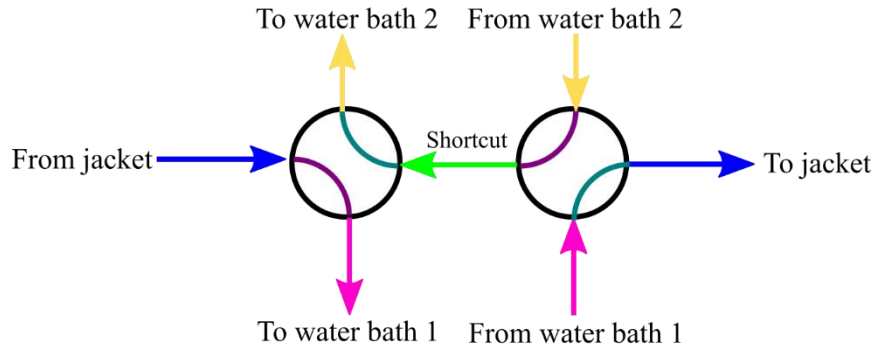
**Figure 4-6** Two thermostat water baths and the switch valves

The switch valves and the mechanism to selectively connect one of the water baths to the crystallizer jacket are illustrated in Figure 4-7. The switch valve was a four-way motorized valve that could be sourced as the original equipment manufacturer (OEM) part in the cooling system of an electric vehicle. These modules were designed to work in various temperature conditions. At any time, the valve would connect the pairs of the adjacent ports in the configurations as shown in Figure 4-7.b-c. The motor could be engaged in different polarities to switch the configurations. The STMicroelectronics L298N motor driver was used to assist the ESP8266 microcontroller to drive the two valves in different polarities. The action time of switching the configuration was only 4 seconds. The shortcut pathway was an optional feature that ensured the circulation of the idle water bath, which prevented the safety alarm of pump failure.

**(a) The switching valves and the control elements**



**(b) Configuration 1: the jacket connects to the water bath 1**



**(c) Configuration 2: the jacket connects to the water bath 2**

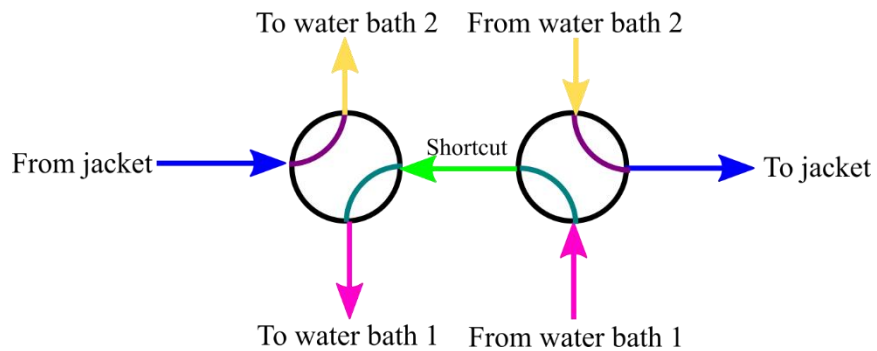


**Figure 4-7** The switching valves and the operation configurations.

#### 4.3.4. Imaging System

The flow-through cell imaging system is illustrated in Figure 4-8. A peristaltic pump (Kamoer KCM) driven by a stepper motor was used to circulate the slurry through a quartz flow-through cell (width: 2 mm, depth: 1 mm). The stepper motor was driven with an Allegro A4988 motor driver under the control of an ESP8266 microcontroller. The pump could provide a flow rate of up to 4 mL per second, which eliminated the undesired sampling classification effect. The cell was clamped between a 3D-printed lens guide and a 3D-printed LED holder. The lens guide ensured the proper spacing for focusing between the cell and the optical lens. The optical lens was repurposed from a low-cost PCB microscope (maximum magnification = 4.5). An industrial camera equipped with the SONY 1/2.9" IMX273 image sensor (resolution: 1440-by-1080) was used to acquire the microscopic crystal images. Due to the high flow rate of the slurry, the microscopic image was prone to motion blur. This issue was resolved using a high-power LED (CREE XHP70.2) and strobing lighting triggered by the exposure signal emitted by the industrial camera. Compared to the commercial crystallization imaging instruments, this set-up can achieve comparable image quality with significantly lower cost.

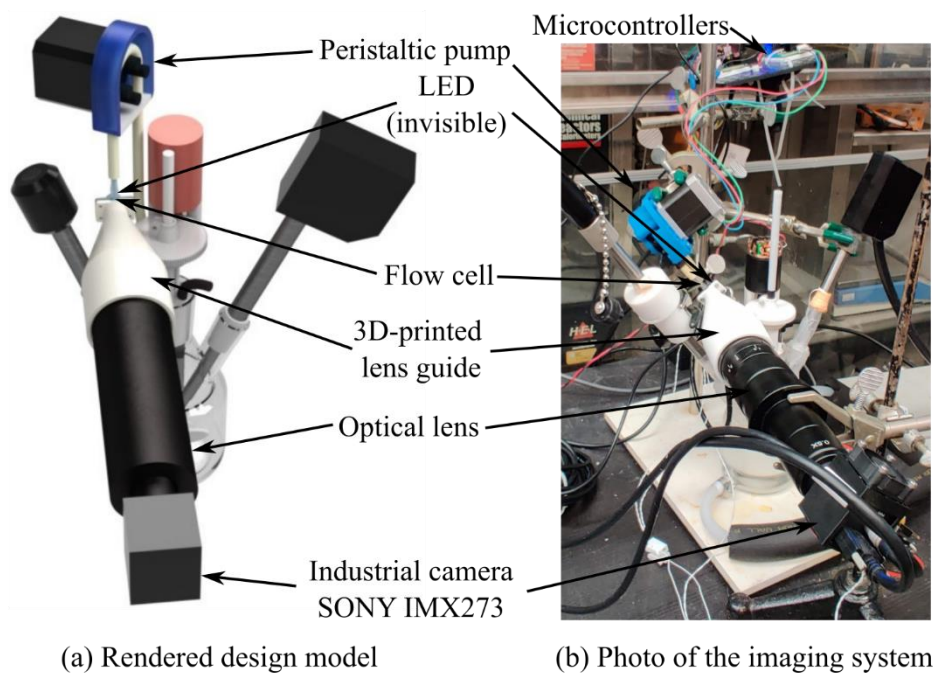


**Figure 4-8** The flow-through cell imaging system

## 4.4. Software Architecture

### 4.4.1. Device Communication and Data Exchange

The data flow of the automated experiment platform is shown in Figure 4-9. A wireless router was used as the network gateway to coordinate all devices including the homemade devices and the dedicated PCs for Raman spectroscopy and FBRM. The router operated a custom OpenWRT firmware with a lightweight MQTT (Message Queuing Telemetry Transport) broker (Eclipse Mosquitto), which coordinated the bi-direction communication between the broker and the devices. MQTT was a standard messaging protocol for the Internet of Things. MQTT worked with the publish-subscription (PubSub) approach: the client device could subscribe to a topic (e.g., the temperature of the crystallizer), and the broker would actively push the message to the client once the temperature was updated by the sensor. This ensured timely handling of the new data and saved lots of network resources compared to the polling approach where the client must repetitively send requests to check for updates. MQTT aimed to provide



efficient and robust IoT communication. For richer data management, storage, and stream process features, the other software including RabbitMQ (Wood, 2016) and Apache Kafka (Narkhede, Shapira & Palino, 2017) can be used.

All data transmitted to the MQTT broker were subscribed and processed on a PC using a Python program. The camera was directly connected to the PC due to the high bandwidth required by image acquisition. The acquired images and data were visualized on a web dashboard composed using the Plotly software package (Plotly Technologies Inc, 2015).

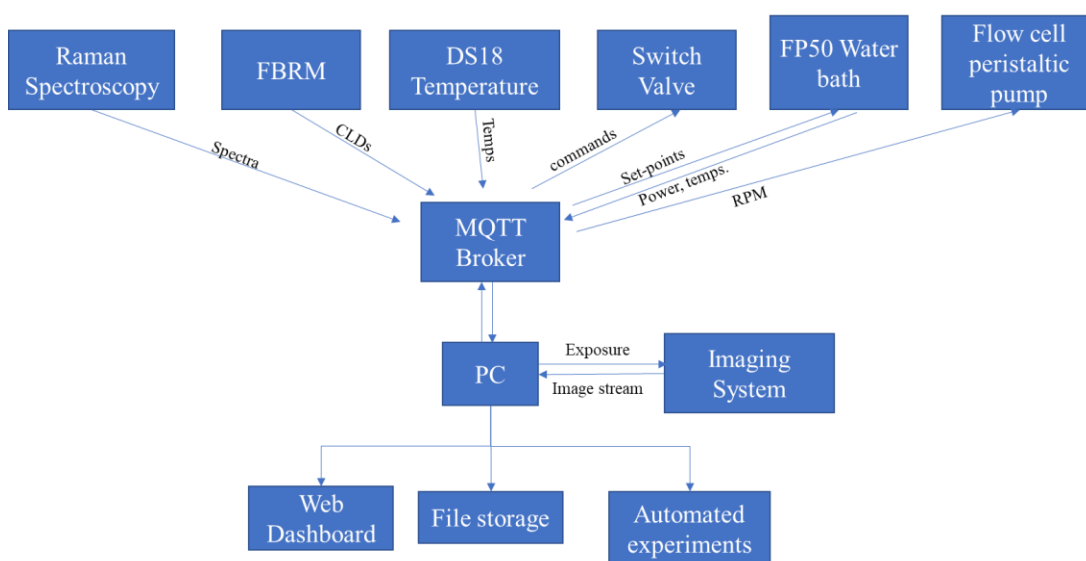


**Figure 4-9** Software architecture and data flow of the platform

#### 4.4.2. Data Hooking for Raman spectroscopy and FBRM

The Raman spectroscopy (Kaiser Optics RXN1) and FBRM S400 used proprietary software (iC Raman and iC FBRM) to control the hardware and visualize the data. The outdated software did not provide a convenient way to fetch the real-time raw measurement data. Therefore, we developed the data hooking programs for the software.

The iC Raman software supported exporting the real-time data as a CSV (Comma-separated values) file. An application was created to monitoring the new file and post it to the MQTT broker. The iC FBRM software only supported exporting the statistics (e.g.,



mean chord length and total counts) instead of the raw size distribution. We developed an application using the Mettler Toledo AutoChem C# SDK (Software Development Kit) to read the raw measurement data directly from the software and upload it to the MQTT broker. The source code of the developed applications can be found in Appendix. B. These applications served as examples to read the data from a non-compatible instrument.

#### 4.4.3. Microcontroller Firmware

The firmware on the microcontrollers of the homemade hardware was developed with Arduino. Arduino is an open-source hardware and software framework, which allows the developers to write the program for a microcontroller using the C++ programming language. Due to the abstraction layer implemented by the Arduino framework, many third-party libraries for interfacing with various sensors and actuators can be shared for many different hardware platforms. The microcontroller firmware for various devices is listed in Appendix. B.

#### 4.4.4. Automated Experiment Execution

The experimental procedures usually involve several operations: reading the real-time measurement; waiting until conditions are satisfied; issuing a command to the actuator. The Python asynchronous programming library “asyncio” is ideal for these tasks. Asynchronous programming is a means of parallelization, but the purpose is not to improve computational performance. In fact, the asynchronous tasks in Python are not executed in parallel by default. The asynchronous task is added to a queue rather than executed immediately. An asynchronous scheduler will execute the task from the queue if the criterion is met, e.g., the delay time has elapsed. This programming technique allows scheduling multiple long-lasting tasks without blocking the program, e.g., waiting for the nucleation onset while executing a linear cooling profile, making it perfect for executing the automated experiments.

Figure 4-10 demonstrates the implementation of the automated experimental tasks to execute the temperature profiles described in Figure 4-2. The material addition was not automated and required human intervention. After the slurry was prepared, the linear cooling experiments protocol was executed. First, the slurry was slowly heated to the dissolution temperature. After the solution was clear, it was cooled to the saturated temperature as the starting point of the linear cooling step. Finally, the slurry was held for about 10 minutes for equilibrium. The process states were monitored by the PATs. The cycle was repeated at different linear cooling rates to complete the measurement of the MSZW. The next phase was the rapid cooling experiment for induction time determination. The dissolution water bath was set to the dissolution temperature manually. The switch valves were configured to engage the dissolution water bath. The primary water bath was set to a supercooling temperature. The program waited for the solution to become clear and the primary water bath was stable. Then, valves were switched to engage the primary water bath. Finally, the cycle was completed if the nucleation onset was detected by the PAT or if the wait time exceeded the timeout. The cycle was repeated for different supercooling temperatures. After the rapid cooling experiment was completed, the solute concentration could be adjusted to a different level by adding materials manually. The automated experiments were restarted to study the kinetic behavior in different saturated temperatures.

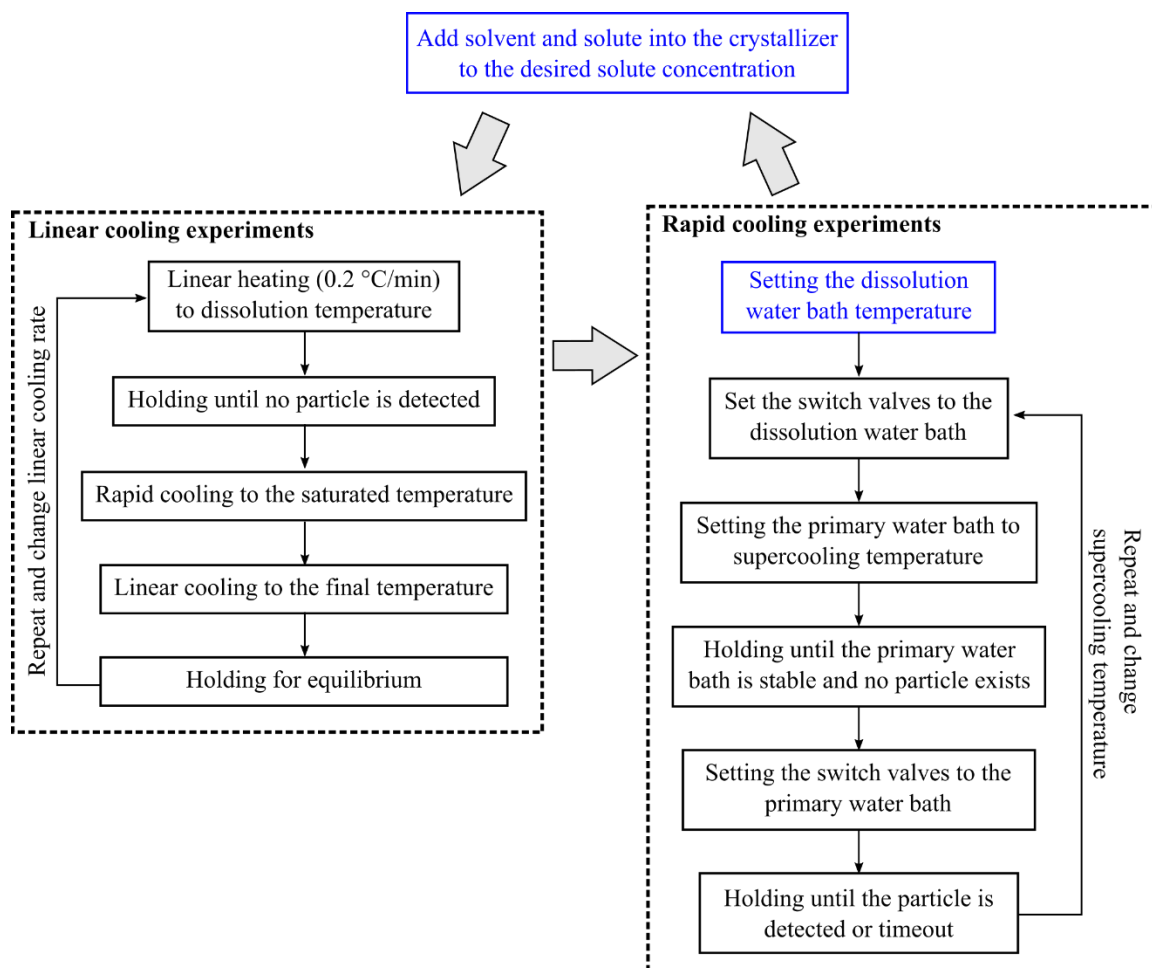


**Figure 4-10** Flow chart of the automated linear cooling and rapid cooling experiments. The blue blocks are the procedures requiring human intervention, and the black blocks are the automated tasks.

## 4.5. Results and Discussion

This section demonstrates and discusses the pilot run of the automated experiment platform with an aqueous taurine solution saturated at 30°C and 40°C. The execution of the automated experimental procedures resulted in the temperature profiles as shown in Figure 4-11. In the linear cooling experiment, the linear heating segment was used for Raman spectroscopy calibration (discussed in Chapter 3). The cooling capacity of the

primary water bath could only provide a cooling rate of up to 1.0 °C/min. By employing the switch valves, the cooling rate could reach 7 – 10 °C/min in the rapid cooling experiments. The supercooling temperature could be reached more rapidly using the feedback control to adjust the setpoint of the primary water bath.

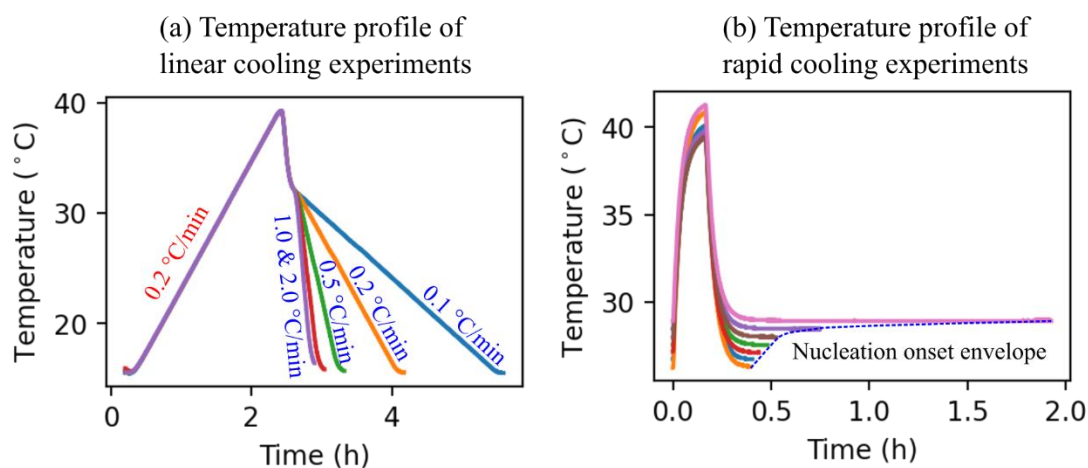


**Figure 4-11** Temperature profiles of the linear and rapid cooling experiments for the aqueous taurine solution saturated at 30°C

Reliable determinations of MSZW and induction time depended on accurate and reproducible nucleation onset detection. Figure 4-12 compares the nucleation onset detection using different techniques. The FBRM chord count was widely used as the PAT to detect the nucleation onset due to its high sensitivity. The nucleation onset was reported when the temperature dropped to 27.3°C. The primitive image analysis techniques could be used to detect the presence of nuclei. The mean grayscale value was the brightness of the image. With the same exposure and illumination condition, the brightness could be correlated to the slurry density. The nucleation onset found with this technique was 27.2°C. Another simple image analysis technique was Canny edge detection, which was a high-pass filter that finds the edges between crystals and background based on the local contrast (Ding & Goshtasby, 2000). This technique was more sensitive than the mean grayscale value since the small number of nuclei could not

significantly affect the brightness of the whole image. With the edge detection method, the nucleation onset was brought forward to 27.6°C. The image analysis count was obtained using the deep learning-based image analysis techniques. The image was manually reviewed (Figure 4-14.c) and confirmed the nucleation onset at 27.7 °C reported by the image analysis method.

In the linear cooling experiments, due to the large supersaturation that caused rapid nucleation, the performance of the techniques was similar. However, in the rapid cooling experiments where the supercooling temperature was close to the saturated temperature, the nucleation rate was much slower. Instead of the sharp changes as demonstrated in Figure 4-12, the trends became much smoother (Figure 4-13). The chord count trend reported by FBRM contained low-frequency baseline noise due to probe contamination, making it difficult to determine the nucleation onset. Solely relying on the FBRM data could lead to a large variation of the induction time measurement. The brightness-based method failed to detect the nucleation onset due to the low sensitivity. The Canny edge detection and deep learning-based approaches were able to detect the insignificant nucleation event and report the correct induction times, which were confirmed by visual examination of the images.

Unlike the FBRM and other techniques, the deep learning-based image analysis could reject the disturbance caused by undesired objects such as air bubbles and debris from the PTFE stirring impeller (Figure 4-14), which might lead to the non-physical spikes and false detection of nucleation in other methods. The ability to get the accurate counts of the nuclei allows specifying the nucleation detection threshold semantically in terms of crystals count instead of the chord counts, image brightness, or edge pixels counts that are difficult to interpret or use as the consistent threshold throughout all experiments. The FBRM S400 is prone to probe contamination (build-up on the probe window) and requires manual probe cleaning, making it less robust as a PAT for the long-running automated experiments. For the image-based technique, the stuck objects on the probe window can be easily rejected by comparing the consecutive frames and excluding the

persisting objects in the same location. The Canny edge detection method could detect the nucleation onset as effectively as the deep learning-based techniques. In the scenario where the computational power does not allow real-time deep learning-based image analysis, the edge detection-based method could serve as the alternative to coordinate the automated induction time measurement. The MSZW and induction time measurements are summarized in Table 4-1 and Table 4-2. The metastable zone and the induction time of the aqueous taurine solution are relatively small and short due to the fast nucleation kinetics. By repeating the same procedures for different saturated temperatures, the complete MSZW curve and induction profile could be built.

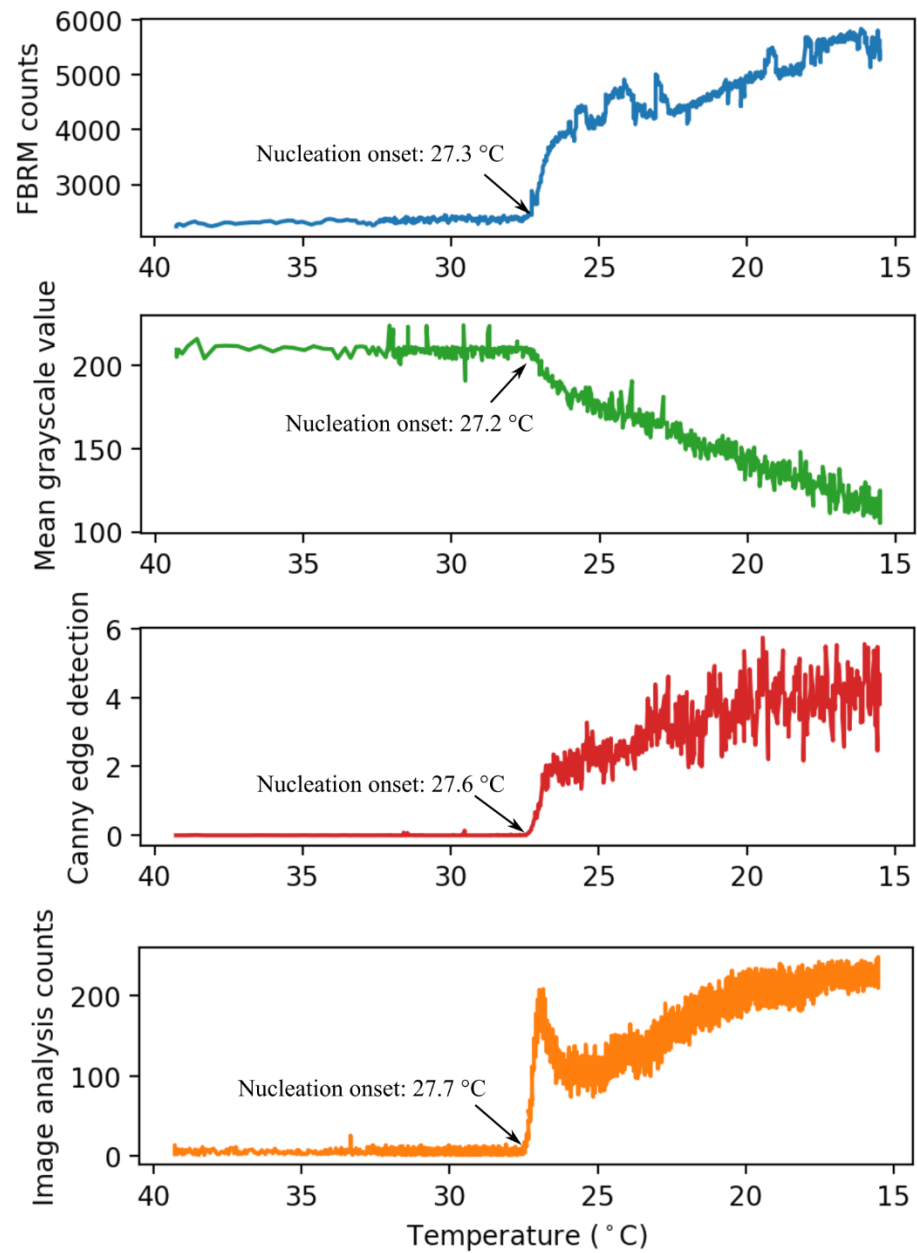


**Figure 4-12** Nucleation onset detection during the linear cooling experiment (0.1 °C/min ) using different techniques. The saturated temperature is 30°C.

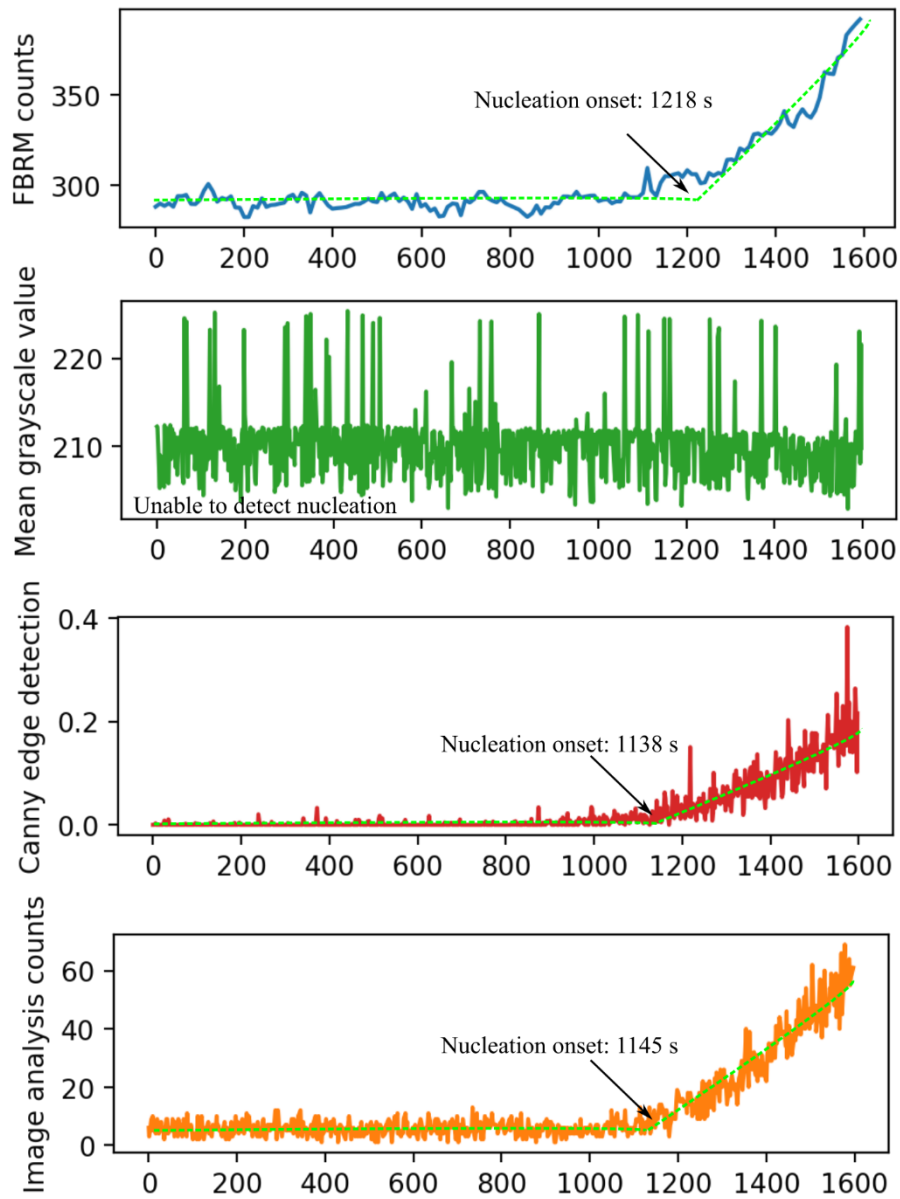


**Figure 4-13** Nucleation onset detection during the rapid cooling experiment (supercooling temperature = **28.5°C**) using different techniques. The saturated temperature is **30°C**.



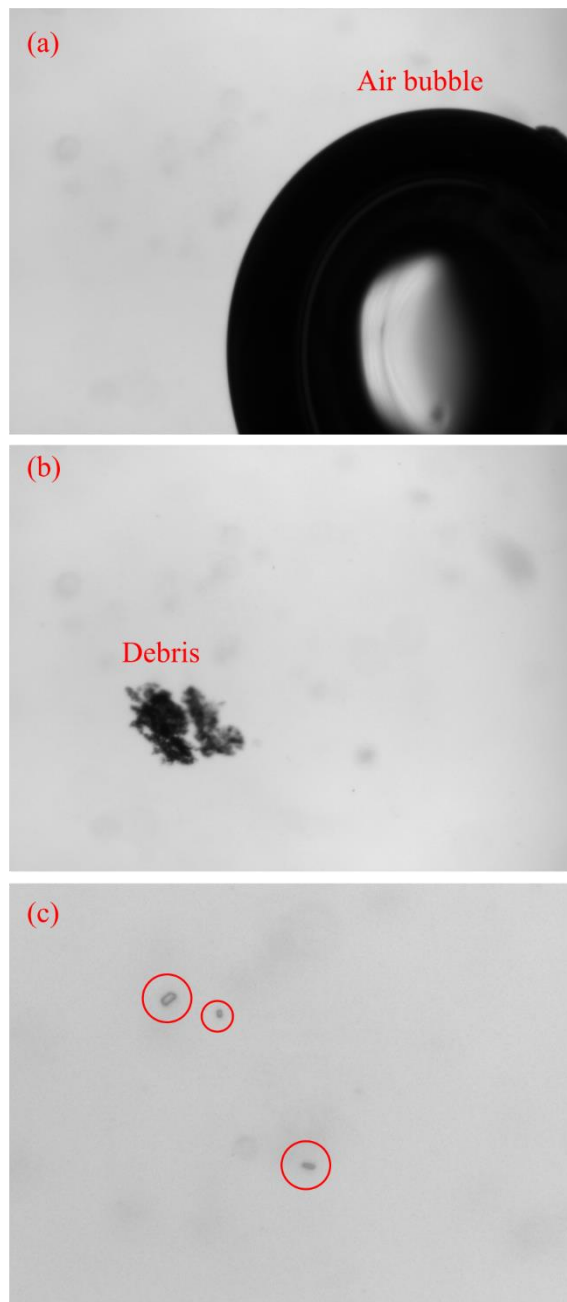


**Figure 4-14** Undesired objects (a, b) that may cause false detection of nucleation and the true nucleation onset (c) with crystals detected in the consecutive images.

**Table 4-1** The 95% confidence of the interval metastable zone width (MSZW) of the aqueous taurine solution measured using FBRM and image analysis.

Saturated temperature (°C)	Linear cooling rate (°C/min)	MSZW by image analysis (°C)	MSZW by FBRM (°C)
30	0.1	27.57 ± 0.23	27.15 ± 0.14
	0.2	27.03 ± 0.12	26.8 ± 0.23
	0.5	26.53 ± 0.11	25.98 ± 0.26
	1.0	25.94 ± 0.20	25.26 ± 0.25
40	0.1	38.86 ± 0.31	39.0 ± 0.29
	0.5	37.67 ± 0.23	37.13 ± 0.81
	1.0	37.1 ± 0.35	36.5 ± 0.40

**Table 4-2** The 95% confidence interval of the induction time of aqueous taurine solution measured using FBRM and image analysis.

Saturated temperature (°C)	Supercooling temperature (°C)	Induction time by image analysis (s)	Induction time by FBRM (s)
30	< 27	Nucleation detected during cooling	
	27	95.3 ± 5.1	157 ± 29.5
	27.5	374.3 ± 24.2	400 ± 20
	28	493.7 ± 8.3	540 ± 5.6
	28.5	1146 ± 64.6	1080 ± 116.3
	> 29	Timeout (> 3000)	
40	< 38.5	Nucleation detected during cooling	
	38.5	177 ± 11.1	215.7 ± 19.6
	39	298.6 ± 69.7	316.7 ± 54.3
	39.5	809.7 ± 30.1	897.7 ± 79.0
	> 39.5	Timeout (> 3000)	

## 4.6. Conclusion

The significance and design of the automated crystallization platform are discussed in this chapter. We discussed the feasibility to build or customize the automated laboratory instruments in a cost-effective fashion with the IoT microcontroller, ESP8266, and 3D-printing techniques. The proposed experimental procedures can achieve automated measurement of the metastable zone width (MSZW) and the induction time. Between the cycles of the automated experiments, the material addition must be performed manually to change the saturation concentration. It is recommended to develop an automated solid addition device to fully automate the experiments and enable more potential applications such as investigating the seeding and feedback control strategies.

## 4.7. References

- Bard, J., Ercolani, K., Svenson, K., Olland, A. & Somers, W. (2004). Automated systems for protein crystallization. *Methods*, 34(3), 329–347. <https://doi.org/10.1016/j.ymeth.2004.03.0297>
- Bysouth, S. R., Bis, J. A. & Igo, D. (2011). Cocrystallization via planetary milling: Enhancing throughput of solid-state screening methods. *International Journal of Pharmaceutics*, 411(1–2), 169–171. <https://doi.org/10.1016/j.ijpharm.2011.03.037>
- Chayen, N. E., Shaw Stewart, P. D. & Baldock, P. (1994). New developments of the IMPAX small-volume automated crystallization system. *Acta Crystallographica Section D Biological Crystallography*, 50(4), 456–458. <https://doi.org/10.1107/s0907444993013320>
- Coliaie, P., Kelkar, M. S., Nere, N. K. & Singh, M. R. (2019). Continuous-flow, well-mixed, microfluidic crystallization device for screening of polymorphs, morphology, and crystallization kinetics at controlled supersaturation. *Lab on a Chip*, 19(14), 2373–2382. <https://doi.org/10.1039/c9lc00343f>
- Ding, L. & Goshtasby, A. (2000). Computer Science and Engineering Department Wright State University. *Pattern Recognition*, 34(34), 721–725.
- Duros, V., Grizou, J., Xuan, W., Hosni, Z., Long, D. L., Miras, H. N. & Cronin, L. (2017). Human versus Robots in the Discovery and Crystallization of Gigantic Polyoxometalates. *Angewandte Chemie - International Edition*, 56(36), 10815–10820. <https://doi.org/10.1002/anie.201705721>
- Fang, C., Tang, W., Wu, S., Wang, J., Gao, Z. & Gong, J. (2020). Ultrasound-assisted intensified crystallization of L-glutamic acid: Crystal nucleation and polymorph transformation. *Ultrasonics Sonochemistry*, 68(November 2019), 105227. <https://doi.org/10.1016/j.ultsonch.2020.105227>
- Florence, A. J., Johnston, A., Fernandes, P., Shankland, N. & Shankland, K. (2006). An automated platform for parallel crystallization of small organic molecules. *Journal of Applied Crystallography*, 39(6), 922–924. <https://doi.org/10.1107/S0021889806040921>
- Gao, Z., Zhu, D., Wu, Y., Rohani, S., Gong, J. & Wang, J. (2017). Motion-based multiple object tracking of ultrasonic-induced nucleation: A case study of L-glutamic acid. *Crystal Growth and Design*, 17(10), 5007–5011. <https://doi.org/10.1021/acs.cgd.7b00730>
- García-Ruiz, J. M. (2003). Nucleation of protein crystals. *Journal of Structural Biology*, 142(1), 22–31. [https://doi.org/10.1016/S1047-8477\(03\)00035-2](https://doi.org/10.1016/S1047-8477(03)00035-2)
- Grön, H., Borissova, A. & Roberts, K. J. K. (2003). In-process ATR-FTIR spectroscopy for closed-loop supersaturation control of a batch crystallizer producing monosodium glutamate crystals of defined size. *Industrial and Engineering Chemistry Research*, 42(1), 198–206. <https://doi.org/10.1021/ie020346d>

- Haer, M., Strahlendorf, K., Payne, J., Jung, R., Xiao, E., Mirabel, C., ... Kirkitadze, M. (2021). PAT solutions to monitor adsorption of Tetanus Toxoid with aluminum adjuvants. *Journal of Pharmaceutical and Biomedical Analysis*, 198, 114013. <https://doi.org/10.1016/j.jpba.2021.114013>
- Hansen, T. B., Simone, E., Nagy, Z. & Qu, H. (2017). Process Analytical Tools to Control Polymorphism and Particle Size in Batch Crystallization Processes. *Organic Process Research and Development*, 21(6), 855–865. <https://doi.org/10.1021/acs.oprd.7b00087>
- Hu, Y., Liang, J. K., Myerson, A. S. & Taylor, L. S. (2005). Crystallization monitoring by raman spectroscopy: Simultaneous measurement of desupersaturation profile and polymorphic form in flufenamic acid systems. *Industrial and Engineering Chemistry Research*, 44(5), 1233–1240. <https://doi.org/10.1021/ie049745u>
- Mettler Toledo. (2021). Automated and Safe Synthesis Reactors for Data-Rich Experimentation. Retrieved from [https://www.mt.com/ca/en/home/products/L1\\_AutochemProducts/Chemical-Synthesis-and-Process-Development-Lab-Reactors/Synthesis-Reactor-Systems.html](https://www.mt.com/ca/en/home/products/L1_AutochemProducts/Chemical-Synthesis-and-Process-Development-Lab-Reactors/Synthesis-Reactor-Systems.html)
- Mitchell, N. A., Frawley, P. J. & Ó'Ciardhá, C. T. (2011). Nucleation kinetics of paracetamolethanol solutions from induction time experiments using Lasentec FBRM®. *Journal of Crystal Growth*, 321(1), 91–99. <https://doi.org/10.1016/j.jcrysgr.2011.02.027>
- Myerson, A. S. (2002). *Handbook of industrial crystallization*. Boston: Butterworth-Heinemann. Retrieved from <http://site.ebrary.com/id/10206621>
- Narkhede, N., Shapira, G. & Palino, T. (2017). *Kafka: The Definitive Guide Real-Time Data and Stream Processing at Scale* (1st ed.). O'Reilly Media, Inc.
- Omar, W., Mohnicke, M. & Ulrich, J. (2006). Determination of the solid liquid interfacial energy and thereby the critical nucleus size of paracetamol in different solvents. *Crystal Research and Technology: Journal of Experimental and Industrial Crystallography*, 41(4), 337–343.
- Parsons, A. R., Black, S. N. & Colling, R. (2003). Automated measurement of metastable zones for pharmaceutical compounds. *Chemical Engineering Research and Design*, 81(6), 700–704. <https://doi.org/10.1205/026387603322150552>
- Plotly Technologies Inc. (2015). *Collaborative data science*. Montreal, QC: Plotly Technologies Inc. Retrieved from <https://plot.ly>
- Saleemi, A., Rielly, C. & Nagy, Z. K. (2012). Automated direct nucleation control for in situ dynamic fines removal in batch cooling crystallization. *CrystEngComm*, 14(6), 2196. <https://doi.org/10.1039/c2ce06288g>
- Saxena, M. & Kuchekar, B. S. (2013). Cocrystal formulation, characterization, and evaluation study. In *International Conference on Advanced Nanomaterials & Emerging Engineering Technologies* (pp. 602–606).

<https://doi.org/10.1109/ICANMEET.2013.6609385>

- Selekman, J. A., Roberts, D., Rosso, V., Qiu, J., Nolfo, J., Gao, Q. & Janey, J. (2016). Development of a Highly Automated Workflow for Investigating Polymorphism and Assessing Risk of Forming Undesired Crystal Forms within a Crystallization Design Space. *Organic Process Research and Development*, 20(1), 70–75.  
<https://doi.org/10.1021/acs.oprd.5b00346>
- Teychené, S., Sicre, N. & Biscans, B. (2010). Is spherical crystallization without additives possible? *Chemical Engineering Research and Design*, 88(12), 1631–1638.  
<https://doi.org/10.1016/j.cherd.2010.02.015>
- Verma, V., Bannigan, P., Lusi, M., Crowley, C. M., Hudson, S., Hodnett, B. K. & Davern, P. (2018). The heterogeneous crystallization of a novel solvate of clozapine base in the presence of excipients. *CrystEngComm*, 20(31), 4370–4382.  
<https://doi.org/10.1039/c8ce00663f>
- Wang, X. Z., Calderon De Anda, J. & Roberts, K. J. (2007). Real-time measurement of the growth rates of individual crystal facets using imaging and image analysis: A feasibility study on needle-shaped crystals of L-glutamic acid. *Chemical Engineering Research and Design*, 85(7 A), 921–927.  
<https://doi.org/10.1205/cherd06203>
- Wood, A. (2016). *Rabbit MQ: For Starters*. North Charleston, SC, USA: CreateSpace Independent Publishing Platform.
- Wood, W. M. L. (1997). Crystal science techniques in the manufacture of chiral compounds. *Chirality in Industry*, Chapter--7.
- Yang, Y., Song, L., Zhang, Y. & Nagy, Z. K. (2016). Application of wet milling-based automated direct nucleation control in continuous cooling crystallization processes. *Industrial and Engineering Chemistry Research*, 55(17), 4987–4996.  
<https://doi.org/10.1021/acs.iecr.5b04956>
- Zhou, G., Moment, A., Cuff, J., Schafer, W., Orella, C., Sirota, E., ... Welch, C. (2015). Process development and control with recent new FBRM, PVM, and IR. *Organic Process Research and Development*, 19(1), 227–235.  
<https://doi.org/10.1021/op5000978>
- Zhou, G., Moment, A., Yaung, S., Cote, A. & Hu, T. E. (2013). Evolution and application of an automated platform for the development of crystallization processes. *Organic Process Research and Development*, 17(10), 1320–1329.  
<https://doi.org/10.1021/op400187h>

## **Chapter 5**

### **A New Highly Efficient and Stable Population Array (PA) Algorithm to Solve Multi-Dimension Population Balance Equation in the Presence of Agglomeration and Breakage**

A version of this chapter will be submitted to *AIChE Journal* under the title: A New Highly Efficient and Stable Population Array (PA) Algorithm to Solve Multi-Dimension Population Balance Equation in the Presence of Agglomeration and Breakage

## **Chapter 5** A New Highly Efficient and Stable Population Array (PA) Algorithm to Solve Multi-Dimension Population Balance Equation in the Presence of Agglomeration and Breakage

### **Abstract**

Solving the population balance equation (PBE) that describes the dynamics behavior of a crystallization process requires a robust and computational-efficient numerical solver. The widely used discretization methods are prone to the numerical diffusion that causes over-prediction of the crystal size, and the multi-dimensional solution is highly inefficient due to the ineffective computations performed on the unused grids. We present a highly efficient numerical solver for the PBE model using the population array (PA) method, which employs an array to store the size and counts information as a sparse grid. The two-dimensional pure-growth case could achieve approximately ten times speedup compared to the high-resolution discretization method since the PA method maintains the high efficiency by avoiding the computation on the unused grids. The numerical difficulties associated with the discretization methods were avoided using the method of characteristics, which also allows approximately five times larger simulation time steps without compromising the stability and accuracy of the solution. A row compression algorithm is proposed to facilitate the PA method to reduce the computational cost by grouping the crystals with similar internal coordinates. Various numerical cases including crystal growth, continuous crystallization, polymorphic transformation, agglomeration, and breakage were simulated and compared with the analytical solutions and the established high-resolution discretization schemes to confirm the accuracy and computational efficiency of the proposed PA algorithm. The superior efficiency of our proposed PA algorithm in handling multi-dimensional PBE makes it a promising technique to utilize the multi-dimensional crystal size measurement obtained using an image-based PAT instrument.

**Keywords:** Crystallization modeling; Multi-dimensional population balance equation; Numerical solution; Agglomeration and breakage modeling



## 5.1. Introduction

Crystallization modeling is an essential tool for design and to investigate the impact of the operating conditions on the system states and crystalline product properties. In the past, due to the difficulty of in-situ solid phase characterization, the model parameters were estimated with the offline size measurement of the final product and the concentration and temperature profiles (Hu, Rohani & Jutan, 2005; Lin, Wu & Rohani, 2019; Qiu & Rasmuson, 1990). Simplified crystallization models without accounting for agglomeration, breakage, and crystal morphology were generally sufficient to match the de-supersaturation curve. The recent improvement of the process analytical technologies (PATs) enables robust real-time monitoring of multi-dimensional crystal size distribution (CSD) and polymorphism with image analysis and spectroscopy, which motivates the development of more general and descriptive crystallization models (Chen et al., 2019; Gao et al., 2018; Lin, Wu & Rohani, 2020b). The population balance equation (PBE) is an established technique to describe the change of crystal size distribution (CSD) caused by various mechanisms such as growth, dissolution, nucleation, agglomeration, and breakage of particles. Eq. 5-1 depicts a general form of the PBE for a well-stirred batch or continuous crystallization system. The model is a partial differential equation (PDE) expressed in terms of the number density of the CSD,  $n$ , with respect to time,  $t$ , and internal coordinates of each dimension (often referred to as the characteristic size),  $L_i$  (Myerson, 2002).

$$\frac{\partial n}{\partial t} + \underbrace{\sum_i \frac{\partial(G_i \cdot n)}{\partial L_i}}_{\text{growth, dissolution}} + \underbrace{\frac{n - n_{in}}{\tau}}_{\text{continuous}} = \underbrace{B - D}_{\substack{\text{agglomeration,} \\ \text{breakage, nucleation}}} \quad (5-1)$$

The second term in Eq. 5-1 describes the propagation of the CSD caused by crystal growth or dissolution, where  $G_i$  is the growth/dissolution rate of the  $i$ -th dimension. The last term on the left-hand side is related to the continuous operation and will diminish in a batch-mode system. The birth and death rates,  $B$  and  $D$ , are the net effects of agglomeration, breakage, and nucleation. Because the breakage and agglomeration terms

involve integral of the CSD, Eq. 5-1 is typically an integrodifferential equation (Gunawan, Fusman & Braatz, 2004). Due to the hyperbolic nature of the growth/dissolution term and the non-linearity from the kinetics and the coupled solute mass balance equation (MBE), analytical solution of a PBE model is not possible except for a few simplified cases (Gunawan, Fusman & Braatz, 2004; Sanjeev, 1996). Thus, numerical solution techniques have to be employed to solve the coupled PBE and MBE problems.

The numerical methods are categorized into three classes: moment method, Monte Carlo method, and discretization method (grid method) (Omar & Rohani, 2017). The moment method involves converting the PBE into a set of ordinary differential equations (ODEs) in terms of the moments, which can be integrated numerically. For a one-dimensional CSD, the  $k$ -th moment,  $M_k$ , is defined in Eq. 5-2.

$$M_k = \int_0^{\infty} n L^k dL \quad (5-2)$$

Specific moments can be interpreted with physical meanings. For example,  $M_0$ ,  $M_3$ ,  $M_4/M_3$  are related to the particle count, volume, and volume-weighted mean size, respectively. Tracking only specific moments instead of the full CSD decreases the computational efforts. However, the moment method is unrealizable if a moment in the set of ODEs depends on a higher-order moment, namely the unclosed moment problem. The moment approximation technique must be chosen to guarantee the moment closure for various complicated kinetics such as size-dependent growth and breakage (Szilágyi, Agachi & Lakatos, 2015; Yuan, Laurent & Fox, 2012). Also, inverting the moment to recover the CSD is not trivial and is still an open area of research (Omar & Rohani, 2017). When the full CSD information or complex kinetics is required, the more general discretization method is preferred.

In the Monte Carlo (MC) method, a large population of crystals is presented by a small sample (often in the order of  $10^7$ ). The simulation tracks the evolving properties of the

sample by randomly triggering the kinetic events such as growth, nucleation, and agglomeration for the crystals (Van Peborgh Gooch & Hounslow, 1996; Yu, Hounslow & Reynolds, 2015). The implementation of the MC method is straightforward by simply adding, removing, or updating the particles even in the presence of complex kinetics. Also, the MC method can efficiently handle multidimensional problems (Rosner, McGraw & Tandon, 2003). The drawback of this method is the high computational cost for simulating a large sample of the population, especially when the particle interaction via agglomeration and breakage is involved. Also, the statistical noise due to the stochastic simulation requires several repetitions to smoothen the solution (Hao et al., 2013).

The discretization method breaks up the continuous internal coordinates into a grid with a finite number of bins that represent the particle count in the given size range. The derivatives in the growth term of PBE and the integral operations in the agglomeration and breakage could be replaced with the discretized arithmetic operations so that the time-derivative of each bin could be computed and integrated. Refining the grid can improve the resolution of the solution and minimize the discretization error at the cost of increased computational complexity. Due to the constraint of the time step size for numerical convergence, known as the Courant-Friedrichs-Levy (CFL) condition (Gunawan, Fusman & Braatz, 2004), linearly increasing the resolution of the grid can result in the quadratic expansion of the computational cost. Also, the refinement of the grid cannot resolve the numerical diffusion (smeared solution) and numerical dispersion (non-physical oscillation) where the local gradient of the CSD is large (Gunawan, Fusman & Braatz 2004). The high resolution (HR) finite volume discretization scheme proposed in (Gunawan, Fusman & Braatz, 2004) could provide high accuracy while avoiding both numerical diffusion and dispersion associated with other finite difference and finite volume schemes, which shows increasing popularity in recent works (Lin, Wu & Rohani, 2020a; Shu et al., 2020; Szilágyi & Nagy, 2016).

Despite the improvement of the discretization algorithm, the use of the fixed grid has computation efficiency problems. The upper limit of the grid must be sufficiently large such that no crystal would grow or agglomerate to the size beyond the scope of the grid, leading to the wasted computation on the grid points without any data. Also, the multi-dimensional grid for solving a multi-dimensional PDE will result in a polynomial scale-up of the computational cost (Szilagyi et al., 2017). The former problem can be addressed with the moving-pivot technique, which uses the method of characteristics to move the bin boundaries and the pivots (the characteristic size of the bin) according to the local growth rate and allocate new bins for nucleation (Kumar & Ramkrishna, 1997). This method eliminates the numerical diffusion due to the growth term. A general PBE with breakage and agglomeration can be solved with this method. It is also very efficient due to the on-demand creation of new bins instead of using a full grid and the ability to convert the fine grid into a coarse grid to reduce the computational scale while maintaining accuracy. Nevertheless, there are a few challenges with this method. For continuous crystallization, it is difficult to merge the different size grids of each stage. The multi-dimensional moving-pivot technique is rarely studied except by Borchert (2012), who used circular cells as the moving grids to solve a 2D PBE.

In this work, we propose a simple numerical approach to model the crystallization process based on the concept of the moving-pivot technique. Instead of tracking the pivots and the boundaries, we found that tracking only the pivots as a series of discrete Dirac pulse enables simple but powerful implementation that can handle multi-dimensional PBE for both batch and continuous operation and complex kinetics including agglomeration and breakage. The pivots in the vicinity can be efficiently binned to reduce the computational cost in a manner that conserves the crystal count and volume. The Python code was accelerated and optimized with the Numba package that compiles the program into efficient native code (Lam, Pitrou & Seibert, 2015). The efficiency and accuracy of the method were validated against the conventional discretization methods and analytical solutions.

## 5.2. Proposed Method

In the proposed method, the crystal population of each polymorph is represented in a population array (Figure 5-1) similar to the Monte Carlo method (Van Peborgh Gooch & Hounslow, 1996). Each row stands for  $N$  crystals sharing the similar characteristic internal coordinates,  $\mathbf{L}$ . Various kinetics were simulated by updating, appending, or removing the rows in this population array. The population array allows duplicated rows of internal coordinates generated from the continuous input, breakage, or agglomeration, so the grid boundaries cannot be implicitly inferred from the population table. Therefore, each row is considered as a discrete Dirac pulse sampled from the number density CSD (Eq. 5-4).

$$N_i = \int n(\mathbf{L})\delta(\mathbf{L} - \mathbf{L}_i)d\mathbf{L} \quad (5-3)$$

With this representation, the total crystal count density (per volume of the crystallizer),  $N_T$ , and volume fraction,  $v_f$ , can be determined from the population array using Eqs. 5-4 and 5-5, where  $k_s$  is the shape factor, and  $w$  is the power of each internal coordinate. For example,  $w_1 = 3$  is the common case for one-dimensional case. For multi-dimensional case, the powers of the dimensions depend on the perspective of the measurement.

$$N_T = \sum_r^R N_r \quad (5-4)$$

$$v_f = k_s \sum_r^R L_{1,r}^{w_1} L_{2,r}^{w_2} \cdots L_{D,r}^{w_D} \quad (5-5)$$

Figure 5-1 depicts the flow diagram of the proposed method. The population balance was solved iteratively after initialized with the initial condition. First, the operating conditions such as the temperature profile are applied. The nucleation and growth or dissolution kinetics are computed with the supersaturation (Eq. 5-6), where  $c^*$  is the solubility of the

form. The growth or dissolution rate can be used to adaptively decide the time step,  $\Delta t$ . Next, the  $B$  and  $D$  are computed from the agglomeration and breakage kinetics. The time step determined from the previous step should be scaled down if any count is negative after applying the death term. After the system is updated with breakage, agglomeration, and continuous inflow of the seeded charge, the population array will contain a lot of rows with duplicating or similar sizes, which will significantly slow down the next simulation step. The row compression algorithm is therefore used to represent the population array with minimum equivalent rows that have the conserved crystal counts and volumes. If the system is polymorphic, the above operations are repeated for each form. Finally, the population array of each form is used to compute the mass difference than the previous step to update the concentration.

$$\sigma = \frac{c}{c^*} - 1 \quad (5-6)$$

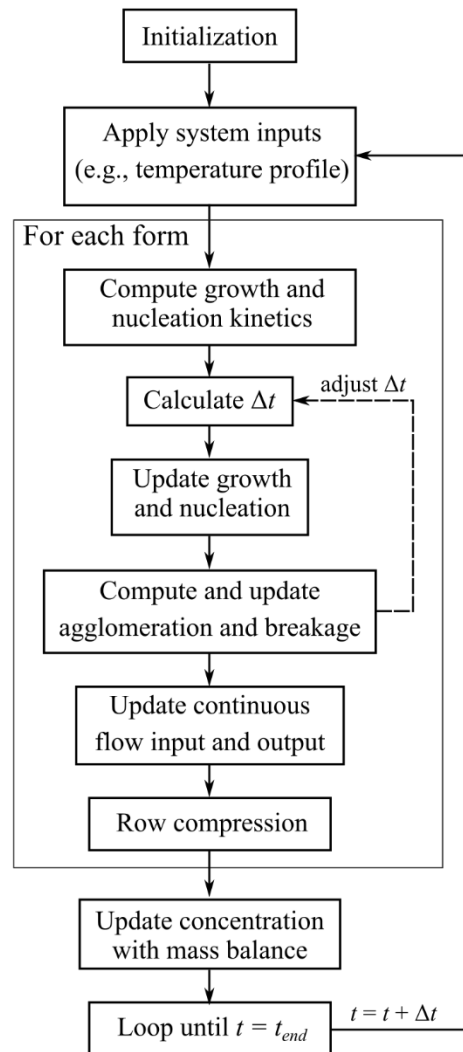
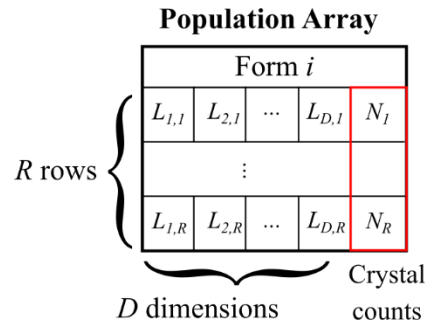


**Figure 5-1** Flow diagram of simulating a crystallization process with the proposed method.

### 5.2.1. Nucleation and Growth Modeling

The nucleation and growth processes are modeled with the method of characteristics. When the relative supersaturation,  $\sigma$  (Eq. 5-6) is positive, the primary and secondary nucleation rates are calculated from Eqs. 5-7 and 5-8 (Omar & Rohani, 2017).

$$B_{pn} = k_{pn}\sigma^{\alpha_{pn}}, \quad \sigma > 0 \quad (5-7)$$

$$B_{sn} = k_{sn}\sigma^{\alpha_{sn}}\nu_f^{\beta_{sn}}, \quad \sigma > 0 \quad (5-8)$$

$$N_0 = (B_{sn} + B_{pn})\Delta t \quad (5-9)$$

The nuclei are recorded by appending a new row to the population array with  $N_0$  from Eq. 5-9 and  $\mathbf{L}$  set to the nuclei size, which can be zeros or the detection limit of the instrument. The growth rate of  $i$ -th internal coordinate is computed with Eq. 5-10, where  $\beta$  and  $\gamma$  are the size-dependent parameters. The vector  $\mathbf{L}$  of each row is updated with Eq. 5-11 to represent the enlargement of crystals due to growth. During dissolution, the nucleation step is skipped, and any row with non-positive  $\mathbf{L}$  after being updated with Eq. 5-11 is removed from the population array. This method is efficient for multi-dimensional growth and dissolution as adding a new dimension only requires updating one extra column of the internal coordinates.

$$G_i = \begin{cases} k_g\sigma^{\alpha_g}(1 + \beta_g)L_i^{\gamma_g}, & \sigma > 0 \\ 0, & \sigma = 0 \\ k_d\sigma^{\alpha_d}(1 + \beta_d)L_i^{\gamma_d}, & \sigma < 0 \end{cases} \quad (5-10)$$

$$\mathbf{L} = \mathbf{L} + \mathbf{G}\Delta t \quad (5-11)$$



### 5.2.2. Agglomeration Modelling

Agglomeration refers to the generation of a larger composite crystal by attachment of two or several crystals, often as a result of the formation of a solid bridge between them. During the agglomeration event, the total particle volume remains constant while the crystal number changes. The birth and death terms, due to agglomeration, are used to quantify the rate of generating new particles and the consumption of the existing particles. In this work, only binary agglomeration is considered.

For one-dimensional agglomeration, every binary inclusive combination of two crystals is involved in generating a new particle. i.e., all rows in the population array belong to only one domain  $\Omega$ . The death rate of the crystal represented by the  $r$ -th row is calculated from Eq. 5-12, where  $\alpha$  is the agglomeration kernel function measuring the size-dependent aggregation frequency of two crystals. The commonly used agglomeration kernel is reviewed in (Omar & Rohani, 2017). The birth rate is computed by enumerating all combinations of two rows in the population array with Eq. 5-13. The size of the new particle is calculated using the volume-weighted average of the parent crystals so that the volume is conserved during agglomeration. The same goal is achieved in the fixed-grid method by converting the grid to volumetric coordination. It is worth noting that the shape is assumed unchanged during agglomeration. i.e., two spherical particles will generate a new spherical particle with the summed volume.

$$D_{aggl}(r) = \sum_{r_1} \alpha(\mathbf{L}_r, \mathbf{L}_{r_1}) N_r N_{r_1} \Big|_{r, r_1 \in \Omega_i} \quad (5-12)$$

$$B_{aggl} = \sum_{r_1} \sum_{r_2} \alpha(\mathbf{L}_{r_1}, \mathbf{L}_{r_2}) N_{r_1} N_{r_2} \Big|_{r_1, r_2 \in \Omega_i} \quad (5-13)$$

The multi-dimensional agglomeration is illustrated in Figure 5-2. Following the work done by Shu et al. (2020), it is assumed that the agglomeration involves the shapes change in only one internal coordinate; i.e., the two involved particles are different in only one internal coordinate (Figure 5-2.b). This assumption ensures the unchanged

shape of the generated crystal, which can be correctly represented by the same set of internal coordinates. The topic of agglomeration of arbitrary crystals is studied by Amrei and Dehkordi (2013) and is out of the scope of this work. Since the population array only stores the information of the pivots, a uniform grid is used to partition the points in the population array into multiple domains. As depicted in Figure 5-2.a, for an arbitrary crystal represented by the row  $r_a$  belonging to the domains  $\Omega_1$  and  $\Omega_2$ , the death and birth terms are calculated with the binary combination of  $r_a$  and any other particle in these domains. Since the non-agglomerating dimensions of the agglomerating particles are not guaranteed to be equal, the mean values are used as the non-agglomerating dimension of the agglomerate. With the summed volume and all other dimensions determined, the agglomerating dimension could be determined with Eq. 5-5. Each domain should only be computed once to prevent duplication. In every stimulation step, the volume of the largest crystal is doubled by agglomerating with itself, resulting in extremely large agglomerates with a negligible count. This can be resolved with a minimum count threshold that excludes the rows with a negligible count from the agglomeration. Compared to the previous work (Shu et al., 2020), our method does not require the iterative search to find the internal coordinates of the generated crystals, and the volume after agglomeration is conserved.

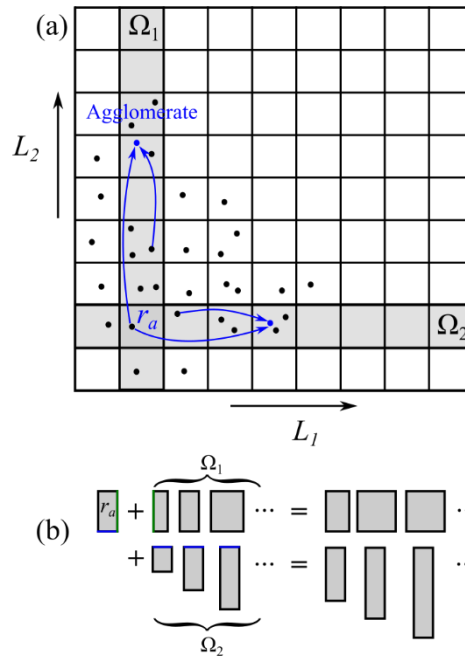


**Figure 5-2** Illustration of two-dimensional agglomeration along the internal coordinates. (a) the grid representation of agglomeration. Each scattering point represents the location of a row in the population array.  $\Omega_1$  and  $\Omega_2$  are the agglomeration domain of the crystal represented by the row  $r_a$ . (b) the visualization of the agglomeration along the two internal coordinates. Note that the agglomerate dimensions are not the summation of the agglomerating dimensions but calculated from the conserved volume.

### 5.2.3. Breakage Modeling

Breakage is the generation of fragments from the existing crystals. Like the agglomeration events, the total crystal volume is conserved while the total crystal count increases. In this work, we only consider the binary breakage where one parent crystal breaks into two complementary daughter crystals.

For one-dimensional breakage, every particle represented by the rows in the population array breaks into pieces symmetrically distributed about the half volume (Figure 5-3.a),

since the probabilities of generating the crystal of volume  $V_p$  and the complementary crystal of volume  $V - V_p$  are the same. The death rate of the existing parent crystal is computed with Eq. 5-14, where  $\beta_i$  is the breakage kernel function measuring the size-dependent breakage frequency along the  $i$ -th breakage dimension. Various breakage kernels are summarized by Omar and Rohani (2017). The birth rate of the new fragments generated by the parent crystal of  $r$ -th row is expressed in Eq. 5-15, where  $P_i$  is the probability of generating the fragment of the internal coordinate  $\mathbf{L}$  along  $i$ -th dimension. The previous study suggests the use of a uniform or parabolic probability distribution of  $P_i$  (Figure 5-3.a) (Bao et al., 2006). For the constant probability distribution,  $P_i = 2/V_p$ , where  $V_p$  is the volume of the breaking parent crystal. The volumes of the daughter particles are converted to its characteristic length using Eq. 5-5 and stored in the population array as new rows.

For multi-dimensional breakage, it is also assumed the breakage event involves the shapes change in only one internal coordinate, which can be represented by the arbitrary cuts along different sides (Figure 5-3.b). Note that due to the different powers ( $w$  in Eq. 5-5) of each internal coordinate in crystal volume calculation, the size of each fragment does not equal the position of the cut. For example, the three-dimensional illustration in Figure 5-3.b can be mapped into the two-dimensional case by projecting from either  $L_2$ - or  $L_3$ - direction. For a needle-like or rod-like crystal, using the representation of projecting from the  $L_3$ -direction is preferred since the internal coordinates matches the size measurement of major and minor dimensions from imaging analysis. By assuming the hidden dimension is the same as the minor dimension ( $L_1$ ), the power of  $L_1$ - and  $L_2$ - dimensions are 2 and 1, respectively. In this case, if evenly cutting along  $L_1$ , the daughter crystals will have the breaking dimension of  $L_1/\sqrt{2}$  instead of  $L_1/2$  so that the volume is conserved after breakage. The death rates of the existing crystals are the summation of the death rate in each internal coordinate (Eq. 5-14). For the daughter crystals, the internal coordinates are determined with a uniform volume grid along the breaking dimension (Figure 5-3.c). The volumes are converted to the length by fixing the non-

breaking dimensions. The birth rates of the daughter crystals are calculated from Eq. 5-15 by using the grid interval  $\Delta V_i$ , and probability distribution,  $P_i$  obtained with the volume grid. The interval of the volume grid can be adjusted based on the internal coordinates to balance the resolution of breaking a large crystal and the efficiency of breaking a small crystal.

$$D_{brk}(r) = \sum_i \beta_i(\mathbf{L}_r) N_r \quad (5-14)$$

$$B_{brk}(r) = \sum_i \beta_i(\mathbf{L}_r) N_r P_i(\mathbf{L}) \Delta V_i \quad (5-15)$$

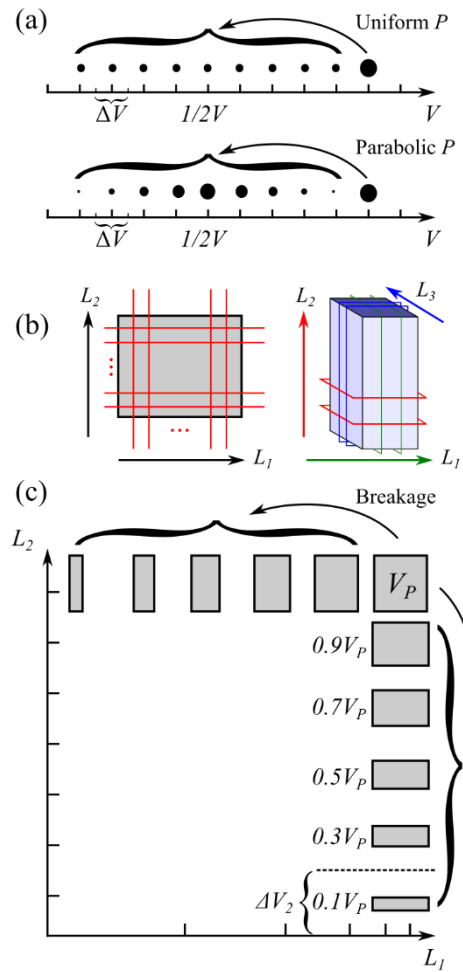


**Figure 5-3** (a) Illustration of one-dimensional breakage on a volume grid for uniform and parabolic probability distributions. The size of the points represents the relative count of the daughter crystals; (b) demonstration of two-dimensional and three-dimensional breakage by cuts along the breakage dimensions; (c) visualization of two-dimensional breakage. Note that the grid is not linear if the volume power of the breaking dimension is not one.

#### 5.2.4. Continuous Operation

For a mixed-suspension mixed-product-removal (MSMPR) continuous crystallizer with a residence time of  $\tau$ , the death rate of the existing crystals due to continuous material removal can be characterized by Eq. 5-16. The population array of the slurry inlet is copied and appended to the population array of the current stage. The counts of the inlet crystals are computed with the time step times the birth rate in Eq. 5-17. For multi-stage crystallizer, the population array of the subsequent stages will inflate much faster than the first stage because of the accumulated rows from the previous stages. The row compression algorithm discussed shortly will reduce the rows and prevent significant slow-down during the multi-stage simulation.

$$D_{r,cont} = \frac{N_r}{\tau} \quad (5-16)$$

$$B_{cont} = \frac{N_{in}}{\tau} \quad (5-17)$$

#### 5.2.5. Row Compression

The number of rows in the population array increases over the simulation steps. Every nucleation step will add one new row to the population array, which is usually not a problem even for a long-running simulation. Nevertheless, the breakage and agglomeration event will introduce a large number of new crystals. For example, one-dimensional agglomeration of  $K$  crystals will produce  $K^2/2$  agglomerates. For multi-stage continuous crystallization, the stream from the previous stage will copy the same number of rows to the current stage. The computation cost on the inflating population array will increase exponentially, making the following simulation step much slower than the previous one.

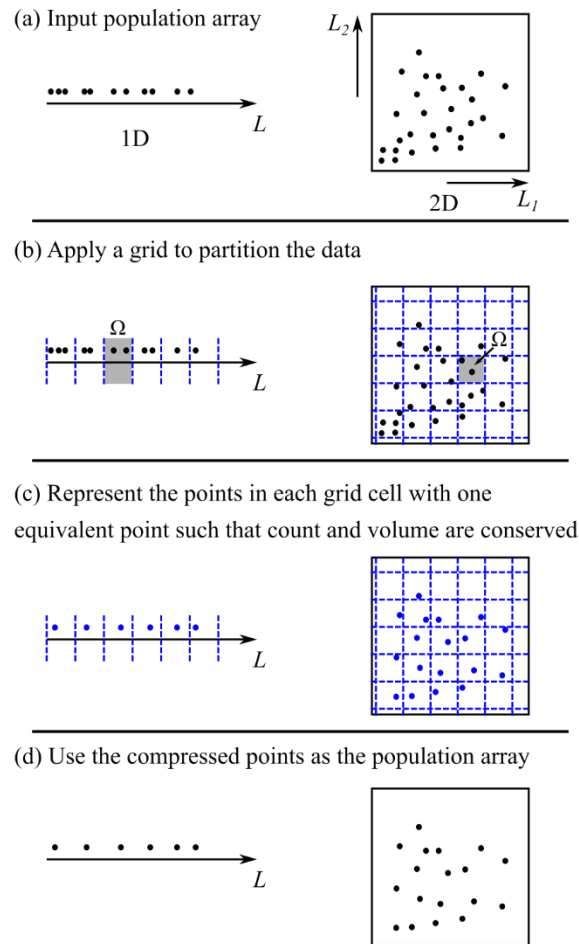


**Figure 5-4** Illustration of row compression procedures of a one-dimensional and a two-dimensional population array.

In the grid-based method, this problem does not exist since the grid automatically bins the crystals to their assigned intervals. Hence generating new crystals only affects the count data stored on each grid. The pivot (characteristic internal coordinates of a grid cell) will also move to ensure both total volume and counts are conserved (Kumar & Ramkrishna, 1996; Sanjeev, 1996). We use the concept of grid to compress the population array into the equivalent pivots by grouping the points in the vicinity. Figure 5-4 depicts the procedures of the row compression algorithm. First, a grid covering the full span of the data in the population array is generated to partition the points. The linear or logarithmic scales and intervals can be decided based on the range of the internal



coordination and the application. Then, the points in each grid cell are replaced with one pivot point, whose count is the summation of the counts (last column in the population array) of the points (Eq. 5-18). The volume-weighted mean sizes of the crystals are used as the internal coordinates of the pivots for one-dimensional cases (Eq. 5-19). For multi-dimensional cases, one dimension,  $d_c$ , is selected as the compression dimension. The  $i$ -th component of the pivot internal coordinate vector,  $L_{p,i}$ , are computed with Eq. 5-20 by first reducing the non-compression dimensions of the crystals using the count-weighted mean. Then, the compression dimension is computed such that the total crystal volume in the cell  $\Omega$  is conserved.

$$N_p(\Omega) = \sum_{r \in \Omega} N_r \quad (5-18)$$

$$L_p(\Omega) = \sqrt[3]{\frac{\sum_{r \in \Omega} L_r^3 N_r}{N_p(\Omega)}} \quad (5-19)$$

$$L_{p,i}(\Omega) = \begin{cases} \frac{\sum_{r \in \Omega} L_r N_r}{N_p(\Omega)}, & i \neq d_c \\ \frac{v_f(\Omega)}{k_s \prod_{j \neq i} L_{p,j}^{w_j}}, & i = d_c \end{cases} \quad (5-20)$$

The row compression can be applied at the end of every simulation step or when the rows stored in the population array exceeds a threshold. Unlike the fixed-grid method where the grid range is defined manually, the partition grid is generated to fit the range of the existing crystals, so that no redundant grid cells above the largest crystal are considered. The multi-modal CSD can be efficiently stored and computed as the cells without data are discarded so that no data point is assigned to the empty gaps between the modals.

### 5.2.6. Adaptive Time Step Size

Compared to the fixed simulation time step size, adaptively computing the time step based on the current state helps to efficiently allocate more computation resources to where the system states change rapidly. This ensures accuracy and stability. In an explicit fixed-grid method, the stable solution is obtained if the Courant–Friedrichs–Lewy (CFL) criterion in Eq. 5-21 is met, where  $\Delta L_i$  is the grid interval along  $i$ -th internal coordinates (Szilágyi & Nagy, 2016). Due to the use of the method of characteristic, the stability of our method is not limited by the CFL criterion. By defining  $\Delta L_i$  as a tunable parameter, we can use Eq. 5-21 as a reference to scale the time step size based on the current growth or dissolution rate. Another constraint on the time step is determined from the death rate of the existing crystals. For any crystal represented by the  $r$ -th row, the remaining count after subtracting the death term should be positive (Eq. 5-22), which prevents the non-physical negative count in the population array (Van Peborgh Gooch & Hounslow, 1996). If the crystallizer is operated continuously, the time step should not exceed the residence time,  $\tau$ , to prevent the negative count (Eq. 5-16). The minimum of the time steps computed for various internal coordinates and polymorphs is then used as the current time step.

$$CFL = \left| \max \left( G_i \frac{\Delta t}{\Delta L_i} \right) \right| \leq 1 \quad (5-21)$$

$$\Delta t < \frac{N_r}{D_r} \quad (5-22)$$

### 5.2.7. CSD Reconstruction

Reconstructing the CSD from the discrete points stored in the population array can be achieved with a count-weighted histogram like the row compression method. Eq. 5-23 computes the number density at the grid cell,  $\Omega$ , where  $\Delta L_i$  is the grid interval along  $i$ -th

internal coordinates. Unlike the row compression where the objective is to combine the crystals with close internal coordinates, the reconstructed CSD histogram should also provide meaningful interpretation. However, as depicted in Figure 5-5, if the grid interval is not properly chosen, the resulting CSD can be fluctuating and misleading. The fluctuation is attributed to the mismatch between the frequencies of the data points and the grid intervals. For example, when the data is evenly distributed, the proper interval will split the data evenly into each bin, while the over-sampling or under-sampling intervals cause uneven binning of the data, resulting in spikes and valleys. The optimal grid interval can be found by evaluating the average rolling standard deviation of the CSD reconstructed with different intervals, which should be minimized to produce a smooth distribution.

$$n(\Omega) = \frac{N_p(\Omega)}{\prod_i \Delta L_i} \quad (5-23)$$

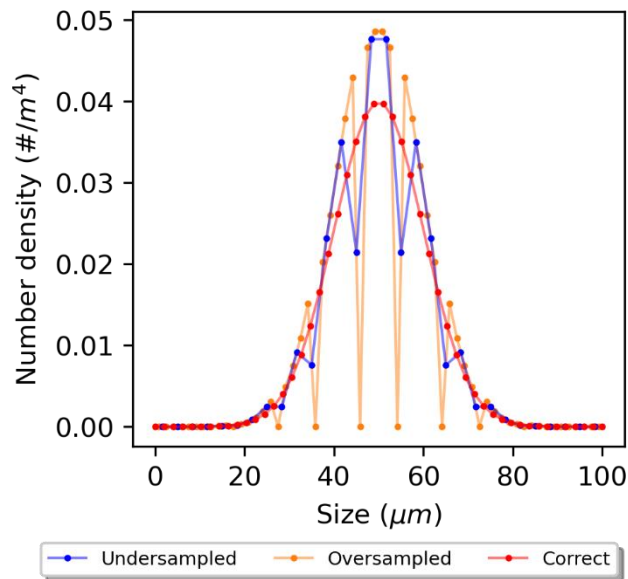


**Figure 5-5** Demonstration of the effect of the grid interval on the reconstructed CSD.

Another approach to reconstruct the smooth CSD from the discrete points is kernel density estimation (KDE), which uses a weighted sum of a known non-negative kernel

density function to represent the CSD (Yuan, Laurent & Fox, 2012). The bandwidth is the tunable parameter that controls the smoothness of the CSD, which can be determined globally or adaptively based on the local structure of the data (Pedretti & Fernández-garcia, 2013). The challenge that often arises in the use of KDE is the boundary bias problem, which predicts unphysical nonzero CSD on the negative internal coordinates and underestimates the density function near the boundary (Sole-mari et al., 2019). These issues have been addressed with various boundary correction techniques (Sole-mari et al., 2019).

### 5.3. Simulation Case Studies

#### 5.3.1. Nucleation and Growth

Pure growth and simplified simultaneous nucleation and growth simulations were performed to demonstrate the accuracy of the proposed population array method in handling the growth term that is challenging in the fixed-grid methods. Figure 5-6.a depicts the one-dimensional growth-only simulation with the initial condition consisting of a rectangle and a smooth normal distribution. The numerical diffusion problems are identified for both fixed-grid methods near the edges of the rectangle where the local gradient is large. Ideally, the size-independent growth will cause the CSD profile to shift along the axis while preserving the shape. However, the first-order accurate upwind (UW) scheme damps the sharp features such as the edges of the rectangle. The high-resolution (HR) method shows improved shape preservation for the smooth normal distribution but the numerical diffusion is still noticeable near the discontinuities (Gunawan, Fusman & Braatz, 2004). Our proposed population array (PA) approach employs the method of characteristics to simulate crystal growth, which moves the internal coordinates of each tracked pivot according to the growth rate. This method not only perfectly matches the analytical solution but also improves the efficiency by dropping the empty grid points and only tracking the data on the initial condition profiles. A similar conclusion can be drawn for the two-dimensional growth-only simulation, where the growth is simulated with a square-patch initial condition that is shifted to

different directions with the same magnitude of growth rate. The contours of the PA method in Figure 5-6.b fit the analytical reference and show no numerical diffusion pattern around the solution. Figure 5-6.c is a simplified case of simultaneous constant nucleation and constant growth where a flipped Heaviside (step) function is the expected solution. This case shows that discontinuities are common during crystal growth simulation and can lead to the over-estimated crystal size. The population array with row compression (PAC) method reduces the increasing computation complexity introduced during the nucleation event. With row compression, the front in the CSD is slightly lower than the analytical solution due to the averaging with the fine nuclei in the same grid cell. The performance gain from row compression is insignificant in this simple case but it is shown that this mechanism can speed up the computation at the cost of negligible accuracy loss. The one-dimensional size-dependent growth on a volumetric coordinate is discussed by Gunawan et al. (2004). For a size-dependent growth rate given by Eq. 5-24 and the initial CSD is given by Eq. 5-25, where the parameter  $G_0 = 0.1 \mu\text{m}^3/\text{s}$ ,  $N_0 = 1$  and  $v_0 = 0.01 \mu\text{m}^3$ , the analytical solution after growing for  $t$  seconds is given by Eq. 5-26 (Ramabhadran, Peterson & Seinfeld, 1976). The simulated results are shown in Figure 5-6.d. While all numerical methods match well with the analytical solution at the large volume range, the fixed-grid methods show a larger deviation at the smaller size. The deviation is explained by the boundary condition at zero volume that is numerically equivalent to a discontinuity, causing the numerical diffusion and large deviation for the fixed-grid method. In this case, the PA method tracks the propagation of the boundary condition much more accurate than the fixed-grid methods.

$$G(v) = G_0 v \quad (5-24)$$

$$n(v, 0) = \frac{N_0}{v_0} e^{-\frac{v}{v_0}} \quad (5-25)$$

$$n(v, t) = \frac{N_0}{v_0} \exp\left(-\frac{v}{v_0} e^{-G_0 t} - G_0 t\right) \quad (5-26)$$

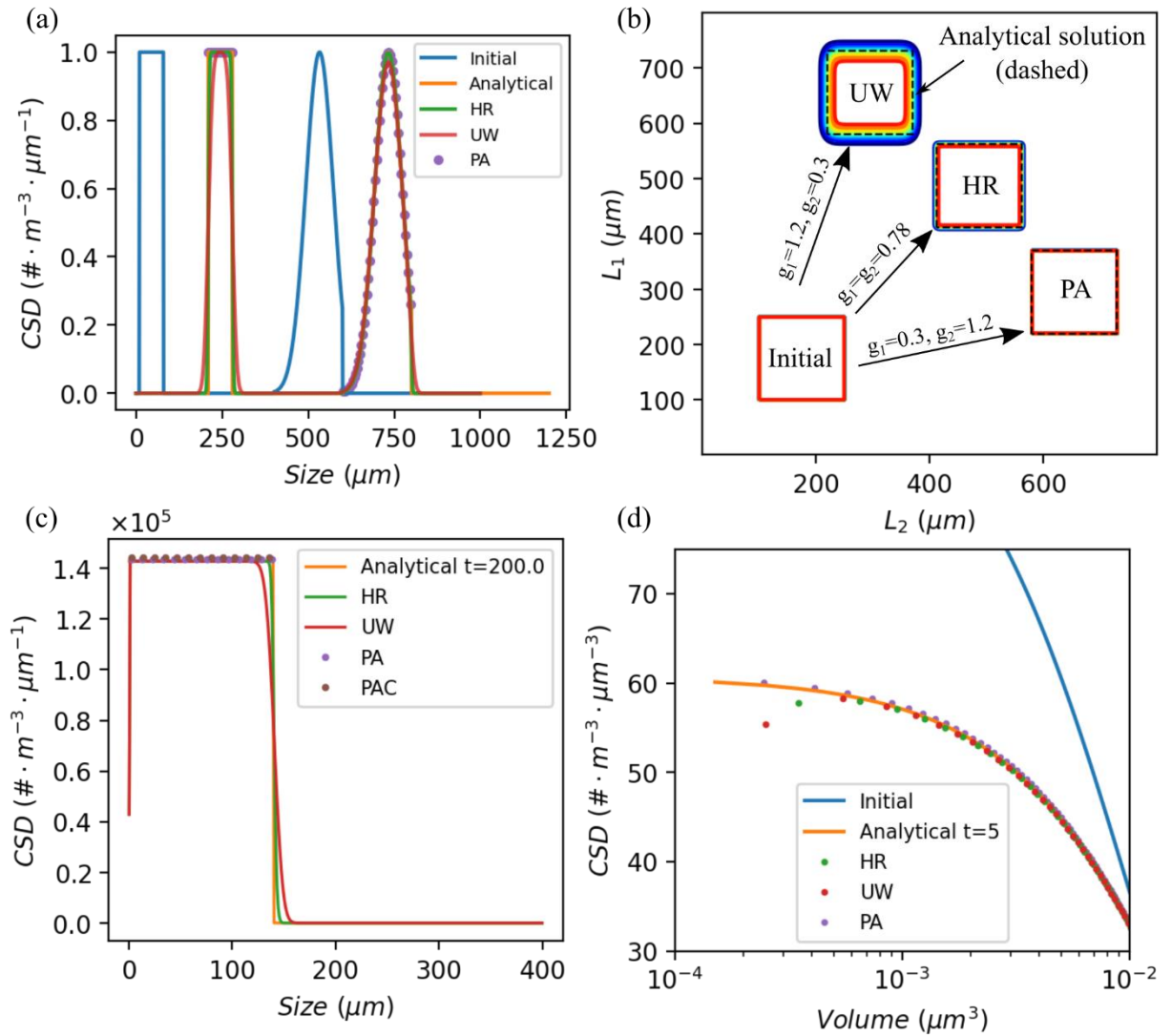


**Figure 5-6** Batch crystallization simulation results obtained with the high-resolution (HR), upwind (UW), and population array (PA) methods compared with the analytical solutions. (a) One-dimensional growth-only simulation ( $G = 0.7 \mu m/s$ ,  $\Delta t = 1 s$ ,  $\Delta L = 1 \mu m$ , and  $t_{end} = 200 s$ ). (b) CSD contours of the two-dimensional growth-only simulation of a step initial condition. (c) Constant nucleation and growth simulation ( $B = 10^5 \# \cdot m^{-3} \cdot s^{-1}$ ,  $G = 0.7 \mu m/s$ ,  $\Delta t = 1 s$ ,  $\Delta L = 1 \mu m$ ). PAC: the rows in the population array are compressed to a grid of  $1 \mu m$  interval at the end of each simulation

step. (d) Size-dependent growth simulation case solved analytically by Ramabhadran et al. (1976).

### 5.3.2. Concentration-dependent Kinetics in Batch and Continuous Crystallization Processes

In the crystallization process, the constant growth and nucleation kinetics do not hold. The growth and nucleation are functions of supersaturation, temperature, and the existing CSD of the current state. The coupled mass balance equation computes the mass difference after nucleation and growth and updates the solute concentration. For a seeded batch crystallization, the secondary nucleation is dominant, which is typically described by a power-law form given in Eq. 5-8. The size-dependent growth rate has a similar power-law expression (Eq. 5-10). In this case study, a seeded batch crystallization process of potassium nitrate ( $\text{KNO}_3$ ) is simulated to validate the performance of the PA method in a realistic context. The initial CSD of seeds is given in Eq. 5-27. The solubility and kinetic parameters of  $\text{KNO}_3$  from literature are given in Eq. 5-28 and Table 5-1 (Miller, 1993). The simulation time step size is determined using the CFL condition (Eq. 5-21).

$$n_{seed}(L) = \begin{cases} -3.48 \times 10^{-4}L^2 + 0.136L - 13.21, & 180.5 \leq L < 210.5 \mu\text{m} \\ 0, & \text{elsewhere} \end{cases} \quad (5-27)$$

$$c^*(T[^\circ\text{C}]) = 1.721 \times 10^{-4}T^2 - 5.88 \times 10^{-3}T + 0.1286 \quad (5-28)$$

**Table 5-1** Kinetic parameters and properties of KNO<sub>3</sub> for the batch process (Miller, 1993)

Parameter	Description	Value
$\rho_c$	Crystal density	$2.11 \times 10^{-12} [g \cdot \mu m^{-3}]$
$k_{sn}$	Nucleation coefficient	$4.64 \times 10^{-7} [\# \cdot \mu m^{-3} \cdot s^{-1}]$
$\alpha_{sn}$	Nucleation supersaturation power	1.78 [-]
$\beta_{sn}$	Nucleation volume power	1 [-]
$k_g$	Growth coefficient	$116 [\mu m \cdot s^{-1}]$
$\alpha_g$	Growth supersaturation power	1.32 [-]
$\beta_g$	Growth size-dependent coefficient	$0.1 [\mu m]$
$\gamma_g$	Growth size-dependent power	1 [-]

The analytical solution for this case does not exist. The high-resolution simulation on a very fine grid was performed by Gunawan et al. (2004) and the numerical accuracy was confirmed using the method of moments. A linear grid with an interval of  $0.5 \mu m$  is used for the fixed-grid method and sampling the seeds CSD for the population array methods. Since the large span of crystal size makes it difficult to reconstruct the CSD using a histogram for the population array method, we used the kernel density estimator with the Epanechnikov kernel and the bandwidth of 1.0 to reconstruct the CSD. The boundary at zero-size was handled using the reflection method (Pedretti & Fernàndez-garcia, 2013). When the nucleation is switched off ( $k_{sn} = 0$ ), the reconstructed CSD using KDE matches the final CSD obtained with the fixed-grid methods. Figure 5-7.a demonstrates the final CSD simulated with various methods. The left part of the distribution is due to the growth of nucleated crystals and the peak on the right is the result of the growth of the seeds. On the CSD generated by nucleation, the right tail is smoother due to the relatively low supersaturation at the beginning. While the supersaturation increases, the CSD becomes steep and the results from different numerical methods start to deviate due to the numerical diffusion of the fixed-grid methods. Due to the lack of sufficient data and the boundary bias caused by KDE, the CSD reconstructed with KDE for the population array method underestimates the size near the zero size. The product CSD of the seeds (Figure



5-7.b) demonstrates the numerical diffusion of high-resolution and upwind methods causes the smoothed peak while the population array method can generate the CSD without smearing the edges. The concentration and count profile are related to the evolution of the third moment and the first moment. The concentration trajectories are insensitive to the minor CSD difference due to the weighting and the results generated by all methods overlap with each other (Figure 5-7.c). However, the crystal count plot shown in Figure 5-7.c revealed a slightly slower count change reported by the fixed-grid method. After refining the grid interval from  $0.5 \mu m$  to  $0.1 \mu m$ , the high-resolution method produces the same count curve as the population array method. This indicates that the population array method is able to accurately simulate the crystallization process that requires a very fine grid and high computation cost to achieve the same level of accuracy for the fixed-grid method. The nucleation expands the population array to more than 1000 rows over time. The row compression used in this case keeps the number of rows in the population array about ten times less than the uncompressed population array method while maintaining the same level of accuracy, making it a very efficient way to speed up the simulation.

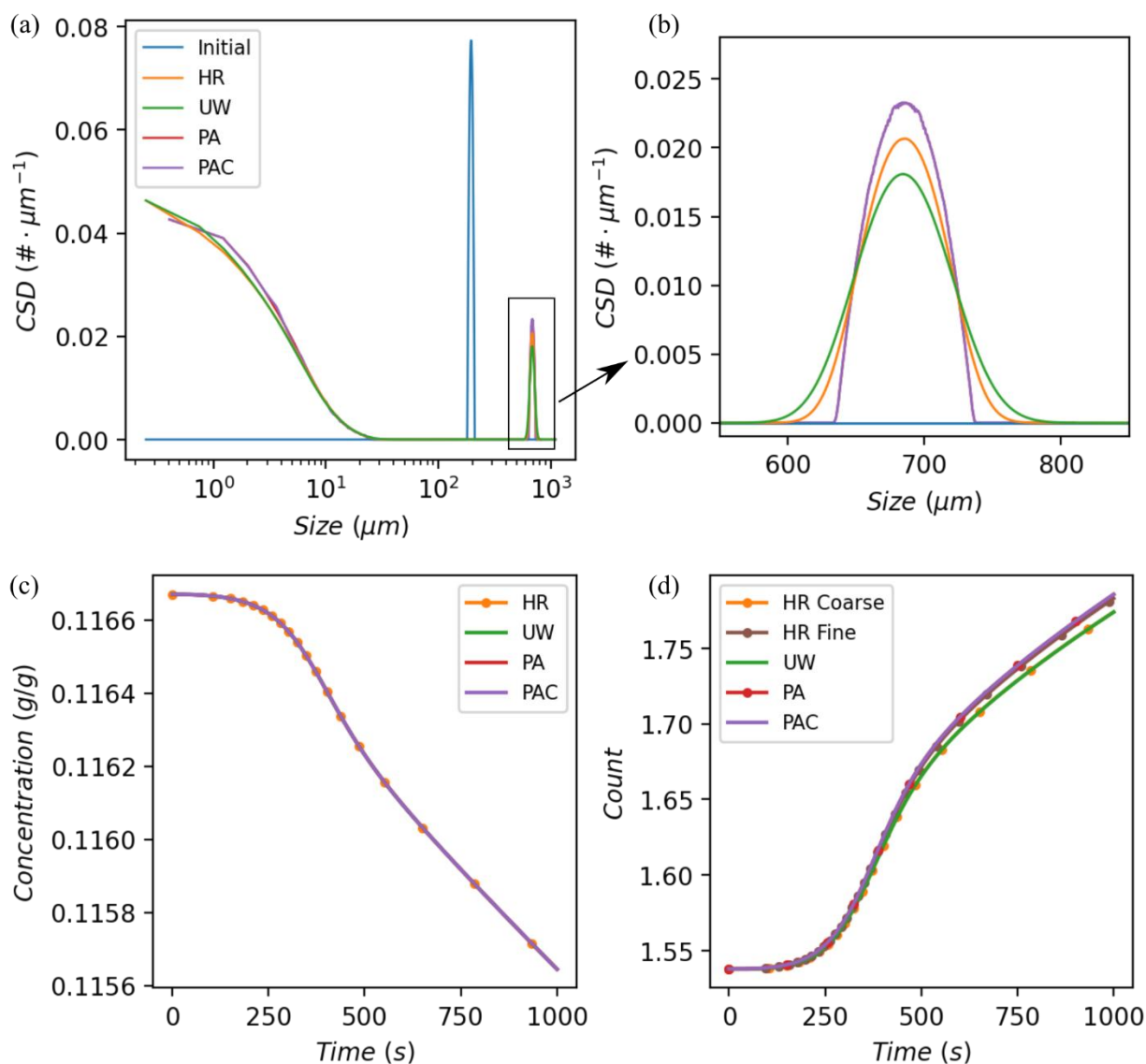


**Figure 5-7** Concentration-dependent kinetics and size-dependent growth simulation for a batch process. (a) Initial and final CSD simulated with high resolution (HR), upwind (UW), population array (PA), and population array with row compression (PAC). (b) CSD of the crystals grown from the seeds. (c) Concentration profiles. (d) Crystal count profiles. The intervals of the coarse and fine grids are  **$0.5 \mu\text{m}$**  and  **$0.1 \mu\text{m}$** , respectively.

Simulating a continuous MSMPR process is similar to the batch process except that the simulation duration is usually much longer to ensure the steady-state result is reached (5 – 6 residence times) (Power et al., 2015). The long simulation potentially causes the CSD leaking problem in the fixed-grid methods, which refers that the grid loses track of the large crystals growing beyond the up limit of the grid. The vanishing crystals will break the conservation of crystal mass and count, causing non-physical fluctuations in the simulated states. This problem is usually overlooked due to the exponential residence time distribution (RTD) of an MSMPR process that implies very low steady-state number density for large crystals, which imposes a negligible effect on the mass and count balances. However, when seeding is used to facilitate the start-up process, the amount of leaked mass and count is substantial. The acute change of the states may lead to elongated steady-state time or even diverging simulation. Therefore, downscaling the time step is usually required for the continuous case to ensure the stability of the solution. The following numerical example of a continuous crystallization process illustrates the accuracy and advantages of the population array (PA) method over the fixed-grid methods. The parameters in Table 5-1 are used except that the volume dependency of the nucleation rate is ignored ( $\beta_{sn} = 0$ ) and the size-dependent growth coefficient  $\beta_g$  is varied among positive (0.005), negative ( $-0.005$ ), and size-independent (0) cases. The inlet stream is clear solution saturated at 32°C. The temperature ( $T$ ) and residence time ( $\tau$ ) of the crystallizer is 31.5°C and 100 seconds, respectively. The fixed-grid methods are simulated on a grid between 0 and 1000  $\mu m$  and the interval is 0.5  $\mu m$ . The simulation results are demonstrated in Figure 5-8. The steady-state CSDs generated by the population array method and the other numerical methods are in good agreement (Figure 5-8) and the trends of the size-dependent growth match the analytical solutions (Myerson, 2002). Figure 5-8.b and c demonstrate the concentration and count profile for the positive size-dependent growth case. The steady-state values converge for all methods, but the fixed-grid method reports a non-physical fluctuation in concentration and count due to the CSD leak of the initial seeding crystals. To prevent this issue, the grid range should be enlarged to ensure the proper tracking of the largest crystal, which significantly

increases the computational cost and needs trial-and-errors to determine the suitable range. The population array can track all crystals regardless of their size, making it suitable for such a long-lasting simulation towards the steady state. However, tracking the large range of crystals is inefficient and usually unnecessary because of the negligible counts. Therefore, the rows with the count below the threshold ( $10^{-15}$  for this case) can be safely removed so that the computation efficiency is maintained while imposing minimal impact on the mass conservation. Due to the overhead of the row compression algorithm, it is the most efficient to compress the population array once the number of rows exceeds 3000 rather than on every time step.

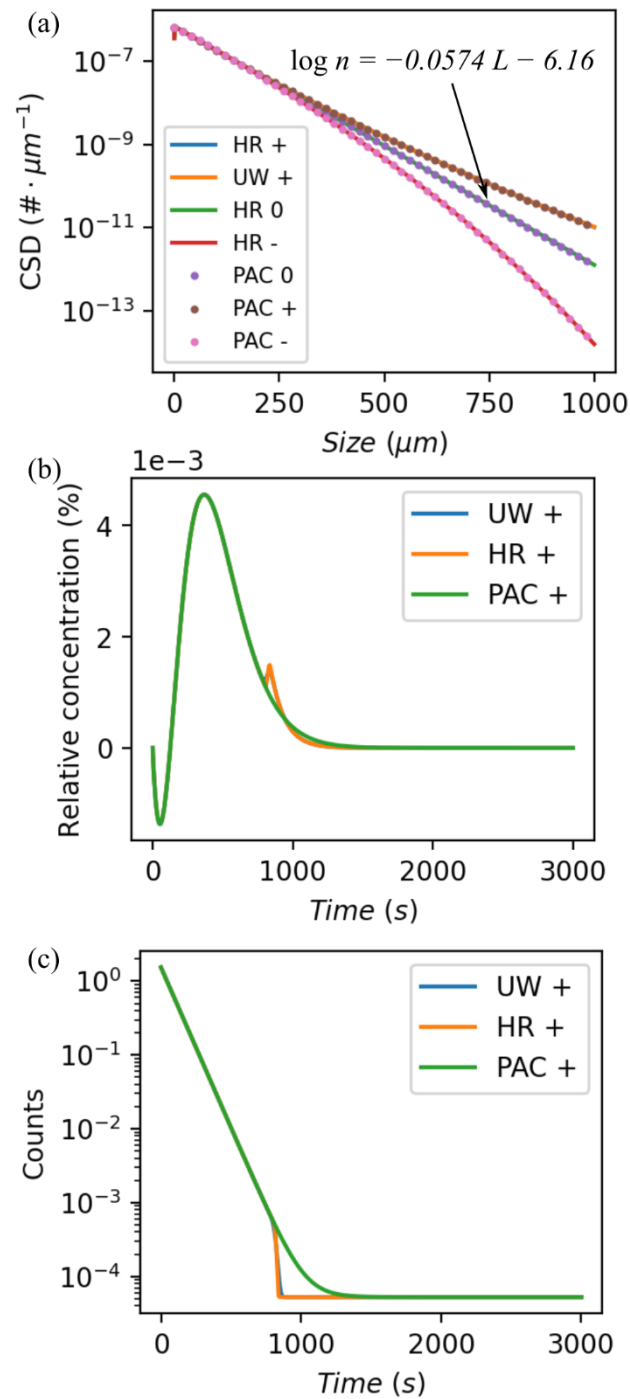


**Figure 5-8** Concentration-dependent kinetics and size-dependent growth simulation for a continuous process. The suffixes +, -, 0 stand for positive, negative size-dependent and size-independent growth kinetics a) steady-state CSD simulated with various numerical

methods. b) Relative concentration profile of the positive size-dependent growth. c)  
Count profile of the positive size-dependent growth.

### 5.3.3. Polymorphic Transformation

Polymorphism refers to the molecules crystallizing in more than one crystal structure with different packing arrangements and/or conformations. The solubility of the stable form is lower than the unstable forms, driving the polymorphic transformation to the most stable form. The previous work showed that the relative kinetics of the forms play an important role in the crystallization process and the expected outcome (Lin, Wu & Rohani, 2020a). When simulating the de-supersaturation process involving polymorphic transformation, it is challenging to correctly describe the behavior when the concentration is between the solubilities of two forms. The time step needs to be downscaled because the simultaneous dissolution and growth may cause the concentration fluctuation near the solubility limits. Also, the dissolution rate is generally the order of magnitudes faster than the growth, resulting in a much finer time step to satisfy the CFL condition (Lin, Wu & Rohani, 2020a).

In this numerical case, the polymorphic transformation from the unstable  $\alpha$ -form to the stable  $\beta$ -form L-glutamic acid crystal in a batch process is simulated with the high-resolution and population array methods. The solubility of the two forms from the literature is given in Eqs. 5-29 and 5-30 (Hermanto et al., 2012). The kinetic parameters for the simulation are listed in Table 5-2. The nucleation coefficients of the unstable  $\alpha$ -form is higher than the stable  $\beta$ -form to emulate the kinetically favorable behavior of the unstable form. In this case, the rate-limiting step is the nucleation of the stable form. Besides, a dissolution-limiting case was simulated where the dissolution coefficient of the unstable form is reduced to  $-0.2 \mu\text{m} \cdot \text{s}^{-1}$ .

$$c_{\alpha}^*(T[{}^{\circ}\text{C}]) = 8.437 \times 10^{-6} T^2 - 3.032 \times 10^{-5} T + 4.564 \times 10^{-3} \quad (5-29)$$

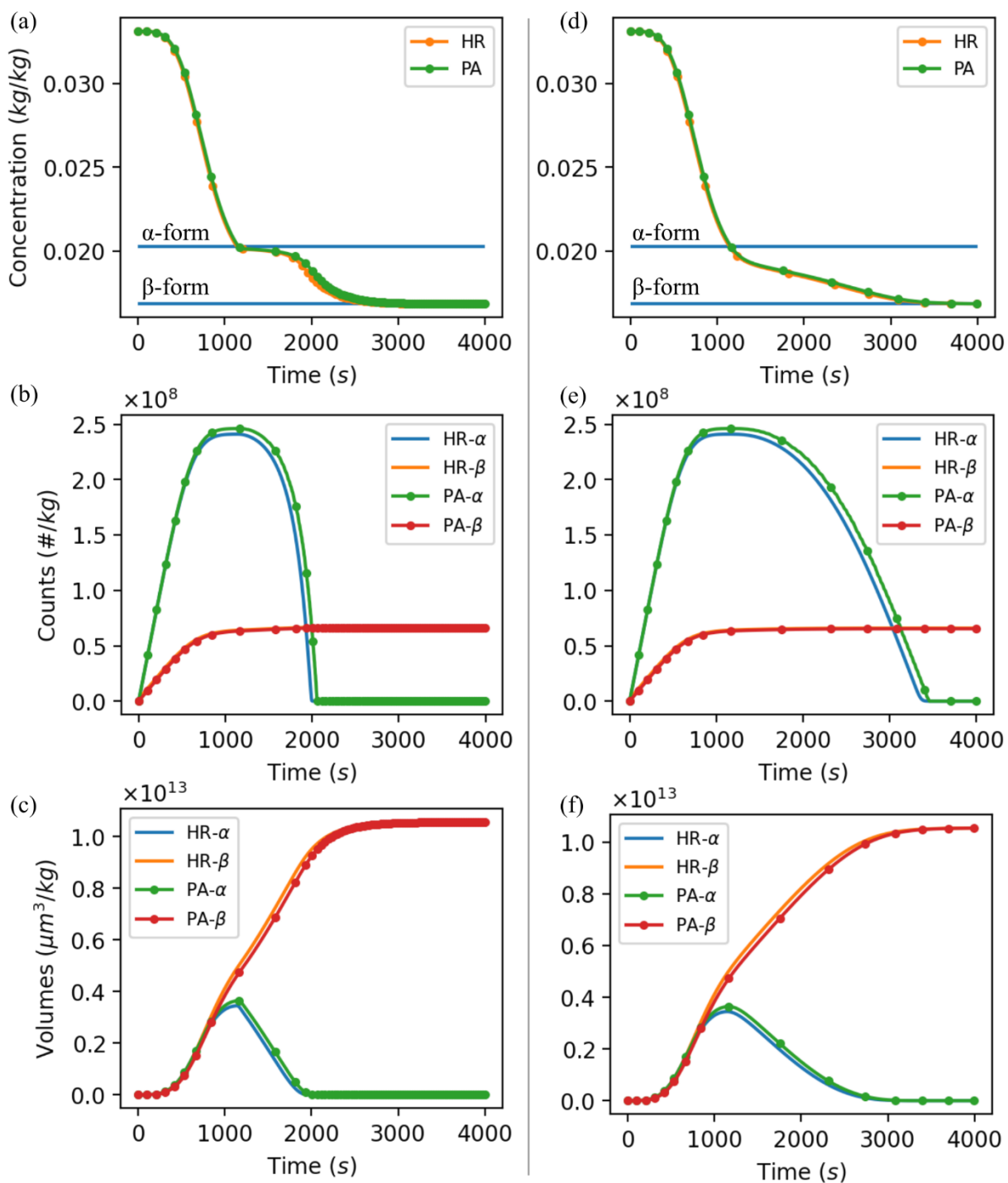
$$c_{\beta}^*(T[{}^{\circ}\text{C}]) = 7.644 \times 10^{-6} T^2 - 1.165 \times 10^{-4} T + 6.622 \times 10^{-3} \quad (5-30)$$

Figure 5-9 demonstrates the simulation results of these cases. When the polymorphic transformation is limited by the nucleation of the stable form, there is a concentration plateau near the solubility of the unstable form, where the dissolution of the  $\alpha$ -form crystals is enough to compensate the solute consumption of the relatively slow nucleation and growth of the stable form. However, if the dissolution rate of the unstable form is slow (dissolution-limiting), the concentration will not plateau but slowly approach the solubility of the stable form. These phenomena are correctly described by both HR and PA methods. Despite the good agreement between the HR and PA methods, there are noticeable differences after the concentration drops below the solubility of the unstable form. It is concluded that the accuracy of the fixed-grid methods is sensitive to the time step. By scaling the time step size determined by the CFL condition, the PA method generates consistent results, and the curves simulated by the HR method are approaching the result of the PA method. Figure 5-10 demonstrates the relative difference between the concentration profile simulated with a very small step (CFL scaled by 0.1) and larger time steps. When the time step is scaled by 0.1, the relative error between the PA method and the HR method is negligible. As the scale factor increases, the difference between the two methods enlarges. The numerical stability of the fixed-grid method is limited by the CFL condition, so the time step factor is cut off at one. The PA method allows the use of much larger time steps without encountering numerical stability issues. When the large time step is used, it invalidates the assumption that the system state is constant within each simulation step, resulting in the loss of accuracy. The stability and accuracy of the PA method enable much faster polymorphic transformation simulation than the HR method.

**Table 5-2** Kinetic parameters and properties of the polymorphic system (L-glutamic acid) (Lin, Wu & Rohani, 2020a)

<b>Parameter</b>	<b>Description</b>	<b>Value</b>
$\rho_c$	Crystal density	$1.54 \times 10^{-12} [g \cdot \mu m^{-3}]$
$k_s$	Shape factor	0.48
$k_{pn}$	Primary nucleation coefficient of two forms	$\{10^5, 10^6\} [\# \cdot kg^{-1} \cdot s^{-1}]$
$k_{sn}$	Secondary nucleation coefficient of two forms	$\{10^5, 10^6\} [\# \cdot \mu m^{-3} \cdot kg^{-1} \cdot s^{-1}]$
$\alpha_{pn}, \alpha_{sn}$	Nucleation supersaturation powers	2
$\beta_{sn}$	Secondary nucleation volume power	1
$k_g$	Growth coefficient	$0.1 [\mu m \cdot s^{-1}]$
$k_d$	Dissolution coefficient	$-2.2$ or $-0.2 [\mu m \cdot s^{-1}]$
$\alpha_g, \alpha_d$	Growth/dissolution supersaturation power	1
$\beta_g, \beta_d$	Size-dependent growth/dissolution coefficient	0
$\gamma_g, \gamma_d$	and power	





**Figure 5-9** The simulated concentration, crystal counts, and crystal volumes profile of the polymorphic transformation from the unstable  $\alpha$ -form to the stable  $\beta$ -form crystals.

(a-c): nucleation-limiting case; (d-f): dissolution-limiting case.

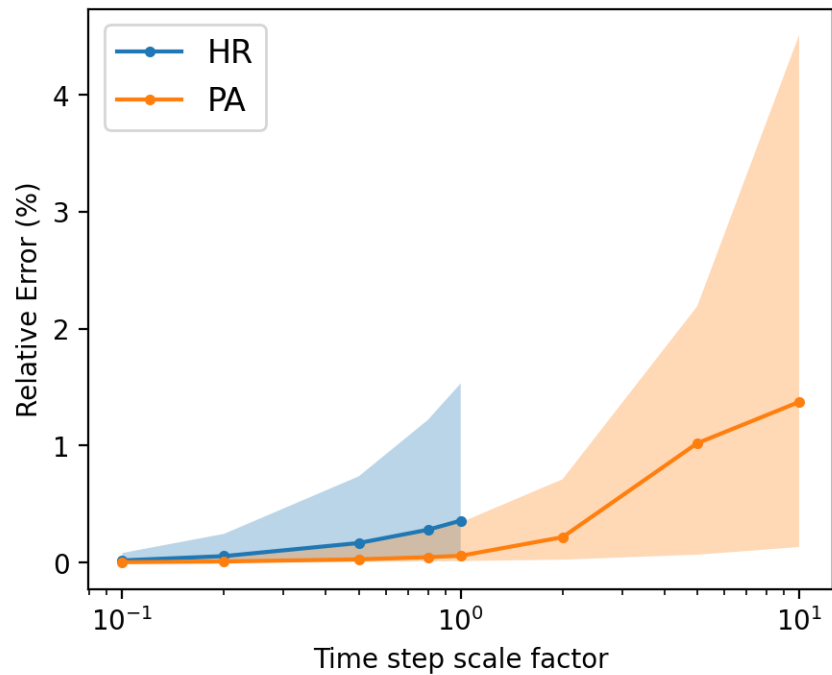


**Figure 5-10** Relative error of the concentration profile compared to the results simulated with the smallest time step (scaled by 0.1). The curves depict the mean relative error and the shaded areas show the 90% confidence interval.

#### 5.3.4. Agglomeration and Breakage

The mechanism of agglomeration simulation borrows features from the grid methods and the population array (PA) method. By iterating every pair of rows/grid cells, the birth rate and the size of the new agglomerates can be calculated. In the grid method, the arbitrary agglomerate size is usually different than the size represented by the grid points. Kumar and Ramkrishna proposed a technique to interpolate the size and count of an arbitrary crystal such that the total volume and count are conserved (Kumar & Ramkrishna, 1997). The PA implements the same concept in two steps. First, the birth rates of each agglomerate produced by any two crystals and their exact sizes are computed using Eqs.

5-12 and 5-13. Then, the PA is compressed to an equivalent array with fewer rows while conserving the crystal count and volume.

$$L_{aggl} = \sqrt[3]{L_1^3 + L_2^3} \quad (5-31)$$

$$n(L, 0) = \frac{N_0}{L_0} \left(\frac{L}{L_0}\right)^2 e^{-\left(\frac{L}{L_0}\right)^3} \quad (5-32)$$

$$n(L, t) = \frac{4 N_0 \left(\frac{L}{L_0}\right)^2}{L_0 \cdot (Y + 2)^2} e^{-\frac{2\left(\frac{L}{L_0}\right)^3}{Y+2}} \quad (5-33)$$

The agglomeration on a linear size grid with a constant agglomeration kernel was solved analytically in the previous work (Gelbard & Seinfeld, 1978). In this case, the agglomerate size generated by two crystals of size  $L_1$  and  $L_2$  is calculated with Eq. 5-31. For the initial CSD given as Eq. 5-32, where  $N_0 = 10^{11}$ ,  $L_0 = 1.5 \mu\text{m}$ , and the agglomeration kernel  $\alpha = 6 \times 10^{-13} \text{ s}^{-1}$ , the analytical solution at time  $t = 300$  is given in Eq. 5-33, where  $Y = N_0 \alpha t$ . This analytical result is referred to as the self-preserving particle size distribution, as the form of the distribution does not vary with time (Van Peborgh Gooch & Hounslow, 1996). Figure 5-11.a demonstrates the consistent numerical results generated by the grid and PA methods that match the analytical solution.

$$v_{aggl} = v_1 + v_2 \quad (5-34)$$

$$n(v, 0) = \frac{N_0 v}{v_0} e^{-\frac{v}{v_0}} \quad (5-35)$$

$$n(L, t) = \frac{N_0 (1 - T)^2}{v_0 \sqrt{T}} e^{-\frac{v}{v_0}} \sinh \frac{v}{v_0} \sqrt{T} \quad (5-36)$$

$$T = \frac{\alpha N_0 t}{2 + \alpha N_0 t} \quad (5-37)$$

Using a volume grid to solve the agglomeration and breakage problem is generally more straightforward as the size can be simply represented by the summation of the volumes (Eq. 5-34). The logarithmic grid is used since agglomeration results in the crystal volumes spanning many orders of magnitudes. The analytical solution was solved by Ramabhadran et al. (2004). The initial CSD is given by Eq. 5-35, where  $N_0$  and  $v_0$  are given as 1.0 and  $1.0 \mu m^3$ , respectively. The constant agglomeration kernel is given by  $\alpha = 10^{-2} s^{-1}$ . The size distribution after agglomerating for  $t = 300 s$  is represented by Eq. 5-36, where  $T$  is defined in Eq. 5-37. As shown in Figure 5-11.b, the simulation results of both numerical methods agree well with the analytical solution.

Similar CSD leaking problems described in the continuous crystallization section also apply to the grid method in the agglomeration case. When the size of agglomerates is larger than the up limit of the grid, the volume and count balances between the death and birth terms no longer hold and will lead to significant errors. Increasing the up limit of the grid will remedy this issue at the cost of quadratically expanding computational effort. All grid cells are involved in agglomeration no matter the crystals exist in the cells or not. It is possible to optimize the computation by filtering out the cells containing data below a threshold such that the accuracy is not impacted. The PA method does not use a fixed grid so that the CSD leaking problem does not apply. The computation cost optimization also works for the PA method, which prevents performance degradation due to the extremely large agglomerates of a very low count. Unlike the grid method whose computation complexity is predictable, the computation cost to compress and compute the agglomerate of the PA method increases over time. If the same grid of the grid method is used for the row compression of the PA method, the computational complexity of generating the agglomerates is equal when the agglomerate is forming in the largest size segment of the grid. The row compression then becomes the extra performance overhead. This is generally an unattainable case since the accuracy of the grid method is

deteriorating due to the CSD leaking so there should always be extra grid cells on the larger size. Due to the large number of new rows in the PA, it is essential to apply the compression algorithm after the agglomeration process to ensure the computation efficiency of the next simulation step. Optimizing the speed of the row compression algorithm ensures minimal performance overhead when dealing with a large population array.

$$n(v, 0) = \delta(v - b) \quad (5-38)$$

$$n(v, t) = e^{-tv} \cdot [\delta(v - b) + \theta(b - v) \cdot (2 + t^2(b - v))] \quad (5-39)$$

$$n(v, t) = e^{-tv^2} \cdot [\delta(v - b) + 2bt \theta(b - v)] \quad (5-40)$$

The binary breakage generates a finite number of daughter crystals determined by the breakage frequency distribution. The analytical solutions of the linear-volume ( $\beta = v$ ) and squared-volume ( $\beta = v^2$ ) breakage kernels and a uniform daughter crystal distribution are available in the literature (Hasseine et al., 2015). The initial condition a monodisperse size distribution (Eq. 5-38) at the largest size defined in the grid,  $b$ . When the breakage kernel function is linear, the rate of crystal breakage is proportional to its volume. The analytical solution at any time is given by Eq. 5-39, where  $\theta$  is the Heaviside (step) function that sets the number density larger than the parent particle to zero (Hasseine et al., 2015). For the squared breakage kernel, the analytical solution is given by Eq. 5-40. Figure 5-11.c and Figure 5-11.d demonstrate that the results of the numerical methods are in good agreement with the analytical solutions at  $t = 10$  s. In the general cases where the simultaneous crystal agglomeration and breakage are considered, the empty grids above the largest existing crystal will reduce the computation efficiency of the grid method, whereas the PA method can maintain the maximum efficiency because only the crystals in the population array are involved. Like the agglomeration

process, the PA method also heavily relies on the row compression algorithm to maintain the computation scale manageable.

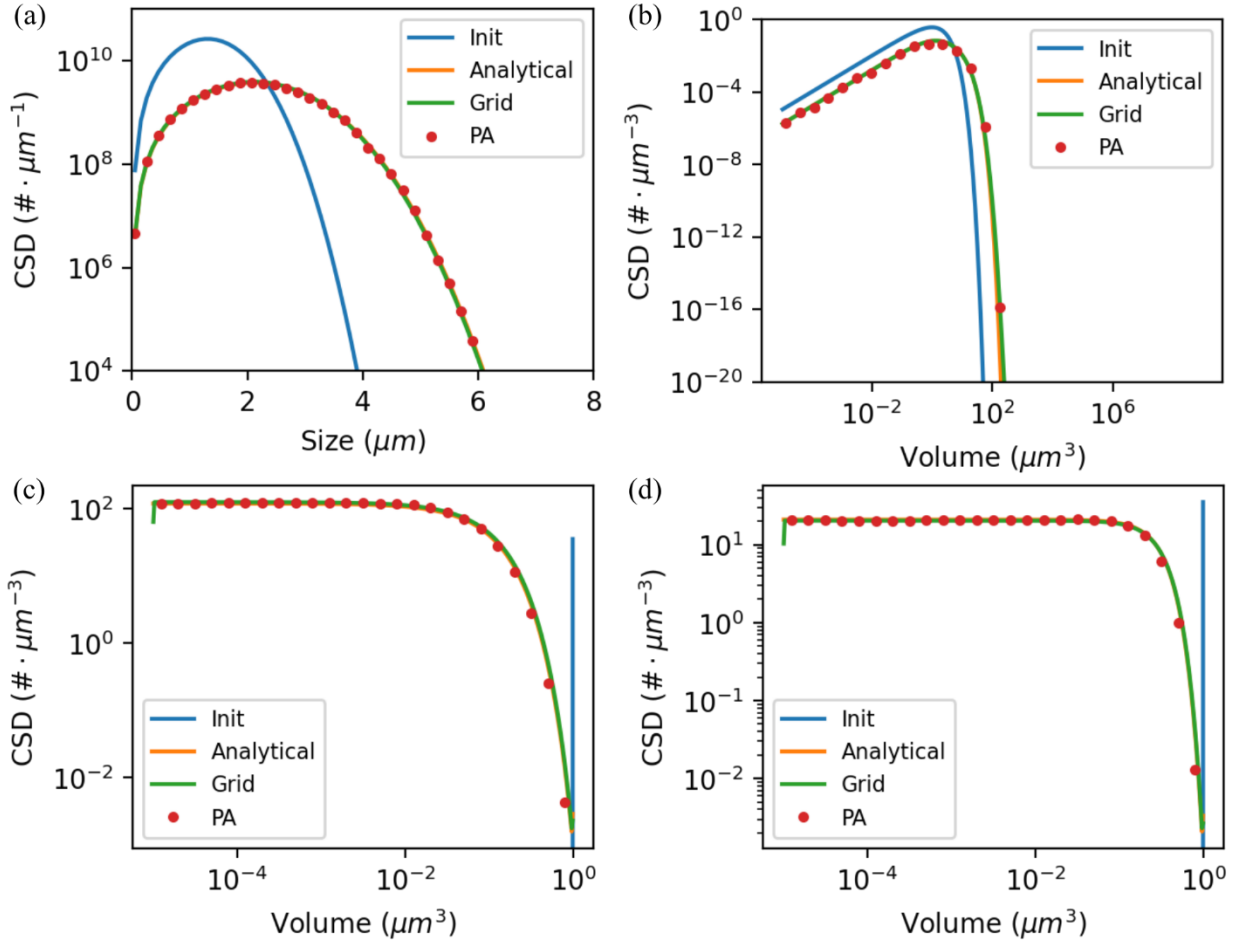


**Figure 5-11** Simulation results of one-dimensional agglomeration and breakage. (a) constant agglomeration kernel on a linear size grid; (b) constant agglomeration kernel on a logarithmic volume grid; (c) linear-volume breakage kernel  $\beta = v$  on a logarithmic volume grid; (d) squared-volume breakage kernel ( $\beta = v^2$ ) on a logarithmic volume grid.

The two-dimensional agglomeration and breakage are computationally more complicated. The analytical solution of the multi-dimensional agglomeration and breakage was reported by Gelbard (1978) and Singh et al. (2020), which considered any combination of two crystals regardless of their shapes. In this work, due to the

assumption that only one dimension is involved in the agglomeration or breakage event, the numerical simulation is not compatible with the analytical results. Instead, we use the grid-based implementation described in (Shu et al., 2020) as a reference to cross-validate the performance of the proposed PA method in two-dimensional agglomeration and breakage.

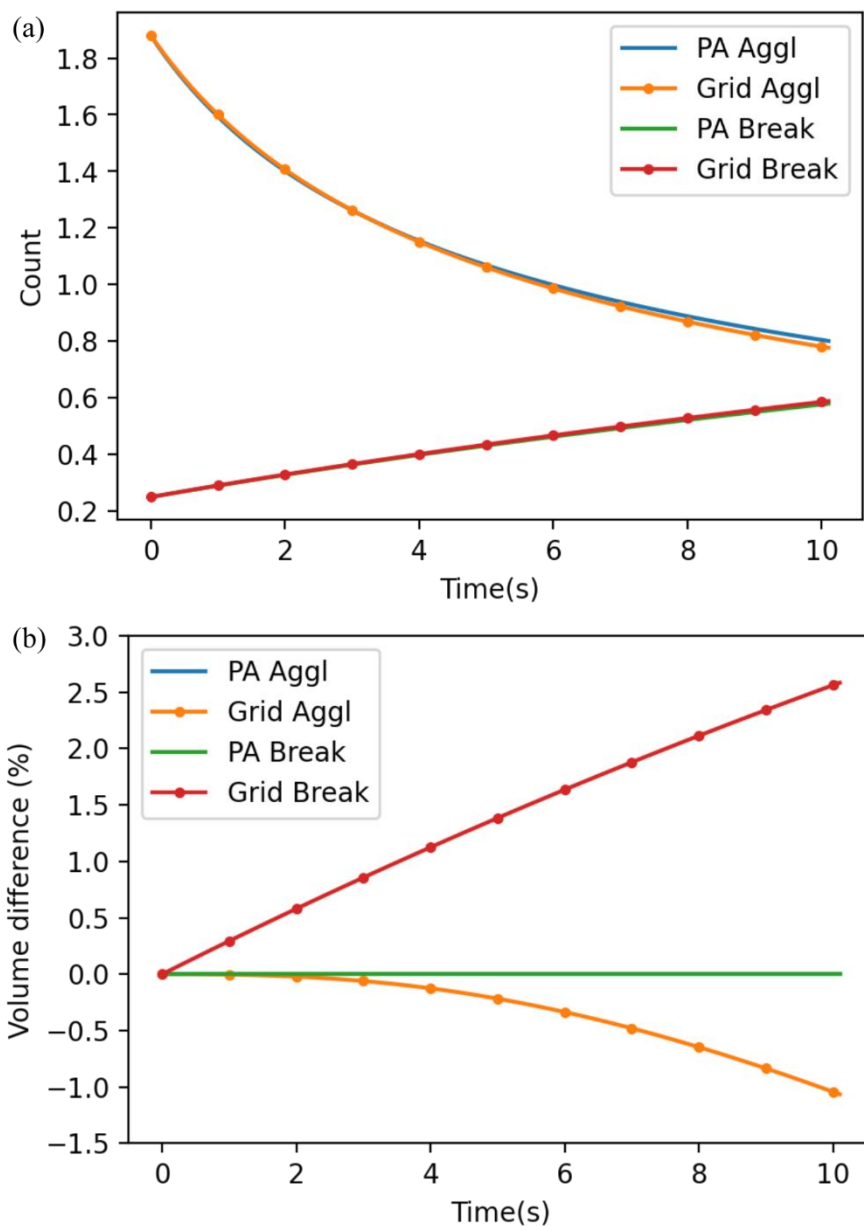
For the agglomeration case, the initial condition is a normal distribution at the origin point with a scale of  $\sigma = 3 \mu m$ . The agglomeration kernel coefficients are assumed to be  $1.0 s^{-1}$  for both dimensions. However, the agglomeration rates along the two dimensions are not equal because the volume powers of the two internal coordinates are different, which are assumed to be 2 and 1, respectively. The partition interval is set to  $0.5 \mu m$ . The breakage simulation starts from the normal distribution offset by  $10 \mu m$  in both directions. The standard deviation of the normal distribution is  $\sigma = 0.4 \mu m$ . The squared-volume kernel is used, and the breakage frequency coefficient is  $\beta_0 = 10^{-7} \mu m^{-6} \cdot s^{-1}$ . The simulation time step of both simulations is set to 0.1 seconds.

Figure 5-12.a depicts the simulated count profiles of agglomeration and breakage simulations. The PA method is able to generate consistent results that closely match the reference implementation. Figure 5-12.b demonstrates that the PA method guarantees the crystal volume conservation in the pure agglomeration or breakage process, while the grid method is showing the accumulating error in the total volume. This mismatch is due to the difference between the size represented by a grid pivot and the size of the newborn crystal, which was confirmed by Shu et al. (2020). This error could be reduced by refining the grids or introducing the correctors (Singh et al., 2020). In the PA method, the volume and count are inherently balanced, which guarantees accuracy without requiring dedicated correction and computationally expensive fine grid.

Figure 5-13 illustrates the contour plots of the initial and final CSDs of the simulations. The agglomeration enlarges the internal coordinates and the agglomeration rate along the height is faster than the width direction, which is explained by the different volume power of the internal coordinates. For two crystals with the internal coordinates of

$(h_1, w_1)$  and  $(h_2, w_2)$ , the agglomeration along the height direction results in a new particle of  $(h_1 + h_2, w_1)$  since the volume power of height is one. In contrast, the volume power of the width is two. To ensure volume conservation, the agglomeration along the width direction results in the internal coordinates of  $(h_1, \sqrt{w_1 + w_2})$ . For the same reason, the breakage rate along the height direction appears faster than the width direction in Figure 5-13.d.





**Figure 5-12** (a) The count profile of the agglomeration and breakage simulation generated by the PA and grid methods. (b) Crystal volume profile to demonstrate the relative volume change during the agglomeration and breakage. The Aggl and Break in the legends refer to agglomeration and breakage, respectively.

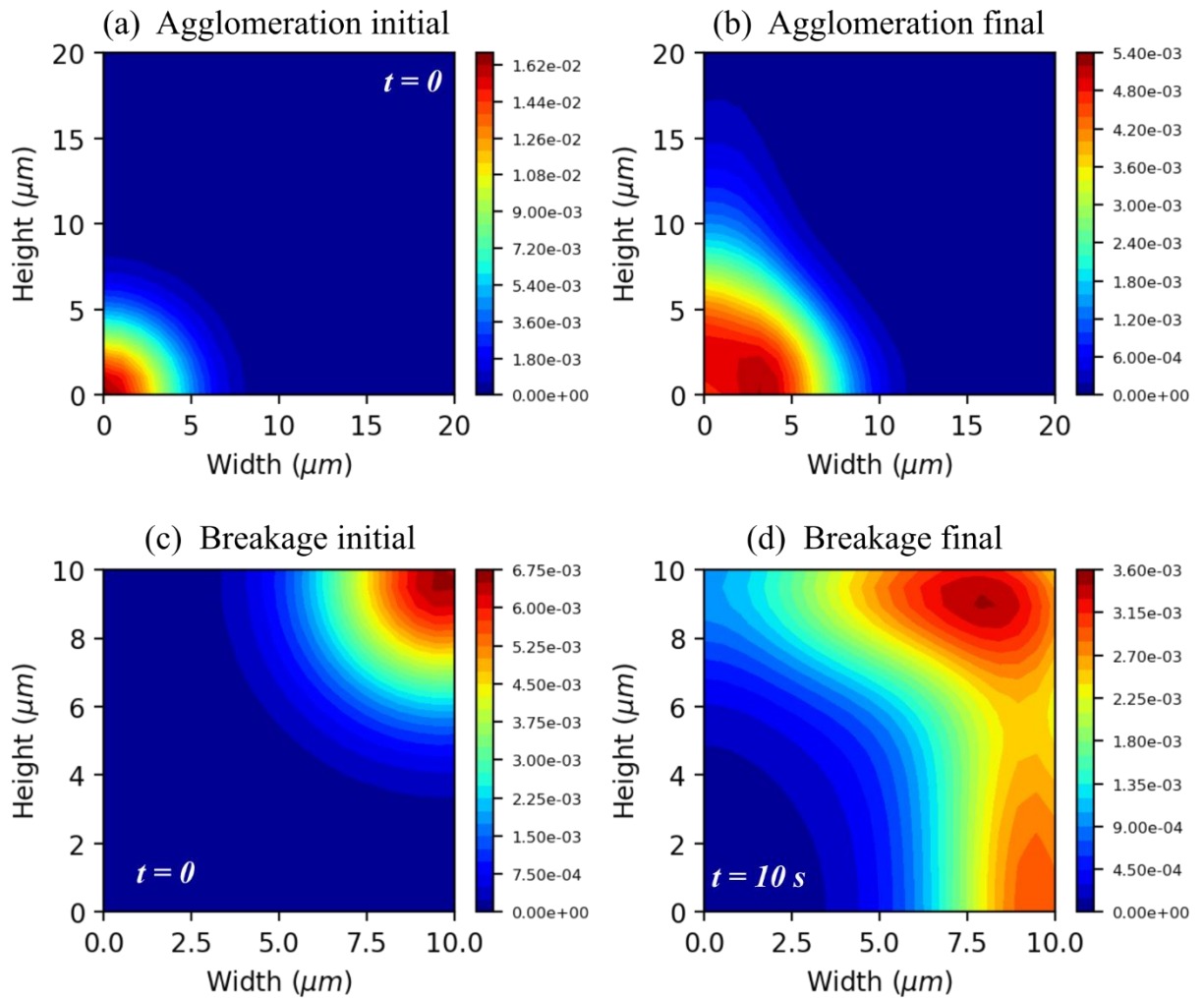


**Figure 5-13** Two-dimensional agglomeration and breakage simulation results using the PA method. (a) The initial condition of the agglomeration simulation. (b) Final CSD of the agglomeration simulation. (c) The initial condition of the breakage simulation. (d) Final CSD of the breakage simulation.

### 5.3.5. Computation Efficiency

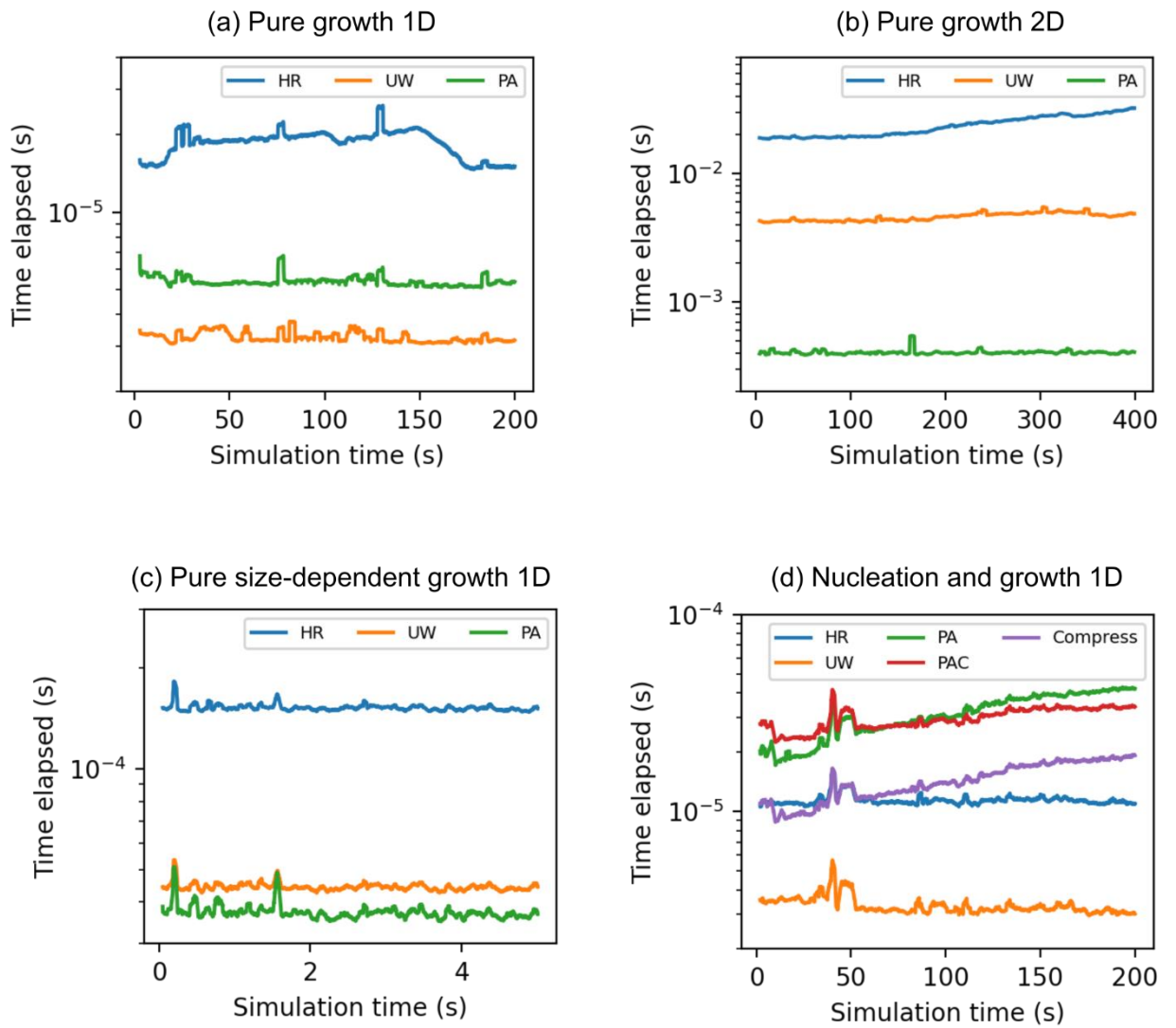
The computational complexity of the PBE is critical when coupling the solver in the computational fluid dynamic (CFD) simulation or deploying the algorithm in the model

predictive control (MPC) that requires in-time on-line optimization of the outputs. For the simulation time-sensitive applications, the method of moments is preferred over the discretization methods due to its efficiency. In this section, the computational efficiency of the PA method coupled with the on-demand row compression is demonstrated. The execution time was measured on a PC with an Intel i7-8750H 4.0GHz CPU and 32GB RAM. The performance of the grid-based discretization methods depends on the span and the resolution of the grid. We used the relatively coarse grids that achieved a similar accuracy of the PA method while maintaining efficiency. All operations of the PA and grid methods are accelerated with the python just-in-time (JIT) compiler, Numba (Lam, Pitrou & Seibert, 2015), to maximize the execution efficiency.

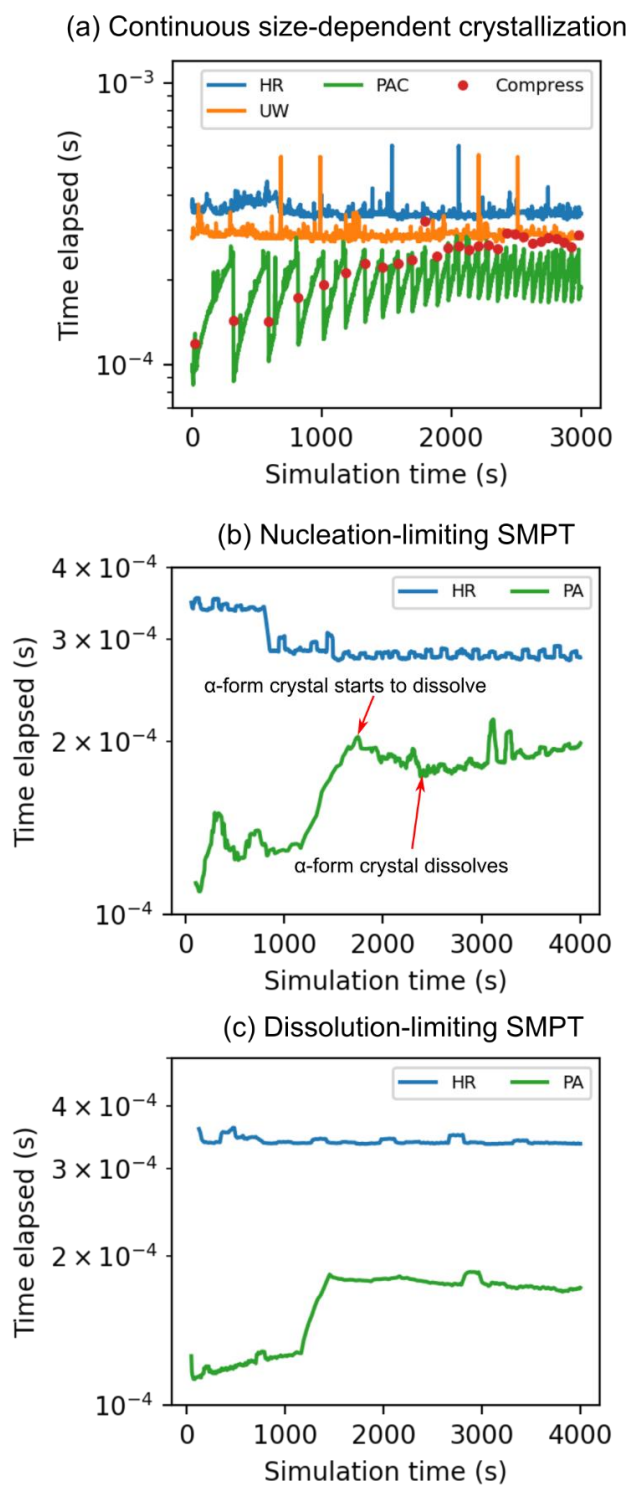
Figure 5-14 demonstrates the computation speed of pure growth and simultaneous nucleation and growth cases. Figure 5-14.a and c show that the one-dimensional pure growth speed is similar for the PA method and the grid methods. However, the PA method is orders of magnitude more efficient than the grid methods in the two-dimensional growth case (Figure 5-14.b). When nucleation is involved, the computational scale varies over time. Figure 5-14.d depicts that the row compression enables a slower increase of the simulation time for each step. The row compression mechanism is efficient and only incurs little overhead in the same order of magnitude of the growth operation.

Figure 5-15 illustrates the more realistic simulation cases where the nucleation and growth depend on the system states. The single-stage MSMR case (Figure 5-15.a) shows the fluctuating computational speed of the PA method due to the nucleation that expands the population array and the row compression mechanism that is triggered when the number of rows in the population array exceeds the threshold. The computation time reaches steady state thanks to the minimum count threshold that prevents the infinite growth due to the exponential residence time distribution in the MSMR. This comparison shows that the PA method with row compression maintains the efficiency in the same order of magnitude as the grid methods in a long-run simulation.

Figure 5-15.b and c are the simulation time of the polymorphic transformation cases presented above. In Figure 5-15.b, the computation time trend of the PA method matches the events of the transformation process. The dissolution of the unstable form leads to the removal of rows from the population array. In Figure 5-15.c, due to the limiting dissolution rate of the  $\alpha$ -form, the decrease of simulation time is not as significant. After the transformation process is completed, there is no computation wasted on the nucleation and growth of the unstable form. For the grid-base HR method, the computation on the grid of the non-existing form lowers the efficiency.



**Figure 5-14** Nucleation and growth simulation speed comparison between the grid methods and the PA method.



**Figure 5-15** Simulation speed comparison of the concentration-dependent cases.

The agglomeration and breakage are more computation-intensive operations. The computational scale of agglomeration increases quadratically with the number of grids/rows. Therefore, the PA method can outperform the grid method in the one-dimensional agglomeration cases (Figure 5-16.a and b) because the grid method has to iterate all combinations of the grid cells while the PA method only considers the existing crystals. The breakage operation is generally faster than agglomeration for the same scales of input since the computational scale has a linear dependency on the input. Figure 5-16.c and Figure 5-16.d demonstrate the similar performance of the grid and PA methods in the one-dimensional breakage simulation. The initial conditions of the numerical cases are the Dirac pulses on the largest size on the grid, which allows the grid method to utilize the full grid at the highest efficiency. When the growth or agglomeration mechanisms are involved, the reserved extra grid cells for the size enlargement will lower the computational efficiency.

The computational time of the two-dimensional agglomeration and breakage simulations is demonstrated in Figure 5-16.e and Figure 5-16.f. It is observed that the number of nodes on each dimension will significantly affect the performance of the grid method. For the PA method, the spatial resolution of the internal coordinates only depends on the grid interval of the efficient row compression algorithm. Since the agglomeration and breakage implementations of the grid and PA method are similar, the performance gain of the PA method is mainly from the excluded calculation on the unused grid.

The simulation time of various operations given the different number of rows in the population array is illustrated in Figure 5-17. Due to the important role of the row compression algorithm in all simulation cases, a native version was implemented using C++ to minimize the performance overhead during row compression, which was about one order of magnitude faster than the JIT-accelerated python implementation. The growth and nucleation are the least time-consuming operations since they only involve updating the columns and inserting new rows in the population array. The on-demand row compression policy can be employed to maintain the number of rows within the most

efficient range (e.g.,  $< 10^4$  rows). For the agglomeration and breakage operations, the computational time has a strong dependency on the size of the population array, and many new rows will be created after these operations. It is beneficial to always use the row compression method at every simulation step when the agglomeration and breakage are involved.



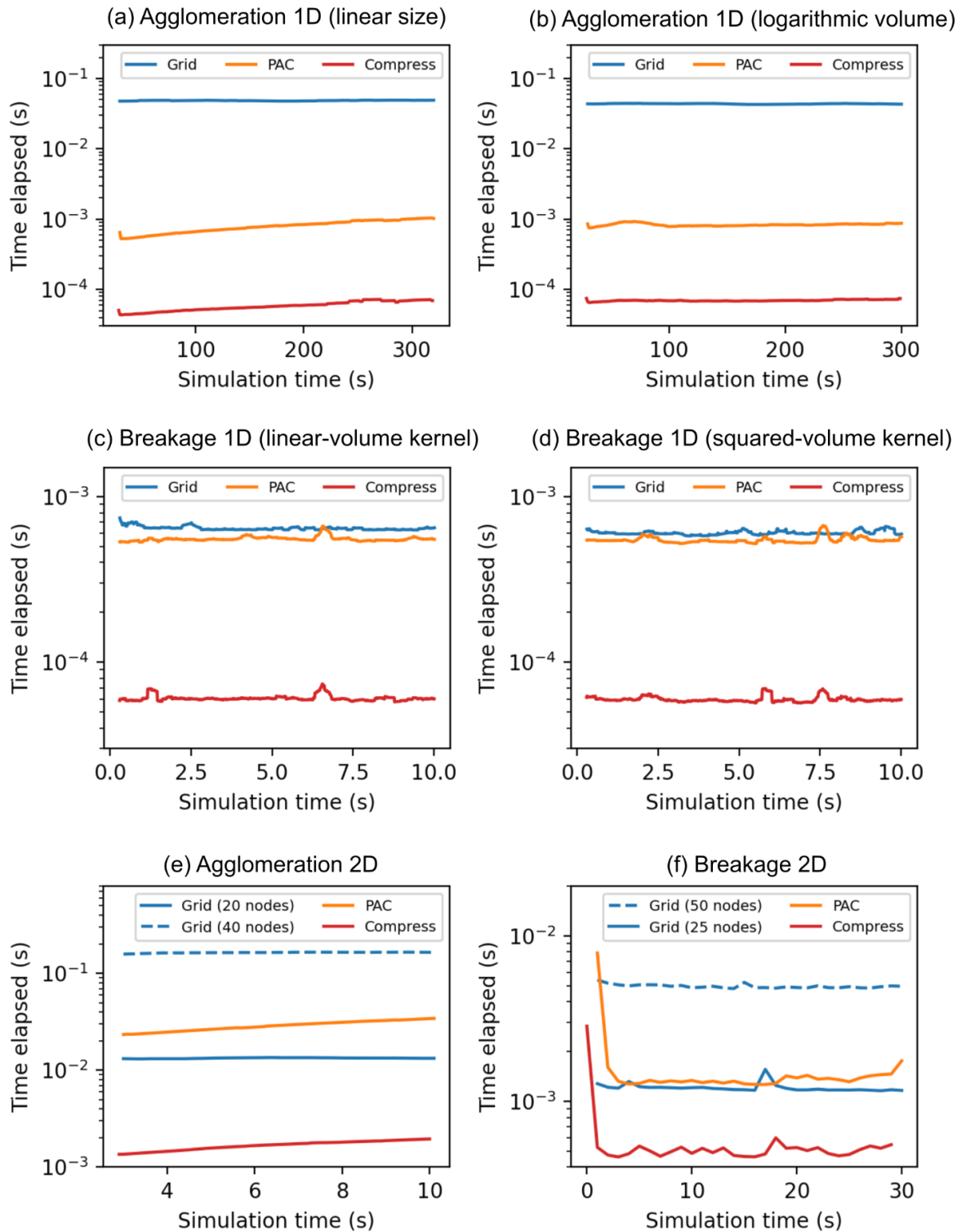


**Figure 5-16** Agglomeration and breakage simulation speed profiling

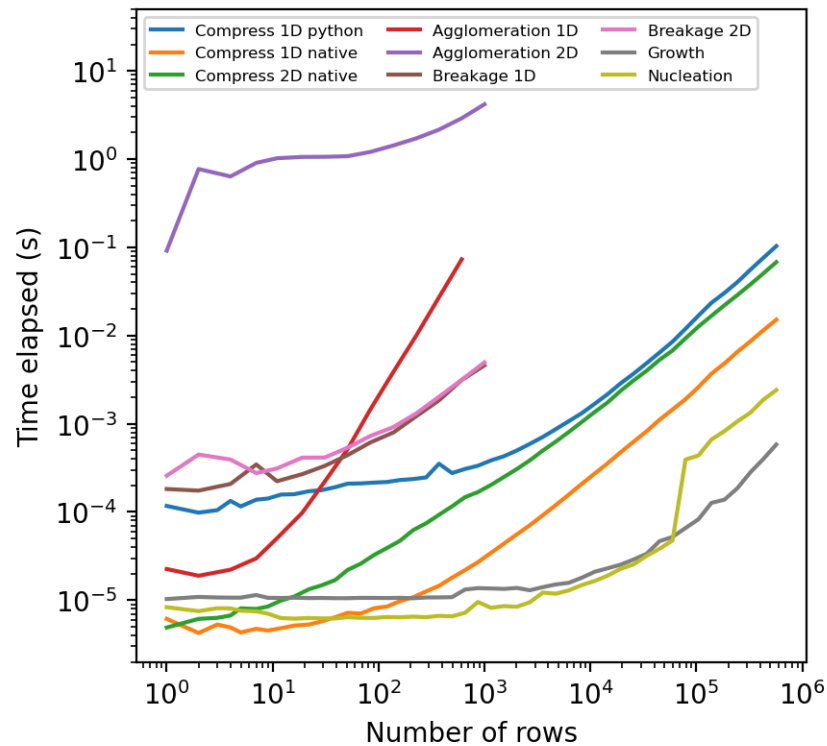


**Figure 5-17** Computation speed of various operations for population array method at different numbers of rows.

## 5.4. Conclusion

A computationally efficient and accurate numerical PBE solution method for studying the crystallization kinetic process is discussed and validated in this work. In the proposed PA method, the crystals are tracked as the pivots represented by the rows in a population array. The numerical difficulties such as numerical diffusion and dispersion in many grid-based discretization methods are avoided by solving the growth and dissolution using the method of characteristic. The limitation of a fixed grid leads to inefficient computation on the unused grid cells and potential CSD leak due to the size-enlargement of the crystals that causes inaccurate crystal mass and count balance, while the efficiency and accuracy are guaranteed in the PA method that performs only the necessary computation with the

existing crystals and keeps tracking every crystal regardless of the size. The simulation time step is decoupled from the grid of the internal coordinates, allowing the larger simulation step size without affecting the stability. An efficient row compression algorithm is used to speed up the PA method by merging the pivots with duplicating or similar internal coordinates while maintaining the conservation of crystal mass and count. The analytical solution or the solution obtained using a very fine grid was used to validate the accuracy of the nucleation, growth, agglomeration, and breakage simulated by the PA method. The complicated operations such as polymorphic transformation and continuous MSMPR processes were studied to ensure the performance of the general crystallization simulation cases. The numerical case studies confirmed the accuracy of the PA method and the numerical stability when a large simulation time step is used. The PA method shows superior computational efficiency especially for the multi-dimensional simulations, which enables the potential application of online optimization and model predictive control. The challenge of the PA method is to recover the CSD from the population array with histogram or kernel density estimation method, where the decision of the optimal parameters such as bandwidths should be further studied to eliminate the influence brought by the manually chosen parameters. The source code of the PA method and the high-resolution discretization method is listed in Appendix. B.

## 5.5. References

- Bao, Y., Zhang, J., Yin, Q. & Wang, J. (2006). Determination of growth and breakage kinetics of l-threonine crystals. *Journal of Crystal Growth*, 289(1), 317–323. <https://doi.org/10.1016/j.jcrysgr.2005.11.001>
- Borchert, C. (2012). Topics in Crystal Shape Dynamics, (April 2012).
- Chen, S., Liu, T., Xu, D., Huo, Y. & Yang, Y. (2019). Image based Measurement of Population Growth Rate for L-Glutamic Acid Crystallization. In *2019 Chinese Control Conference (CCC)* (pp. 7933–7938). <https://doi.org/10.23919/ChiCC.2019.8866441>
- Gao, Z., Wu, Y., Bao, Y., Gong, J., Wang, J. & Rohani, S. (2018). Image Analysis for In-line Measurement of Multidimensional Size, Shape, and Polymorphic

- Transformation of L-Glutamic Acid Using Deep Learning-Based Image Segmentation and Classification. *Crystal Growth and Design*, 18(8), 4275–4281. <https://doi.org/10.1021/acs.cgd.8b00883>
- Gelbard, F. M. & Seinfeld, J. H. (1978). Coagulation and Growth of a Multicomponent Aerosol, 63(3).
- Gelbard, F. & Seinfeld, J. H. (1978). Numerical solution of the dynamic equation for particulate systems. *Journal of Computational Physics*, 28(3), 357–375. [https://doi.org/https://doi.org/10.1016/0021-9991\(78\)90058-X](https://doi.org/https://doi.org/10.1016/0021-9991(78)90058-X)
- Gunawan, R., Fusman, I. & Braatz, R. D. (2004). High resolution algorithms for multidimensional population balance equations. *AIChE Journal*, 50(11), 2738–2749. <https://doi.org/10.1002/aic.10228>
- Hao, X., Zhao, H., Xu, Z. & Zheng, C. (2013). Population balance-monte carlo simulation for gas-to-particle synthesis of nanoparticles. *Aerosol Science and Technology*, 47(10), 1125–1133. <https://doi.org/10.1080/02786826.2013.823642>
- Hashemi Amrei, S. M. H. & Dehkordi, A. M. (2013). Discretized n -dimensional population balance for agglomeration. *Industrial and Engineering Chemistry Research*, 52(49), 17487–17500. <https://doi.org/10.1021/ie401287w>
- Hasseine, A., Senouci, S., Attarakih, M. & Bart, H. J. (2015). Two Analytical Approaches for Solution of Population Balance Equations: Particle Breakage Process. *Chemical Engineering and Technology*, 38(9), 1574–1584. <https://doi.org/10.1002/ceat.201400769>
- Hermanto, M. W., Kee, N. C., Tan, R. B. H., Chiu, M., Braatz, R. D., Qiao, Z., Wang, J. (2012). Robust Bayesian Estimation of Kinetics for the Polymorphic Transformation of L-Glutamic Acid Crystals. *AIChE Journal*, 59(4), 215–228. <https://doi.org/10.1002/aic>
- Hu, Q., Rohani, S. & Jutan, A. (2005). Modelling and optimization of seeded batch crystallizers. *Computers and Chemical Engineering*. <https://doi.org/10.1016/j.compchemeng.2004.09.011>
- Kumar, S. & Ramkrishna, D. (1996). On the solution of population balance equations by discretization - II. A moving pivot technique. *Chemical Engineering Science*, 51(8), 1333–1342. [https://doi.org/10.1016/0009-2509\(95\)00355-X](https://doi.org/10.1016/0009-2509(95)00355-X)
- Kumar, S. & Ramkrishna, D. (1997). On the solution of population balance equations by discretization - III. Nucleation, growth and aggregation of particles. *Chemical Engineering Science*, 52(24), 4659–4679. [https://doi.org/10.1016/S0009-2509\(97\)00307-2](https://doi.org/10.1016/S0009-2509(97)00307-2)
- Lam, S. K., Pitrou, A. & Seibert, S. (2015). Numba: a LLVM-based Python JIT compiler. *Proceedings of the Second Workshop on the LLVM Compiler Infrastructure in HPC - LLVM '15*, 1–6. Retrieved from

<http://dx.doi.org/10.1145/2833157.2833162>.%0A<http://dl.acm.org/citation.cfm?doid=2833157.2833162>

- Lin, M., Wu, Y. & Rohani, S. (2019). A kinetic study of crystallization process of imatinib mesylate with polymorphic transformation phenomenon. *Journal of Crystal Growth*, 507 (August 2018), 146–153.  
<https://doi.org/10.1016/j.jcrysgro.2018.10.061>
- Lin, M., Wu, Y. & Rohani, S. (2020a). Identifying the Polymorphic Outcome of Hypothetical Polymorphs in Batch and Continuous Crystallizers by Numerical Simulation. *Crystal Growth and Design*, 20(11), 7312–7319.  
<https://doi.org/10.1021/acs.cgd.0c00986>
- Lin, M., Wu, Y. & Rohani, S. (2020b). Simultaneous Measurement of Solution Concentration and Slurry Density by Raman Spectroscopy with Artificial Neural Network. *Crystal Growth and Design*, 20(3), 1752–1759.  
<https://doi.org/10.1021/acs.cgd.9b01482>
- Miller, S. M. (1993). *Modelling and Quality Control Strategies for Batch Cooling Crystallizers*. University of Texas at Austin. Retrieved from  
<https://books.google.ca/books?id=vLZZtQAACAAJ>
- Myerson, A. S. (2002). Handbook of industrial crystallization. Boston: Butterworth-Heinemann. Retrieved from <http://site.ebrary.com/id/10206621>
- Omar, H. M. & Rohani, S. (2017). Crystal Population Balance Formulation and Solution Methods: A Review. *Crystal Growth and Design*, 17(7), 4028–4041.  
<https://doi.org/10.1021/acs.cgd.7b00645>
- Pedretti, D. & Fernández-garcia, D. (2013). Advances in Water Resources An automatic locally-adaptive method to estimate heavily-tailed breakthrough curves from particle distributions. *Advances in Water Resources*, 59, 52–65.  
<https://doi.org/10.1016/j.advwatres.2013.05.006>
- Power, G., Hou, G., Kamaraju, V. K., Morris, G., Zhao, Y. & Glennon, B. (2015). Design and optimization of a multistage continuous cooling mixed suspension, mixed product removal crystallizer. *Chemical Engineering Science*, 133, 125–139.  
<https://doi.org/10.1016/j.ces.2015.02.014>
- Qiu, Y. & Rasmuson, ke C. (1990). Growth and dissolution of succinic acid crystals in a batch stirred crystallizer. *AIChE Journal*, 36(5), 665–676.  
<https://doi.org/10.1002/aic.690360504>
- Ramabhadran, T. E., Peterson, T. W. & Seinfeld, J. H. (1976). Dynamics of aerosol coagulation and condensation. *AIChE Journal*, 22(5), 840–851.  
<https://doi.org/10.1002/aic.690220505>
- Rosner, D. E., McGraw, R. & Tandon, P. (2003). Multivariate population balances via moment and Monte Carlo simulation methods: An important sol reaction engineering bivariate example and “mixed” moments for the estimation of

- deposition, scavenging, and optical properties for populations of nonspherical. *Industrial and Engineering Chemistry Research*, 42(12), 2699–2711. <https://doi.org/10.1021/ie0206271>
- Sanjeev, K. & D., R. (1996). On the solution of population balance equations by discretization—I. A fixed pivot technique, *51*(8), 1311–1332.
- Shu, Y. D., Liu, J. J., Zhang, Y. & Wang, X. Z. (2020). Considering nucleation, breakage and aggregation in morphological population balance models for crystallization processes. *Computers and Chemical Engineering*, 136, 106781. <https://doi.org/10.1016/j.compchemeng.2020.106781>
- Singh, M., Singh, R., Singh, S., Walker, G. & Matsoukas, T. (2020). Discrete finite volume approach for multidimensional agglomeration population balance equation on unstructured grid. *Powder Technology*, 376, 229–240. <https://doi.org/10.1016/j.powtec.2020.08.022>
- Sole-mari, G., Bolster, D., Fernández-garcia, D. & Sanchez-vila, X. (2019). Advances in Water Resources Particle density estimation with grid-projected and boundary-corrected adaptive kernels ☆. *Advances in Water Resources*, 131(May), 103382. <https://doi.org/10.1016/j.advwatres.2019.103382>
- Szilágyi, B., Agachi, P. Ş. & Lakatos, B. G. (2015). Numerical analysis of crystallization of high aspect ratio crystals with breakage. *Powder Technology*, 283, 152–162. <https://doi.org/10.1016/j.powtec.2015.05.029>
- Szilagy, B., Borsos, A., Simone, E. & Nagy, Z. K. (2017). *Model Based Estimation of 2D Crystallization Kinetics From Concentration and CLD Measurements. Computer Aided Chemical Engineering* (Vol. 40). Elsevier Masson SAS. <https://doi.org/10.1016/B978-0-444-63965-3.50030-1>
- Szilágyi, B. & Nagy, Z. K. (2016). Graphical processing unit (GPU) acceleration for numerical solution of population balance models using high resolution finite volume algorithm. *Computers and Chemical Engineering*, 91, 167–181. <https://doi.org/10.1016/j.compchemeng.2016.03.023>
- Van Peborgh Gooch, J. R. & Hounslow, M. J. (1996). Monte Carlo Simulation of Size-Enlargement Mechanisms in Crystallization. *AIChE Journal*, 42(7), 1864–1874. <https://doi.org/10.1002/aic.690420708>
- Yoon, C. & McGraw, R. (2004). Representation of generally mixed multivariate aerosols by the quadrature method of moments: II. Aerosol dynamics. *Journal of Aerosol Science*, 35(5), 577–598. <https://doi.org/10.1016/j.jaerosci.2003.11.012>
- Yu, X., Hounslow, M. J. & Reynolds, G. K. (2015). Accuracy and Optimal Sampling in Monte Carlo Solution of Population Balance Equations. *AIChE Journal*, 59(4), 215–228. <https://doi.org/10.1002/aic>

Yuan, C., Laurent, F. & Fox, R. O. (2012). An extended quadrature method of moments for population balance equations. *Journal of Aerosol Science*, 51, 1–23.  
<https://doi.org/10.1016/j.jaerosci.2012.04.003>

## **Chapter 6**

### **Conclusions and Recommendations**



## Chapter 6 Conclusions and Recommendations

The studies in this thesis proposed several methodologies and novel process analytical technologies (PATs) to improve the crystallization field. The results contribute to developing efficient crystallization processes for new crystalline products while maintaining the crystalline product quality via process monitoring and control. In addition, an efficient algorithm was developed for the solution of the multi-dimension population balance equation, in the presence of agglomeration and breakage. The conclusions and recommendations for future study are given in the following sections.

### 6.1. Conclusions

The most significant achievement in this thesis was the development of the image-based PAT powered by the deep learning models for online measurement of the multi-dimensional particle size distribution and morphological information, which filled in the gaps of the conventional particle sizing PATs. Our studies confirmed the superb accuracy of the proposed PAT in a challengingly high solids concentration, which largely resolved the bottleneck that limited the application of the image-based PATs. The classification capability of the deep learning model was used to realize the quantitative measurement of agglomeration level and build the size distributions of different classes of visually distinct particles, which were impossible for the existing solid-phase monitoring PATs. The computerized crystallization platform powered by the image-based PAT demonstrated the potentials to automate the time-consuming experiments for determining the metastable zone width (MSZW) and induction time of a crystallization system, which was an important contribution to the crystallization field that could simplify and speed up the research and development stage of a crystallization process. In addition, the computational efficiency issues of solving a multi-dimensional population balance equation model with the discretization methods were addressed using the developed population array method, whose accuracy and efficiency were validated for various complicated cases such as polymorphic transformation, continuous operation, and agglomeration and breakage. The efficient computation of the PA method will greatly

benefit the use of model predictive control that requires timely model optimization and the modeling of crystal morphology that requires solving a complex multi-dimensional PBE. The summaries and contributions of the individual subjects are detailed below.

#### 6.1.1. Development of Image-based PAT for Particle Size and Shape Characterization

The measurement of multi-dimensional crystal size and shape was achieved using the proposed image-based PAT powered by the novel deep learning algorithms. The imaging hardware was designed and built using microcontrollers and 3D-printing rapid prototyping technologies. The accuracy of the image analysis model was confirmed by comparing it with the established particle sizing techniques and the manually examined images. The neural network image analysis method was able to classify the particles and perform high-accuracy object segmentation for the contacting or overlapping objects. We proposed the scale-invariant solid concentration measurement, pixel fill ratio (PFR), to quantify the image complexity. The challenging image analysis task in the highly concentrated slurry was performed to demonstrate the potential of the proposed method. We successfully extracted accurate size information from the slurry of three times higher solids concentration than that of the previous studies reported by Borchert et al. (2014). The ability to differentiate the particles using the classification of the deep learning model enabled measuring the individual size distributions of multiple classes of visually distinct particles, for example, tracking the polymorphic forms of the L-glutamic acid (Gao et al., 2018). The effort to build a robust deep learning model was significantly reduced with a proposed progressive labeling strategy. This study confirmed that the deep learning-based image analysis algorithm could serve as an effective process monitoring technology for the crystallization process.

The developed PAT was deployed to monitor the seeded batch crystallization process of the aqueous taurine solution to further exploit the potential of multi-dimensional size and shape characterization. The classification capability was extended to detect and quantify the agglomeration. It was shown that the proposed PAT was able to effectively track the

crystal counts, the two-dimensional CSDs, the aspect ratios, and the agglomeration levels. The accuracy of size measurement and sensitivity of nucleation detection outperformed the conventional PATs such as the FBRM.

In the experimental study, the image-based PAT revealed a negative correlation between the seed loading and the level of agglomeration, which was confirmed by the previous study (Kubota et al., 2001). This study demonstrated the promising application of the image-based PAT in optimizing the seeding strategy of a crystallization system prone to agglomeration, which not only improves productivity but also provides a desired narrow size distribution.

Finally, the multi-dimensional size recorded by the image-based PAT and the solute concentration measured by Raman spectroscopy were used to estimate the parameters of the nucleation and growth models. The simulation study confirmed the consistent concentration prediction and the estimation of the count density and multi-dimensional sizes prior to the agglomeration onset, which motivated the development of an efficient numerical solver that can handle complex crystallization mechanisms such as agglomeration and breakage.

### 6.1.2. Development of An Automated Crystallization Platform

The experience in successfully designing and building the homemade imaging system for the image-based PAT, motivated the development of an automated versatile crystallization platform. In this work, we integrated a few automated laboratory instruments using the IoT wireless microcontroller and 3D-printing techniques. The various automated instruments included switch valves that enabled rapid temperature switching between two thermostat water baths and the stirring motor assembly that allowed remote control and monitoring of the crystallizer temperature and the stirring rate. The software architecture was discussed, and the repositories of the source code were listed in Appendix. B. The proposed experimental setup was used for the automated

measurement of the metastable zone width (MSZW) and the induction time, which showed the potential to automatically carry out the lengthy experiments and data processing works encountered in crystallization research.

### 6.1.3. Development of An Efficient Population Array (PA) Numerical Solver for Modelling Crystallization Process

Modeling is an effective way to process and summarize the large amount of data generated by the proposed PAT. The significance of a reproducible, efficient, and general numerical solver that could handle multi-dimensional growth, agglomeration, and breakage was recognized. Therefore, we developed a computationally efficient and accurate numerical PBE solution method. In the proposed population array (PA) method, the crystals are tracked as the pivots and no discretization grid was used, which avoided the CSD leaking problem due to the insufficient grid limit and the numerical difficulties such as numerical diffusion and dispersion. The efficiency and accuracy of the PA method are guaranteed by performing only the necessary computation with the existing crystals. The simulation time step is decoupled from the grid of the internal coordinates, allowing the larger simulation step size without affecting the stability. An efficient row compression algorithm is used to speed up the PA method by merging the pivots with duplicating or similar internal coordinates while maintaining the conservation of crystal mass and count. The analytical solution or the solution obtained using a very fine grid was used to validate the accuracy of the nucleation, growth, agglomeration, and breakage simulated by the PA method. The complicated operations such as polymorphic transformation and continuous processes were tested to ensure the PA method can be generalized for broader simulation cases. The PA method shows superior computational efficiency especially for the multi-dimensional simulations, which makes it an ideal tool to facilitate processing the multi-dimensional size measurements obtained using the image-based PAT.

## 6.2. Recommendation of The Future Works

1. Develop a robust insertable imaging probe for the image-based PAT.

The proposed image-based PAT relied on the homemade flow-through cell imaging system for acquiring sharp microscopic images. The main advantage of the flow-through cell is to alleviate the space constraints in the overhead of a laboratory crystallizer. However, there are a few limitations and drawbacks associated with the use of external circulation. First, the crystals and other impurities may stick to the inside of the cell that are difficult to remove, resulting in irreversible deterioration in the image quality. Also, the external circulation may cause undesired heat transfer and nucleation outside the crystallizer, especially when the crystallizer temperature is much higher than the room temperature. The solution was to use resistive heating coils on the external tubing and flow cell. However, controlling the temperature of the heating coil requires extra feedback control, which complicates the problem. With an insertable imaging probe, the window can be cleaned easily, and the issues caused by the external circulation are also resolved. Developing the insertable probe involves multi-discipline engineering work that requires proper optical design, mechanical sealing, and software development. Despite the difficulty and cost, it is worthwhile to equip the image-based PAT with the hardware for broader applications.

2. Set up benchmark procedures and datasets to quantify the performance of the image analysis models.

Motivated by the tremendous demand in various applications such as remote sensing, autonomous driving car, and medical diagnosis, the computer vision algorithms and deep learning models are iterating at a considerable speed. In the thesis, two different deep learning-based image analysis models were used for different tasks. It is important to follow up on the trend and upgrade the image analysis algorithm to the latest state-of-the-art. The researchers and engineers in the computer vision field have set up several

contests as the benchmark protocol to unify the comparison of the speed and accuracy of the emerging image analysis models with the representative image dataset (Lin et al., 2014). However, there is no such benchmark for the crystallization image analysis field. It is recommended to set up a standard dataset using different imaging hardware and a reproducible benchmark protocol to compare the performance of the image analysis models.

### 3. Develop the solids addition device for the automated crystallization platform.

The automated crystallization platform could automate the studies of the measurement of the metastable zone width (MSZW) and the induction time. However, to investigate the kinetic behavior at different saturated concentrations, the material had to be manually added. To adjust the saturated concentration of the crystallization system, one can start from the high saturated concentration, and use a controlled dosing pump to feed solvent into the crystallizer to dilute the concentration. Alternatively, an automated solids addition device could be designed that feeds the crystals into the system to increase the solute concentration. This device enables not only the fully automated MSZW and induction time experiments at different saturated concentrations, but also allows the automated experiments for investigating the optimal seeding level.

### 4. Reconstruct the population array (PA) for visualization and number density estimation


The proposed population array (PA) is able to efficiently solve the population balance equation. However, unlike the grid data generated by the discretization method, the data in the population array cannot be directly visualized or used to compute the number density. In Chapter 5, the histogram and kernel density estimation (KDE) approaches were introduced. It is recommended to investigate the estimation of the optimal parameters for these approaches to generate reproducible results without human decision and intervention.


### 6.3. References


- Borchert, C., Temmel, E., Eisenschmidt, H., Lorenz, H., Seidel-Morgenstern, A. & Sundmacher, K. (2014). Image-based in situ identification of face specific crystal growth rates from crystal populations. *Crystal Growth and Design*, 14(3), 952–971. <https://doi.org/10.1021/cg401098x>
- Gao, Z., Wu, Y., Bao, Y., Gong, J., Wang, J. & Rohani, S. (2018). Image Analysis for In-line Measurement of Multidimensional Size, Shape, and Polymorphic Transformation of L-Glutamic Acid Using Deep Learning-Based Image Segmentation and Classification. *Crystal Growth and Design*, 18(8), 4275–4281. <https://doi.org/10.1021/acs.cgd.8b00883>
- Kubota, N., Doki, N., Yokota, M. & Sato, A. (2001). Seeding policy in batch cooling crystallization. *Powder Technology*, 121(1), 31–38. [https://doi.org/10.1016/S0032-5910\(01\)00371-0](https://doi.org/10.1016/S0032-5910(01)00371-0)
- Lin, T. Y., Maire, M., Belongie, S., Hays, J., Perona, P., Ramanan, D., ... Zitnick, C. L. (2014). Microsoft COCO: Common objects in context. *Lecture Notes in Computer Science (Including Subseries Lecture Notes in Artificial Intelligence and Lecture Notes in Bioinformatics)*, 8693 LNCS(PART 5), 740–755. [https://doi.org/10.1007/978-3-319-10602-1\\_48](https://doi.org/10.1007/978-3-319-10602-1_48)


# Appendices


## Appendix A: Copyright permission








  
Home

  
Help

  
Email Support

  
Sign in

  
Create Account



**ACS Publications**  
Most Trusted. Most Cited. Most Read.

**A Deep Learning Image-Based Sensor for Real-Time Crystal Size Distribution Characterization**

**Author:** V. Manee, W. Zhu, J. A. Romagnoli

**Publication:** Industrial & Engineering Chemistry Research

**Publisher:** American Chemical Society

**Date:** Dec 1, 2019

Copyright © 2019, American Chemical Society

**PERMISSION/LICENSE IS GRANTED FOR YOUR ORDER AT NO CHARGE**

This type of permission/license, instead of the standard Terms & Conditions, is sent to you because no fee is being charged for your order. Please note the following:

- Permission is granted for your request in both print and electronic formats, and translations.
- If figures and/or tables were requested, they may be adapted or used in part.
- Please print this page for your records and send a copy of it to your publisher/graduate school.
- Appropriate credit for the requested material should be given as follows: "Reprinted (adapted) with permission from (COMPLETE REFERENCE CITATION). Copyright (YEAR) American Chemical Society." Insert appropriate information in place of the capitalized words.
- One-time permission is granted only for the use specified in your request. No additional uses are granted (such as derivative works or other editions). For any other uses, please submit a new request.

If credit is given to another source for the material you requested, permission must be obtained from that source.

[BACK](#)

[CLOSE WINDOW](#)

© 2021 Copyright - All Rights Reserved | [Copyright Clearance Center, Inc.](#) | [Privacy statement](#) | [Terms and Conditions](#)  
Comments? We would like to hear from you. E-mail us at [customer@copyright.com](mailto:customer@copyright.com)





RightsLink®



Home



Help



Email Support



Sign in



Create Account

### Particle characterization with on-line imaging and neural network image analysis

**Author:** Yuanyi Wu, Mengxing Lin, Sohrab Rohani

**Publication:** Chemical Engineering Research and Design

**Publisher:** Elsevier

**Date:** May 2020

© 2020 Institution of Chemical Engineers. Published by Elsevier B.V. All rights reserved.

#### Journal Author Rights

Please note that, as the author of this Elsevier article, you retain the right to include it in a thesis or dissertation, provided it is not published commercially. Permission is not required, but please ensure that you reference the journal as the original source. For more information on this and on your other retained rights, please visit: <https://www.elsevier.com/about/our-business/policies/copyright#Author-rights>

BACK

CLOSE WINDOW

## Appendix B: Source code repositories

- Chapter 4:

Data hooking applications

**iC Raman**      <https://github.com/wuyuanyi135/Raman-MQTT-Broker>

**iC FBRM**      <https://github.com/UWO-CCPL/FBRMBroker>

Microcontroller firmware

### DS18B20

**Temperature sensor**      <https://github.com/wuyuanyi135/ArduinoSimpleDS18B20>

### Julabo FP50

**Water bath**      [https://github.com/wuyuanyi135/Julabo\\_FP50\\_DS18B20\\_Control](https://github.com/wuyuanyi135/Julabo_FP50_DS18B20_Control)

**Peristaltic pump driver**

<https://github.com/wuyuanyi135/ArduinoSimpleStepperPumpDriver>

**Switch valves**      <https://github.com/wuyuanyi135/ArduinoSwitchingValve>

**Stirring motor**      <https://github.com/wuyuanyi135/ArduinoTachoStir>

- Chapter 5:

Demo source code for comparing the computational efficiency and accuracy with the reference high-resolution discretization method is available at:

[https://github.com/wuyuanyi135/Population\\_array\\_demonstration\\_code](https://github.com/wuyuanyi135/Population_array_demonstration_code)

## Curriculum Vitae

**Name:** Yuanyi Wu

**Post-secondary Education and Degrees:** Zhejiang University of Technology  
Hangzhou, Zhejiang, China  
2012 – 2014 B.A.

The University of Western Ontario  
London, Ontario, Canada,  
2014 – 2016 B.E.Sc.

The University of Western Ontario  
London, Ontario, Canada,  
2016 – 2021 Ph.D.

**Honors** Dean’s Honor List, 2014-2015

**Related Work** Teaching assistant of Process Dynamics and Control and Engineering

**Experience:** Thermodynamics  
The University of Western Ontario (2016 – 2020)

### Publications:

A version of Chapter 2 has been published in *Chemical Engineering Research and Design*: Wu, Y., Lin, M. & Rohani, S. (2020). Particle characterization with on-line imaging and neural network image analysis. *Chemical Engineering Research and Design*, 157, 114-125.

A version of Chapter 3 has been submitted to *Chemical Engineering Research and Design* under the title: Deep Learning-Based Oriented Object Detection for In-Situ Image Monitoring and Analysis: A Process Analytical Technology (PAT) Application for Taurine Crystallization. The status is under review.

A version of Chapter 4 will be submitted to *Organic Process Chemistry and Development* under the title: Automated measurement of the MSZW and induction time: Comparison of a new platform to the existing platforms

A version of Chapter 5 will be submitted to *AIChE Journal* under the title: A New Highly Efficient and Stable Population Array (PA) Algorithm to Solve Multi-Dimension Population Balance Equation in the Presence of Agglomeration and Breakage

### Co-authored Publications:

- Gao, Z., Wu, Y., Bao, Y., Gong, J., Wang, J. & Rohani, S. (2018). Image analysis for in-line measurement of multidimensional size, shape, and polymorphic transformation of l-glutamic acid using deep learning-based image segmentation and classification. *Crystal Growth & Design*, 18(8), 4275-4281.
- Gao, Z., Wu, Y., Gong, J., Wang, J. & Rohani, S. (2019). Continuous crystallization of  $\alpha$ -form L-glutamic acid in an MSMPR-Tubular crystallizer system. *Journal of Crystal Growth*, 507, 344-351.
- Lin, M., Wu, Y. & Rohani, S. (2020). Simultaneous measurement of solution concentration and slurry density by Raman spectroscopy with artificial neural network. *Crystal Growth & Design*, 20(3), 1752-1759.
- Gao, Z., Wu, Y., Wu, Y., Gong, J., Bao, Y., Wang, J. & Rohani, S. (2018). Self-induced nucleation during the antisolvent crystallization process of candesartan cilexetil. *Crystal Growth & Design*, 18(12), 7655-7662.
- Lin, M., Wu, Y. & Rohani, S. (2020). Identifying the Polymorphic Outcome of Hypothetical Polymorphs in Batch and Continuous Crystallizers by Numerical Simulation. *Crystal Growth & Design*, 20(11), 7312-7319.
- Ahmadi, S., Wu, Y. & Rohani, S. (2019). Molecular dynamics simulation of homogeneous nucleation of supersaturated potassium chloride (KCl) in aqueous solutions. *CrystEngComm*, 21(48), 7507-7518.
- Gao, Z., Zhu, D., Wu, Y., Rohani, S., Gong, J. & Wang, J. (2017). Motion-Based Multiple Object Tracking of Ultrasonic-Induced Nucleation: A Case Study of l-Glutamic Acid. *Crystal Growth & Design*, 17(10), 5007-5011.
- Rohani, S. (2017). (seven chapters as the second author) Coulson and Richardson's Chemical Engineering: Volume 3B: Process Control. Netherlands: Elsevier Science.

### Conferences:

- Wu, Y. & Rohani, S. (2018, November). Process Control Laboratory on Arduino and Simulink Platform. In 2018 AIChE Annual Meeting. AIChE.
- Gao, Z., Zhu, D., Wu, Y., Rohani, S., Gong, J. & Wang, J. (2017, October). Ultrasound-assisted crystallization in a two-stage continuous MSMPR crystallizer system. In 2017 AIChE Annual Meeting. AIChE.
- Gao, Z., Wu, Y., Gong, J., Bao, Y., Wang, J. & Rohani, S. (2018, November). Imaging Crystallization Using Deep Learning to Quantitatively Track the Polymorphic Transformation of Carbamazepine. In 2018 AIChE Annual Meeting. AIChE.